



# Nonlinear aeroelastic analysis of airfoils: bifurcation and chaos

B.H.K. Lee<sup>a,\*</sup>, S.J. Price<sup>b</sup>, Y.S. Wong<sup>c</sup>

<sup>a</sup>*Aerodynamics Laboratory, Institute for Aerospace Research, National Research Council, Ottawa,  
Ontario, Canada K1A 0R6*

<sup>b</sup>*Department of Mechanical Engineering, McGill University, Montreal, Quebec, Canada H3A 2K6*

<sup>c</sup>*Department of Mathematical Sciences, University of Alberta, Edmonton, Alberta, Canada T6G 2G1*

Received 17 July 1998

## Contents

1. Introduction	207	5. Bifurcation and chaos of airfoils with structural nonlinearities	248
2. Nonlinearities encountered in aeroelastic behavior of aircraft structures	208	5.1. Stability and bifurcation analysis	248
2.1. Structural nonlinearities	208	5.2. Cubic nonlinearity	257
2.2. Aerodynamics nonlinearities	217	5.3. Freeplay with preload	271
3. Formulation of the nonlinear aeroelastic equations for airfoils	221	5.4. Hysteresis nonlinearity	286
3.1. Equations with structural nonlinearities and subsonic aerodynamics	221	5.5. Forced oscillations	296
3.2. Equations with nonlinear aerodynamics	228	6. Bifurcation and chaos of airfoils with aerodynamic nonlinearities	300
4. Solution techniques of equations with structural nonlinearities	239	6.1. Transonic flows	300
4.1. Finite difference scheme	239	6.2. Dynamic stall	308
4.2. Runge–Kutta scheme	240	7. Gust effects: airfoils in longitudinal atmospheric turbulence	319
4.3. Describing function	242	8. Conclusions	326
4.4. Analytical techniques	245	References	328
		Appendix	332

## Nomenclature

$a_h$	non-dimensional distance from airfoil mid-chord to elastic axis	$C_L$	aerodynamic lift coefficient
$b$	airfoil semi-chord	$C_M$	pitching moment coefficient
$C_i$	generalized damping	$c$	chord
		DOF	degree of freedom

---

\* Corresponding author. Tel.: 001 613 998 3401; fax: 001 613 998 1281; e-mail: ben.lee@nrc.ca.

$e$	total energy	$u$	velocity in the $x$ -direction
$F_i$	generalized force of $i$ th mode	$u_g$	gust velocity
$G(\xi)$	structural nonlinearity in plunge	$v$	velocity in the $y$ -direction
$G_{wn}$	Gaussian white noise	$w$	velocity in the $z$ -direction
$h$	plunge displacement	$\mathbf{X}$	system variable vector
$\mathbf{J}$	Jacobian matrix	$\mathbf{X}_E$	system equilibrium point
$K_i$	generalized stiffness of $i$ th mode	$x_\alpha$	non-dimensional distance from elastic axis to center of mass
$K_\alpha, K_\xi$	linear stiffness in pitch and plunge	$\mathbf{y}$	variable vector
$k$	reduced frequency based on semi-chord ( $=\omega b/U$ )	$\alpha$	pitch angle of airfoil
$k_c$	reduced frequency based on chord ( $=\omega c/U$ )	$\alpha_A$	pitch angle amplitude of limit cycle oscillation
$L$	turbulence scale	$\alpha_D$	dynamic stall angle
LCO	limit cycle oscillations	$\alpha_S$	static stall angle
$L_{n,d}$	non-dimensional turbulence scale ( $=L/b$ )	$\alpha_W$	unsteady decay parameter
$M$	Mach number	$\beta_\alpha, \beta_\xi$	coefficients of cubic spring in pitch and plunge
$M_i$	generalized mass of $i$ th mode	$\delta$	pitch angle for the central region of the freeplay stiffness, see Fig. 2b
$M(\alpha)$	structural nonlinearity in pitch	$\varepsilon_1, \varepsilon_2$	constants in Wagner's function
$m$	airfoil mass	$\Phi_g$	gust velocity PSD
$P$	externally applied force	$\Phi_{g,nd}$	non-dimensional gust velocity PSD
PDD	probability density distribution	$\Phi_{w,n}$	white noise PSD
PSD	power spectral density	$\phi$	Wagner's function
$p$	pressure	$\phi_i$	mode shape of $i$ th mode
$Q$	externally applied moment	$\lambda$	eigenvalue
$Q_o$	amplitude of applied moment	$\mu$	airfoil/air mass ratio ( $=m/\pi\rho b^2$ )
$q_i$	generalized coordinates	$\rho$	density
$R$	response amplitude of pitch motion	$\sigma_g^2$	gust velocity variance
$r$	response amplitude of plunge motion	$\sigma_{g,nd}^2$	non-dimensional gust velocity variance
$r_\alpha$	radius of gyration about elastic axis	$v$	parameter
$S$	static moment about elastic axis	$\tau$	non-dimensional time ( $=Ut/b$ )
$T$	temperature	$\nu$	viscosity
TSD	transonic small disturbance	$\omega$	frequency
$t$	time	$\omega_\alpha, \omega_\xi$	natural frequencies in pitch and plunge
$U$	free stream velocity	$\bar{\omega}$	frequency ratio ( $=\omega_\xi/\omega_\alpha$ )
$U_L$	linear flutter speed	$\xi$	non-dimensional plunge displacement ( $=h/b$ )
$U_m$	mean free stream velocity	$\xi_A$	plunge amplitude of limit cycle oscillation
$U^*$	non-dimensional velocity ( $=U/b\omega_\alpha$ )	$\psi_1, \psi_2$	constants in Wagner's function
$U_1^*, U_2^*$	non-dimensional bifurcation speeds	$\zeta_\alpha, \zeta_\xi$	viscous damping ratios in pitch and plunge
$U_m^*$	non-dimensional velocity ( $=U_m/b\omega_\alpha$ )		
$U_L^*$	non-dimensional linear flutter speed		

## Abstract

Different types of structural and aerodynamic nonlinearities commonly encountered in aeronautical engineering are discussed. The equations of motion of a two-dimensional airfoil oscillating in pitch and plunge are derived for a structural nonlinearity using subsonic aerodynamics theory. Three classical nonlinearities, namely, cubic, freeplay and hysteresis are investigated in some detail. The governing equations are reduced to a set of ordinary differential equations suitable for numerical simulations and analytical investigation of the system stability. The onset of Hopf-bifurcation, and amplitudes and frequencies of limit cycle oscillations are investigated, with examples given for a cubic hardening spring. For various geometries

of the freeplay, bifurcations and chaos are discussed via the phase plane, Poincaré maps, and Lyapunov spectrum. The route to chaos is investigated from bifurcation diagrams, and for the freeplay nonlinearity it is shown that frequency doubling is the most commonly observed route. Examples of aerodynamic nonlinearities arising from transonic flow and dynamic stall are discussed, and special attention is paid to numerical simulation results for dynamic stall using a time-synthesized method for the unsteady aerodynamics. The assumption of uniform flow is usually not met in practice since perturbations in velocities are encountered in flight. Longitudinal atmospheric turbulence is introduced to show its effect on both the flutter boundary and the onset of Hopf-bifurcation for a cubic restoring force. © 1999 Elsevier Science Ltd. All rights reserved.

---

## **1. Introduction**

Aeroelasticity is a multi-disciplinary field of study dealing with the interaction of inertia, structural and aerodynamic forces. Classical theories assume linear aerodynamics and structures, and the problem reduces to the solution of a set of linear equations that can readily be programmed for the computer. For many decades, the classical approach has been successful in providing approximate estimates of aircraft response to gust, turbulence and external excitations. The flutter boundaries are often quite accurately predicted when compared to flight test results. However, when the airspeed increases to high subsonic or transonic Mach numbers, linear aerodynamics usually give insufficiently accurate results, an example of which is the transonic dip that linear aerodynamics fail to detect. Also, flow separation and shock oscillations can introduce phenomena, such as limit cycle oscillations which classical aeroelasticity is unable to handle. Nonlinear aerodynamic effects are more difficult to analyze since the fluid motion is governed by equations where analytical solutions are practically non-existent. Usually, we have to resort to numerical techniques to solve the aerodynamic equations. Coupling them to the structural motion can be achieved using a numerical time marching scheme. The computation is usually extremely involved and time-consuming, and often only a specific aircraft configuration or flight condition is analyzed.

Structural nonlinearities arise from worn hinges of control surfaces, loose control linkages, material behavior and various other sources. Aging aircraft and combat aircraft that carry heavy external stores are more likely to be influenced by effects associated with nonlinear structures. This type of nonlinearity can be treated as a concentrated nonlinearity, and usually can be approximated by one of the three classical structural nonlinearities, namely, cubic, bilinear and hysteresis. In this review, emphasis is placed on structural nonlinearities since they can be analyzed more readily using existing theories in nonlinear system dynamics. Stability, bifurcation and chaos are amongst the subjects commonly encountered in nonlinear aeroelasticity where tools developed to study nonlinear dynamics problems can readily be applied. In order to limit the complexity of the aeroelastic system with structural nonlinearities, we consider a two-dimensional airfoil oscillating in pitch and plunge using subsonic aerodynamics where approximate expressions for the force and moment are available. A two-degree-of-freedom system is of particular interest when we deal with binary flutter, which offers a good physical insight into the instability problem. Extending the analysis to more than two modes is straightforward, but the algebra is considerably more complex.

This review gives an introductory exposure to theoretical developments in nonlinear aeroelasticity. In the discussion on analytical solutions, the emphasis is placed on structural nonlinearities, since more theoretical studies have been carried out and published in the open literature on this subject. Section 2.1 discusses the types of structural nonlinearities often used to represent aircraft structures, and introduces the cubic, bilinear and hysteresis springs. The types of aerodynamic nonlinearities associated with transonic Mach numbers, flow separation and viscous effects are given in Section 2.2. The equations of motion of a two-dimensional airfoil with structural nonlinear restoring forces are derived in Section 3.1. These equations are reduced to a set of ordinary differential equations for convenience in numerical simulation and analytical investigation. The equations of motion with nonlinear aerodynamics are discussed in Section 3.2.1 for transonic flows where the full potential, Euler and Navier–Stokes formulations are briefly discussed. The methodology used to analyze separated flows in dynamic stall is given in Section 3.2.2. The solution techniques for airfoil motion in subsonic flows are presented in Section 4.1, where the details of a finite difference scheme are given. The Runge–Kutta method is outlined in Section 4.2, while the describing function technique, whereby the nonlinear spring is replaced by an equivalent linear spring for harmonic motion is derived in Section 4.3. Analytical techniques where the airfoil motion is periodic are derived in Section 4.4. Stability and bifurcation analyses are carried out in Section 5.1, and examples of limit-cycle-oscillations, bifurcations and chaos for the cubic, bilinear and hysteresis springs are discussed in Sections 5.2, 5.3 and 5.4. Examples of forced oscillations are shown in Section 5.5, and the only example available in the literature is for a cubic restoring force. Examples of bifurcation and chaos of airfoil motion with aerodynamic nonlinearities are given in Section 6.1 for transonic flows and Section 6.2 for dynamic stall. Section 7 considers the effect of longitudinal atmospheric turbulence on the dynamics of an airfoil with a hardening cubic structural nonlinearity showing the flutter speed is advanced by the presence of the gust, while the Hopf bifurcation is postponed. Finally, some concluding remarks on the subject of nonlinear aeroelasticity and analysis techniques are given in Section 8.

## **2. Nonlinearities encountered in aeroelastic behavior of aircraft structures**

### *2.1. Structural nonlinearities*

The assumption of structural linearity is frequently made so that the available standard computational methods can be used to determine the divergence and flutter characteristics of aerodynamic surfaces. Linear theory predicts the magnitude of dynamic pressure or flight velocity above which the system under consideration becomes unstable and the motion grows exponentially in time. However, aircraft structures often exhibit nonlinearities that affect not only the flutter speed, but also the characteristics of the motion itself. Little effort has been devoted to nonlinear effects and this subject remained relatively unexplored until the 1950s when Woolston et al. [120,121] and Shen [96] initiated analog and numerical studies on this subject. An understanding of the nonlinear behavior of the system is crucial to the efficient and safe design of aircraft wings and control surfaces.

The structure of an aircraft is very complicated and consequently it is virtually impossible to know the nature of any nonlinearity from knowledge of the behavior of the material and parts of

which it is made. An excellent review of some possible structural nonlinearities and their effect on aeroelastically induced vibrations is given by Brietbach [18,19]. Structural nonlinearities may be classified as being either distributed or concentrated. In general, distributed structural nonlinearities are governed by elastodynamic deformations that affect the whole structure. Concentrated nonlinearities, on the other hand, act locally and are commonly found in control mechanisms or in the connecting parts between wing, pylon, engine or external stores. In this review, we shall consider only concentrated nonlinearities and investigate their effects on the aeroelastic behavior of aerosurfaces.

A thin wing or propeller blade which is being twisted will most likely behave as a cubic hardening spring which becomes stiffer as the angle of twist increases. If buckling occurs, its effects can be approximated by a softening spring whose stiffness decreases when the displacement is increased. This may be of importance to panel flutter. Kinetic heating at high Mach numbers can produce large reductions in structural stiffness. Depending on the temperature and initial conditions, the nonlinearity can be a hardening or softening spring type. The force versus displacement curves are shown in Fig. 1 for both types of cubic nonlinearities. Cubic nonlinearities in one-degree-of-freedom (DOF) mechanical and electrical systems can often be represented by a Duffing's equation which has been the subject of investigation for many years. The two classical books by Stoker [99] and Hayashi [43] give an excellent account of the behavior of Duffing's equation, and more recent studies by Ueda [112] deal with chaotic characteristics of this equation. Experimentally, a cubic hardening spring for a one DOF system can easily be demonstrated in the classroom by vibrating a thin steel strip fastened at one end and driven magnetically by a small coil at the other. Under the correct conditions, the jump phenomenon in Duffing's equation can be simulated.

In power-operated control systems and spring-tab systems, the most common cause for non-linear behavior is backlash in, say, a control linkage. This produces a flat spot nonlinearity which possesses a force–displacement characteristic of the type shown in Fig. 2a. For small displacements the spring offers no resistance to the movement of the control surface. A modified form of the flat

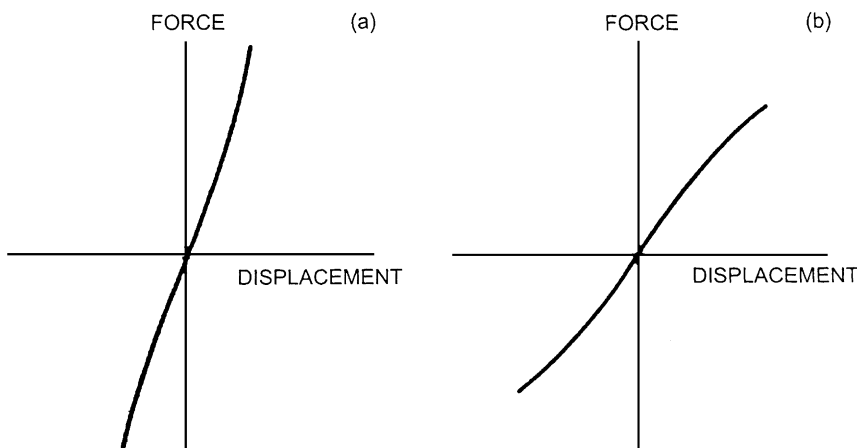


Fig. 1. Force versus displacement curve for (a) cubic hardening spring, (b) cubic softening spring.

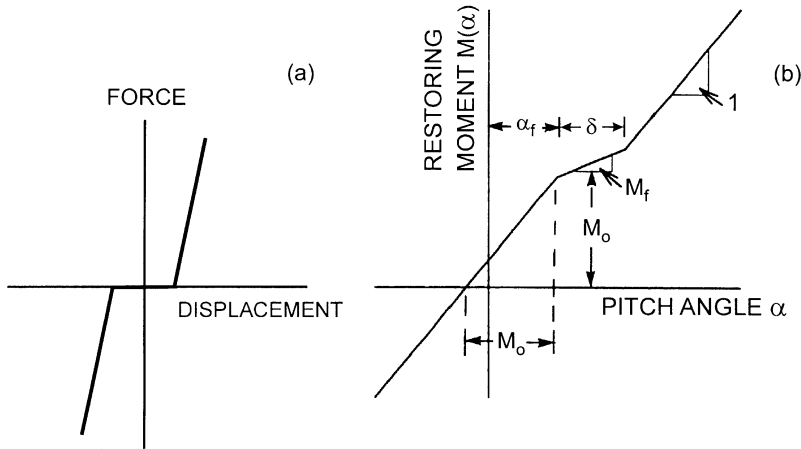


Fig. 2. Force versus displacement curve for (a) flat spot without preload, (b) general bilinear spring.

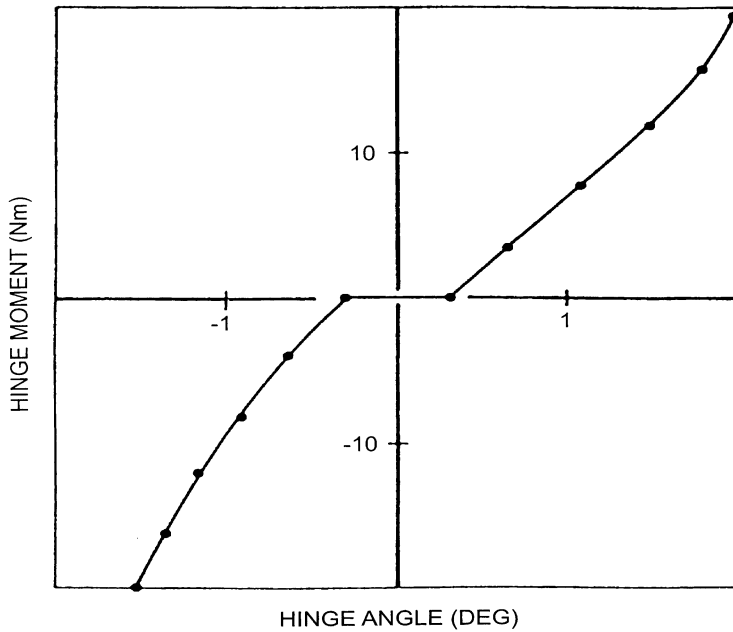


Fig. 3. Aileron hinge moment of a glider versus hinge angle, symmetrical loading (from Ref. [18]).

spot arises if the spring has a preload shown in Fig. 2b. The flat spot can also be replaced by a spring of different stiffness located not at the equilibrium position, but at a certain displacement from it. Fig. 3 shows experimental data of the aileron hinge moment [18] of a glider versus hinge angle for the case of static moments symmetrically acting in the sense opposite to the regular operation of the aileron system. This behavior can be adequately represented by the model shown in Fig. 2a.

Certain types of spring tab systems that use preload springs encounter a stiffness nonlinearity which is important in flutter prediction. This nonlinearity can be deliberately introduced so that the pilot operates the main control surface directly when the airloads are small, while for large airloads, he moves it indirectly by deflecting a tab. The result is that the main surface stiffness coefficient has one value when its displacement is less than a certain amount, and a smaller value at larger displacements. It behaves like a softening spring, though one in which there is a sudden drop in stiffness at a certain displacement rather than one like a cubic softening spring in which there is a continuous decrease in stiffness as the displacement increases. A schematic of a simple spring tab system and the force–deflection curve are shown in Figs. 4 and 5.

Hinges of aircraft control surfaces often exhibit a freeplay with preload characteristics. The preload depends on the aerodynamic forces acting on the control surfaces for given flight

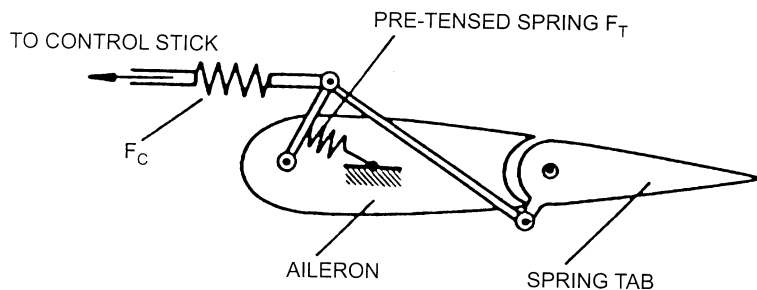


Fig. 4. Sketch of a spring tab system (from Ref. [18]).

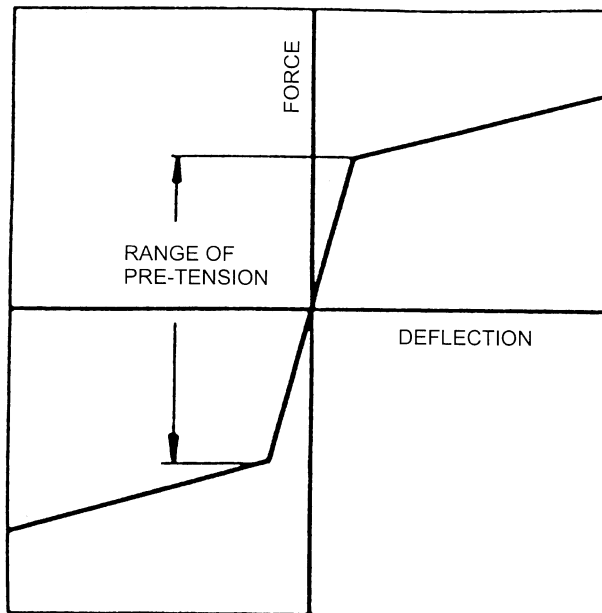


Fig. 5. Schematic force deflection diagram of a pre-tensioned spring tab (from Ref. [18]).

conditions. The F/A-18 aircraft wing folds at about 1/4 span measured from the wing tip. Over years of usage, there is a decrease in stiffness and it was observed from flight tests that with light-to-intermediate weight outboard stores and with wing tip missiles off, the aircraft was subject to lightly damped low-frequency limit cycle oscillations (LCO). There is also another nonlinearity at the outboard leading-edge flap hinge that may cause flap oscillations. The locations of these two hinges on the aircraft wing are shown in Fig. 6. Lee and Tron [66] investigated limit cycle oscillations using a describing function technique. Ground testing of the aircraft was carried out using a static test rig. A typical curve of the hinge moment versus wing-fold rotation is shown in Fig. 7. A small amount of hysteresis is present, but Lee and Tron [66] neglected this in their investigation and treated the nonlinearity as a bilinear spring. Here  $K_1$  is the design stiffness and  $\delta$  is the amount of freeplay. Fig. 8 shows a typical ground test moment–displacement curve for the outboard leading-edge hinge. Again a small hysteresis is detected and the nonlinearity from static tests is a slightly non-symmetrical freeplay without preload when the small amount of hysteresis present is neglected.

Since the flight conditions determine the amount of preload, Lee and Tron [66] used different flap settings and calculated the loads corresponding to one particular test point at  $M = 0.95$  and altitude of 7000 ft above sea level using a transonic small disturbance aerodynamic code. They presented the normalized wing-fold stiffness for three flap settings according to the flap schedule as shown in Table 1.

The equivalent stiffness (to be discussed in Section 4.3) is given in Fig. 9 for the wing-fold hinge. For the leading-edge flap, they used four flap settings and also obtained a set of equivalent stiffness curves.

Another simple cause of nonlinearity is solid friction. A control surface restrained only by solid friction will ideally have a force–velocity characteristic like that shown in Fig. 10a. In practice, it

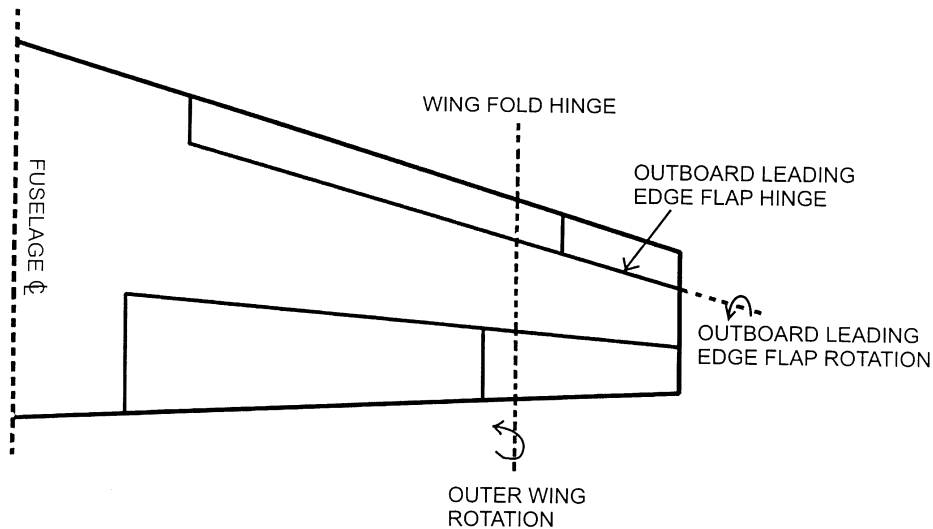


Fig. 6. Schematic of locations of wing-fold and outboard leading-edge flap hinges on the CF-18 wing (from Ref. [66]).



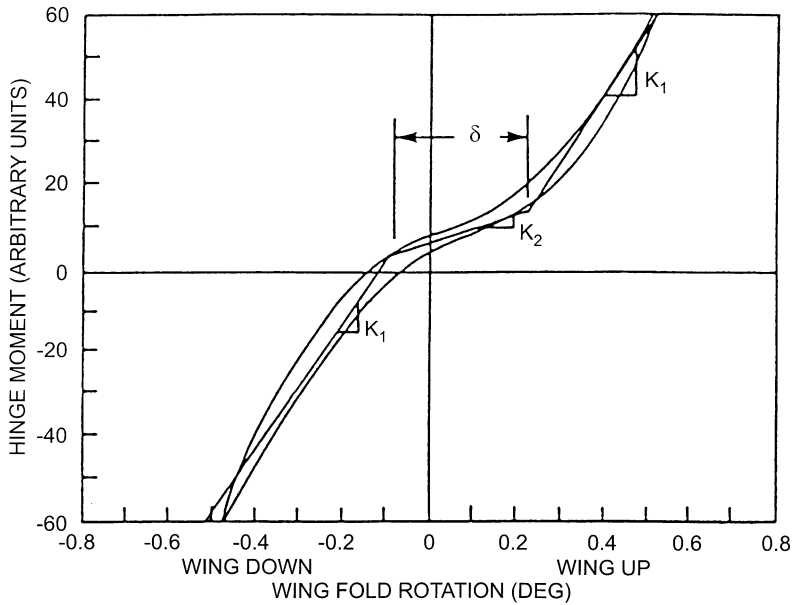


Fig. 7. Moment versus wing-fold hinge rotation of the CF-18 wing (from Ref. [66]).

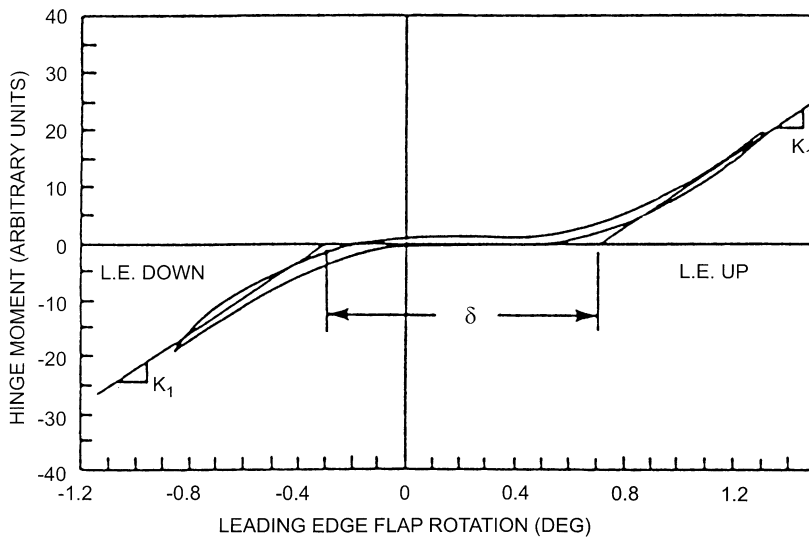


Fig. 8. Moment versus leading-edge flap rotation of the CF-18 wing (from Ref. [66]).

will probably behave more like Fig. 10b. If there is both friction and backlash, we have a hysteresis nonlinearity shown in Fig. 11.

A hysteresis nonlinearity is characterized by a force or moment which increases linearly with displacement until a value is reached at which a jump occurs, after which the system is again linear.

Table 1  
Flap settings

Case	Trailing-edge flap angle (TEF) (deg)	Aileron angle (AIL) (deg)	Leading-edge flap angle (LEF) (deg)
a	1	− 4	2
b	1	− 2	− 3
c	1	4	0

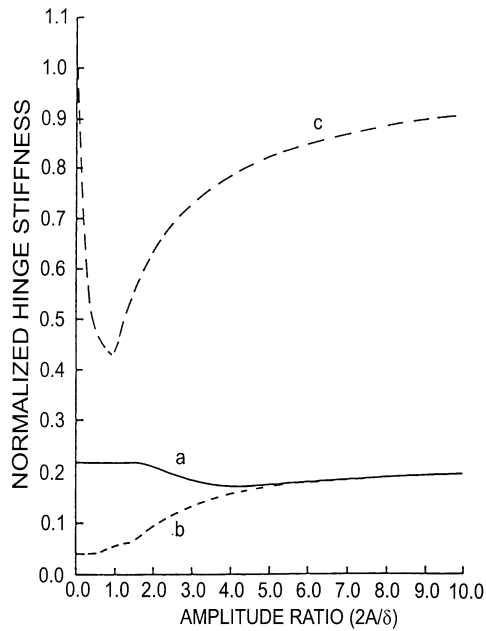


Fig. 9. Normalized equivalent wing-fold stiffness vs. amplitude ratio at flap-aileron settings: curve (a) AIL = − 4°, LEF = 2°; curve (b) AIL = − 2°, LEF = − 3°; curve (c) AIL = 4°, LEF = 0°; TEF is fixed at 1° in all cases, A is the amplitude of LCO and  $\delta$  is the dimensional of the freeplay (from Ref. [66]).

On the return path, a corresponding jump occurs at another value of the force or moment. The hysteresis introduces damping, and the time variations of displacement for a one-DOF mechanical vibration system usually shows damping to vary with amplitude of oscillations for moderately large amplitudes. However, for small amplitudes the system oscillates on a line through the box with a linear spring constant and the hysteretic damping becomes zero. For very large amplitudes, the effect of the hysteresis is small and can be neglected in the limit when the ratio of the width of the hysteresis box  $\delta$  to the oscillation amplitude approaches zero.

Another effect of hysteresis on the structural properties of a vibrating system is to introduce an effectively weaker spring as in the case of a freeplay. At amplitudes of oscillation for which the system passes completely through the hysteresis box, the frequency of oscillation is less than

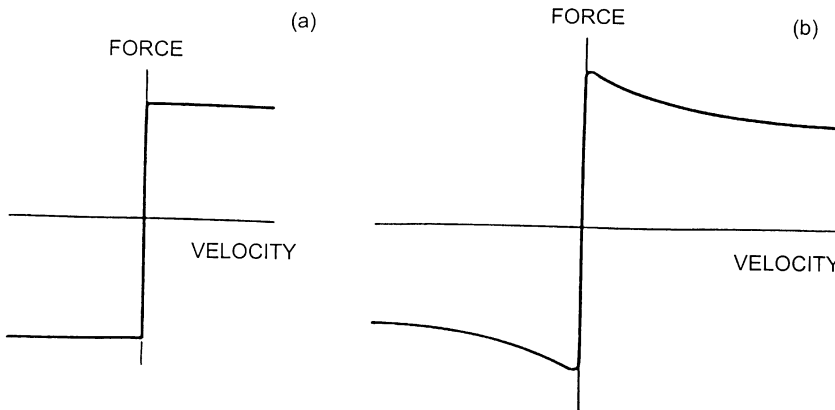


Fig. 10. Schematic of force versus velocity for a solid friction nonlinearity: (a) ideal, (b) practical.

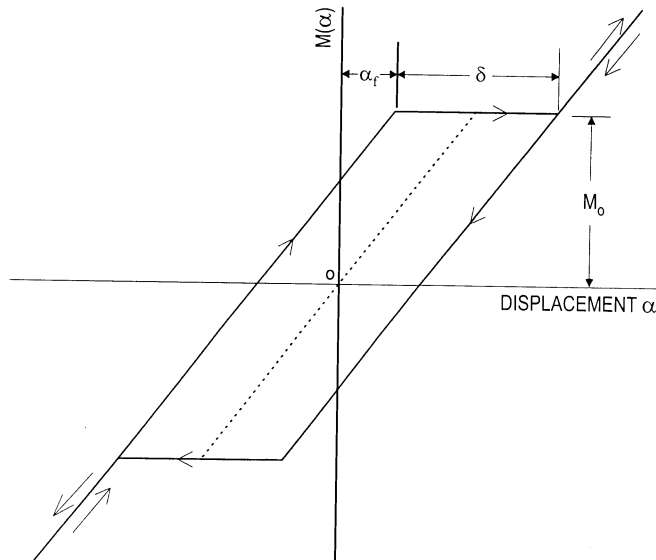


Fig. 11. Notations used for a hysteresis nonlinearity.

the frequency at low amplitudes where the system is linear. For very large amplitudes, the effective stiffness is again approximately linear.

Many structural systems are composed of ductile materials and are assembled in such a way that they exhibit a hardening hysteresis behavior under cyclic loading. An example of a hardening system can be found in riveted and bolted structures where slipping connections provide a major contribution to the overall damping within the structure. In general, this type of hardening hysteresis behavior occurs in the large deformation of composite structural systems where secondary structural elements contribute to the response only after the primary structural elements have

yielded or slipped at the connections. Miller [80] gave a physical model of a hysteresis by considering a structural assemblage consisting of linear springs with linear stiffnesses and a Coulomb friction element with a slip force.

For sweepable wing and sweepable wing mounted stores like the *F-111* aircraft, large nonlinearities can exist because a considerable number of joints (with possible freeplay) and bearings (with freeplay and friction) are necessary. A view of the wing sweep-underwing stores alignment mechanical system [22] for static ground test is shown in Fig. 12. This can be represented schematically by Fig. 13 using a combination of springs and dampers. At low amplitude, the store yaw motion involves the pylon and wing fore and aft stiffness (the pylon behaves as if it was clamped to the wing). When a certain amplitude at which the friction preload in the pylon bearings is exceeded, there is a relative motion of the pylon with respect to the wing, and also the control rod stiffness becomes important after the backlash is exceeded. Hysteresis measurements were made for the store yaw, and typical static test results for an inboard store are shown in Fig. 14.

Basically, the concentrated nonlinearities can be classified roughly into three types. The aero-elastic response can be quite different and these will be the subject of investigation in this review.

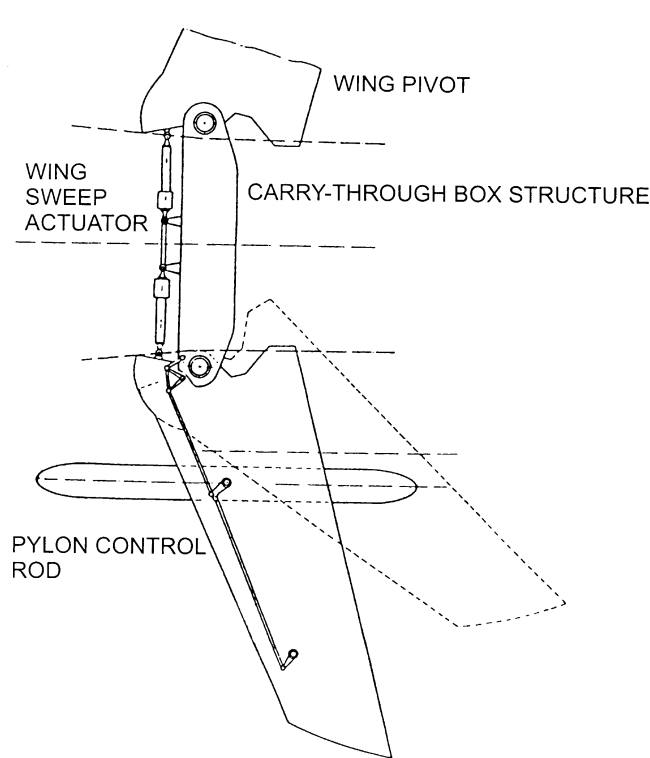


Fig. 12. Schematic view of the wing sweep-underwing stores alignment system (from Ref. [22]).

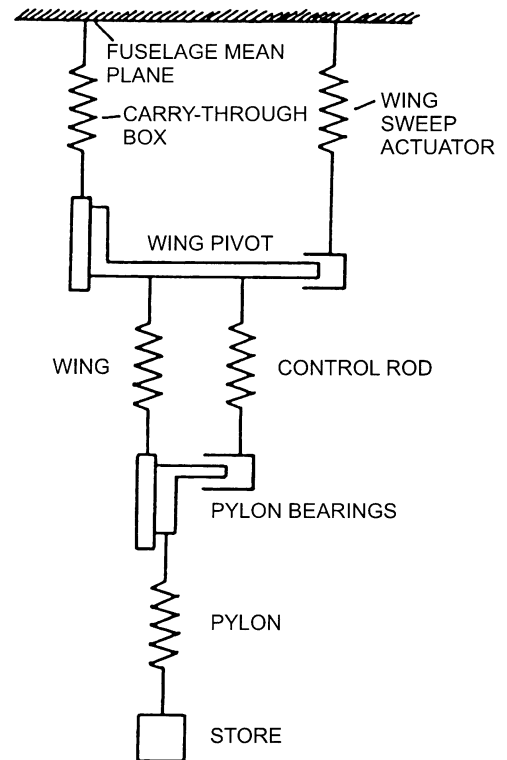


Fig. 13. Idealization of the system for Fig. 12 for wing and store yaw motion (from Ref. [22]).

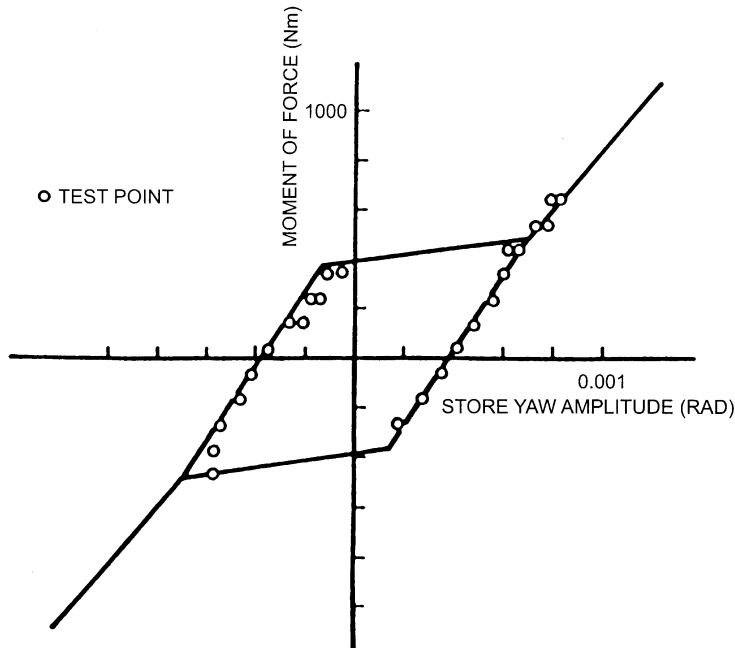


Fig. 14. Measured hysteresis curve of in-board store yaw deflections (from Ref. [22]).

## 2.2. Aerodynamic nonlinearities

When the flow velocity is large, compressibility effects are important and they can have a pronounced influence on the aeroelastic characteristics of the airfoil response compared to that using incompressible theory. We shall consider a few situations in which aerodynamic nonlinearities are important in their interaction with the structural dynamics of the airfoil.

The first is associated with the presence of shock waves in transonic flows. The flow is assumed to be inviscid and separation does not occur. In this situation, the unsteady forces generated by the motion of the shock wave have been shown to destabilize single degree-of-freedom airfoil pitching motion and affect the bending-torsional flutter by lowering the flutter speed at the so called transonic dip regime. Ashley [4] pointed out that the shock waves located on the upper and lower wing surfaces move periodically with large phase lags with the oscillatory airfoil motion. Their motions are the predominant factor in the anomalies observed when the Mach number approaches unity. He quoted an example when the flutter boundary can be 25% lower in dynamic pressure than its conventional shock-free counterpart. The distance traversed by the shocks on the airfoil surfaces depends on the frequency and can be quite large compared with the airfoil motion. A number of computer codes are available to calculate the unsteady airloads at transonic flow conditions. They range from transonic small disturbance formulation [8,9], full potential [49], to the Euler equations [11]. Fig. 15 shows the shock wave time history for plunging oscillation of a NACA 64A006 airfoil at  $M = 0.85$  and reduced frequency based on the chord  $k_c = 0.5$  and 2 calculated by Lee [62] using a 2D transonic small disturbance aerodynamics code. At  $k_c = 0.5$ , we see a peculiar shock behavior occurs. During part of the oscillation cycle, the shock disappears only

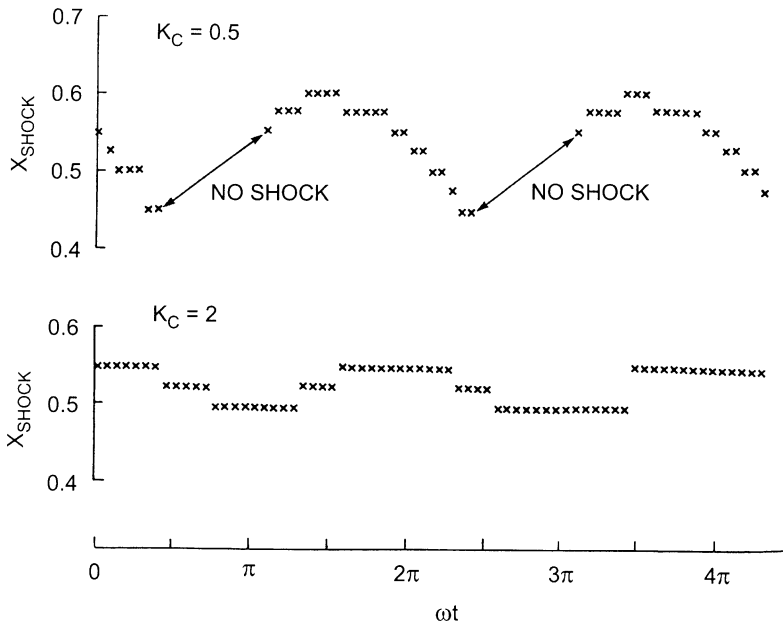


Fig. 15. Shock wave position for plunging oscillation of a NACA64A006 airfoil at  $M = 0.85$ , reduced frequency  $k_c = 0.5$  and 2 (from Ref. [62]).

to reappear at a later time. The forces generated are nonlinear and usually a number of harmonics are present.

When viscous effects are considered, flow separation can occur due to shock-boundary layer interaction. This can cause single DOF flutter, control surface buzz and buffeting. Lee [67] studied shock oscillations on a rigid supercritical airfoil and showed the growth of the shock induced separation bubble with increase in angle-of-attack  $\alpha$  for given Mach numbers. For small incidence, the separation reattaches on the airfoil surface and the bubble size grows with  $\alpha$ . The shock can also induce trailing-edge separation and the two separation regions can merge to produce a fully separated flow behind the shock as shown in Fig. 16. The unsteady air loads are quite large and have characteristic frequencies that can be near those involved in flutter. Lee [67] proposed a feedback mechanism for self-sustained shock motion on a 2D supercritical airfoil based on experimental measurements. Later, Lee et al. [68] carried out a theoretical analysis using a wave propagation approach to demonstrate the coupling between the unsteady Kutta waves generated at the airfoil trailing edge and the shock oscillation. The unsteady shock motion occurs at a discrete frequency that can excite the structural vibration modes resulting in limit cycle flutter for an elastic structure. This type of shock-induced excitation can be calculated theoretically using a viscous-inviscid interactive method [26] or a solution of the Navier–Stokes equations [50]. For an oscillating airfoil, the motion of the shock waves and the wake are illustrated in Fig. 17 for an 18% circular arc airfoil studied in the NASA LaRC Transonic Dynamics Tunnel [12]. For a particular test condition, small separation regions appear at the foot of the weak shock and at the trailing edge on the lower surface. As the shock strength increases with increase in  $\alpha$  at a latter part of the

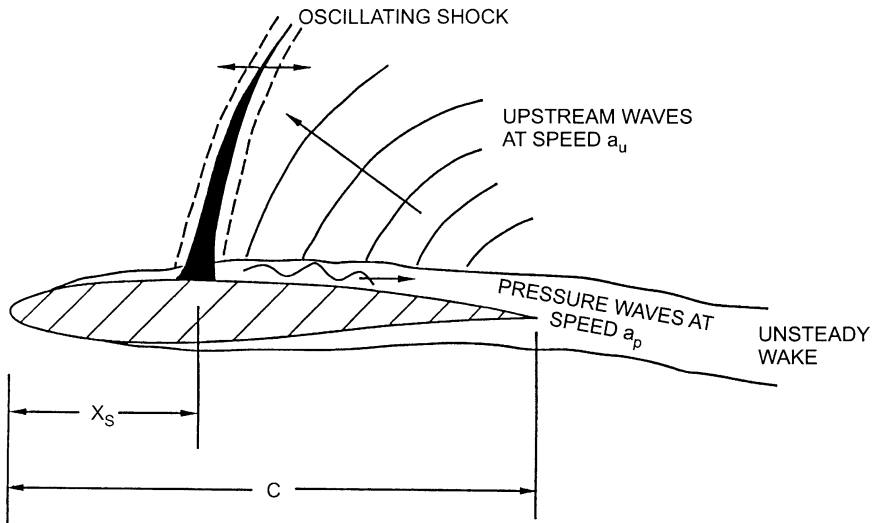


Fig. 16. Model of self-sustained shock oscillations (from Ref. [67]).

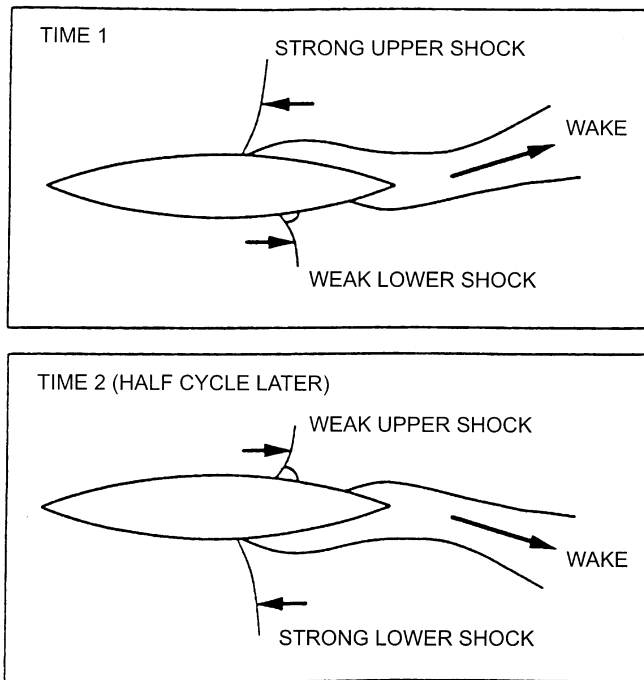


Fig. 17. Sketch of transonic shock-boundary layer oscillation on circular-arc airfoil (from Ref. [12]).

oscillation cycle, these two regions merge and the upper surface shock wave weakens producing a flow structure similar to the earlier one on the lower surface.

Aerodynamic nonlinearities associated with flow separation at low speed are found in dynamic stall of helicopter blades or propeller blades. The events of dynamic stall are illustrated in Fig. 18

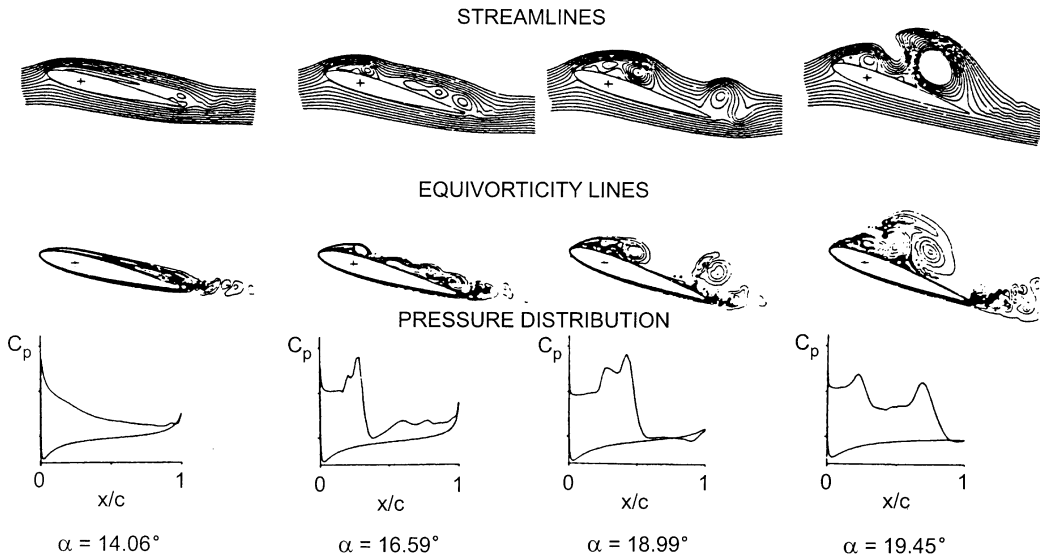


Fig. 18. Dynamic stall from Navier–Stokes simulation showing streamlines, equi-vorticity lines and pressure distribution at  $k_c = 0.25$  (from Ref. [79]).

taken from a numerical simulation using the Navier–Stokes equations [79]. At low angle-of-attack, the flow is attached but leading-edge separation begins as  $\alpha$  reaches a certain critical angle. The leading-edge vortex moves downstream along the airfoil surface, and after traversing a certain distance from the leading edge, lifts off from the surface and finally convects away from the trailing edge. During the downstroke cycle, the flow reattaches on the upper surface starting from the trailing edge and moves upstream while separation occurs on the lower surface following events on the upper surface during the upstroke. The empirical method using wind tunnel data [32–34] is widely used although Navier–Stokes solvers [122] are available at much higher computational costs. The use of reliable NS solvers to analyze stall characteristics is of great help since time-synthesization methods using experimental data have limited use and required large amounts of loop data to cover a wide range of conditions, such as, angle of attack, Mach number, amplitude of oscillations, frequency, etc. Also, the transition from attached to separated flow using the empirical models is usually not accurately determined.

Another type of aerodynamic nonlinearities arises from the formation of wing tip vortices. This was investigated by Strganac et al. [100] for a finite wing and the flow modeling is illustrated in Fig. 19. The vortices oscillate with time and their strengths depend on the static angle of attack and the amplitude of airfoil motion. This type of flow can readily be computed using an unsteady vortex lattice method. The wing and wake are modeled as a vortex lattice. The position of the wing portion, called the bound vortex lattice, is specified and there is a finite pressure jump across it. The position of the wake portion, referred to as the free-vortex lattice, is not specified but is force-free and is predicted as part of the solution. The aerodynamic loading is determined by calculating the pressure jump across each individual element in the bound vortex. This model has been used to study vortex dominated flows coupled to the equations of motion of the airfoil structure. However,



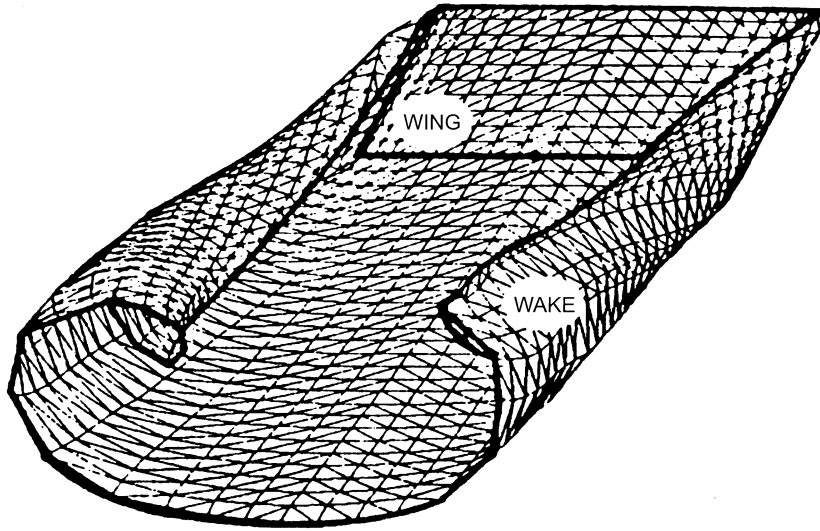


Fig. 19. Flowfield predicted by the unsteady vortex-lattice method (from Ref. [100]).

for very large amplitude motions when the roll-up vortices are formed alternatively on the upper and lower surfaces of the wing, the phase lag with respect to the wing oscillation can be very large. Very few studies on this topic have been carried out, although some investigations have been conducted for delta wings at high incidence and pitch amplitudes.

### 3. Formulation of the nonlinear aeroelastic equations for airfoils

#### 3.1. Equations with structural nonlinearities and subsonic aerodynamics

A simple and efficient method to investigate the dynamic response of a wing structure is to use the concept of generalized coordinates [77]. Consider a cartesian coordinate system  $x$ ,  $y$  and  $z$  fixed on a thin wing as illustrated in Fig. 20. The displacement of the wing can be expressed in terms of a set of generalized coordinates  $q_i(t)$  as

$$z(x, y, t) = \sum_{i=1}^I \phi_i(x, y) q_i(t) \quad (1)$$

where  $\phi_i(x, y)$  is the mode shape of the  $i$ th mode, and  $I$  is the number of modes required to adequately represent  $z(x, y, t)$  in the form of a series.  $I$  may vary from two to three for a simple beam structure to a few dozens for complicated aircraft configurations. The dynamic aeroelastic equations governing the response of  $q_i(t)$  to external forces is given in generalized coordinates

$$M_i \ddot{q}_i + C_i \dot{q}_i + K_i q_i = F_i \quad (2)$$

for the  $i$ th mode. The dots denote differentiation with respect to time, and  $M_i$ ,  $C_i$ ,  $K_i$  and  $F_i$  are the generalized mass, damping, stiffness and force, respectively. The fact that the equation does not

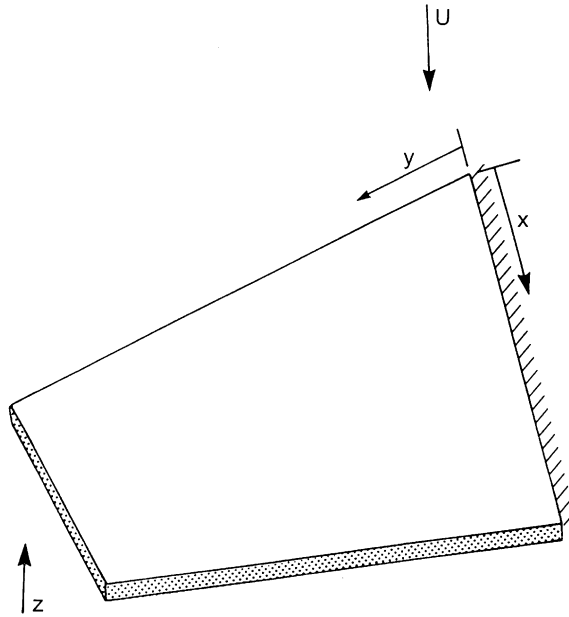


Fig. 20. Schematic of a wing showing the coordinate system.

contain any other general coordinates  $q_i$  is due to the characteristic ‘normal’ property of the natural modes. Actually, a set of terms  $\sum_{j=1(\neq i)}^I C_{ij}\dot{q}_j$  should be included on the left-hand side of Eq. (2) since this ‘normal’ property does not always apply to the system of damping forces acting on the wing, but these modal coupling forces are usually small enough to be ignored.

The generalized mass  $M_i$  has the same magnitude of a mass which when moving with the velocity  $\dot{q}_i$  has the same kinetic energy as the whole system moving with the velocity  $\dot{q}_i\phi_i$ . It can be written as

$$M_i = \int_A m\phi_i^2 dA, \quad (3)$$

where  $m$  is the mass per unit area of the wing, and the integration is taken over the whole wing surface area  $A$ . The generalized stiffness  $K_i$  is the stiffness of the spring which, when displaced from its unstrained position by  $q_i$ , has the same potential energy as the actual system when displaced by  $q_i\phi_i$ . If we approximate the wing by a beam of length equal to, say, the span  $s$ , we can write  $K_i$  as follows:

$$K_i = \int_s EI \left\{ \frac{d^2\phi_i}{dx^2} \right\}^2 dx, \quad (4)$$

where  $EI$  is the flexural stiffness of the beam and  $\phi_i = \phi_i(x)$  in this case. There are other ways to represent the stiffness, for example, using a lumped parameter structural idealization.

The generalized damping coefficient  $C_i$  can be considered as the rate of the damper which, when moved at a velocity  $\dot{q}_i$  dissipates energy at the same rate as the whole system of damping forces and

pressures acting on and within the system when moving with a velocity of  $\dot{q}_i\phi_i$ . We can express  $C_i$  in terms of a local viscous damping pressure per unit velocity  $p_{di}(x, y)$  in counter phase with the velocity  $\dot{q}_i\phi_i$  as follows:

$$C_i = \int_q p_{di}\phi_i^2 dA . \quad (5)$$

Finally, the generalized force  $F_i$  is a single force which, when moved through a displacement  $\delta q_i$ , does the same amount of work as all the external forces and pressures acting on the system after displaced by a distance  $\delta q_i\phi_i$ . In terms of the pressure  $p(x, y, t)$  acting at a point  $(x, y)$ , it can be written as

$$F_i(t) = \int_A p(x, y, t)\phi_i dA . \quad (6)$$

In matrix formulation, Eq. (2) can be written as

$$[\mathbf{M}]\{\ddot{\mathbf{q}}\} + [\mathbf{C}]\{\dot{\mathbf{q}}\} + [\mathbf{K}]\{\mathbf{q}\} = \{\mathbf{F}\} , \quad (7)$$

where  $[\mathbf{M}]$ ,  $[\mathbf{C}]$  and  $[\mathbf{K}]$  are the mass, damping and stiffness matrices.  $\{\mathbf{F}\}$  is the aerodynamic force vector. For a nonlinear structure, we replace the stiffness term  $[\mathbf{K}]\{\mathbf{q}\}$  by a nonlinear term  $\{\mathbf{Q}(\mathbf{q})\}$ .

Eq. (7) is useful when we couple a three-dimensional wing motion to an aerodynamics code and use a time integration technique to solve the structural motion. The system we shall investigate in detail in later sections is a two-dimensional airfoil oscillating in pitch and in plunge. We shall express the dynamic equations of motion in a slightly different form which will be useful in later sections.

Fig. 21 gives the symbols used in the analysis of a two-degree-of-freedom airfoil motion. The plunge deflection is denoted by  $h$ , positive in the downward direction, and  $\alpha$  is the pitch angle about the elastic axis, positive nose up. The elastic axis is located at a distance  $a_h b$  from the midchord, while the mass centre is located at a distance  $x_a b$  from the elastic axis. Both distances are positive when measured towards the trailing edge of the airfoil. The aeroelastic equations of motion for linear springs have been derived by Fung [31]. For nonlinear restoring forces such as those considered in Section 2.1, the coupled bending-torsion equations for the airfoil can be written as follows:

$$m\ddot{h} + S\ddot{\alpha} + C_h\dot{h} + \bar{G}(h) = p(t) , \quad (8)$$

$$S\ddot{h} + I_\alpha\ddot{\alpha} + C_\alpha\dot{\alpha} + \bar{M}(\alpha) = r(t) , \quad (9)$$

where the symbols  $m$ ,  $S$ ,  $C_h$ ,  $I_\alpha$  and  $C_\alpha$  are the airfoil mass, airfoil static moment about the elastic axis, damping coefficient in plunge, wing mass moment of inertia about elastic axis, and torsion damping constant, respectively.  $\bar{G}(h)$  and  $\bar{M}(\alpha)$  are the nonlinear plunge and pitch stiffness terms, and  $p(t)$  and  $r(t)$  are the forces and moments acting on the airfoil, respectively.

In Section 2.1 we have discussed the various types of structural nonlinearities. In this review, we shall consider only the three common ones, namely, cubic, freeplay and hysteresis nonlinearities. Consider the torsion degree-of-freedom nonlinearity for the time being, we use the same representation of a cubic spring as that of Woolston et al. [120,121] and Lee and LeBlanc [64]. We write

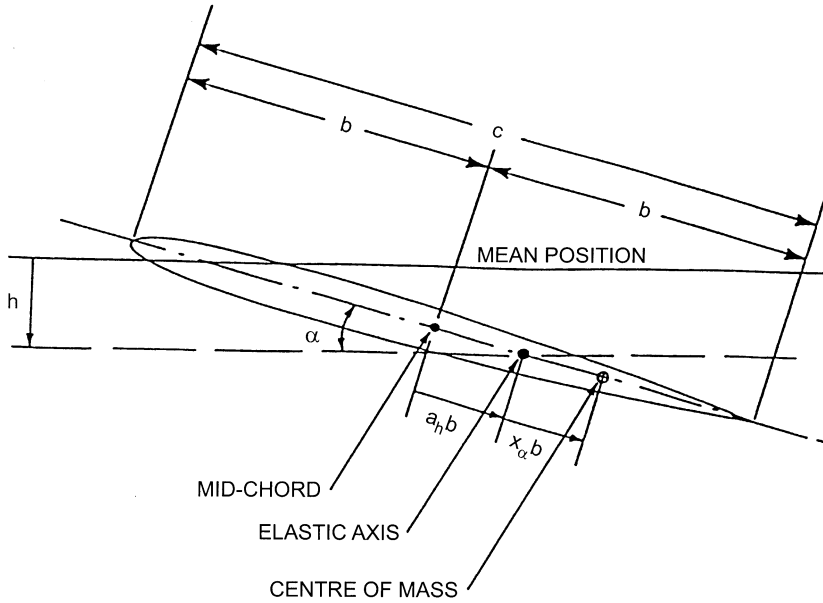


Fig. 21. Two-degree-of-freedom airfoil motion.

$\bar{M}(\alpha) = K_\alpha(\alpha + \beta_\alpha \alpha^3)$ , where  $K_\alpha$  is the linear spring constant and  $\beta_\alpha$  is a constant less than unity for the type of problems they investigated. For the freeplay and hysteresis,  $\bar{M}(\alpha) = K_\alpha \alpha$ , and  $K_\alpha$  is specified as a piecewise function of  $\alpha$ . For the plunge degree-of-freedom, we can write down similar expressions for  $\bar{G}(h)$  simply by replacing  $\alpha$  with  $h$ . We shall discuss these functions in greater detail in Section 5.

Define  $\xi = h/b$ ,  $K_\xi = K_h$ ,  $x_\alpha = S/bm$ ,  $\omega_\xi = (K_\xi/m)^{1/2}$ ,  $\omega_\alpha = (K_\alpha/I_\alpha)^{1/2}$ ,  $r_\alpha = (I_b/m b^2)^{1/2}$ ,  $\zeta_\xi = C_h/2(m K_h)^{1/2}$ ,  $\zeta_\alpha = C_\alpha/2(I_\alpha K_\alpha)^{1/2}$ . Eqs. (8) and (9) can be written in non-dimensional form as [65]

$$\xi'' + x_\alpha \alpha'' + 2\zeta_\xi \frac{\bar{\omega}}{U^*} \xi' + \left( \frac{\bar{\omega}}{U^*} \right)^2 G(\xi) = -\frac{1}{\pi\mu} C_L(\tau) + \frac{P(\tau)b}{mU^2}, \quad (10)$$

$$\frac{x_\alpha}{r_\alpha^2} \xi'' + \alpha'' + 2\frac{\zeta_\alpha}{U^*} \alpha' + \frac{1}{U^{*2}} M(\alpha) = \frac{2}{\pi\mu r_\alpha^2} C_M(\tau) + \frac{Q(\tau)}{mU^2 r_\alpha^2}, \quad (11)$$

where  $G(\xi) = \bar{G}(h)/K_\xi$  and  $M(\alpha) = \bar{M}(\alpha)/K_\alpha$ .

In Eqs. (10) and (11),  $U^*$  is a non-dimensional velocity defined as

$$U^* = \frac{U}{b\omega_\alpha} \quad (12)$$

and  $\bar{\omega}$  is given by

$$\bar{\omega} = \frac{\omega_\xi}{\omega_\alpha}, \quad (13)$$

where  $\omega_\xi$  and  $\omega_\alpha$  are the uncoupled plunging and pitching modes natural frequencies, and the ' denotes differentiation with respect to the nondimensional time  $\tau$  defined as

$$\tau = \frac{Ut}{b} \quad (14)$$

$C_L(\tau)$  and  $C_M(\tau)$  in Eqs. (10) and (11) are the lift and pitching moment coefficients, respectively. For incompressible flow, Fung [31] gives the following expressions for  $C_L(\tau)$  and  $C_M(\tau)$ :

$$C_L(\tau) = \pi(\xi'' - a_h\alpha'' + \alpha') + 2\pi\{\alpha(0) + \xi'(0) + [\tfrac{1}{2} - a_h]\alpha'(0)\}\phi(\tau) \\ + 2\pi \int_0^\tau \phi(\tau - \sigma)[\alpha'(\sigma) + \xi''(\sigma) + (\tfrac{1}{2} - a_h)\alpha''(\sigma)] d\sigma, \quad (15)$$

$$C_M(\tau) = \pi(\tfrac{1}{2} + a_h)\{\alpha(0) + \xi'(0) + [\tfrac{1}{2} - a_h]\alpha'(0)\}\phi(\tau) \\ + \pi(\tfrac{1}{2} + a_h) \int_0^\tau \phi(\tau - \sigma)\{\alpha'(\sigma) + \xi''(\sigma) + (\tfrac{1}{2} - a_h)\alpha''(\sigma)\} d\sigma \\ + \frac{\pi}{2}a_h(\xi'' - a_h\alpha'') - (\tfrac{1}{2} - a_h)\frac{\pi}{2}\alpha' - \frac{\pi}{16}\alpha'', \quad (16)$$

where the Wagner function  $\phi(\tau)$  is given by

$$\phi(\tau) = 1 - \psi_1 e^{-\varepsilon_1 \tau} - \psi_2 e^{-\varepsilon_2 \tau} \quad (17)$$

and the constants  $\psi_1 = 0.165$ ,  $\psi_2 = 0.335$ ,  $\varepsilon_1 = 0.0455$  and  $\varepsilon_2 = 0.3$  are obtained from Jones [53].  $P(\tau)$  and  $Q(\tau)$  are the externally applied forces and moments, respectively.

For unforced oscillations, Eqs. (10) and (11) were solved by Lee and Desrochers [65] and Price et al. [88,89] using a finite difference scheme which will be discussed in Section 4.1. Due to the existence of the integral terms in the integro-differential equations (10) and (11), it is cumbersome to integrate them numerically. A simpler set of equations was derived by Lee et al. [69], and they introduced four new variables

$$w_1 = \int_0^\tau e^{-\varepsilon_1(t-\sigma)} \alpha(\sigma) d\sigma, \quad w_2 = \int_0^\tau e^{-\varepsilon_2(t-\sigma)} \alpha(\sigma) d\sigma, \\ w_3 = \int_0^\tau e^{-\varepsilon_1(t-\sigma)} \xi(\sigma) d\sigma, \quad w_4 = \int_0^\tau e^{-\varepsilon_2(t-\sigma)} \xi(\sigma) d\sigma. \quad (18)$$

The equations given by Lee et al. [69] can be written in general form for cubic, freeplay or hysteresis nonlinearities as

$$c_0 \xi'' + c_1 \alpha'' + c_2 \xi' + c_3 \alpha' + c_4 \xi + c_5 \alpha + c_6 w_1 + c_7 w_2 + c_8 w_3 + c_9 w_4 \\ + \left( \frac{\bar{\omega}}{U^*} \right)^2 G(\xi) = f(\tau), \quad (19)$$

$$d_0 \xi'' + d_1 \alpha'' + d_2 \alpha' + d_3 \alpha + d_4 \xi' + d_5 \xi + d_6 w_1 + d_7 w_2 + d_8 w_3 + d_9 w_4 + \left( \frac{1}{U^*} \right)^2 M(\alpha) = g(\tau) \quad (20)$$

where  $G(\xi)$  and  $M(\alpha)$  are nonlinear functions of  $\xi$  and  $\alpha$ , respectively. The coefficients  $c_0, c_1, \dots, d_0, \dots, d_9$  are given in Appendix A.  $f(\tau)$  and  $g(\tau)$  are functions of initial conditions and terms in the Wagner function. In the absence of external forcing, i.e.  $P(\tau) = Q(\tau) = 0$ , they are given by

$$f(\tau) = \frac{2}{\mu} \left( \left( \frac{1}{2} - a_h \right) \alpha(0) + \xi(0) \right) (\psi_1 \varepsilon_1 e^{-\varepsilon_1 \tau} + \psi_2 \varepsilon_2 e^{-\varepsilon_2 \tau}), \quad (21)$$

$$g(\tau) = - \frac{(1 + 2a_h)f(\tau)}{2r_a^2}. \quad (22)$$

If  $P(\tau)$  and  $Q(\tau) \neq 0$ ,  $f(\tau)$  and  $g(\tau)$  are given in Eqs. (108) and (109). After introducing a variable vector  $\mathbf{X} = (x_1, x_2, \dots, x_8)^T$  defined as

$$x_1 = \alpha, \quad x_2 = \alpha', \quad x_3 = \xi, \quad x_4 = \xi', \quad x_5 = w_1, \quad x_6 = w_2, \quad x_7 = w_3, \quad x_8 = w_4, \quad (23)$$

Eqs. (19) and (20) can be written as a set of eight first-order ordinary differential equations,

$$\dot{\mathbf{X}} = \mathbf{f}(\mathbf{X}). \quad (24)$$

In terms of vector components, Eq. (24) can be expressed as

$$\begin{aligned} x'_1 &= x_2, \quad x'_2 = (c_0 H - d_0 P)/(d_0 c_1 - c_0 d_1), \quad x'_3 = x_4, \quad x'_4 = (-c_1 H + d_1 P)/(d_0 c_1 - c_0 d_1), \\ x'_5 &= x_1 - \varepsilon_1 x_5, \quad x'_6 = x_1 - \varepsilon_2 x_6, \quad x'_7 = x_3 - \varepsilon_1 x_7, \quad x'_8 = x_3 - \varepsilon_2 x_8, \end{aligned} \quad (25)$$

where

$$\begin{aligned} P &= c_2 x_4 + c_3 x_2 + c_4 x_3 + c_5 x_1 + c_6 x_5 + c_7 x_6 + c_8 x_7 + c_9 x_8 + \left( \frac{\bar{\omega}}{U^*} \right)^2 G(x_3) - f(\tau), \\ H &= d_2 x_2 + d_3 x_1 + d_4 x_4 + d_5 x_3 + d_6 x_5 + d_7 x_6 + d_8 x_7 + d_9 x_8 + \left( \frac{1}{U^*} \right)^2 M(x_1) - g(\tau). \end{aligned} \quad (26)$$

Eq. (24) can be integrated numerically once the initial conditions  $\alpha(0)$ ,  $\alpha'(0)$ ,  $\xi(0)$ ,  $\xi'(0)$  are given. These equations are easier to solve than Eqs. (10) and (11), especially when we investigate the system behavior analytically.

Assuming the existence of the third and fourth derivatives, Alighanbari and Price [1] expressed Eqs. (10) and (11) as a set of fourth-order differential equations. Eight initial conditions are required in this approach since a fourth-order solution requires  $\alpha'''(0)$ ,  $\alpha''(0)$ ,  $\xi'''(0)$  and  $\xi''(0)$  to be specified in addition to  $\alpha(0)$ ,  $\alpha'(0)$ ,  $\xi'(0)$  and  $\xi(0)$  for a set of second-order differential equations.

According to Alighanbari and Price's [1] method, both sides of Eqs. (10) and (19) are differentiated twice and the following two equations are obtained:

$$m_1 \xi^{IV} + m_2 \alpha^{IV} + m_3 \xi''' + m_4 \alpha''' + m_5 \xi'' + m_6 \alpha'' + m_7 \xi' + m_8 \alpha' + m_9 \xi + m_{10} \alpha + \left( \frac{\bar{\omega}}{U^*} \right)^2 [N_\xi(\xi)] = 0 \quad (27)$$

$$n_1 \xi^{IV} + n_2 \alpha^{IV} + n_3 \xi''' + n_4 \alpha''' + n_5 \xi'' + n_6 \alpha'' + n_7 \xi' + n_8 \alpha' + n_9 \xi + n_{10} \alpha + \left( \frac{1}{U^*} \right)^2 [N_\alpha(\alpha)] = 0 . \quad (28)$$

The coefficients  $m_i$  and  $n_i$  in Eqs. (27) and (28) are given in the appendix.  $N_\xi(\xi)$  and  $N_\alpha(\alpha)$  are given as

$$N_\xi(\xi) = G''(\xi) + (\varepsilon_1 + \varepsilon_2)G'(\xi) + \varepsilon_1 \varepsilon_2 G(\xi) , \quad (29)$$

$$N_\alpha(\alpha) = M''(\alpha) + (\varepsilon_1 + \varepsilon_2)M'(\alpha) + \varepsilon_1 \varepsilon_2 M(\alpha) . \quad (30)$$

The nonlinear functions  $G(\xi)$  and  $M(\alpha)$  given in Eqs. (19) and (20) for the three types of concentrated structural nonlinearities we shall discuss in details can be written as follows using the symbols defined in Figs. 2 and 11:

*Cubic spring:*

$$M(\alpha) = \beta_0 + \beta_1 \alpha + \beta_2 \alpha^2 + \beta_3 \alpha^3 , \quad (31)$$

where  $\beta_0$ ,  $\beta_1$ ,  $\beta_2$ , and  $\beta_3$  are constants.

*Bilinear spring:*

$$M(\alpha) = \begin{cases} M_0 + \alpha - \alpha_f & \text{for } \alpha < \alpha_f , \\ M_0 + M_f(\alpha - \alpha_f) & \text{for } \alpha_f \leq \alpha \leq \alpha_f + \delta , \\ M_0 + \alpha - \alpha_f + \delta(M_f - 1) & \text{for } \alpha_f + \delta < \alpha . \end{cases} \quad (32)$$

*Hysteresis:*

$$M(\alpha) = \begin{cases} \alpha - \alpha_f + M_0 & \text{for } \alpha < \alpha_f; \alpha \text{ increasing} , \\ \alpha + \alpha_f - M_0 & \text{for } \alpha > -\alpha_f; \alpha \text{ decreasing} , \\ M_0 & \text{for } \alpha_f \leq \alpha \leq \alpha_f + \delta; \alpha \text{ increasing} , \\ -M_0 & \text{for } -\alpha_f \leq \alpha \leq -\alpha_f - \delta; \alpha \text{ decreasing} , \\ \alpha - \alpha_f - \delta + M_0 & \text{for } \alpha > \alpha_f + \delta; \alpha \text{ increasing} , \\ \alpha + \alpha_f + \delta - M_0 & \text{for } \alpha < -\alpha_f - \delta; \alpha \text{ decreasing} . \end{cases} \quad (33)$$

Here we give the expressions for  $M(\alpha)$  in the pitch degree of freedom. Similar expressions for  $G(\xi)$  for the plunge motion can be written by replacing  $\alpha$  with  $\xi$ . Note that  $M''(\alpha)$  does not exist if  $M(\alpha)$  is

defined by Eq. (32) for the bilinear spring. To overcome this difficulty,  $M(x)$  can be expressed as an analytical function given in Eq. (167).

### 3.2. Equations with nonlinear aerodynamics

#### 3.2.1. Transonic flows

A number of mathematical models are available to compute nonlinear unsteady transonic aerodynamic loads. The article by Edwards and Malone [25] reviews recent developments in the field of computational methods for unsteady transonic aerodynamics with aeroelastic applications. The first computational model, the LTRAN2 code, was proposed by Ballhaus and Goorjian [5] in which the alternating direction implicit (ADI) algorithm was used for the solution of the two-dimensional low-frequency transonic small disturbance (TSD) equation. The three-dimensional TSD equation in Cartesian coordinates can be expressed in the following form [9]:

$$\frac{\partial f_0}{\partial t} + \frac{\partial f_1}{\partial x} + \frac{\partial f_2}{\partial y} + \frac{\partial f_3}{\partial z} = 0, \quad (34)$$

where  $x$ ,  $y$  and  $z$  denote the non-dimensional physical coordinates in the streamwise, spanwise and vertical directions, respectively, and

$$\begin{aligned} f_0 &= -A\phi_t - B\phi_x, \\ f_1 &= E_1\phi_x + F_1\phi_x^2 + G_1\phi_y, \\ f_2 &= \phi_y + H_1\phi_x\phi_y, \\ f_3 &= \phi_z. \end{aligned} \quad (35)$$

Here  $\phi$  is the velocity potential and the coefficients in Eq. (35) are defined as

$$\begin{aligned} A &= M^2, \quad B = 2M^2, \quad E_1 = 1 - M^2, \\ F_1 &= -[3 - (2 - \gamma)M^2]M^2/2, \quad G_1 = -M^2/2, \quad H_1 = -M^2, \end{aligned} \quad (36)$$

where  $\gamma$  is the specific heat ratio. The TSD formulation has been widely used to compute unsteady transonic flows about isolated wings and complete aircraft configurations. The XTRAN3S [17], ATRAN3S [40], and CAP-TSD [8] computer simulation codes are essentially based on the TSD formulation given in Eq. (34), and a time integration numerical procedure is used in conjunction with an ADI or approximate factorization (AF) algorithm. A time linearization procedure for solving the TSD equation has also been applied by Wong and Lee [118] to develop the UST3D code, in which the velocity potential is expressed as

$$\phi(x, y, z, t) = \phi^s(x, y, z) + \varepsilon\phi^u(x, y, z, t) \quad \text{and} \quad \varepsilon \ll 1, \quad (37)$$

where the steady component  $\phi^s$  satisfies the nonlinear, mixed elliptic-hyperbolic differential equation, and the unsteady component  $\phi^u$  is calculated from the linear time-dependent differential equation whose coefficients are determined from the steady solution of  $\phi^s$ . Generally speaking, in the TSD formulation, we assume that the flow is isentropic, irrotational and a small perturbation of the steady uniform flow in the  $x$ -direction. The TSD theory, however, has been modified to include



entropy and vorticity effects, so that it can be used to deal with flowfields with stronger shock waves [9]. For some test cases, it was found that numerical simulations from the TSD model are almost as accurate as those obtained by the Euler equations.

A second formulation for unsteady transonic calculations is based on the full potential (FP) model. The FP model also assumes the flow to be inviscid and the shock wave to be weak. Let  $\Phi$  denote the velocity potential, then the governing equation for the FP formulation in conservation form is given by

$$\rho_t + (\rho\Phi_x)_x + (\rho\Phi_y)_y + (\rho\Phi_z)_z = 0, \quad (38)$$

where the density  $\rho$  satisfies the unsteady Bernoulli equation:

$$\rho = \left( 1 + \frac{\gamma + 1}{2} M^2 (I - \Phi_x^2 - \Phi_y^2 - \Phi_z^2 - 2\Phi_t) \right)^{1/\gamma - 1}. \quad (39)$$

The FTRAN3 code developed by Hounjet [47] and the USTF3 program by Iosgai and Suetsugu [49] are based on the FP formulation. In using the FP equation for transonic flows, Steinhoff and Jameson [98] have shown that the equation can admit non-unique solutions due to the entropy generation within the shocks violating the isentropic assumption. To circumvent the non-unique solution, Osher et al. [83] and Whitlow et al. [116] proposed an entropy correction method that satisfies the approximations for the FP equation. The method is used to rule out the non-physical expansion shocks and to accurately track the sonic conditions.

Until a decade ago, unsteady transonic flow computations for aeroelastic problems were mostly carried out using the TSD and FP formulations. Numerical methods for solving unsteady Euler and Navier–Stokes (NS) equations were available, but they have not been widely used in practice because these procedures are very costly. However, with the recent advances in computer technology, numerical simulation codes using these accurate formulations have been developed for aeroelastic analysis because of their ability to model complex flow phenomena, such as strong shocks, vortices and flow separations.

The NS equations in a Cartesian coordinate system can be expressed as follows:

$$\frac{\partial}{\partial t}(\mathbf{Q}) + \frac{\partial}{\partial x}(\mathbf{F} - \mathbf{F}_v) + \frac{\partial}{\partial y}(\mathbf{G} - \mathbf{G}_v) + \frac{\partial}{\partial z}(\mathbf{H} - \mathbf{H}_v) = 0, \quad (40)$$

where the conserved variables  $\mathbf{Q}$  and the inviscid flux vectors  $\mathbf{F}$ ,  $\mathbf{G}$ ,  $\mathbf{H}$  are defined by

$$\mathbf{Q} = \begin{pmatrix} \rho \\ \rho u \\ \rho v \\ \rho w \\ \rho e \end{pmatrix}, \quad \mathbf{F} = \begin{pmatrix} \rho u \\ \rho u^2 + p \\ \rho uv \\ \rho uw \\ \rho eu + pu \end{pmatrix}, \quad \mathbf{G} = \begin{pmatrix} \rho v \\ \rho uv \\ \rho v^2 + p \\ \rho vw \\ \rho ev + pv \end{pmatrix}, \quad \mathbf{H} = \begin{pmatrix} \rho w \\ \rho uw \\ \rho vw \\ \rho w^2 + p \\ \rho ew + pw \end{pmatrix}. \quad (41)$$

The total energy is denoted by  $e$ , where

$$e = \frac{p}{(\gamma - 1)\rho} + \left[ \frac{u^2 + v^2 + w^2}{2} \right]. \quad (42)$$

The corresponding viscous flux vectors are denoted by  $\mathbf{F}_v$ ,  $\mathbf{G}_v$ ,  $\mathbf{H}_v$  and they are given as follows:

$$\begin{aligned} \mathbf{F}_v &= \begin{pmatrix} 0 \\ \tau_{xx} \\ \tau_{xy} \\ \tau_{xz} \\ u\tau_{xx} + v\tau_{xy} + w\tau_{xz} - q_x \end{pmatrix}, & \mathbf{G}_v &= \begin{pmatrix} 0 \\ \tau_{xy} \\ \tau_{yy} \\ \tau_{yz} \\ u\tau_{xy} + v\tau_{yy} + w\tau_{yz} - q_y \end{pmatrix}, \\ \mathbf{H}_v &= \begin{pmatrix} 0 \\ \tau_{xz} \\ \tau_{yz} \\ \tau_{zz} \\ u\tau_{xz} + v\tau_{yz} + w\tau_{zz} - q_z \end{pmatrix}. \end{aligned} \quad (43)$$

The components of the shear stress tensor and the heat flux vector are defined by

$$\begin{aligned} \tau_{xx} &= \frac{2}{3}\nu \left( 2\frac{\partial u}{\partial x} - \frac{\partial v}{\partial y} - \frac{\partial w}{\partial z} \right), & \tau_{yy} &= \frac{2}{3}\nu \left( 2\frac{\partial v}{\partial y} - \frac{\partial u}{\partial x} - \frac{\partial w}{\partial z} \right), & \tau_{zz} &= \frac{2}{3}\nu \left( 2\frac{\partial w}{\partial z} - \frac{\partial u}{\partial x} - \frac{\partial v}{\partial y} \right), \\ \tau_{xy} &= \nu \left( 2\frac{\partial u}{\partial y} - \frac{\partial v}{\partial x} \right) = \tau_{yx}, & \tau_{xz} &= \nu \left( 2\frac{\partial w}{\partial x} - \frac{\partial u}{\partial z} \right) = \tau_{zx}, & \tau_{yz} &= \nu \left( 2\frac{\partial v}{\partial z} - \frac{\partial w}{\partial y} \right) = \tau_{zy}, \\ q_x &= -k \frac{\partial T}{\partial x}, & q_y &= -k \frac{\partial T}{\partial y}, & q_z &= -k \frac{\partial T}{\partial z}. \end{aligned} \quad (44)$$

where  $T$  is the temperature and  $\nu$ ,  $k$  denote the coefficient of the viscosity and the thermal conductivity, respectively. In Eq. (41),  $p$  is the pressure and  $u$ ,  $v$ , and  $w$  are the velocity components in the  $x$ ,  $y$ , and  $z$  directions, respectively. For viscous flows with mild separation, the NS formulation can be simplified to the thin-layer NS equations. A further simplification can be made when the viscous effects are small and can be neglected. The Euler equations can be obtained from Eq. (40) by setting the viscous flux vectors  $\mathbf{F}_v$ ,  $\mathbf{G}_v$ ,  $\mathbf{H}_v$  to zero. Unlike the TSD and FP formulations where the governing equation is a single equation, the Euler and NS formulations lead to a system of five equations in three-dimensional problems. Consequently, the resulting discrete approximations from the Euler and NS will be five times larger than those obtained by TSD and FP. As a result, a significant increase in computing power is required to deal with simulations based on these equations.

To analyse aeroelastic problems, the normal procedure is to solve the structural and aerodynamic equations simultaneously. The methodology is quite involved and depends on the particular approach used to solve the aerodynamic equations. We consider in this review only a simple example useful for solving the coupled TSD equations following the approach given by Borland and Rizzetta [16]. In solving the unsteady equations, we assume the wing section to be thin. The

boundary conditions for the flowfield are:  $\phi = 0$  far upstream;  $\phi_x + \phi_t = 0$  far downstream;  $\phi_z = 0$  far above and below the wing;  $\phi_y = 0$  far from the wing tip and at the wing root;  $\Delta\phi_z = 0$  and  $\Delta(\phi_x + \phi_t) = 0$  across the trailing edge vortex sheet in the wake region defined by  $z = 0$  for  $x > x_{TE}$ , and  $\Delta$  indicates a jump across the wake. The initial conditions  $\phi(x, y, z, 0) = g(x, y, z)$  and  $\phi_t(x, y, z, 0) = h(x, y, z)$  are specified for the particular problem to be considered.

On the wing surface,

$$\phi_z^\pm = S_x^\pm + S_t^\pm \quad \text{for } x_{LE} \leq x \leq x_{TE}, y \leq y_{TIP}, z = 0^\pm, \quad (45)$$

where the superscript  $\pm$  refers to the airfoil upper and lower surface, and  $S(x, y, t)$  denotes the wing shape. The solution to the system of structural equations of motion is coupled to the aerodynamic solution through the boundary conditions on the wing surface. We first determine the actual time-dependent deformed shape and motion as the sum of contributions from the static rigid, static flexible, dynamic rigid, and dynamic flexible components of the structure. The pressure distribution and integrated forces on this deformed shape are then calculated in a time dependent fashion. The response is determined from these computed forces using the structural equations of motion. The wing surface boundary conditions for static aeroelastic analysis are given by

$$\{\phi_z^\pm\} = \{S_{x_{RIGID}}^\pm\} + \{S_{x_{FLEXIBLE}}^\pm\}, \quad \begin{cases} x_{LE} \leq x \leq x_{TE} \\ y \leq y_{TIP} \end{cases}, \quad (46)$$

where  $S_{x_{RIGID}}^\pm$  can contain contributions from the local slope of the airfoil section coordinate definition on the upper and lower surface  $z_s^\pm$ , the geometrical angle of attack, the static rigid twist distribution, and static control surface deflections. The other component  $S_{x_{FLEXIBLE}}^\pm$ , which is the same for the upper and lower surface, is defined as

$$\{S_{x_{FLEXIBLE}}^\pm\} = [\Phi'_A] \{q\}, \quad (47)$$

where  $[\Phi'_A]$  is the matrix of streamwise slopes of the natural vibration modes given at the aerodynamic control points, and  $\{q\}$  is the matrix of static values of the generalized coordinates. For dynamic aeroelastic analysis, the wing surface boundary conditions are given by

$$\{\phi_z^\pm\} = \{S_{x_{RIGID}}^\pm\}_{STEADY} + \{(S_x^\pm + S_t^\pm)_{RIGID}\}_{UNSTEADY} + \{(S_x^\pm + S_t^\pm)_{FLEXIBLE}\}_{UNSTEADY}. \quad (48)$$

The first term is identical to the corresponding term for static aeroelastic analysis in Eq. (46). The second term accounts for rigid-body motion such as pitch and plunge, and the last term deals with the time-dependent elastic motion. It can be written as

$$\{(S_x^\pm + S_t^\pm)_{FLEXIBLE}\}_{UNSTEADY} = [\Phi'_A] \{q\} + \frac{1}{U} [\Phi_A] \{\dot{q}\}. \quad (49)$$

The generalized coordinates  $\{q\}$  are determined from the equation of motion given by Eq. (7). Here, we shall consider the equation for a linear structure and the procedure can be extended to a nonlinear one.

For a static solution, Eq. (7) can be written as

$$[K] \{q\} = \{F\}. \quad (50)$$

Once the static solution of the generalized coordinates is determined, Eq. (47) is used to recompute the flowfield, and the process is repeated until the solution converges.

In using Eq. (7) to solve the dynamic response, Borland and Rizetta [16] adopted a simple central difference scheme with a constant time step  $\Delta T$ . The first and second time derivatives of the generalized coordinate are written as

$$\{\dot{\mathbf{q}}\} = \left\{ \frac{\mathbf{q}^{n+1} - \mathbf{q}^{n-1}}{2\Delta T} \right\}, \quad (51)$$

$$\{\ddot{\mathbf{q}}\} = \left\{ \frac{\mathbf{q}^{n+1} - 2\mathbf{q}^n + \mathbf{q}^{n-1}}{(\Delta T)^2} \right\}, \quad (52)$$

where  $n$  denotes the time step. Substituting Eqs. (51) and (52) into the structural equations of motion, we have a simple implicit relation for the generalized coordinates at the  $(n + 1)$ th time given by the following:

$$\begin{aligned} \{\mathbf{q}^{n+1}\} = & \left[ \left( \frac{1}{\Delta T} \right)^2 \mathbf{M} + \left( \frac{1}{2\Delta T} \right) \mathbf{C} \right]^{-1} \{\mathbf{F}^n\} \\ & + \left[ \left( \frac{1}{\Delta T} \right)^2 \mathbf{M} + \left( \frac{1}{2\Delta T} \right) \mathbf{C} \right]^{-1} \left[ 2 \left( \frac{1}{\Delta T} \right)^2 \mathbf{M} - \mathbf{K} \right] \{\mathbf{q}^n\} \\ & + \left[ \left( \frac{1}{\Delta T} \right)^2 \mathbf{M} + \left( \frac{1}{2\Delta T} \right) \mathbf{C} \right]^{-1} \left[ \left( \frac{1}{2\Delta T} \right) \mathbf{C} - \left( \frac{1}{\Delta T} \right)^2 \mathbf{M} \right] \{\mathbf{q}^{n-1}\} \end{aligned} \quad (53)$$

The time-marching scheme can proceed once the initial conditions, such as, displacement and velocity of the generalized coordinates are specified.

For higher order aerodynamics codes, the coupling with the structural motion can be handled similarly but the procedure is more complex. Guruswamy [41] developed a computer code ENSAERO to calculate unsteady aerodynamics loads, and he coupled the aerodynamic computations with the linear structural equations for aeroelastic applications. The ENSAERO is based on Euler/NS equations with an algebraic model to compute the turbulence effects. Another computer program, ENS3DAE, which is also based on Euler/NS formulation has been developed by Schuster et al. [93]. The ENS3DAE is coupled with a linear structural optimization program ASTROS (Automated STRuctural Optimization System) to compute aeroelastic responses [82]. The various computational models based on TSD, FP, Euler and Navier–Stokes formulations have been successfully used to investigate the aeroelastic response of isolated wings and complete aircraft configurations.

### 3.2.2. Dynamic stall

An aerodynamic nonlinearity with considerable potential for producing interesting dynamic behavior, and possibly chaotic motion is dynamic stall. There are many practical aeronautical applications where airfoils are required to operate under stalled conditions; including aircraft operating at high angles of attack and helicopter blades in the retreating part of the cycle.

Dynamic stall of an airfoil, with its associated flow separation and reattachment, is an extremely complex phenomenon, and a detailed explanation of the dynamic stall process is not attempted here. The interested reader is referred to Ericsson and Reding [29,30], where a detailed discussion of the physics of dynamic stall is given. Instead, a semi-empirical model is described in this review since this type of formulation of the nonlinear aerodynamics has been used by a number of researchers in their investigations of airfoil dynamics under stall conditions. There are a number of different empirical models of dynamic stall available, for example: the quasi-steady model of Ericsson and Reding [28]; the Tran and Petot [109] model developed at the Office National d'Études et de Recherches Aéronautiques, ONERA; the Beddoes [10] model, later extended by Leishman and Beddoes [73]; or the Gangwani [32,34] and Bielawa et al. [15] model developed at the National Aeronautics and Space Administration, NASA. Some of these models are reviewed by Reddy and Kaza [92].

The semi-empirical ONERA model [109] assumes that the aerodynamic forces can be written as a function of the variables describing the motion of the airfoil. These functions are obtained by curve fitting expressions to available experimental data. Although the results of this model give good agreement with experimental data for harmonically oscillating airfoils, no attempt is made in this approach to model the effects of any of the physical flow phenomena associated with dynamic stall. As shown by Tang and Dowell [102] when the flow over the airfoil remains attached, the ONERA model is equivalent to Theodorsen [107] unsteady aerodynamics. Recently, Tang and Dowell [104] extended the ONERA model, and employed it for the analysis of a low aspect ratio three-dimensional wing. Good comparison between theory and experimental results was obtained for the case of pure pitch motion. A number of different authors have made use of the ONERA model to investigate the aeroelastic response of stalled airfoils. For example, Tran and Falchero [110] used it to investigate the response of a helicopter blade in forward flight. Dunn and Dugundji [24] also employed the ONERA model in their investigation of the nonlinear aeroelastic behavior of rectangular graphite/epoxy cantilevered wings when subject to dynamic stall. Also, Tang and Dowell [101–106] have made extensive use of the ONERA model to investigate the aeroelastic response of stalled non-rotating helicopter blades.

The Beddoes [10] and Leishman and Beddoes [73] model of dynamic stall uses an indicial response and superposition method, incorporating corrections to account for the effect of compressibility. The nonlinear effects of trailing edge separation are implemented using Kirchhoff theory, enabling the force and moment characteristics to be related to the trailing edge separation point. Extensive validation of this model is given by Leishman and Beddoes [73] for a NACA 0012 airfoil.

The method described in this review is taken from Price and Keleris [90] who used a model based on the work of Gangwani [32,34] and Bielawa et al. [15]. This model has the advantage that it is formulated in the time domain, and the aerodynamic forces can be calculated easily from the pitch and pitch-rate of the airfoil. However, one drawback of this model is that it accounts for the pitch motion only; thus, it is restricted to cases where there is no heave.

*3.2.2.1. The semi-empirical dynamic stall model.* Dynamic stall occurs after the angle of attack of an airfoil,  $\alpha$ , has exceeded the static stall angle,  $\alpha_s$ , and when the leading edge vortex breaks away from the airfoil. In order to accurately model dynamic stall it is important to be able to predict the onset of three major events: the formation and shedding of a leading edge vortex, the arrival of this vortex

at the trailing edge, and the reattachment of flow over the airfoil. The model described in this review, developed by Gangwani [32] and Bielawa et al. [15] is illustrated in Fig. 18, and involves several analytical expressions, which are simple mathematical models of these main dynamic stall events. These expressions include numerous unknown coefficients, which are determined by curve fitting data from wind tunnel tests on oscillating airfoils. Since this model gives the aerodynamics in the time domain, the main parameters required to predict the pitching moment  $C_M$  are  $\alpha$  and the pitch-rate, both of which are simple to define physically and mathematically. Furthermore, the model does not require the frequency of oscillation to be known, which is advantageous for the present analysis because of the difficulty of defining the instantaneous frequency of an airfoil undergoing quasi-periodic or chaotic motion.

In order to account for the time history of the airfoil motion, an effective angle of attack, obtained using Duhamel's integral, is defined as

$$\alpha_E = \alpha(0)\phi_C(\tau, M) + \int_0^\tau \frac{\partial \alpha}{\partial \sigma} \phi_C(\tau - \sigma, M) d\sigma, \quad (54)$$

where  $\alpha(0)$  is the initial angle of attack, and  $\phi_C$  is Wagner's function corrected for compressibility effects [10]. As suggested by Beddoes [10],  $\phi_C$  is given approximately by

$$\phi_C(\tau, M) = (1 - 0.165 \exp(-0.0455\beta^2)\tau - 0.335 \exp(-0.3\beta^2)\tau)/\beta, \quad (55)$$

where  $\beta = \sqrt{1 - M^2}$ . The difference between the geometric angle of attack,  $\alpha$ , and  $\alpha_E$  is defined as the unsteady decay parameter,  $\alpha_W$ . This interpretation of  $\alpha_W$  is strictly correct only when the flow is attached. However, as suggested by Gangwani [32] it is also used to predict certain dynamic stall events, and to approximate the aerodynamic loads even when the airfoil is stalled.

To predict the instantaneous angle of attack at which dynamic stall occurs,  $\alpha_D$  a semi-empirical relationship is assumed between  $\alpha_D$  and the static stall angle  $\alpha_S$ , the pitch-rate, and  $\alpha_E$ . Linearizing this expression about  $\alpha_S$  gives

$$\alpha_D = (1 + \varepsilon + C_1 A_D + C_2 \alpha_{WM}) \alpha_S, \quad (56)$$

where  $A_D$  and  $\alpha_{WM}$  are the airfoil pitch-rate and the unsteady decay parameter, respectively, evaluated at the point of dynamic stall, and  $\varepsilon$ ,  $C_1$  and  $C_2$  are empirically determined constants.

After dynamic stall occurs the leading edge vortex is convected downstream over the upper surface of the airfoil, and its strength and distance from the airfoil strongly influence the aerodynamic loads. Its main effect is to increase the negative (nose down)  $C_M$ , which reaches a maximum when the vortex arrives at the trailing edge. A semi-empirical relationship is used to predict the nondimensional time required for the vortex to travel from the leading to the trailing edges of the airfoil,  $\tau_T$ , given by

$$\tau_T = \frac{1.0}{C_3 A_D + C_4 \alpha_D}, \quad (57)$$

where  $C_3$  and  $C_4$  are empirically determined constants.

The instantaneous angle of attack at which the flow reattaches,  $\alpha_R$  is obtained using the same method as for predicting  $\alpha_D$ , and an appropriate expression is

$$\alpha_R = (1 - \varepsilon + C_5 A_D + C_6 \alpha_{WM}) \alpha_S, \quad (58)$$

where  $\varepsilon$  is the same as in Eq. (56), and  $C_5$  and  $C_6$  are new constants.

The aerodynamic pitching moment,  $C_M$ , is then approximated as

$$C_M = C_{MS}(\alpha - \Delta\alpha_2) + a_0 \Delta\alpha_2 + \Delta C_M, \quad (59)$$

where

$$\Delta C_M = P_1 A + P_2 \alpha_W + P_3 \left( \frac{\alpha}{\alpha_S} \right) + P_4 |\alpha_W| + P_5 \delta_1 + P_6 \Delta\alpha_2 + P_7 \alpha_D A_D \tau_M, \quad (60)$$

$$\Delta\alpha_2 = \delta_2 \alpha_S, \quad (61)$$

$$\tau_M = \frac{U(t - t_D)}{b}, \quad (62)$$

$$\delta_1 = \begin{cases} 0, & \text{for } \alpha \leq \alpha_S, \\ \left( \frac{\alpha}{\alpha_S} - 1 \right), & \text{for } \alpha_S < \alpha \leq \alpha_D, \\ \left( \frac{\alpha_D}{\alpha_S} - 1 \right) \left( 1 - \left( \frac{\tau_M}{\tau_T} \right)^2 \right), & \text{for } 0 \leq \tau_M \leq \tau_T, \\ 0, & \text{for } \tau_M > \tau_D. \end{cases} \quad (63)$$

$$\delta_2 = \begin{cases} 0, & \text{for } \alpha \leq \alpha_S, \\ \left( \frac{\alpha}{\alpha_S} - 1 \right), & \text{for } \alpha_S < \alpha \leq \alpha_D, \\ \left( \frac{\alpha_D}{\alpha_S} - 1 \right), & \text{for } 0 \leq \tau_M \leq \tau_T, \\ \left( \frac{\alpha_D}{\alpha_S} - 1 \right) \frac{\alpha - \alpha_R}{\alpha_T - \alpha_R}, & \text{for } \alpha_R \leq \alpha \leq \alpha_T, \\ 0, & \text{for } \alpha < \alpha_R. \end{cases} \quad (64)$$

The parameter  $a_0$  is the static moment coefficient curve slope at zero angle of attack.

As shown in Eq. (59),  $C_M$  is modeled as the sum of the static moment coefficient,  $C_{MS}$ , at a shifted angle of attack,  $\alpha - \Delta\alpha_2$ , plus the static moment curve slope,  $a_0$ , multiplied by the incremental

angle of attack,  $\Delta\alpha_2$ , plus an incremental moment coefficient,  $\Delta C_M$ . The term  $\Delta\alpha_2$ , which is non-zero for stalled flow only, accounts for dynamic stall and flow reattachment,  $\alpha_T$  is the value of  $\alpha$  when the vortex reaches the trailing edge, and  $t_D$  is the time at which dynamic stall occurs. The term  $\Delta C_M$  accounts for the effect of the shed leading edge vortex, and the constants,  $P_1 \dots P_7$ , are determined by curve fitting wind tunnel data to the above expressions using a least-squares technique.

**3.2.2.2. Modification and verification of the dynamic stall model.** Price and Keleris [90] made two simple modifications to the dynamic stall model described above. The first modification was to restrict the domains of  $\alpha_D$  and  $\alpha_R$  such that they are greater and less than  $\alpha_S$ , respectively. It can be argued that  $\alpha_D$  should always be greater than  $\alpha_S$  due to the boundary layer improvements as  $\alpha$  is increasing [29]. Similarly, it can be argued that  $\alpha_R$  must always be less than  $\alpha_S$  since dynamic effects are present as  $\alpha$  is decreasing, and they will destabilize the boundary layer and delay reattachment of the flow. However, by introducing these assumptions the model is restricted to cases where stall is not induced by local shocks, i.e. approximately  $M$  must be  $\leq 0.6$ .

The second modification was made to ensure that  $C_M$  remain piece-wise continuous. Often the model predicted that the shed vortex did not reach the trailing edge before  $\alpha$  had decreased below  $\alpha_R$ . In other words, the two conditions,  $\tau_M < \tau_T$  and  $\alpha < \alpha_R$ , existed simultaneously, which results in discontinuous functions for  $C_M$  and  $\delta_2$  and (see Eqs. (59) and (64)). To avoid this, the expressions for  $\delta_2$  and  $\Delta C_M$  were modified for the cases where  $\alpha < \alpha_R$  and  $\tau_M < \tau_T$ , to give

$$\delta_2 = \left( \frac{\alpha_D}{\alpha_S} - 1 \right) [1 - \exp(K_1(\tau_M - \tau_T))] . \quad (65)$$

$$\begin{aligned} \Delta C_M = & P_1 A + P_2 \alpha_W + P_3 \frac{\alpha}{\alpha_S} + P_4 |\alpha_W| + P_5 \delta_1 + P_6 \Delta\alpha_2 \\ & + P_7 \alpha_D A_D \tau_M [1 - \exp(K_1(\tau_M - \tau_T))] , \end{aligned} \quad (66)$$

where  $K_1 = 0.3$  is a new constant determined by comparing the modified expressions with wind tunnel data. The modified terms are those which are supposed to be zero when the vortex detaches from the leading edge and reach a certain value as the flow reattaches after the vortex has been shed. These terms are multiplied by  $[1 - \exp(K_1(\tau_M - \tau_T))]$ , which ensures that they tend to appropriate values as  $\tau_M$  becomes increasingly larger than  $\tau_T$ .

Eighteen sets of data measured by Gray and Liiva [38] for a NACA 0012 airfoil at a Mach number  $M = 0.6$  and Reynolds number  $Re = 6.2 \times 10^6$  were used to obtain the empirical constants. The nondimensional frequency of forced oscillation ( $k = \omega b/U$ ) was in the range  $0.044 \leq k \leq 0.256$ , the amplitude of oscillation was  $2.5^\circ \leq \bar{\alpha} \leq 7.5^\circ$ , and the mean angle of attack varied from  $0.0^\circ \leq \alpha_0 \leq 10.0^\circ$ , thus, ensuring that the model would be valid over a wide range of parameters. The test data were curve fit to the semi-analytical expressions for  $C_M$  using the “Amoeba” subroutine from Press et al. [87] and a least-squares method. The coefficients obtained are:  $P_1 = -1.757$ ,  $P_2 = -0.08255$ ,  $P_3 = 0.006019$ ,  $P_4 = -0.06206$ ,  $P_5 = 0.04894$ ,  $P_6 = -0.7773$ ,  $P_7 = -5.964$ ,  $C_1 = 54.93$ ,  $C_2 = 10.52$ ,  $C_3 = 5.420$ ,  $C_4 = 0.4884$ ,  $C_5 = 16.65$ ,  $C_6 = -8.669$  and  $\varepsilon = -0.0139$ .



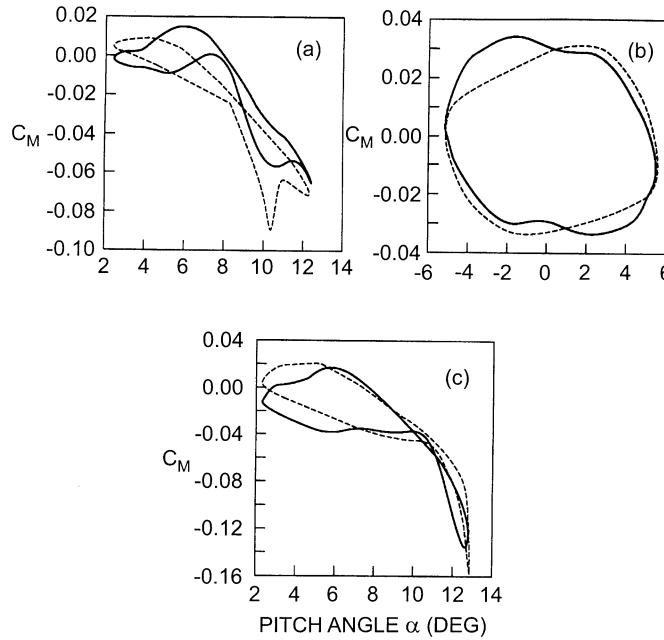


Fig. 22. Comparison of the actual moment coefficient data obtained from Gray and Liiva [38], —, with the moment coefficient predicted by the dynamic stall Bielawa et al. [15] model ...,  $Re = 6.2 \times 10^6$ ,  $M = 0.6$ . (a)  $k = 0.045$ ,  $\alpha_0 = 7.39^\circ$ ,  $\bar{\alpha} = 4.94^\circ$ ; (b)  $k = 0.165$ ,  $\alpha_0 = 0.20^\circ$ ,  $\bar{\alpha} = 5.49^\circ$ ; and (c)  $k = 0.129$ ,  $\alpha_0 = 7.62^\circ$ ,  $\bar{\alpha} = 5.28^\circ$  (from Ref. [90]).

Some typical comparisons between measured  $C_M$  and the values predicted by the modified dynamic stall model are shown in Fig. 22 for three different non-dimensional frequencies, amplitudes and mean angles of attack. These comparisons show neither the best nor worst agreement between the experimental data and the dynamic stall model (a complete comparison for all of the experimental data is given by Keleris [54]). As shown in Fig. 22, although the comparison is far from excellent in terms of the magnitude of  $C_M$ , the model does give a reasonable representation of the main events occurring in the dynamic stall process.

**3.2.2.3. Solution of the aeroelastic equations.** Price and Keleris [90] studied a rigid NACA 0012 airfoil, flexibly mounted in pitch in subsonic flow. No heave motion is allowed, which corresponds to a system much stiffer in heave than in pitch. The oscillations are not self excited, an externally applied sinusoidal torque continuously drives the system, and it is the response of the airfoil to this applied torque which they examined. However, the results obtained are potentially of some significance to those interested in self excited flutter. For example, the results indicate the type of complexities which can be obtained in the dynamics of an airfoil executing two-degree-of-freedom flutter when large pitch amplitude oscillations occur. Furthermore, the results presented are directly applicable to an airfoil executing single degree-of-freedom flutter in pitch.

Considering an airfoil with freedom to oscillate in pitch only, then the equation of motion is given from Eq. (11) as

$$r_\alpha^2 \left( \alpha'' + 2 \frac{\zeta_\alpha}{U^*} \alpha' + \frac{1}{U^{*2}} \alpha \right) = \frac{2}{\pi \mu} C_M(\tau) + \frac{Q(\tau)}{m U^2}, \quad (67)$$

where  $C_M(\tau)$  is the aerodynamic moment coefficient taken about the elastic axis, and  $Q(\tau)$  the externally applied torque about the elastic axis which drives the system.

To solve the aeroelastic equations, Houbolt's [46] implicit finite difference method was used, giving  $\alpha$  at the  $n$ th time step as follows [90]:

$$\alpha_n = Z_1/Z_2, \quad (68)$$

where

$$\begin{aligned} Z_1 = & C_{Mn} \left( \frac{a_8}{a_5} \right) + Q_n \left( \frac{1}{a_5} \right) + \alpha_{n-1} \left( \frac{5}{(\Delta\tau)^2} + \frac{3}{\Delta\tau} \frac{a_6}{a_5} \right) \\ & - \alpha_{n-2} \left( \frac{4}{(\Delta\tau)^2} + \frac{3}{2\Delta\tau} \frac{a_6}{a_5} \right) + \alpha_{n-3} \left( \frac{1}{(\Delta\tau)^2} + \frac{1}{3\Delta\tau} \frac{a_6}{a_5} \right), \end{aligned} \quad (69)$$

$$Z_2 = \frac{2}{(\Delta\tau)^2} + \frac{11}{6\Delta\tau} \frac{a_6}{a_5} + \frac{a_7}{a_5}, \quad (70)$$

and

$$a_5 = r_\alpha^2, \quad a_6 = \frac{2r_\alpha^2 \zeta_\alpha}{U^*}, \quad a_7 = \frac{r_\alpha^2}{U^{*2}}, \quad a_8 = \frac{2}{\pi\mu}. \quad (71)$$

The following recursive relationships were used to obtain the pitch rate,  $A_n$ , and the unsteady decay parameter,  $(\alpha_w)_n$ , at each time step [15]:

$$A_n = \frac{(\Delta\alpha)_n}{(\Delta\tau)_n}, \quad (72)$$

and

$$(\alpha_w)_n = x_n + y_n, \quad (73)$$

where

$$x_n = x_{n-1} \exp(-0.0455(1 - M^2)(\Delta\tau)_n) + 0.165(\alpha_n - \alpha_{n-1}), \quad (74)$$

$$y_n = y_{n-1} \exp(-0.3(1 - M^2)(\Delta\tau)_n) + 0.355(\alpha_n - \alpha_{n-1}). \quad (75)$$

Houbolt's method requires  $C_{Mn}$  at any time step,  $n$ , in order to calculate  $\alpha_n$  at the same time step. However, because  $C_{Mn}$  depends on  $\alpha_n$  at the same time, a recursive predictor-corrector procedure must be implemented. First,  $C_{Mn}$  is calculated at time step  $n$  based on  $\alpha_{n-1}$ . Next, this value of  $C_{Mn}$  is used to calculate the predictor value of  $\alpha_n$ , and based on this  $C_{Mn}$  is recalculated. Finally, the recalculated  $C_{Mn}$  is used to find the corrector value of  $\alpha_n$ . If the absolute difference between the predictor and the corrector values is within a specified tolerance (approximately  $1.0 \times 10^{-6}$ ), then the corrector value is accepted. If the absolute difference is greater than the tolerance the entire procedure is halted. Convergence of this corrector-predictor method was investigated extensively,

as was the convergence of the whole numerical procedure, and is discussed in some detail by Keleris [54]. In all cases it was ensured that the time step was sufficiently small such that a further reduction had no effect on the amplitude of motion, when the motion was periodic, or on the character of the attractor when it was chaotic.

#### 4. Solution techniques of equations with structural nonlinearities

##### 4.1. Finite difference scheme

To solve Eqs. (10) and (11), Houbolt's [46] finite difference method can be used. This has been shown to be more efficient than higher order finite difference schemes [52], yet still have good accuracy. The derivatives at time  $\tau + \Delta\tau$  are replaced by backward difference formulas using values at three previous times. For example

$$\alpha''(\tau + \Delta\tau) = [2\alpha(\tau + \Delta\tau) - 5\alpha(\tau) + 4\alpha(\tau - \Delta\tau) - \alpha(\tau - 2\Delta\tau)]/\Delta\tau^2, \quad (76)$$

$$\alpha'(\tau + \Delta\tau) = [11\alpha(\tau + \Delta\tau) - 18\alpha(\tau) + 9\alpha(\tau - \Delta\tau) - 2\alpha(\tau - 2\Delta\tau)]/6\Delta\tau, \quad (77)$$

and similar expressions can be written for  $\xi''(\tau + \Delta\tau)$  and  $\xi'(\tau + \Delta\tau)$ . Hence, in difference form, Eqs. (10) and (11) can be expressed, after considerable algebra [65], as

$$\bar{P}_{11}\alpha(\tau + \Delta\tau) + \bar{P}_{12}\xi(\tau + \Delta\tau) = \bar{X}_1 + T_\xi(\xi), \quad (78)$$

$$\bar{P}_{21}\alpha(\tau + \Delta\tau) + \bar{P}_{22}\xi(\tau + \Delta\tau) = \bar{X}_2 + T_\alpha(\alpha), \quad (79)$$

where  $\bar{P}_{11} \dots \bar{P}_{22}$  are coefficients depending on the airfoil parameters and the constants in the Wagner's function.  $T_\alpha(\alpha)$  and  $T_\xi(\xi)$  contain functions of the nonlinear structures. These are long algebraic terms and are given in Lee and Desrochers [65], Lee and LeBlanc [64], and Price et al. [88] for the freeplay and cubic nonlinearities.

As shown in Eqs. (15) and (16), the aerodynamic forces and moments depend on two integrals:

$$I_1(\tau) = \int_0^\tau \lambda(\sigma) e^{-\varepsilon_1(\tau-\sigma)} d\sigma, \quad (80)$$

$$I_2(\tau) = \int_0^\tau \lambda(\sigma) e^{-\varepsilon_2(\tau-\sigma)} d\sigma,$$

where

$$\lambda(\sigma) = \alpha'(\sigma) + \xi''(\sigma) + (1/2 - a_h)\alpha''(\sigma). \quad (81)$$

These integrals have to be evaluated at each time step, and in order to reduce the amount of computations, Lee and Desrochers [65] derived a recurrence formula using Simpson's rule and obtained

$$I_1(\tau + \Delta\tau) = e^{-\varepsilon_1\Delta\tau} I_1(\tau) + \frac{\Delta\tau}{24} \left\{ 9\lambda(\tau + \Delta\tau) + 19\lambda(\tau) e^{-\varepsilon_1\Delta\tau} - 5\lambda(\tau - \Delta\tau) e^{-2\varepsilon_1\Delta\tau} \right. \\ \left. + \lambda(\tau - 2\Delta\tau) e^{-3\varepsilon_1\Delta\tau} \right\} \quad (82)$$

and a similar expression for  $I_2(\lambda)$  after replacing  $\varepsilon_1$  by  $\varepsilon_2$  in the above equation.

Houbolt's finite difference scheme requires values of  $\alpha$  and  $\xi$  at times  $\tau - 2\Delta\tau$ ,  $\tau - \Delta\tau$  and  $\tau$  in order to determine the respective values at  $\tau + \Delta\tau$ . Hence, at time  $\tau = 0$ , a starting procedure is required. Using Taylor's series the following can be written:

$$\alpha(-\Delta\tau) = \alpha(0) - \Delta\tau\alpha'(0) + \frac{\Delta\tau^2}{2}\alpha''(0) + O(\Delta\tau^3), \quad (83)$$

$$\alpha(\Delta\tau) = \alpha(0) + \Delta\tau\alpha'(0) + \frac{\Delta\tau^2}{2}\alpha''(0) + O(\Delta\tau^3), \quad (84)$$

with similar expressions for  $\alpha'$ ,  $\alpha''$ ,  $\xi$ ,  $\xi'$  and  $\xi''$ . The initial conditions  $\alpha(0)$ ,  $\alpha'(0)$ ,  $\xi(0)$  and  $\xi'(0)$  are known and the higher derivatives up to fourth order are required. They can be obtained from Eqs. (10) and (11) and are given by

$$\begin{bmatrix} \alpha^{(n)}(0) \\ \xi^{(n)}(0) \end{bmatrix} = [Q]^{-1} \begin{bmatrix} Y_1^{(n)} \\ Y_I^{(n)} \end{bmatrix}, \quad (85)$$

where  $Q_{11}$ ,  $Q_{12}$ ,  $Q_{21}$ ,  $Q_{22}$ ,  $Y_1^{(n)}$  and  $Y_I^{(n)}$  can be found in Lee and Desrochers [65], Lee and LeBlanc [64] and Price et al. [88]. For the next step, Houbolt's scheme can be used since  $\alpha$  and  $\xi$  at  $\tau = -\Delta\tau$ , 0 and  $\Delta\tau$  are known. The accuracy of the numerical scheme is  $O(\Delta\tau^4)$  at each step while Eq. (83) and (84) limit the accuracy to  $O(\Delta\tau^3)$ . A starting accuracy higher than  $O(\Delta\tau^3)$  is not necessary since Jones and Lee [52] showed that the error per cycle in the numerical scheme is  $(2\pi/\omega)O(\Delta\tau^3)$ . They also found that a step size of  $1/256$  of the period of the highest frequency component yields sufficiently accurate results.

#### 4.2. Runge–Kutta scheme

The aeroelastic equations given by Eq. (24) are formulated as a set of first-order ordinary differential equations, and a number of numerical integration methods are available to solve this initial-value problem. Lee et al. [70] used a fourth-order Runge–Kutta scheme to integrate the system of equations for given initial conditions in their study of cubic restoring forces.

The airfoil motion from Eq. (24) is given by

$$\frac{d\mathbf{X}}{d\tau} = \mathbf{f}(\mathbf{X}, \tau). \quad (86)$$

Replacing the differentials  $d\mathbf{X}$  and  $d\tau$  by finite increments  $\Delta\mathbf{X}$  and  $\Delta\tau$ , Eq. (86) becomes

$$\Delta\mathbf{X} = \mathbf{f}(\mathbf{X}, \tau) \Delta\tau. \quad (87)$$

Denoting  $\mathbf{X}^{(n)}$  and  $\mathbf{X}^{(n+1)}$  as eight-component vectors at time step  $n$  and  $n+1$ , we can write

$$\mathbf{X}^{(n+1)} = \mathbf{X}^{(n)} + \Delta\mathbf{X}. \quad (88)$$

The derivative  $\mathbf{f}(\mathbf{X}, \tau)$  is evaluated at specified values of  $\mathbf{X}$  and  $\tau$  which depends on the numerical scheme selected. As pointed by Press et al. [87], numerical schemes vary in complexity, accuracy and efficiency as well. The fourth-order Runge–Kutta scheme is commonly used and has been found to be sufficiently accurate for solving engineering problems.

To implement the Runge–Kutta method, the right-hand side of Eq. (86) is evaluated four times for each time step  $\Delta\tau$ : once at the initial point, twice at trial midpoints, and once at a trial endpoint. Multiplying these derivatives by  $\Delta\tau$ , we obtain four different increments for the next time step. The procedure can be represented by the following equations:

$$\Delta\mathbf{X}_1 = \mathbf{f}(\mathbf{X}^{(n)}, \tau^{(n)}) \Delta\tau, \quad (89)$$

$$\Delta\mathbf{X}_2 = \mathbf{f}\left(\mathbf{X}^{(n)} + \frac{\Delta\mathbf{X}_1}{2}, \tau^{(n)} + \frac{\Delta\tau}{2}\right) \Delta\tau, \quad (90)$$

$$\Delta\mathbf{X}_3 = \mathbf{f}\left(\mathbf{X}^{(n)} + \frac{\Delta\mathbf{X}_2}{2}, \tau^{(n)} + \frac{\Delta\tau}{2}\right) \Delta\tau, \quad (91)$$

$$\Delta\mathbf{X}_4 = \mathbf{f}(\mathbf{X}^{(n)} + \Delta\mathbf{X}_3, \tau^{(n)} + \Delta\tau) \Delta\tau, \quad (92)$$

$$\mathbf{X}^{(n+1)} = \mathbf{X}^{(n)} + \frac{\Delta\mathbf{X}_1}{6} + \frac{\Delta\mathbf{X}_2}{3} + \frac{\Delta\mathbf{X}_3}{3} + \frac{\Delta\mathbf{X}_4}{6} + 0(\Delta\tau^5). \quad (93)$$

In Eqs. (89)–(93),  $\Delta\mathbf{X}_1$  to  $\Delta\mathbf{X}_4$  are eight-component vector increments, and  $\tau^{(n)}$  is the  $n$ th time step. These equations can be written in terms of vector components, and from Eqs. (25) and (26), the corresponding set of equations for Eq. (89) is given as

$$\begin{aligned} \Delta x_{1,1} &= x_2^{(n)} \Delta\tau, \Delta x_{1,2} = (c_0 H^{(n)} - d_0 P^{(n)}) \Delta\tau / (d_0 c_1 - c_0 d_1), \Delta x_{1,3} = x_4^{(n)} \Delta\tau, \\ \Delta x_{1,4} &= (-c_1 H^{(n)} + d_1 P^{(n)}) \Delta\tau / (d_0 c_1 - c_0 d), \Delta x_{1,5} = (x_1^{(n)} - \varepsilon_1 x_5^{(n)}) \Delta\tau, \\ \Delta x_{1,6} &= (x_1^{(n)} - \varepsilon_2 x_6^{(n)}) \Delta\tau, \Delta x_{1,7} = (x_3^{(n)} - \varepsilon_1 x_7^{(n)}) \Delta\tau, \Delta x_{1,8} = (x_3^{(n)} - \varepsilon_2 x_8^{(n)}) \Delta\tau, \end{aligned} \quad (94)$$

where

$$\begin{aligned} P^{(n)} &= c_2 x_4^{(n)} + c_3 x_2^{(n)} + c_4 x_3^{(n)} + c_5 x_1^{(n)} + c_6 x_5^{(n)} \\ &\quad + c_7 x_6^{(n)} + c_8 x_7^{(n)} + c_9 x_8^{(n)} + \left(\frac{\bar{\omega}}{U_*}\right)^2 G(x_3^{(n)}) - f(\tau^{(n)}), \\ H^{(n)} &= d_2 x_2^{(n)} + d_3 x_1^{(n)} + d_4 x_4^{(n)} + d_5 x_3^{(n)} + d_6 x_5^{(n)} \\ &\quad + d_7 x_6^{(n)} + d_8 x_7^{(n)} + d_9 x_8^{(n)} + \left(\frac{1}{U_*}\right)^2 M(x_1^{(n)}) - g(\tau^{(n)}). \end{aligned} \quad (95)$$

In Eqs. (94) and (95),  $\Delta x_{1,j}$  is the  $j$ th component of the vector increment  $\Delta\mathbf{X}_1$ , the superscript  $n$  indicates that the associated values of the system variables  $x_1 \dots x_8$ ,  $P$ ,  $H$  and independent variable  $\tau$  are evaluated at the  $n$ th time step. Replacing  $\Delta x_{1,i}$ ,  $x_i^{(n)}$  and  $\tau^{(n)}$  in the above two equations with  $\Delta x_{2,i}$ ,  $(x_i^{(n)} + \Delta x_{1,i}/2)$  and  $(\tau^{(n)} + \Delta\tau/2)$  respectively, we can get a set of equations in

component form for Eq. (90). In a similar manner, Eqs. (91) and (92) can be evaluated. Substituting into Eq. (93) we obtain  $x_1^{(n+1)} \dots x_8^{(n+1)}$ .

From the definitions of  $w_1$  to  $w_4$  (see Eq. (18)), the initial values of  $w_1$  to  $w_4$  are equal to zero while the other four variables  $\alpha$ ,  $\alpha'$ ,  $\xi$ ,  $\xi'$  can take on arbitrary values. The initial conditions of the system can be expressed as

$$\mathbf{X}(0) = \mathbf{X}^{(0)} = [x_1(0), x_2(0), \dots, x_8(0)]^T = [\alpha(0), \alpha'(0), \xi(0), \xi'(0), 0, 0, 0, 0]^T, \quad (96)$$

where  $\alpha(0)$ ,  $\alpha'(0)$ ,  $\xi(0)$ ,  $\xi'(0)$  are the initial values of pitch displacement, pitch velocity, plunge displacement, and plunge velocity, respectively.

Given initial values of the system variables, the starting procedure of the Runge–Kutta method is straightforward. The formulas for the first-step integration can be obtained by simply replacing  $\mathbf{X}^{(n)}$  and  $\tau^{(n)}$  in Eqs. (89) and (90) by  $\mathbf{X}^{(0)}$  or  $\mathbf{X}(0)$  and  $\tau^{(0)} = 0$ . The Runge–Kutta method is an explicit and stable numerical procedure, and the only input parameter required is the time step  $\Delta\tau$ .

#### 4.3. Describing function

The describing function technique, sometimes referred to as the harmonic balance method, is a method of obtaining an equivalent linear system such that traditional linear aeroelastic methods of analysis can be employed. This method is essentially the same as the first approximation of Kryloff and Bogoliuboff [58].

The first example of the use of the describing function method in aeroelastic systems known to the present authors is by Shen [96], who analyzed a wing control-surface flutter with nonlinear structural stiffnesses. The nonlinear elements chosen included freeplay and hysteretic structural restoring forces and moments. A favorable comparison was made between results obtained from the describing function method and those previously obtained by Woolston et al. [120,121] using an analog computer. Johnson [51] extended the analysis to the next higher approximation and used the term sinusoidal analysis. Brietbach [18,19] also used the describing function method to assess the effect of various structural nonlinearities on the aeroelastic response of airfoils. Laurenson and Trn [60] used this method to investigate the aeroelastic response of missile control surfaces containing either one or two structural nonlinearities. The describing function results were compared with those obtained from numerical simulations showing excellent agreement. Laurenson and Trn [60] also demonstrated that for systems with structural nonlinearities, limit cycle oscillations can be obtained at velocities below the linear flutter boundary. Both Brietbach [18,19] and Lee [72] showed how the describing function method could be extended for use on systems with multiple structural nonlinearities. Ueda and Dowell [111] employed the describing function method for the case of aerodynamic nonlinearities in the analysis of a typical section subject to transonic aerodynamics. They also compared their describing function results with those obtained from numerical integration, verifying the describing function method of solution. Comparisons between results obtained from a describing function method and numerical integration are also given by Tang and Dowell [101,102] for the aeroelastic analysis of non-rotating helicopter blades, and by Yang and Zhao [123], Zhao and Yang [125] and Liu and Zhao [75] in an investigation of a typical section subject to nonlinear structural restoring forces. Dunn and Dugundji [24] used the harmonic balance method, combined with the ONERA stall model, to investigate the aeroelastic response of a three-dimensional wing. A Fourier analysis was employed to extract harmonics from

the ONERA aerodynamics, then the describing function method was used in conjunction with a Newton–Raphson technique to solve the resulting nonlinear Rayleigh–Ritz equations.

Price et al. [89] analyzed a two-degree-of-freedom airfoil motion with either bilinear or cubic structural restoring moments in pitch. As previously shown by Lee and Tron [66], such nonlinearities are representative of loose control surface hinges. A describing function for a bilinear stiffness is given by Lee and Tron [66], obtained using the method of Laurenson et al. [61]. However, this describing function is applicable only where there is no preload. If a preload is applied, as in the general case presented by Price et al. [89], then the airfoil does not oscillate about the zero mean position. Instead the airfoil pitch motion is of the form

$$\alpha(\tau) = B + A \sin \omega \tau, \quad (97)$$

where  $A$  and  $B$  are constants. To account for this offset, a dual-input describing function technique must be used, as discussed by Gelb and Vander Velde [35], which results in a mean component for the describing function. A similar study of a dual-input describing function technique is also presented by Kim and Lee [55] for a flexible airfoil with a freeplay nonlinearity where the airfoil is modeled as finite beam elements.

The dual-input describing function is given by

$$N = N_B + N_A \sin \omega \tau + N_C \cos \omega \tau. \quad (98)$$

Considering only the fundamental components of the restoring moment response, the following expressions for  $N_A$ ,  $N_B$  and  $N_C$  are obtained:

$$N_B = \frac{1}{2\pi} \int_{-\pi}^{\pi} M(\alpha) d(\omega \tau), \quad N_A = \frac{1}{\pi} \int_{-\pi}^{\pi} M(\alpha) \sin \omega \tau d(\omega \tau),$$

and (99)

$$N_C = \frac{1}{\pi} \int_{-\pi}^{\pi} M(\alpha) \cos \omega \tau d(\omega \tau).$$

Evaluating the above integrals for the bilinear stiffness with  $M(\alpha)$  given in Eq. (32), Price et al. [89] obtained

$$N_B = A[(M_0 + M_f \delta/2)/A - (\gamma + \beta)/2 - (1 - M_f)g(\gamma) + (1 - M_f)g(\beta)],$$

$$N_A = A[1 + (1 - M_f)(f(\gamma) - f(\beta))] \quad \text{and} \quad N_C = 0, \quad (100)$$

where

$$f(x) = \begin{cases} 1/\pi(\sin^{-1} x + x(1 - x^2)^{1/2}) & \text{for } |x| < 1, \\ -1/2 & \text{for } x \leq -1, \\ 1/2 & \text{for } x \geq 1, \end{cases}$$

$$g(x) = \begin{cases} 1/\pi(x \sin^{-1} x + (1 - x^2)^{1/2}) & \text{for } |x| \leq 1, \\ |x|/2 & \text{for } |x| > 1 \end{cases} \quad (101)$$

and  $\gamma = (\alpha_f - B)/A$  and  $\beta = (\alpha_f + \delta - B)/A$ .

For a cubic nonlinearity given by Eq. (31), the describing function is given by [89]

$$\begin{aligned} N_B &= B[\beta_0/B + \beta_1 + \beta_2 B + \beta_3 B^2 + \frac{1}{2}A^2(\beta_2/B + 3\beta_3)] , \\ N_A &= A[\beta_1 + 2\beta_2 B + 3\beta_3 B^2 + \frac{3}{4}\beta_3 A^2] , \end{aligned} \quad (102)$$

and

$$N_C = 0 .$$

For a hysteresis nonlinearity of the type shown in Fig 11, Shen [96] derived the describing function using the equations in dimensional form similar to those given by Eqs. (8) and (9).

Using the notations in this review, we can reproduce Shen's [96] results, and for the sake of brevity, consider only a hysteresis nonlinearity in the pitch degree-of-freedom. We replace

$$\begin{aligned} \bar{G}(h) &= K_h h , \\ \bar{M}(\alpha) &= K_\alpha(\alpha) \alpha , \end{aligned} \quad (103)$$

where  $K_h$  is a constant and  $K_\alpha$  is a function of  $\alpha$ . We express  $\alpha$  in a form similar to Eq. (97) setting  $B = 0$  as follows:

$$\alpha = A e^{i\omega t} . \quad (104)$$

Retaining only the fundamental harmonics, Shen [96] obtained

$$K_\alpha(\alpha) = I_\alpha \omega_\alpha'^2 A K'_\alpha(A) . \quad (105)$$

Here  $\omega'_\alpha$  is the reference frequency and  $K'_\alpha(A)$  is the describing function. When the describing function is real, Eqs. (8) and (9) are a set of linear equations with different natural frequency  $\omega_\alpha$  and stiffness  $K_\alpha$  which depend on the amplitude of oscillation. By specifying  $A$ , we can proceed to compute the airfoil motion. When the describing function is complex, our equivalent linear system will have structural damping introduced which is a function of the amplitude.

For  $\alpha_f = 0$  in Fig. 11, Shen [96] derived the following expressions for  $K_\alpha(\alpha)$ :

$$\begin{aligned} K_\alpha(\alpha) &= -M_0 + (2M_0/\delta)A \cos \omega t, \quad 0 < \omega t < \pi/2 , \\ K_\alpha(\alpha) &= -M_0, \quad \pi/2 < \omega t < \pi/2 + \phi , \\ K_\alpha(\alpha) &= M_0 - (2M_0/\delta)A \cos \omega t, \quad \pi/2 + \phi < \omega t < 3\pi/2 , \\ K_\alpha(\alpha) &= M_0, \quad 3\pi/2 < \omega t < 3\pi/2 + \phi \\ K_\alpha(\alpha) &= -M_0 + (2M_0/\delta)A \cos \omega t, \quad 3\pi/2 + \phi < \omega t < 2\pi , \end{aligned} \quad (106)$$

where

$$\phi = \sin^{-1}(\delta/A) \leq \pi/2 .$$

The first harmonic now consists of both sine and cosine terms and is given by

$$K_\alpha(\alpha) = K e^{i(\omega t - \psi)} , \quad (107)$$



where

$$K = (K_c^2 + K_s^2)^{1/2}, \quad \psi = \tan^{-1}(K_s/K_c)$$

and

$$K_c = -4M_0 \cos \phi/\pi + (2M_0/\delta)A[1 - \phi/\pi + \sin 2\phi/\pi],$$

$$K_s = -4M_0 \sin \phi/\pi + (2M_0/\delta)A \sin 2\phi/\pi.$$

The presence of structural damping is apparent from the imaginary part of  $K_\alpha(\alpha)$ .

Once the describing function has been obtained, the method of solution is relatively straightforward. Using the non-dimensional equations (10) and (11), Price et al. [89] replaced the nonlinear term  $M(\alpha)$  by the appropriate describing function, given by Eqs. (100) or (102) for bilinear and cubic nonlinearities, respectively. The describing function depends on the amplitude of oscillation  $A$  and  $B$ , and thus, an iterative approach is required. First, it should be realized that there is no steady external moment, aerodynamic or otherwise, acting on the airfoil, hence, there can be no steady component to the restoring moment, or  $N_B$  must be equal to zero. Hence, in the iterative procedure a value of  $A$  is initially assumed, then setting  $N_B = 0$  the value of  $B$  obtained, and the equivalent linear stiffness given by the describing function is now known. From this point on the equations are solved using standard linear aeroelastic techniques, in this case the  $U$ - $g$  method [31] was employed to determine the required value of  $U$  to give simple harmonic motion (which will be of amplitude equal to the assumed value of  $A$ ). The above procedure is repeated for different values of  $A$ , and the variation of  $A$  and  $B$  with  $U$  is then obtained. For the hysteresis nonlinearity, the describing function given by Eqs. (107) is to be used with Eqs. (8) and (9), but they can be changed to be compatible with the non-dimensional equations (10) and (11).

#### 4.4. Analytical techniques

Analytic solutions in nonlinear aeroelastic problems are only possible for special cases. We shall consider structural nonlinearities where the restoring force or moment term can be represented by an analytic function. The case of forced oscillating was studied by Lee et al. [69]. The governing equations are given by Eq. (24), and to make the analysis general, the forcing terms are included in Eqs. (21) and (22) such that

$$f(\tau) = \frac{2}{\mu} \left( \left( \frac{1}{2} - a_h \right) \alpha(0) + \zeta(0) \right) (\psi_1 \varepsilon_1 e^{-\varepsilon_1 \tau} + \psi_2 \varepsilon_2 e^{-\varepsilon_2 \tau}) + \frac{P(\tau)b}{mU^2} \quad (108)$$

and

$$g(\tau) = -\frac{(1 + 2a_h)}{2r_\alpha^2} f(\tau) + \frac{Q(\tau)}{mU^2 r_\alpha^2}. \quad (109)$$

We assume that the external applied forces and moments are sinusoidal, and, without loss in generality, the excitation is only applied in the pitch degree of freedom. In this case,  $P(\tau) = 0$  and we write

$$Q(\tau) = Q_0 \sin \omega \tau, \quad (110)$$

and let

$$F = Q_0/mU^2r_\alpha^2. \quad (111)$$

At sufficiently large values of  $\tau$  when transients are damped out and steady-state solutions are obtained,  $f(\tau) \rightarrow 0$ . For sinusoidal external excitation forces, we assume the plunge and pitch motions together with the expressions for  $w$  defined in Eq. (18) to be of the following form:

$$\begin{aligned} \xi(\tau) &= a_1(\tau)\cos(\omega\tau) + b_1(\tau)\sin(\omega\tau), & \alpha(\tau) &= a_2(\tau)\cos(\omega\tau) + b_2(\tau)\sin(\omega\tau), \\ w_1(\tau) &= a_3(\tau)\cos(\omega\tau) + b_3(\tau)\sin(\omega\tau), & w_2(\tau) &= a_4(\tau)\cos(\omega\tau) + b_4(\tau)\sin(\omega\tau), \\ w_3(\tau) &= a_5(\tau)\cos(\omega\tau) + b_5(\tau)\sin(\omega\tau), & w_4(\tau) &= a_6(\tau)\cos(\omega\tau) + b_6(\tau)\sin(\omega\tau). \end{aligned} \quad (112)$$

Here,  $a_i$  and  $b_i$  ( $i = 1, 2, \dots, 6$ ) are assumed to be slowly varying function in  $\tau$ . The amplitudes of  $\xi(\tau)$  and  $\alpha(\tau)$  are written as

$$r^2 = a_1^2 + b_1^2 \quad (113)$$

and

$$R^2 = a_2^2 + b_2^2. \quad (114)$$

From Eq. (112), we can obtain expressions for various time derivatives. Assuming the second derivatives are small and can be neglected, we obtain a system of 12 first-order nonlinear differential equations after matching the coefficients of  $\cos(\omega\tau)$  and  $\sin(\omega\tau)$ . The resulting system in a matrix notation is given by

$$\mathbf{A}\mathbf{X}' = \mathbf{Y}(\mathbf{X}), \quad (115)$$

where

$$\mathbf{X} = \begin{bmatrix} a_1 \\ b_1 \\ \cdot \\ \cdot \\ a_6 \\ b_6 \end{bmatrix} \quad \text{and} \quad \mathbf{Y}(\mathbf{X}) = \begin{bmatrix} y_1(x) \\ y_2(x) \\ \cdot \\ \cdot \\ y_{11}(x) \\ y_{12}(x) \end{bmatrix}. \quad (116)$$

Here  $\mathbf{A}$  is a matrix whose elements depend on the airfoil parameters and the structural nonlinearity. If the structural nonlinearity, such as a freeplay or hysteresis, can be represented by a simple polynomial expression, then  $G(\xi)$  and  $M(\alpha)$  can be used to evaluate  $\mathbf{A}$  and  $\mathbf{Y}(\mathbf{X})$ . Lee et al. [69] consider cubic nonlinear functions of the form

$$G(\xi) = \xi + \beta_\xi \xi^3, \quad (117)$$

and

$$M(\alpha) = \alpha + \beta_\alpha \alpha^3. \quad (118)$$

The nonlinear terms  $\xi^3(\tau)$  and  $\alpha^3(\tau)$  can be expressed as

$$\begin{aligned}\xi^3(\tau) &= \frac{3}{4}r^2[a_1(\tau)\cos(\omega\tau) + b_1\sin(\omega\tau)] + \text{higher harmonics in } 3\omega\tau, \dots, \\ \alpha^3(\tau) &= \frac{3}{4}R^2[a_2(\tau)\cos(\omega\tau) + b_2\sin(\omega\tau)] + \text{higher harmonics in } 3\omega\tau, \dots\end{aligned}\quad (119)$$

In deriving the 12 first-order nonlinear differential equations, we substitute Eq. (119) for the nonlinear terms  $\xi^3(\tau)$  and  $\alpha^3(\tau)$ , and assume that the higher harmonic terms are small and can be neglected. The same procedure can be applied for nonlinear terms in the form  $\xi^n(\tau)$  and  $\alpha^n(\tau)$  where  $n$  is an integer  $\geq 2$ . For the case where the nonlinear functions  $G(\xi)$  and  $M(\alpha)$  are given in Eqs. (117) and (118), the resulting matrix  $\mathbf{A}$  in Eq. (115) can be expressed as

$$\mathbf{A} = \begin{bmatrix} \mathbf{H} & \mathbf{0} \\ \mathbf{0} & \mathbf{I} \end{bmatrix}. \quad (120)$$

Here  $\mathbf{I}$  is an  $8 \times 8$  identity matrix given by

$$\mathbf{I} = \begin{bmatrix} 1 & 0 & \dots & 0 \\ 0 & 1 & \dots & 0 \\ . & . & \dots & . \\ 0 & 0 & \dots & 1 \end{bmatrix}. \quad (121)$$

The elements of  $\mathbf{H}$  are functions of  $c_0, c_1, \dots, d_0, d_1, \dots$ , and the vector components  $y_1(x), \dots, y_{12}(x)$  in Eq. (116) are functions of  $c_0, c_1, \dots, d_0, d_1, \dots, a_1, a_2, \dots, b_1, b_2, \dots, F, \omega, r, R$ . They are long algebraic expressions given by Lee et al. [69].

Since the interest is in the harmonic solutions of Eq. (24) subject to an external excitation  $g(\tau) = F \sin(\omega\tau)$ , the periodicity condition is enforced by requiring the coefficients  $a_i$  and  $b_i$  to be constants. Here,  $a_1, b_1, \dots, a_6, b_6$  are the equilibrium points for the system given in Eq. (115), and they are determined by setting  $\mathbf{X}' = 0$  and solving for  $\mathbf{Y}(\mathbf{X}) = 0$ . The harmonic solutions of the dynamical system given in Eq. (115) are identified by  $a_1, b_1, \dots, a_6, b_6$ . In deriving the expressions for the equilibrium points, Eq. (115) is first solved for  $a_3, b_3, \dots, a_6, b_6$ , which are then substituted into the expressions for  $a_1, b_1, a_2$ , and  $b_4$ . Lee et al. [69] derived a frequency–amplitude relationship given by

$$D_1 R^2 - D_2 F^2 = 0 \quad (122)$$

where  $D_1$  and  $D_2$  are functions of  $c_0, c_1, \dots, d_0, d_1, \dots, r, R, \omega$  and are given in their paper. The amplitudes  $R$  and  $r$  are related by the expression

$$R^2 = k_1 r^2 + k_2 r^4 + k_3 r^6, \quad (123)$$

where  $k_1, k_2$ , and  $k_3$  are functions of  $c_0, c_1, \dots, d_0, d_1, \dots, \omega$ .

Eqs. (122) and (123) give the relation between  $r$  and  $R$  with  $\omega$ . Lee et al. [69] showed that the resulting equation after evaluating all the coefficients and substituting into the above two equations give a polynomial of degree 11 in  $r^2$ . Once  $r$  is computed, then  $R$  can be determined from Eq. (123). For certain values of  $\omega$ , both equations admit multi-valued amplitudes.

If a more accurate analytical prediction is required, the expressions given in Eq. (112) can include terms associated with higher harmonic. For example, the first two expressions for  $\xi(\tau)$  and  $\alpha(\tau)$  in

Eq. (112) can be replaced by

$$\xi(\tau) = a_1(\tau) \cos(\omega\tau) + b_1(\tau) \sin(\omega\tau) + c_1(\tau) \cos(k\omega\tau) + d_1(\tau) \sin(k\omega\tau), \quad (124)$$

$$\alpha(\tau) = a_2(\tau) \cos(\omega\tau) + b_2(\tau) \sin(\omega\tau) + c_2(\tau) \cos(j\omega\tau) + d_2(\tau) \sin(j\omega\tau), \quad (125)$$

with similar expressions for  $w_1, \dots, w_1$ . The values of  $k$  and  $j$  in the above equations will be determined according to the form of the nonlinear functions. If the nonlinear functions  $G(\xi)$  is

$$G(\xi) = \xi + \beta_\xi \xi^2, \quad (126)$$

and Eq. (118) is used for  $M(\alpha)$ , we should take  $k = 2$  and  $j = 3$ . The value for  $j \neq 2$  because the first part of the approximation in  $\omega\tau$  when cubed gives a higher harmonic in  $3\omega\tau$  and not  $2\omega\tau$ . Substituting the modified expressions which include the higher harmonic terms into Eq. (24), we obtain a linear system given by Eq. (115) but with a higher dimension.

The procedure presented here can also be applied to a self-excited system, in which  $f(\tau)$  and  $g(\tau)$  in Eqs. (108) and (109) are equal to zero. Lee et al. [70] derived the amplitude-frequency relation for a self-excited system in which  $G(\xi)$  is a linear function  $G(\xi) = \xi$  and  $M(\alpha)$  is a nonlinear function given by Eq. (118). Substituting the expressions given in Eq. (112) into Eq. (24), and after considerable algebraic simplifications, the amplitude of the pitch and plunge motions are obtained, and they are expressed as

$$R^2 = f_1(\omega) \pm \sqrt{f_2(\omega)}, \quad (127)$$

and

$$r^2 = A(\omega)R^2. \quad (128)$$

Here,  $f_1, f_2$ , and  $A$  are functions of  $c_0, c_1, \dots, d_0, d_1, \dots, \omega$ , and can be obtained from Lee et al. [70].

Unlike the case for the system subject to a sinusoidal driving force  $F \sin(\omega\tau)$ , we do not have a reference value for the frequency  $\omega$  for the self-excited system. Consequently, the amplitude relations given in Eqs. (127) and (128) are not complete, and we need to derive an additional relation for  $\omega$ . Lee et al. [70] discussed various methods to estimate  $\omega$ . One possible approach is to apply the center manifold theory to Eq. (24). By rewriting in its normal form, a linear equation which relates the frequency of the limit cycle oscillations can be derived. Using this equation which provides the value for  $\omega$ , and Eqs. (127) and (128), the amplitudes of the limit cycle oscillations for the self-excited system can be determined analytically. The details on the application of the center manifold theorem is given in Liu et al. [76] and an example which demonstrates the accuracy of the analytical predictions will be presented in Section 5.2.

## 5. Bifurcation and chaos of airfoils with structural nonlinearities

### 5.1. Stability and bifurcation analysis

#### 5.1.1. Linear stability analysis of autonomous systems

In Eq. (24) the terms  $f(\tau)$  and  $g(\tau)$  for unforced motion can be neglected if  $\alpha(0) \ll 1$  and  $\xi(0) \ll 1$ , or  $\tau \gg 1$ . Lee et al. [70] considered the system response at large times when transients are damped

out (that is,  $\tau \gg 1$ ). The equations governing the airfoil motion are then a set of autonomous differential equations, and the vector components for  $\mathbf{X}$  and  $\mathbf{f}(\mathbf{X})$  are given by Eqs. (25) and (26) with  $f(\tau) = g(\tau) = 0$ .

To investigate the stability of the nonlinear system, we first apply a linearization technique and then examine the stability using a linear analysis. This approach has been in use for a long time, and the justification has been given by Poincaré [84] more than a hundred years ago. It is well known that the flow of the nonlinear dynamical system in the neighborhood of the singularity (i.e. the equilibrium point of the vector field  $\mathbf{f}$ ) is topologically equivalent to the flow of the linearized system around that fixed point. A dynamical system is said to be structurally stable if small disturbances introduced to the system lead to approximately the same results as those obtained in the absence of those disturbances.

Denoting  $\mathbf{X}_E$  to be a fixed point of the system, we define  $\mathbf{y}(\tau)$  to be a small perturbation about  $\mathbf{X}_E$  given by

$$\mathbf{y}(\tau) = \mathbf{X}(\tau) - \mathbf{X}_E. \quad (129)$$

To investigate whether the perturbation decays or grows, a differential equation for  $\mathbf{y}(\tau)$  is obtained by differentiating Eq. (129) with respect to  $\tau$  to give

$$\mathbf{y}' = \frac{d}{d\tau} (\mathbf{X} - \mathbf{X}_E) = \mathbf{X}' = \mathbf{f}(\mathbf{X}) = \mathbf{f}(\mathbf{X}_E + \mathbf{y}). \quad (130)$$

Expanding  $\mathbf{f}(\mathbf{X})$  about  $\mathbf{X}_E$  using Taylor's series, we obtain

$$\mathbf{f}(\mathbf{X}_E + \mathbf{y}) = \mathbf{f}(\mathbf{X}_E) + \left. \frac{\partial \mathbf{f}(\mathbf{X})}{\partial \mathbf{X}} \right|_{\mathbf{X}_E} \mathbf{y} + O(y^2), \quad (131)$$

where  $O(y^2)$  denotes a second order term in  $\mathbf{y}$  and can be neglected. Since  $\mathbf{X}_E$  is a fixed point,  $\mathbf{f}(\mathbf{X}_E) = 0$ , we obtain

$$\mathbf{y}' = \left. \frac{\partial \mathbf{f}(\mathbf{X})}{\partial \mathbf{X}} \right|_{\mathbf{X}_E} \mathbf{y} = \mathbf{J} \mathbf{y}, \quad (132)$$

where  $\mathbf{J} = \partial \mathbf{f}(\mathbf{X}) / \partial \mathbf{X}|_{\mathbf{X}_E}$  denotes the Jacobian matrix, and Eq. (132) is linear in  $\mathbf{y}$ . If the fixed point is non-degenerate, then  $\det \mathbf{J} \neq 0$ , and there exists a real and non-singular matrix  $\mathbf{T}$  such that

$$\mathbf{T}^{-1} \mathbf{J} \mathbf{T} = \Lambda_J = \begin{bmatrix} \lambda_1 & & & \\ & \lambda_2 & & \\ & & \ddots & \\ & & & \lambda_8 \end{bmatrix}. \quad (133)$$

Using a linear transformation,  $\mathbf{y} = \mathbf{T} \mathbf{Z}$ , we obtain a simple system in  $\mathbf{Z}$ , such that

$$\mathbf{Z}' = \Lambda_J \mathbf{Z}. \quad (134)$$

The solution for the above system is given by  $Z_i = C_i \exp(\lambda_i \tau)$ , for  $i = 1, 2, \dots, 8$ , where  $C_i$  is a constant. If all eigenvalues of  $\mathbf{J}$  are non-zero and have non-zero real part for the complex conjugate eigenvalues, and if all the real part of  $\lambda < 0$ ,  $\mathbf{Z}(\tau) \rightarrow 0$  as  $\tau \rightarrow \infty$ , the perturbation  $\mathbf{y}(\tau)$  decays, and the system is said to be stable. On the other hand, if the real part of  $\lambda > 0$ ,  $\mathbf{y}(\tau)$  will grow exponentially with  $\tau$ , and the system is unstable.

Another approach to analyze the stability of the nonlinear system is to use the stable and unstable manifold theorem [20,42]. The nonlinear system given in Eq. (24) can be rewritten as

$$\mathbf{X}' = \mathbf{A}\mathbf{X} + \mathbf{G}(\mathbf{X}), \quad (135)$$

where  $\mathbf{A}$  is a constant  $8 \times 8$  matrix of which all eigenvalues have non-zero real parts. The term  $\mathbf{A}\mathbf{X}$  represents the linear part of the system and  $\mathbf{G}(\mathbf{X})$  represents the nonlinear part. The stable and unstable manifold theorem deals with the autonomous system in the form given by Eq. (135). If the nonlinear term  $\mathbf{G}(\mathbf{X})$  is smooth, and

$$\lim_{\|\mathbf{X}\| \rightarrow 0} \frac{\|\mathbf{G}(\mathbf{X})\|}{\|\mathbf{X}\|} = 0, \quad (136)$$

then, in the neighborhood of the fixed point, there exists stable and unstable manifolds  $\mathbf{W}_s$  and  $\mathbf{W}_u$  with the same dimensions as the stable and unstable manifolds  $\mathbf{E}_s$  and  $\mathbf{E}_u$  of the linear system

$$\mathbf{y}' = \mathbf{A}\mathbf{y}, \quad (137)$$

in which  $\mathbf{E}_s$  and  $\mathbf{E}_u$  are tangent to  $\mathbf{W}_s$  and  $\mathbf{W}_u$ . Thus, the stability can be analyzed by determining the sign of the eigenvalues of  $\mathbf{A}$  following the approach used to investigate the linearized system given in Eq. (132).

### 5.1.2. Nonlinear analysis

In using a linear stability analysis, we assume that all eigenvalues of  $\mathbf{J}$  in Eq. (132) and all eigenvalues of  $\mathbf{A}$  in Eq. (137) have non-zero real part. If this condition is not satisfied, i.e., either we have a zero eigenvalue  $\lambda = 0$  or a pair of purely imaginary eigenvalues  $\lambda = \pm i\omega$ , then a nonlinear analysis is needed to determine the stability of the dynamical system. An important tool in the nonlinear analysis of dynamical system is to use the theorem of center manifolds, which can be used to separate the influence of the stable and unstable manifolds. A detailed discussion on the theoretical background and applications of the center manifold is given by Gukenheim and Holmes [39], Verhulst [115], Beyn [14], Wiggins [117], and Kuznetsov [59]. Here, we present only the basic idea and describe the method to analyze the bifurcation of dynamical systems associated with one parameter  $\delta$ . Eq. (24) can be rewritten as

$$\mathbf{X}' = \mathbf{f}(\mathbf{X}, \delta), \quad (138)$$

where  $\delta \in \mathbf{R}^1$ ,  $\mathbf{X} \in \mathbf{R}^8$ , and the system is known as the co-dimension one bifurcation problem. By changing the parameter  $\delta$ , the asymptotic system behavior may switch from one state to another. For certain values of  $\delta$ , one type of invariant set may lose its stability and a new type of invariant set may be created which takes over the stability. This is generally referred to as a bifurcation. If the Jacobian matrix has a real eigenvalue which crosses zero as  $\delta$  changes, we have a turning point or

saddle-node bifurcation. If  $\mathbf{J}$  has a pair of complex conjugate eigenvalues which cross the imaginary axis, we have a Hopf-bifurcation.

The center manifold theory can be applied to analyze the behavior of the dynamical system in nonlinear aeroelasticity. The main attractive feature of the center manifold is that it can be used to lower the dimensionality of the system under investigation, so that the dynamics of a high-dimensional system can be studied in a low-dimensional system.

For the autonomous system given in Eq. (138), we introduce a parameter  $\delta$  such that

$$\frac{1}{U^*} = \frac{1}{U_L^*} (1 - \delta), \quad (139)$$

where  $U_L^*$  is constant and equal to the linear flutter speed. By substituting the expression for  $U^*$  given in Eq. (138) into Eq. (139), the system of equations can be rewritten as

$$\begin{aligned} \mathbf{X}' &= \mathbf{A}\mathbf{X} + \mathbf{B}\delta\mathbf{X} + (1 - \delta)^2 \mathbf{F}(\mathbf{X}), \\ \delta' &= 0, \end{aligned} \quad (140)$$

where

$$\mathbf{A} = \begin{bmatrix} \mathbf{A}_1 & \mathbf{A}_2 \\ \mathbf{A}_3 & \mathbf{A}_4 \end{bmatrix}, \quad \mathbf{B} = \begin{bmatrix} \mathbf{B}_1 & 0 \\ 0 & 0 \end{bmatrix}, \quad (141)$$

and

$$\begin{aligned} \mathbf{A}_1 &= \begin{bmatrix} 0 & 1 & 0 & 0 \\ a_{21} & a_{22} & a_{23} & a_{24} \\ 0 & 0 & 0 & 1 \\ a_{41} & a_{42} & a_{43} & a_{44} \end{bmatrix}, \quad \mathbf{A}_2 = \begin{bmatrix} 0 & 0 & 0 & 0 \\ a_{25} & a_{26} & a_{27} & a_{28} \\ 0 & 0 & 0 & 0 \\ a_{45} & a_{46} & a_{47} & a_{48} \end{bmatrix}, \quad \mathbf{A}_3 = \begin{bmatrix} 1 & 0 & 0 & 0 \\ 1 & 0 & 0 & 0 \\ 0 & 0 & 1 & 0 \\ 0 & 0 & 1 & 0 \end{bmatrix}, \\ \mathbf{A}_4 &= \begin{bmatrix} -\varepsilon_1 & 0 & 0 & 0 \\ 0 & -\varepsilon_2 & 0 & 0 \\ 0 & 0 & -\varepsilon_1 & 0 \\ 0 & 0 & 0 & -\varepsilon_2 \end{bmatrix}, \quad \mathbf{B}_1 = \begin{bmatrix} 0 & 0 & 0 & 0 \\ b_{21} & b_{22} & b_{23} & b_{24} \\ 0 & 0 & 0 & 0 \\ b_{41} & b_{42} & b_{43} & b_{44} \end{bmatrix}. \end{aligned} \quad (142)$$

The first two terms in Eq. (140) represent the linear part of the dynamical system, and the nonlinear part is represented by  $\mathbf{F}(\mathbf{X})$  given by

$$\mathbf{F}(\mathbf{X}) = (0, f_2, 0, f_4, 0, 0, 0, 0)^T, \quad (143)$$

where

$$\begin{aligned}
 f_2 &= j \left[ c_0 \left( \frac{1}{U_L^*} \right)^2 M(x_1) - d_0 \left( \frac{\bar{\omega}}{U_L^*} \right)^2 G(x_3) \right], \\
 f_4 &= -j \left[ c_1 \left( \frac{1}{U_L^*} \right)^2 M(x_1) - d_1 \left( \frac{\bar{\omega}}{U_L^*} \right)^2 G(x_3) \right], \\
 j &= c_1 d_0 - d_1 c_0.
 \end{aligned} \tag{144}$$

The coefficients  $a_{ij}$ ,  $b_{ij}$  are defined as follows:

$$\begin{aligned}
 a_{21} &= j(d_3 c_0 - c_5 d_0), & a_{41} &= -j(d_3 c_1 - c_5 d_1), \\
 a_{22} &= j(d_2 c_0 - c_3 d_0), & a_{42} &= -j(d_2 c_1 - c_3 d_1), \\
 a_{23} &= j(d_5 c_0 - c_4 d_0), & a_{43} &= -j(d_3 c_1 - c_4 d_1), \\
 a_{24} &= j(d_4 c_0 - c_2 d_0), & a_{44} &= -j(d_4 c_1 - c_2 d_1), \\
 a_{25} &= j(d_6 c_0 - c_6 d_0), & a_{45} &= -j(d_6 c_1 - c_6 d_1), \\
 a_{26} &= j(d_7 c_0 - c_7 d_0), & a_{46} &= -j(d_7 c_1 - c_7 d_1), \\
 a_{27} &= j(d_8 c_0 - c_8 d_0), & a_{47} &= -j(d_8 c_1 - c_8 d_1), \\
 a_{28} &= j(d_9 c_0 - c_9 d_0), & a_{48} &= -j(d_9 c_1 - c_9 d_1), \\
 b_{21} &= 0, & b_{22} &= -j d_2 c_0, & b_{23} &= 0, & b_{24} &= j c_2 d_0, \\
 b_{41} &= 0, & b_{42} &= j d_2 c_1, & b_{43} &= 0, & b_{44} &= -j c_2 d_1,
 \end{aligned} \tag{145}$$

where  $c_0, d_0, \dots, c_9, d_9$  are given in appendix A with  $U^*$  replaced by  $U_L^*$ . The functions  $G(x_3)$  and  $M(x_1)$  are the plunge and pitch degree-of-freedom structural nonlinearities (see Eqs. (10) and (11)) and  $x_3 = \xi$ ,  $x_1 = \alpha$ . Here,  $M(\alpha)$  and  $G(\xi)$  are assumed to contain only nonlinear functions in  $\alpha$  and  $\xi$ , respectively. When linear terms are included, some modifications are needed in which  $b_{21}$ ,  $b_{23}$ ,  $b_{41}$ ,  $b_{43}$  become non-zero. The details can be found in Liu et al. [76].

### 5.1.3. Hopf-bifurcation point

We denote  $(\mathbf{X}(\delta), \delta)$  to be a stationary branch of Eq. (138), and assume that at  $\delta = \delta_0$  the Jacobian matrix  $f_X(\mathbf{X}(\delta_0), \delta_0)$  has a simple eigenvalue  $i\omega_0$ ,  $\omega_0 \neq 0$  with eigenvector  $\mathbf{P}_1 + i\mathbf{P}_2$ , and no other eigenvalue of the type  $ik\omega_0$ ,  $k = 0, 2, 3, \dots$ . If the condition

$$\left. \frac{d[\text{Re}(\lambda)]}{d\delta} \right|_{\delta_0} \neq 0, \tag{146}$$

is satisfied, then there exists a smooth branch of periodic solutions. A Hopf-point can be regarded as the transition point where a stable equilibrium solution changes to an oscillatory solution [94].



Let  $\mathbf{q}$  be a vector such that  $\mathbf{q} \in \mathbf{R}^8$ , and satisfies the following condition:

$$\mathbf{q}^T \mathbf{P}_1 = 0, \text{ and } \mathbf{q}^T \mathbf{P}_2 = 1, \quad (147)$$

where  $\mathbf{P}_1$  and  $\mathbf{P}_2$  are the eigenvectors. The condition expressed in Eq. (146) is satisfied if and only if  $(\mathbf{X}(\delta_0), \delta_0, \mathbf{P}_1, \mathbf{P}_2, \omega_0) \in \mathbf{R}^{26}$  is a regular solution of the following equation:

$$\mathbf{T}(\mathbf{X}, \delta, \mathbf{P}_1, \mathbf{P}_2, \omega) = \begin{pmatrix} \mathbf{f}(\mathbf{X}, \delta) \\ \mathbf{f}_x(\mathbf{X}, \delta) \mathbf{P}_1 + \omega \mathbf{P}_2 \\ \mathbf{f}_x(\mathbf{X}, \delta) \mathbf{P}_2 - \omega \mathbf{P}_1 \\ \mathbf{q}^T \mathbf{P}_1 \\ \mathbf{q}^T \mathbf{P}_2 - 1 \end{pmatrix} = 0. \quad (148)$$

The Hopf-point is determined by setting  $\delta_0 = 0$  in Eq. (140) and the value of  $U_L^*$  is determined from the condition that the eigenvalues of  $\mathbf{A}$  consist of a pair of imaginary eigenvalues  $\pm i\omega_0$ . From the eigenspace of  $\mathbf{A}$ , a transformation matrix  $\mathbf{P}$  is determined, such that

$$\mathbf{P}^{-1} \mathbf{A} \mathbf{P} = \begin{bmatrix} 0 & \omega_0 & & & & & & \\ -\omega_0 & 0 & & & & & & \\ & & b & c & & & & \\ & & -c & b & & & & \\ & & & & a_1 & & & \\ & & & & & a_2 & & \\ & & & & & & a_3 & \\ & & & & & & & a_4 \end{bmatrix} = \mathbf{J}. \quad (149)$$

The characteristic equation of  $\mathbf{A}$  has two pairs of complex eigenvalues  $\pm i\omega_0, b \pm ic$ , and four real eigenvalues  $a_1, \dots, a_4$ . By introducing a new variable  $\mathbf{Z} \in \mathbf{R}^8$ , such that  $\mathbf{Z} = \mathbf{P}^{-1} \mathbf{X}$ , the system given in Eq. (140) can be rewritten as

$$\begin{aligned} \mathbf{Z}' &= \mathbf{J} \mathbf{Z} - \delta(\mathbf{P}^{-1} \mathbf{B} \mathbf{P}) \mathbf{Z} + (1 - \delta)^2 \mathbf{P}^{-1} \mathbf{F}(\mathbf{P} \mathbf{Z}), \\ \delta' &= 0. \end{aligned} \quad (150)$$

The standard form of Eq. (150) can be expressed as

$$\begin{aligned} z'_1 &= \omega_0 z_2 + f_1(z_1, z_2, \dots, z_8, \delta), \quad z'_2 = -\omega_0 z_1 + f_2(z_1, z_2, \dots, z_8, \delta), \\ z'_3 &= b z_3 + c z_4 + f_3(z_1, z_2, \dots, z_8, \delta), \quad z'_4 = -c z_3 + b z_4 + f_4(z_1, z_2, \dots, z_8, \delta), \\ z'_5 &= a_1 z_5 + f_5(z_1, z_2, \dots, z_8, \delta), \quad z'_6 = a_2 z_6 + f_6(z_1, z_2, \dots, z_8, \delta), \\ z'_7 &= a_3 z_7 + f_7(z_1, z_2, \dots, z_8, \delta), \quad z'_8 = a_4 z_8 + f_8(z_1, z_2, \dots, z_8, \delta), \quad \delta' = 0. \end{aligned} \quad (151)$$

By the application of the center manifold principle, and after solving a set of algebraic equations, the above nine-dimensional system can be reduced to the following two-dimensional system:

$$\begin{aligned} u_1' &= \omega_0 u_2 + g_1(u_1, u_2, \delta), \\ u_2' &= -\omega_0 u_1 + g_2(u_1, u_2, \delta), \end{aligned} \quad (152)$$

where  $g_1$  and  $g_2$  contain the nonlinearity terms of  $u_1, u_2, \delta$ . Since the center manifold is an invariant manifold, the system behavior of the eight-dimensional equations given in Eq. (138) can be studied by analyzing the two-dimensional system given in Eq. (152).

As an example, the center manifold technique was applied by Lee et al. [70] to analyze the bifurcation of the system given in Eq. (138) with  $\mu = 100, x_\alpha = 0.25, r_\alpha = 0.25, \bar{\omega} = 0.2$ . They found that the stationary points loose the hyperbolicity property when a pair of complex conjugate eigenvalues crosses the imaginary axis. From the solution of Eq. (152), we obtain a stationary solution for  $\delta < 0$ , and the solution loses its stability and switches to a limit-cycle oscillation when  $\delta > 0$ . These solutions are not dependent on the value of the initial condition  $\alpha(0)$ . This transition also confirms that we have a supercritical Hopf-bifurcation. The dynamical behavior of the system defined by Eq. (152) agrees with that computed numerically from Eq. (138) using a fourth-order accurate Runge–Kutta scheme.

A further simplification can be obtained by rewriting the two-dimensional center manifold equations first in normal form so that they can be reduced to a single first-order differential equation. When this equation is expressed in polar coordinates, Liu et al. [76] derived a relation for the frequency expressed as a function of  $\delta$  as follows:

$$\omega = \omega_0 + C\delta, \quad (153)$$

where  $C$  is a constant depending on the system parameters and is determined by the transformation from the center manifold equations to the normal form. Substituting the frequency determined from the above equation into Eqs. (127) and (128), the amplitudes of limit cycle oscillations (LCO) for the self-excited system can be computed.

#### 5.1.4. Analysis of non-autonomous systems

We consider the system to be subject to a sinusoidal excitation, and without loss in generality, the excitation given in Eqs. (108) and (109) is applied only in the pitch degree of freedom (i.e.,  $P(\tau) = 0$ ). In this case,  $f(\tau) = 0$  and  $g(\tau) = F \sin \omega\tau$ , and the system of equations expressed in Eq. (24) is non-autonomous. Time-dependent systems are more complicated than autonomous systems, since the solutions depend upon both  $\mathbf{X}$  and  $\tau$  instead of solely on  $\mathbf{X}$ . Moreover, the concept of a fixed point is no longer available. Consequently, the linear stability analysis and the center manifold theory discussed above cannot be directly applied to examine the stability and bifurcation of the non-autonomous system. However, a method can be derived whereby a non-autonomous system can be rewritten as an autonomous system.

When an external excitation  $F \sin(\omega\tau)$  is included, Eq. (20) can be expressed as

$$\begin{aligned} d_0 \xi'' + d_1 \alpha'' + d_2 \alpha' + d_3 \alpha + \left( \frac{1}{U^*} \right)^2 M(\alpha) + d_4 \xi' + d_5 \xi + d_6 w_1 + d_7 w_2 + d_8 w_3 + d_9 w_4 \\ = F \sin(\omega\tau). \end{aligned} \quad (154)$$

The resulting system of first-order differential equations comprising of Eqs. (19) and (154) leads to a non-autonomous system due to the presence of the external excitation forcing. However, it is easy to verify that the solution for the following system:

$$\begin{aligned}y'' + \omega^2 y &= 0, \\y(0) &= 0, \\y'(0) &= \omega F\end{aligned}\tag{155}$$

is given by  $y(\tau) = F \sin(\omega\tau)$ . Eq. (154) can be rewritten in the form:

$$\begin{aligned}d_0 \xi'' + d_1 \alpha'' + d_2 \alpha' + d_3 \alpha + \left(\frac{1}{U_*}\right)^2 M(\alpha) + d_4 \xi' + d_5 \xi + d_6 w_1 \\+ d_7 w_2 + d_8 w_3 + d_9 w_4 - y &= 0, \\y'' + \omega^2 y &= 0.\end{aligned}\tag{156}$$

The system of first-order differential equations given by Eqs. (19) and (156) becomes an autonomous system. In this case,  $\mathbf{X} \in \mathbf{R}^{10}$ , where

$$\mathbf{X} = (\alpha, \alpha', \xi, \xi', w_1, w_2, w_3, w_4, y, y')^T.\tag{157}$$

The stability and bifurcation analysis presented earlier can be applied to the new system.

Another useful result in the stability analysis for non-autonomous systems is due to Poincaré [115]. For a system given by

$$\mathbf{X}' = \mathbf{A}\mathbf{X} + \mathbf{B}(\tau)\mathbf{X} + \mathbf{f}(\tau, \mathbf{X}),\tag{158}$$

if  $\mathbf{A}$  is a constant matrix with all eigenvalues having a negative real part,  $\mathbf{B}(\tau)$  is a matrix with the property

$$\lim_{\tau \rightarrow \infty} \|\mathbf{B}(\tau)\| = 0,\tag{159}$$

and the vector function  $\mathbf{f}(\tau, \mathbf{X})$  is continuous in  $\tau$  and  $\mathbf{X}$ , and is Lipschitz continuous in  $\mathbf{X}$  in the neighborhood  $\mathbf{X} = 0$ , while satisfying

$$\lim_{\|\mathbf{X}\| \rightarrow 0} \frac{\|\mathbf{f}(\tau, \mathbf{X})\|}{\|\mathbf{X}\|} = 0,\tag{160}$$

uniformly in  $\tau$ , then the solution  $\mathbf{X} = 0$  is asymptotically stable. On the other hand, if the matrix  $\mathbf{A}$  has at least one eigenvalue with a positive real part, then the solution is unstable.

#### 5.1.5. Numerical analysis of stability and bifurcation – AUTO program

Another approach to analyze stability and bifurcation of dynamical systems is by numerical methods. Alighanbari and Price [1] investigated Eqs. (27) and (28) using the AUTO software package [23]. Bifurcation diagrams with stable and unstable branches were obtained, and the types of bifurcations were verified by calculating the Floquet multipliers.

A brief description of the method is given here. AUTO can perform a limited bifurcation analysis of algebraic systems, or of a system of ordinary differential equations given in Eq. (138). The differential equations are approximated by the method of orthogonal collocation [86] at  $m$  Gauss points with piecewise polynomials; in AUTO  $m$  is an integer between 2 and 7. More precisely, defining an  $N$ -point mesh on each time interval, then for any general mesh-point  $j$  the Lagrange basis polynomials are introduced, which are defined by

$$w_{j,i}(\tau) = \prod_{k=0, k \neq i}^m \frac{\tau - \tau_{j+(k/m)}}{\tau_{j+(i/m)} - \tau_{j+(k/m)}}, \quad \tau_{j+(i/m)} = \tau_j + \frac{i}{m}(\tau_{j+1} - \tau_j), \quad (161)$$

where  $j = 0, 1, \dots, N-1$  and  $i = 0, 1, \dots, m$ . The collocation method consists of finding a summation of the form

$$p_j(\tau) = \sum_{i=0}^m w_{j,i}(\tau) X_{j+(i/m)}, \quad (162)$$

such that it satisfies the differential equation at zeros of the  $m$ th degree Legendre polynomial relative to each subinterval

$$p'_j(z_{j,i}) = f(p_j(z_{j,i}), v), \quad i = 1, \dots, m, j = 0, 1, \dots, N-1, \quad (163)$$

where  $v$  is a parameter such as air speed. With the above choice of basis polynomials the continuous solution  $\mathbf{X}(\tau)$  is approximated by  $X_j$  and  $X_{j+(i/m)}$  at  $\tau_j$  and  $\tau_{j+(i/m)}$ , respectively. Therefore the procedure required to take one step along a solution branch consists of solving a system of nonlinear algebraic equations, which is done by Newton or Newton–Chord iteration.

AUTO also computes the approximate Floquet multipliers by applying a standard eigenvalue routine to an approximation of the linearized Poincaré map. The stability of periodic solutions is determined by the Floquet multipliers of the linearized equations. One of these multipliers is always equal to  $+1$ , and if the remaining multipliers lie inside the unit circle of the complex plane the periodic solution is stable. Loss of stability of the periodic solution, accompanied by a bifurcation, occurs when one of the Floquet multipliers exits from the unit circle as velocity is varied.

Eqs. (27) and (28) can be written in equivalent first-order form as

$$[\mathbf{A}]\{\mathbf{X}'\} = [\mathbf{B}]\{\mathbf{X}\} + \{\mathbf{F}\}, \quad (164)$$

where  $\{\mathbf{F}\}$  and  $\{\mathbf{X}\}$  are vectors given by

$$\{\mathbf{F}\} = \{0, 0, 0, 0, 0, 0, -(\bar{\omega}/U^*)^2 N_\xi(\xi), -N_\alpha(\alpha)/U^{*2}\}^T \quad (165)$$

and

$$\{\mathbf{X}\} = \{x_1, x_2, x_3, x_4, x_5, x_6, x_7, x_8\}^T. \quad (166)$$

In Eq. (166),  $x_1 = \xi$ ,  $x_2 = \alpha$ ,  $x_3 = \xi'$ ,  $x_4 = \alpha'$ ,  $x_5 = \xi''$ ,  $x_6 = \alpha''$ ,  $x_7 = \xi'''$  and  $x_8 = \alpha'''$ .  $[\mathbf{A}]$  and  $[\mathbf{B}]$  are  $8 \times 8$  sparse matrices given in Alighanbari and Price [1].

Once the structural nonlinearity  $G(\xi)$  and  $M(\alpha)$  are specified, a bifurcation analysis can be performed using AUTO. Alighanbari and Price [1] used a third-order rational function to

approximate a freeplay nonlinearity in the pitch degree of freedom and expressed the restoring moment as

$$M(\alpha) = \frac{c_1 + \alpha(c_2 + \alpha(c_3 + c_4\alpha))}{1 + \alpha(c_5 + \alpha(c_6 + c_7\alpha))} \quad (167)$$

where  $c_1, \dots, c_7$  are constants. The nonlinearity in the plunge degree of freedom  $G(\xi)$  can be represented by a similar expression.

## 5.2. Cubic nonlinearity

Cubic nonlinearities in one-degree-of-freedom mechanical and electrical systems can often be represented by a Duffing's equation that has been the subject of investigation for many years. The dynamic response of a coupled 2-DOF system with cubic nonlinearities was investigated analytically and numerically by Wong et al. [119] who showed that the amplitude-frequency response curve has a much more complex structure compared to a 1 DOF system. The amplitude-frequency relation changes from a cubic equation for a 1 DOF system to a polynomial of degree nine for a 2 DOF system. The coupled Duffing's equations were further investigated by Gong et al. [36] who showed that harmonic, quasi-periodic and chaotic motions can exist for system parameters that correspond to those commonly used to analyze aeroelastic behavior of aircraft structures. The first attempt to study the effects of a cubic structural nonlinearity in aeroelasticity was carried out by Woolston et al. [120,121] using an analog computer. They analyzed a 2 DOF system for hard and soft springs in the torsional degree of freedom of a pitch and plunge system.

Lee and LeBlanc [64] analyzed numerically a 2 DOF airfoil motion with a cubic nonlinearity in the pitch degree of freedom. They investigated the effects of initial pitch displacement on the flutter boundaries of soft and hard springs, as well as the amplitudes of pitch and plunge motion of limit cycle oscillations for various system parameters using Eqs. (78) and (79). The cubic nonlinearity is represented by Eq. (31), and similar to Woolston et al. [120,121]  $\beta_0$  and  $\beta_2$  were set to zero. In Eqs. (19) and (20),  $G(\xi) = \xi$  and  $M(\alpha) = \alpha + \beta_\alpha \alpha^3$  after setting  $\beta_1 = 1$  and  $\beta_3 = \beta_\alpha$  for the pitch nonlinearity. The elastic axis of the airfoil was placed at the 1/4 chord point (that is  $a_h = -1/2$ ),  $\zeta_\xi = \zeta_\alpha = 0$  and  $r_\alpha$  was kept constant at 0.5. Other properties of the airfoil, such as  $\mu$ ,  $x_\alpha$ ,  $\bar{\omega}$  and  $\beta_\alpha$  were varied in their studies.

The deviation from linearity of the restoring moment is shown in Fig. 23 where the term  $\alpha + \beta_\alpha \alpha^3$  is plotted against  $\alpha$  for three values of  $\beta_\alpha$  up to  $\pm 3$ . At the largest value of  $\beta_\alpha = 3$ , the contribution of the cubic term is about 37% at  $\alpha = 20^\circ$ , approximately 20% at  $\alpha = 15^\circ$  and can be neglected for  $\alpha < 5^\circ$ . For values of  $\alpha \approx 10\text{--}15^\circ$  where linear aerodynamic theory can be used (Eqs. (15) and (16)), the nonlinear term can be considered small and the system is dominated by the linear stiffness.

### 5.2.1. Flutter boundaries for soft and hard springs

For a soft spring,  $\beta_\alpha$  is negative, Lee and LeBlanc [64] investigated the effects of initial conditions by a numerical simulation study using the finite difference scheme given in Section 4.1. The linear flutter velocity  $U_L^*$  was used as a reference velocity and was determined numerically by setting the nonlinear term  $\beta_\alpha$  to zero.

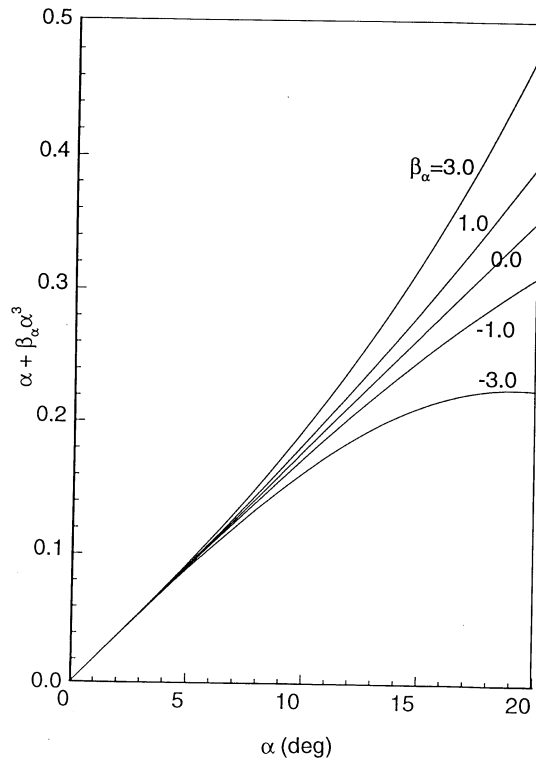


Fig. 23. Effects of  $\beta_\alpha$  on nonlinear moment  $M(\alpha) = \alpha + \beta_\alpha \alpha^3$  (from Ref. [64]).

Fig. 24 shows flutter boundaries obtained by Lee et al. [70] for  $-22^\circ < \alpha(0) < 22^\circ$  and  $\alpha'(0) = 0.0, 1.15, 1.72$  and  $2.29^\circ/\text{unit time}$  while keeping  $\xi(0) = \xi'(0) = 0$ . When a large value of  $\alpha(0)$  is used, the transient solution at small values of time is in error since the linear aerodynamics in the formulation given in Section 3.1 becomes invalid. As long as the steady-state solution decays to zero or reaches an amplitude of less than approximately  $10\text{--}15^\circ$  in the case of limit cycle oscillations, the results are acceptable. However, if the solution is chaotic, the initial transients may affect the solution at large values of time, and we should avoid using large values of  $\alpha(0)$  and limit  $\alpha(0)$  to less than approximately  $10\text{--}15^\circ$ . The motion is unstable to the right of the flutter boundary. The airfoil parameters are:  $\mu = 100$ ,  $\bar{\omega} = 0.2$ ,  $r_\alpha = 0.5$ ,  $a_h = -1/2$ ,  $x_\alpha = 0.25$  and  $\beta_\alpha = -3.0$ . The destabilizing effect of a soft spring is illustrated in this figure which shows that flutter can be induced at a velocity  $U^*$  below the linear flutter velocity  $U_L^*$ . This effect increases with increasing  $\alpha'(0)$ . The flutter boundary curve for  $\alpha'(0) = 0$  is symmetrical about the axis  $\alpha(0) = 0$ . For the other three values of  $\alpha'(0)$ , the flutter boundaries are not symmetrical because an initial positive velocity is given to the airfoil.

Fig. 25 shows the destabilizing effect of initial  $\alpha'(0)$  on flutter boundaries for  $-3 < \alpha'(0) < 3^\circ/\text{unit time}$  at  $\alpha(0) = 0, 5, 10, 15^\circ$  for the same values of  $\mu$ ,  $\beta_\alpha$ ,  $x_\alpha$ ,  $r_\alpha$  and  $\bar{\omega}$ . As expected, the curve for  $\alpha(0) = 0^\circ$  is symmetric about the axis  $\alpha'(0) = 0$ , while for  $\alpha(0) > 0$ , the flutter boundaries are displaced downwards and the amount of the shift increases with  $\alpha(0)$ .

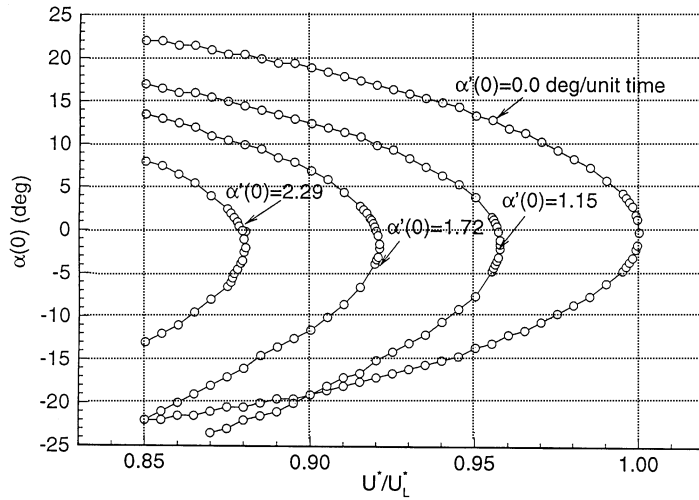


Fig. 24. Flutter boundary ( $\alpha(0)$  vs.  $U^*/U_L^*$ ) for a soft spring;  $\bar{\omega} = 0.2$ ,  $\mu = 100$ ,  $a_h = -0.5$ ,  $x_\alpha = 0.25$ ,  $r_\alpha = 0.5$ ,  $\zeta_\alpha = \zeta_\xi = 0$  and  $\beta_\alpha = -3$  (from Ref. [70]).

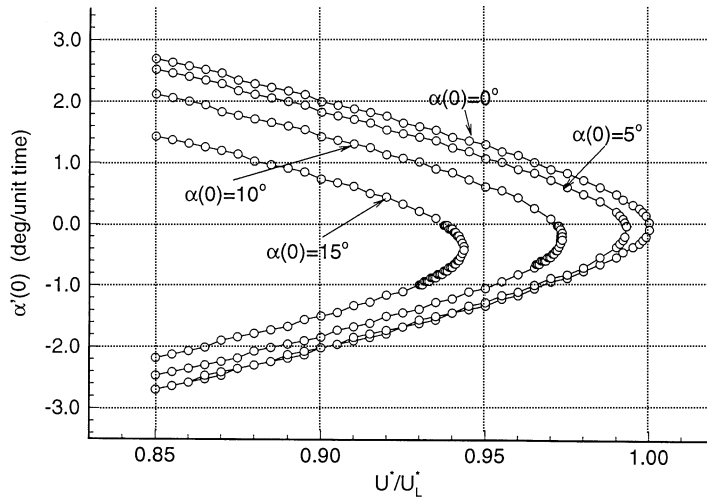


Fig. 25. Flutter boundary ( $\alpha'(0)$  vs.  $U^*/U_L^*$ ) for a soft spring;  $\bar{\omega} = 0.2$ ,  $\mu = 100$ ,  $a_h = -0.5$ ,  $x_\alpha = 0.25$ ,  $r_\alpha = 0.5$ ,  $\zeta_\alpha = \zeta_\xi = 0$  and  $\beta_\alpha = -3$  (from Ref. [70]).

The flutter boundaries for  $-0.6 < \xi(0) < 0.6$  corresponding to  $\xi'(0) = 0.0, 0.01, 0.02, 0.03$  and  $0.04$  are shown in Fig. 26 for the same values of  $\mu$ ,  $\beta_\alpha$ ,  $x_\alpha$ ,  $r_\alpha$  and  $\bar{\omega}$ . The criterion for selecting the ranges of  $\xi(0)$  and  $\xi'(0)$  is similar to that for  $\alpha(0)$  and  $\alpha'(0)$ , that is, the amplitudes of plunge and pitch motions are sufficiently small for the linear aerodynamics to be applicable. The flutter boundary for  $\xi'(0) = 0.0$  is symmetric with respect to the  $\xi(0)$ -axis while for other values of  $\xi'(0)$  it is highly non-symmetric. The value of  $\xi(0)$  at the maximum  $U^*/U_L^*$  moves downwards in the negative  $\xi(0)$

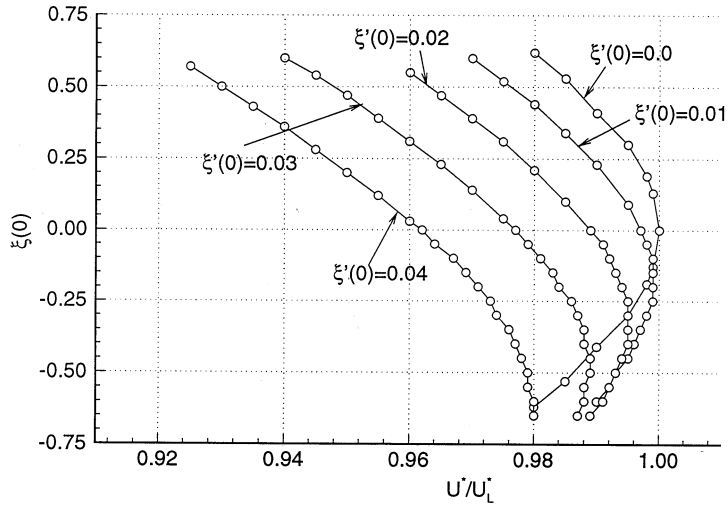


Fig. 26. Flutter boundary ( $\xi(0)$  vs.  $U^*/U_L^*$ ) for a soft spring;  $\bar{\omega} = 0.2$ ,  $\mu = 100$ ,  $a_h = -0.5$ ,  $x_\alpha = 0.25$ ,  $r_\alpha = 0.5$ ,  $\zeta_\alpha = \zeta_\xi = 0$  and  $\beta_\alpha = -3$  (from Ref. [70]).

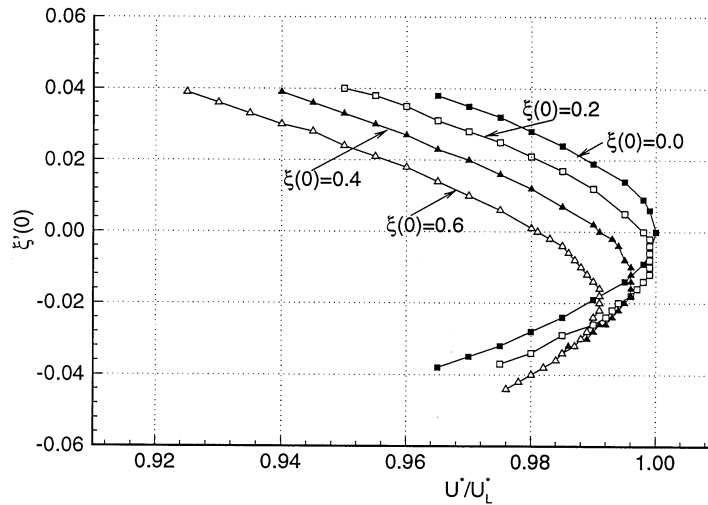


Fig. 27. Flutter boundary ( $\xi'(0)$  vs.  $U^*/U_L^*$ ) for a soft spring;  $\bar{\omega} = 0.2$ ,  $\mu = 100$ ,  $a_h = -0.5$ ,  $x_\alpha = 0.25$ ,  $r_\alpha = 0.5$ ,  $\zeta_\alpha = \zeta_\xi = 0$  and  $\beta_\alpha = -3$  (from Ref. [70]).

direction. Each of the curves for which  $\xi'(0) \neq 0$  intersects with the flutter boundary for  $\xi'(0) = 0$  in the region of negative  $\xi(0)$ .

Fig. 27 gives the flutter boundaries for  $-0.04 < \xi'(0) < 0.04$  at  $\xi(0) = 0.0, 0.2, 0.4, 0.6$  for the same values of  $\mu$ ,  $\beta_\alpha$ ,  $x_\alpha$ ,  $r_\alpha$  and  $\bar{\omega}$ . The curves cross each other in the region of negative  $\xi'(0)$ .

The flutter boundary is affected by the system parameters such as  $\mu$ ,  $\beta_\alpha$ ,  $\bar{\omega}$  and  $x_\alpha$ . These effects have been studied by Lee and LeBlanc [64] and Fig. 28, taken from their report, shows the effects



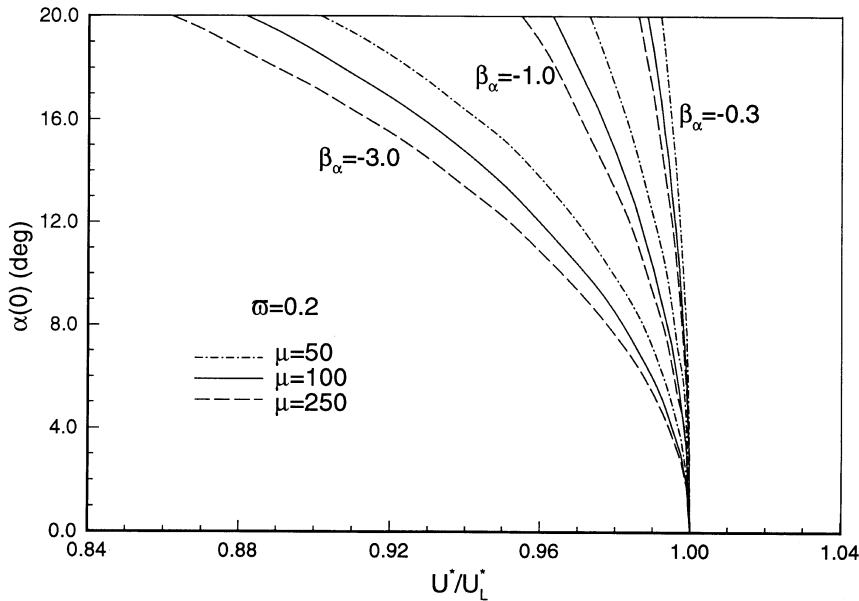


Fig. 28. Effect of  $\mu$  on flutter boundary ( $\alpha(0)$  vs.  $U^*/U_L^*$ ) for  $\bar{\omega} = 0.2$ ,  $a_h = -0.5$ ,  $x_\alpha = 0.25$ ,  $r_\alpha = 0.5$  and  $\zeta_\alpha = \zeta_\xi = 0$  (from Ref. [64]).

of airfoil/air mass ratio on the flutter boundaries. This figure shows that increasing  $\mu$  has a destabilizing effect, and that the boundary curves are all displaced more towards the left for the larger values of  $\mu$ . The effect is more pronounced as the value of  $\beta_\alpha$  decreases.

Increasing the distance between the centre of mass and the elastic axis has a stabilizing effect, and results from Lee and LeBlanc [64] at  $\mu = 250$  show the flutter boundaries to move closer to the linear flutter speed as  $x_\alpha$  is increased. In the same report, the effect of  $\bar{\omega}$  was investigated and the results show that as the uncoupled natural frequency for plunging motion approaches that of the pitching motion, the flutter boundaries move closer to the linear flutter boundary and the destabilizing effect becomes smaller. At  $\bar{\omega} = 1.2$ , it was shown [64] that the flutter boundaries are virtually independent of the coefficient  $\beta_\alpha$ .

The system stability near equilibrium points can be presented in a plot similar to a bifurcation diagram. For  $\beta_\alpha < 0$ , a subcritical Hopf-bifurcation [108] occurs at  $U^*/U_L^* = 1$ . In Fig. 29,  $\alpha(0)$  is plotted against  $U^*/U_L^*$  for  $\alpha(0)' = \zeta(0) = \zeta'(0) = 0$  with  $\beta_\alpha = -3.0$ ,  $\mu = 100$ ,  $\bar{\omega} = 0.2$ ,  $x_\alpha = 0.25$  and  $r_\alpha = 0.5$ . The dotted lines for  $U^*/U_L^* \leq 1.0$  is the flutter boundary. For values of  $\alpha(0)$  bounded by these two curves, the motion is stable. The inset of four figures showing the trajectories of the pitch oscillation are plotted in the phase plane ( $\alpha'$  vs  $\alpha$ ). They are obtained at  $U^*/U_L^* = 0.94, 0.98, 1.02, 1.06$  and  $\alpha(0) = 10, 7.5, -0.2$  and  $-0.2^\circ$ , respectively. The system converges to the equilibrium points ( $\alpha' = \alpha = 0$ ) for  $U^*/U_L^* < 1.0$  and diverges away from the unstable equilibrium points ( $\alpha' = \alpha = 0$ ) for  $U^*/U_L^* > 1.0$ . The Hopf-bifurcation point is located at  $U^*/U_L^* = 1$ .

For positive values of  $\beta_\alpha$  (hard spring), divergent flutter is not encountered. Instead, the flutter boundaries (e.g.  $\alpha(0)$  vs.  $U^*/U_L^*$ ) for all  $\beta_\alpha$  coalesce into a straight line at the linear flutter speed. This was shown by Woolston et al. [120,121] and numerically by Lee and LeBlanc [64] for a cubic

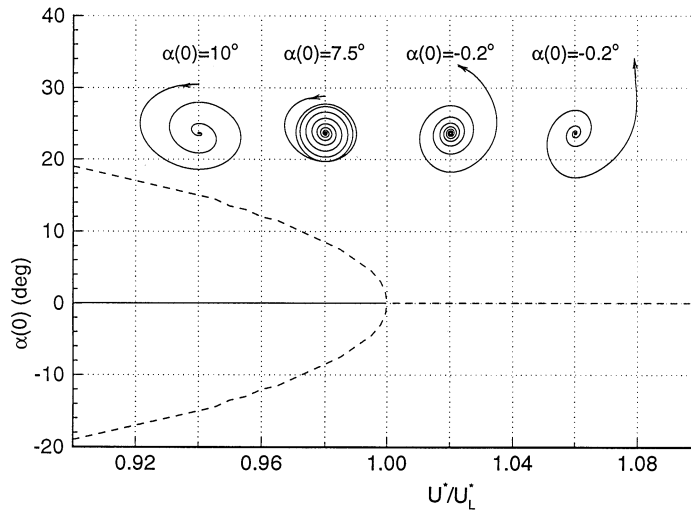


Fig. 29. Subcritical Hopf-bifurcation for a soft spring with  $\beta_x = -3$  (from Ref. [70]).

nonlinearity in the pitch degree of freedom and various airfoil parameters. To the right of this boundary, the oscillations maintain a self-limited amplitude which is independent of the initial angular displacement  $\alpha(0)$ .

For a given  $\alpha(0)$ , the time it takes for the airfoil motion to reach a steady value depends on the velocity ratio  $U^*/U_L^*$ . If a solution is required very close to the flutter boundary, a large number of cycles of oscillations have to be computed. Using the same airfoil parameters as those for a soft spring (that is,  $\mu = 100$ ,  $\bar{\omega} = 0.2$ ,  $x_\alpha = 0.25$  and  $r_\alpha = 0.5$ ), Lee and LeBlanc [64] showed that at  $\beta_x = 0.3$  it takes approximately 250 cycles for the solution to decay to practically zero at  $U^*/U_L^* = 0.9992$  (0.08% less than linear flutter speed) with initial amplitude  $\alpha(0) = 10^\circ$  and  $\alpha(0)' = \xi(0) = \xi'(0) = 0$ . At smaller values of  $\alpha(0) = 1$  and  $3^\circ$ , it requires approximately the same number of cycles for the oscillation amplitude to reach zero. In the LCO region where  $U^*/U_L^* > 1$ , the time it takes to reach steady state depends on the initial conditions. At  $U^*/U_L^* = 1.0008$  (0.08% greater than linear flutter speed), the solution takes 130 cycles at  $\alpha(0) = 10^\circ$  to reach a constant amplitude, compared to 190 cycles at  $\alpha(0) = 1^\circ$ . Increasing the value of  $U^*/U_L^*$  increases the convergence rate. At  $U^*/U_L^* = 1.0024$ , steady pitch amplitudes are reached after 60 and 100 cycles for  $\alpha(0) = 10$  and  $1^\circ$ , respectively. Eq. (24) has been used to repeat the Lee and LeBlanc [64] investigation and identical results were obtained. It was found that when larger values of  $\beta_x$  were used, the time it takes to decay to a zero value ( $U^*/U_L^* < 1$ ) or reach a constant value ( $U^*/U_L^* > 1$ ) is considerably shorter than those at  $\beta_x = 0.3$  shown in Lee and LeBlanc's [64] report.

Lee and LeBlanc [64] concluded from a number of case studies for different airfoil parameters that there is no noticeable change in the amplitude of the pitch motion when the airfoil/air mass ratio is varied, while the plunge amplitude increases with an increase in that ratio. Increasing the distance between the centre of mass and the elastic axis results in a larger pitch amplitude while the plunge amplitude gets smaller. As the ratio of the uncoupled natural frequencies of the plunge to pitch motion approaches and exceeds unity, there is an increase in the pitch amplitude while a much larger drop in the plunge amplitude is detected.

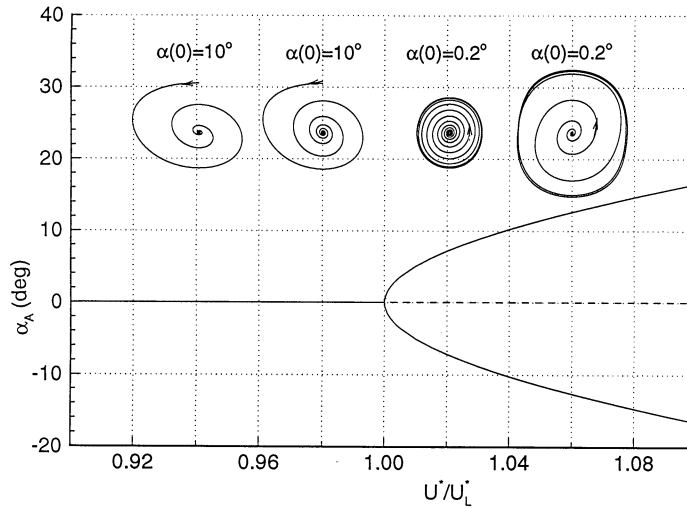


Fig. 30. Subcritical Hopf-bifurcation for a hard spring with  $\beta_x = 3$  (from Ref. [70]).

Similar to Fig. 29 the stability behavior of the airfoil near equilibrium points can be presented in a bifurcation diagram. For  $\beta_x = 3$ ,  $\mu = 100$ ,  $\bar{\omega} = 0.2$ ,  $r_x = 0.5$ ,  $a_h = -1/2$  and  $x_x = 0.25$ , Fig. 30 shows a plot of the pitch amplitude  $\alpha_A$  against  $U^*/U_L^*$ . This figure is obtained by varying  $\alpha(0)$  only, while keeping  $\alpha'(0) = \zeta(0) = \zeta'(0) = 0$ . For  $U^*/U_L^* < 1$ , the solution is stable for all initial displacement  $\alpha(0)$ . The solutions in the phase plane ( $\alpha'$  vs.  $\alpha$ ) at  $U^*/U_L^* = 0.94$ ,  $\alpha(0) = 10^\circ$  and  $U^*/U_L^* = 0.98$ ,  $\alpha(0) = 10^\circ$  are shown in the inset. The phase curve spirals into the origin ( $\alpha' = \alpha = 0$ ) for all  $\alpha(0)$ , showing the solution to be stable for  $U^*/U_L^* < 1$ . For  $U^*/U_L^* > 1$ , the two insets of the phase diagram at  $U^*/U_L^* = 1.02$  and  $1.04$  for  $\alpha(0) = 0.2^\circ$  show the trajectories to spiral away from the origin and becomes periodic with constant amplitude. The solid line shows the amplitude of pitch motion  $\alpha_A$  obtained numerically using Eq. (24). This value is independent of initial displacement  $\alpha(0)$  since all solution with different  $\alpha(0)$  will eventually reach a limit-cycle state. The transition from a stable equilibrium solution to limit cycle oscillation is known as a supercritical Hopf-bifurcation [108].

### 5.2.2. System behavior near equilibrium points

For various values of  $U^*/U_L^*$  with  $\mu = 100$ ,  $x_x = 0.25$ ,  $r_x = 0.5$  and  $\bar{\omega} = 0.2$ , the eigenvalues of the Jacobian matrix at equilibrium points can be calculated using Eq. (132). The solution of the Jacobian matrix for a given value of  $U^*/U_L^*$  has eight eigenvalues. There are two pairs of conjugate eigenvalues (modes I and II denoted by dashed and solid lines, respectively) and their real and imaginary parts are plotted against  $U^*/U_L^*$  in Fig. 31. The other four eigenvalues have zero imaginary parts and they do not represent oscillatory motion.

On examining a typical time series of  $\alpha$  from numerical integration of Eq. (24) shown in Fig. 32, we see that the pitch motion can be adequately represented by a single mode. We can denote the pitch motion by  $\alpha = \alpha_0 e^{(\lambda_r + i\lambda_i)\tau}$  where  $\alpha_0$  is a constant,  $\lambda_r$  and  $\lambda_i$  are the real and imaginary parts of the exponential coefficient  $\lambda$ . Superimposed in Fig. 31 are results obtained from numerical simulation for  $\beta_x = 3$ . The initial conditions are  $\alpha(0) = 1^\circ$  (for  $U^*/U_L^* < 1$ ) and  $\alpha(0) = 0.1^\circ$  (for

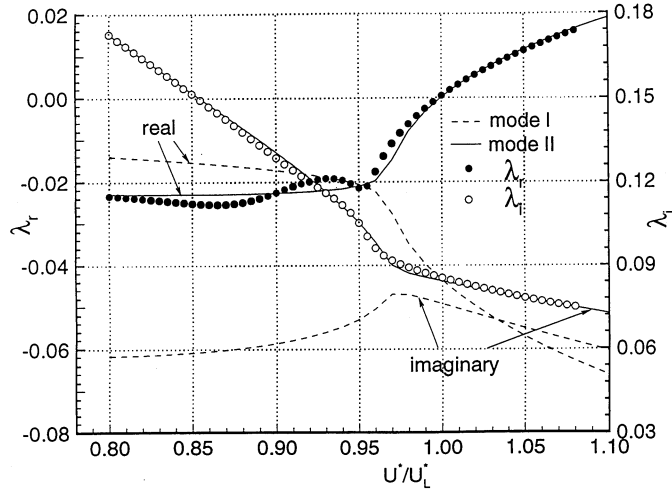


Fig. 31. Variation of  $\lambda$  with  $U^*/U_L^*$  for the pitch motion with  $\bar{\omega} = 0.2$ ,  $\mu = 100$ ,  $a_h = -0.5$ ,  $x_x = 0.25$ ,  $r_x = 0.5$ ,  $\zeta_x = \zeta_\xi = 0$ , and  $\beta_x = 3$  (from Ref. [70]).

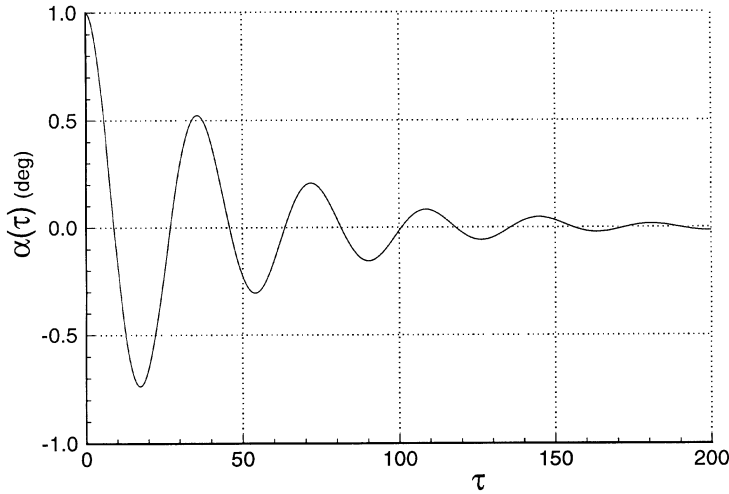


Fig. 32. Time series of pitch at  $U^*/U_L^* = 0.8$  with  $\bar{\omega} = 0.2$ ,  $\mu = 100$ ,  $a_h = -0.5$ ,  $x_x = 0.25$ ,  $r_x = 0.5$ ,  $\zeta_x = \zeta_\xi = 0$ , and  $\beta_x = 3$  (from Ref. [70]).

$U^*/U_L^* > 1$ ) with  $\alpha'(0) = \xi(0) = \xi'(0) = 0$ . The imaginary part  $\lambda_i$  is calculated by the following equation  $\lambda_i = 2\pi(n_2 - n_1)/(\tau_2 - \tau_1)$  where time  $\tau_2$  and  $\tau_1$  correspond to cycle numbers  $n_2$  and  $n_1$ , respectively. The real part  $\lambda_r$  is determined by  $\lambda_r = (\log \alpha_{2A} - \log \alpha_{1A})/(\tau_2 - \tau_1)$  where  $\alpha_{1A}$  and  $\alpha_{2A}$  are the amplitudes of pitch angles corresponding to  $\tau_1$  and  $\tau_2$ .

The maximum values of  $\alpha_{1A}$  and  $\alpha_{2A}$  are kept below  $10^\circ$  in the numerical simulation. The first  $\frac{1}{2}$  to  $3\frac{1}{2}$  cycles in the time series are used to calculate  $\lambda_r$  and  $\lambda_i$ .

The analytical and numerical simulation results are in excellent agreement for mode II for  $U^*/U_L^* > 1$ . However, for  $U^*/U_L^* < 1$ , the results from numerical simulation have some scatter about the analytical solution in  $\lambda_r$  only.

Time series of  $\xi$  (Fig. 33) show that for  $U^*/U_L^* < 1$  more than one mode is present. We can write  $\xi$  as the sum of two modes as  $\xi = \sum_{n=1}^2 \xi_{0n} e^{\lambda_n \tau}$ . The two modes can be obtained by decomposing the time series using wavelets. The real and imaginary parts of  $\lambda$  can then be solved and their values are plotted in Fig. 34 which shows fair agreement with the solution from the Jacobian matrix. It is

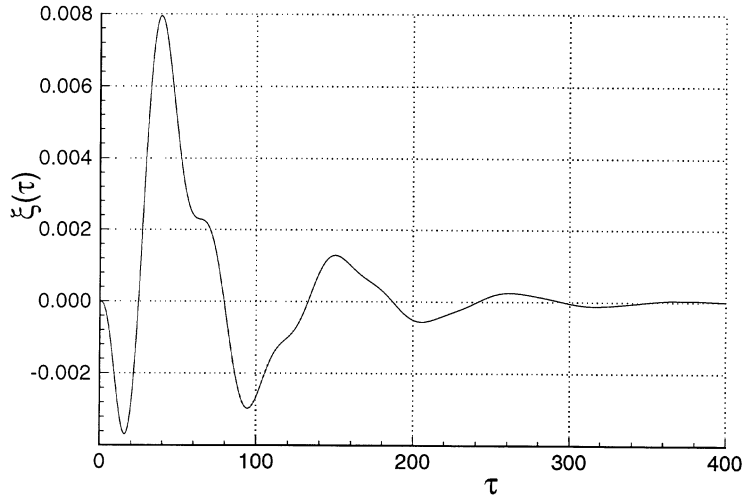


Fig. 33. Time series of plunge motion at  $U^*/U_L^* = 0.8$  with  $\bar{\omega} = 0.2$ ,  $\mu = 100$ ,  $a_h = -0.5$ ,  $x_\alpha = 0.25$ ,  $r_\alpha = 0.5$ ,  $\zeta_\alpha = \zeta_\xi = 0$ , and  $\beta_\alpha = 3$  (from Ref. [70]).

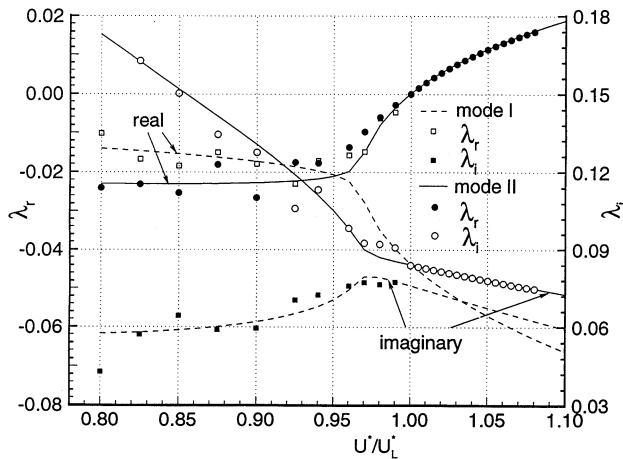


Fig. 34. Variation of  $\lambda$  with  $U^*/U_L^*$  for the plunge motion with  $\bar{\omega} = 0.2$ ,  $\mu = 100$ ,  $a_h = -0.5$ ,  $x_\alpha = 0.25$ ,  $r_\alpha = 0.5$ ,  $\zeta_\alpha = \zeta_\xi = 0$ , and  $\beta_\alpha = 3$  (from Ref. [70]).

difficult to obtain good accuracy of  $\lambda$  when only a few cycles of the time series are available. This is especially true for mode I which decays to practically zero in less than three cycles. The results show the coalescence of the two modes and after a short transient period, only the mode II is present for  $U^*/U_L > 1$ . In the region  $0.97 \leq U^*/U_L \leq 1$ , the use of wavelets to separate the two modes becomes increasingly difficult as the two frequencies approach each other. Experience [71] with wavelets shows that  $\lambda_r$  is difficult to obtain accurately when frequency separation between the two modes is not large.

In Fig. 35 the eigenvalues of mode II for the pitch motion together with  $\lambda$  from numerical simulations shown in Fig. 31 are re-plotted in the real and imaginary plane for  $U^*/U_L^* = 0.97$  to 1.08. The filled circle symbols denote numerical results while the solid lines represent solutions from the eigenvalues of the Jacobian matrix. We can see that the real part of the complex conjugates increases with  $U^*/U_L^*$  and passes through zero at  $U^*/U_L^* = 1.0$  where a Hopf-bifurcation occurs. With further increase in  $U^*/U_L^*$ , the real part of the conjugates switches sign and becomes positive, changing the stable equilibrium state to an unstable one.

### 5.2.3. Flutter velocity and angular frequency at Hopf-Bifurcation point

By solving Eq. (148), Lee et al. [70] determined the Hopf-bifurcation point and found the linear flutter velocity and angular frequency at this point. These two quantities have been calculated for various airfoil parameters and compared with numerical simulation. The results show that up to the fourth decimal point there were no noticeable differences detected.

Fig. 36 illustrates the variation of the linear flutter velocity and angular frequency at the Hopf-point as functions of the frequency ratio  $\bar{\omega}$  for  $\mu = 100$ ,  $x_\alpha = 0.25$  and  $r_\alpha = 0.5$ . The flutter velocity decreases with  $\bar{\omega}$  until  $\bar{\omega} = 0.8$  is reached and increases from then on with increasing  $\bar{\omega}$ . The angular frequency increases rapidly with  $\bar{\omega}$  initially until a maximum is reached at  $\bar{\omega} = 1.1$  and then decreases gradually. The effect of airfoil–air mass ratio on flutter velocity and frequency shows

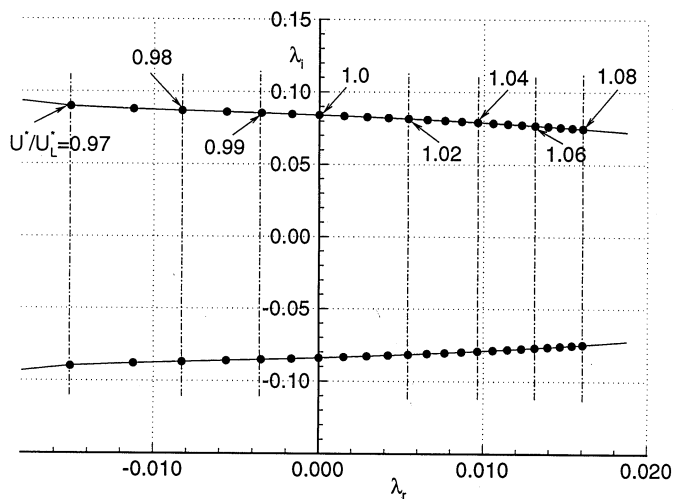


Fig. 35. Variation of conjugate eigenvalues with  $U^*/U_L^*$  for pitch motion in the  $\lambda$ -plane for  $\bar{\omega} = 0.2$ ,  $\mu = 100$ ,  $a_h = -0.5$ ,  $x_\alpha = 0.25$ ,  $r_\alpha = 0.5$ ,  $\zeta_\alpha = \zeta_\xi = 0$  and  $\beta_\alpha = 3$  (from Ref. [70]).

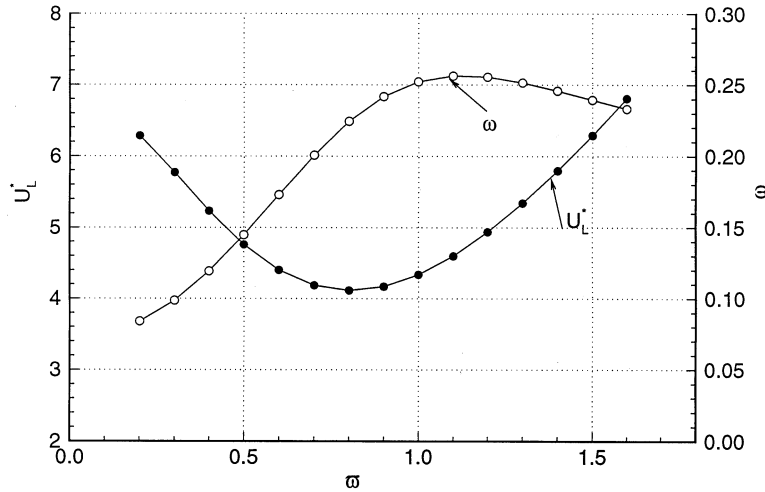


Fig. 36. Variation of flutter velocity and frequency at the Hopf-point for  $\mu = 100$ ,  $a_h = -0.5$ ,  $x_\alpha = 0.25$ ,  $r_\alpha = 0.5$  and  $\zeta_\alpha = \zeta_\xi = 0$  (from Ref. [70]).

the linear flutter velocity increases almost linearly with  $\mu$  while the frequency decreases monotonically. The effect of the distance between the center of mass and the elastic axis shows that  $U_L^*$  decreases and  $\omega$  increases with increases in  $x_\alpha$ . The radius of gyration about the elastic axis has the effect of increasing the flutter velocity while at the same time causes a decrease in frequency for increasing  $r_\alpha$ .

#### 5.2.4. Amplitude and frequency of limit cycle oscillations

The amplitudes of pitch and plunge motion of LCO have been calculated for various values of  $U^*/U_L^*$  from Eqs. (127) and (128) by Lee et al. [70] using various methods to determine the frequency  $\omega$ . The approximate methods they proposed depend on  $\bar{\omega}$ , and for some cases the agreement with numerical simulation is rather poor. The method by Liu et al. [76] using the center manifold theory gives a much better match between analytical and numerical computations for all values of  $\bar{\omega}$  and airfoil parameters. In Fig. 37, the frequency  $\omega$  is plotted against  $U^*/U_L^*$  for  $\bar{\omega} = 0.2$ ,  $\mu = 100$ ,  $x_\alpha = 0.25$ ,  $r_\alpha = 0.5$  and  $\beta_\alpha = 3$ . The open circle symbol denotes  $\omega$  obtained from numerical simulation using Eq. (24) while the solid line represents results using Eq. (153). The two methods give extremely close results and we can draw similar conclusions by comparison with other values of  $\bar{\omega}$ .

Figs. 38 and 39 show the variations of the amplitudes of pitch and plunge LCO with  $U^*/U_L^*$  for  $\bar{\omega} = 0.2$ ,  $\mu = 100$ ,  $x_\alpha = 0.25$ ,  $r_\alpha = 0.5$  and  $\beta_\alpha = 3$ . The solid line is obtained using Eqs. (127) and (128), and the numerical simulation results are given by the open circles. We observe that the two methods give almost identical results, and other values of  $\bar{\omega}$  also compare favorably.

#### 5.2.5. Chaotic oscillations

The investigations carried out by Lee and LeBlanc [64] and Lee et al. [70] assumed the cubic nonlinearity is small compared to the linear stiffness term in the equations governing the airfoil

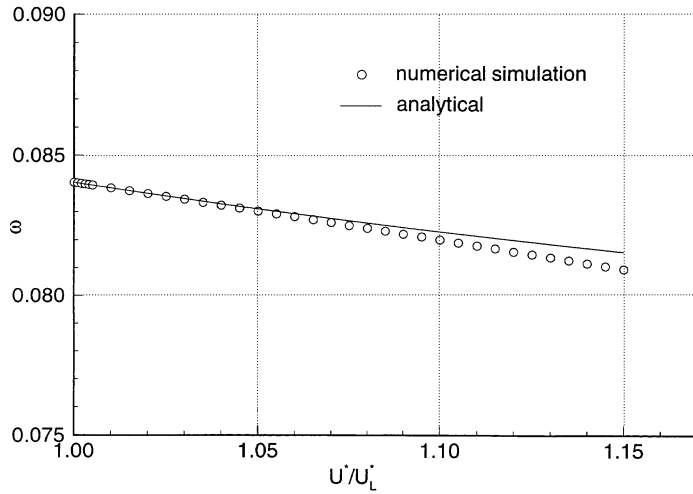


Fig. 37. Variation of  $\omega$  with  $U^*/U_L^*$  for pitch motion in post-Hopf-bifurcation for  $\bar{\omega} = 0.2$ ,  $\mu = 100$ ,  $a_h = -0.5$ ,  $x_\alpha = 0.25$ ,  $r_\alpha = 0.5$ ,  $\zeta_\alpha = \zeta_\xi = 0$  and  $\beta_\alpha = 3$  (from Ref. [76]).

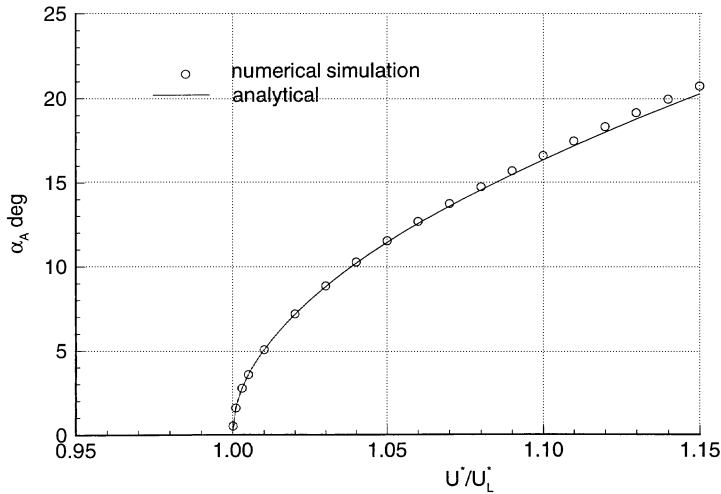


Fig. 38. Variation of pitch amplitude with  $U^*/U_L^*$  in post-Hopf-bifurcation for  $\bar{\omega} = 0.2$ ,  $\mu = 100$ ,  $a_h = -0.5$ ,  $x_\alpha = 0.25$ ,  $r_\alpha = 0.5$ ,  $\zeta_\alpha = \zeta_\xi = 0$  and  $\beta_\alpha = 3$  (from Ref. [76]).

motion. For hard spring, a Hopf-bifurcation occurs at  $U^*/U_L^* = 1$  and chaotic motion was not detected for the airfoil and spring parameters used. However, chaos was observed by Price et al. [89] and Zhao and Yang [125] and they studied cases where the nonlinearity dominates over the linear term in the restoring force or moment.

In the Price et al. [89] investigation, the nonlinear equations for the airfoil plunge and pitch response were solved using both the finite difference and describing function methods for a range of airfoil parameters similar to those used by Lee and LeBlanc [64]. Only results for  $\bar{\omega} = 0.2$ ,  $\mu = 100$ , 200,  $a_h = -1/2$ ,  $x_\alpha = 0.25$ ,  $r_\alpha = 0.5$ , and  $\zeta_\alpha = \zeta_\beta = 0$  were presented in their paper.



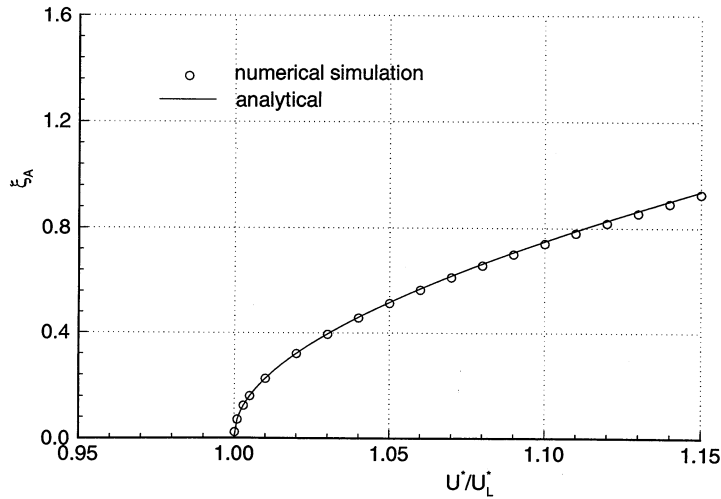


Fig. 39. Variation of plunge amplitude with  $U^*/U_L^*$  in post-Hopf-bifurcation for  $\bar{\omega} = 0.2$ ,  $\mu = 100$ ,  $a_h = -0.5$ ,  $x_\alpha = 0.25$ ,  $r_\alpha = 0.5$ ,  $\zeta_\alpha = \zeta_\xi = 0$  and  $\beta_\alpha = 3$  (from Ref. [76]).

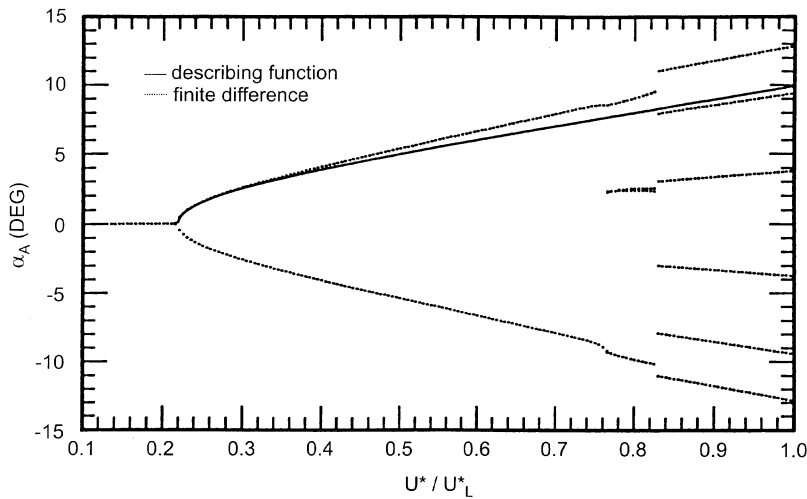


Fig. 40. Bifurcation diagram of a cubic nonlinearity for  $\bar{\omega} = 0.2$ ,  $\mu = 100$ ,  $a_h = -1/2$ ,  $x_\alpha = 0.25$ ,  $r_\alpha = 0.5$ ,  $\zeta_\alpha = \zeta_\beta = 0$ ,  $\beta_0 = 0$ ,  $\beta_1 = 0.1$ ,  $\beta_2 = 0$ ,  $\beta_3 = 40$  (from Ref. [89]).

Fig. 40 shows a typical bifurcation diagram of the pitch response for a cubic nonlinearity as a function of velocity obtained using both the finite difference method and the describing function technique. In this example, the constants in  $M(\alpha)$  given by Eq. (31) is chosen as follows:  $\beta_0 = \beta_2 = 0$ ,  $\beta_1 = 0.1/\text{rad}$  and  $\beta_3 = 40.0/\text{rad}$ . It is seen that the nonlinear term dominates over the linear stiffness term. The finite difference results show the value of  $\alpha$  when  $\alpha' = 0$ . If two points occur at one velocity this suggests that the motion is period-one, and four points suggests period-two. Hence, for

period-one motion the value of  $\alpha$  shown in the figure represents the magnitude of the LCO. It should be realized that the finite difference solution may possibly be dependent on the particular set of initial conditions for the airfoil. Thus, this bifurcation diagram is particular to the set of initial conditions  $\alpha(0) = 7.0^\circ$ ,  $\alpha'(0) = \xi(0) = \xi'(0) = 0$ .

The results presented in the figure obtained using the describing function method show the value of  $\alpha_A$  as a function of air speed; the describing function solution does not require the initial conditions to be specified, and thus the describing function solution shown is good for any set of initial conditions, not just those used in the numerical simulation.

It can be seen that in this case both the finite difference and describing function solutions indicate a supercritical Hopf-bifurcation at  $U^*/U_L^* = 0.22$ , giving a period-one LCO. Furthermore, for  $0.22 \leq U^*/U_L^* \leq 0.5$  approximately, the describing function and finite difference methods predict essentially the same magnitude of LCO motion. However as  $U^*/U_L^*$  increases, the describing function method gives an increasingly smaller prediction for the magnitude of the LCO motion compared with the finite difference solution.

At  $U^*/U_L^* = 0.76$  the finite difference solution undergoes a further bifurcation to give period-two motion, and a final bifurcation is obtained at  $U^*/U_L^* = 0.83$  giving another periodic solution. The period-one motion is symmetrical about the  $\alpha = 0$  axis. In the region  $0.76 \leq U^*/U_L^* \leq 0.83$  approximately, this symmetry is lost. Because the describing function used in this analysis assumes period-one motion, it is not capable of predicting the bifurcations at higher velocities.

In Fig. 41a, a bifurcation diagram for  $\mu = 200$  with the rest of the airfoil parameters similar to those in Fig. 40 is shown. An even stronger nonlinear spring ( $\beta_0 = \beta_2 = 0$ ,  $\beta_1 = 0.01/\text{rad}$  and  $\beta_3 = 50.0/\text{rad}$ ) is considered in this case. In the finite difference integration, the initial conditions were set at  $\alpha(0) = 3.0^\circ$ ,  $\alpha'(0) = \xi(0) = \xi'(0) = 0$ . In the region  $0.46 \leq U^*/U_L^* \leq 0.49$ , approximately, the motion is chaotic. A Poincaré map constructed at  $U^*/U_L^* = 0.475$  shown in Fig. 41b shows there is some “structure” indicating the motion is not random but most probably chaotic [81]. Price et al. [89] computed the Lyapunov spectrum at different velocities for the bifurcation diagram of Fig. 41a. In those cases where the bifurcation diagram indicated periodic motion, all of the Lyapunov exponents were either negative or zero, in agreement with the bifurcation diagram. However, for  $U^*/U_L^* = 0.47$ , in the middle of the apparently chaotic region of the bifurcation

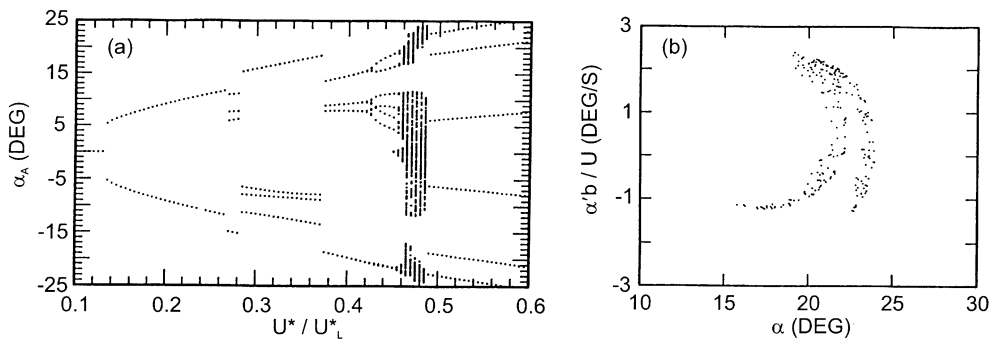


Fig. 41. (a) Bifurcation diagram of a cubic nonlinearity; (b) Poincaré map for  $U^*/U_L^* = 0.475$ ,  $\bar{\omega} = 0.2$ ,  $\mu = 200$ ,  $a_h = -1/2$ ,  $x_z = 0.25$ ,  $r_z = 0.5$ ,  $\zeta_z = \zeta_\beta = 0$ ,  $\beta_0 = 0$ ,  $\beta_1 = 0.01$ ,  $\beta_2 = 0$ ,  $\beta_3 = 50$  (from Ref. [89]).

diagram shown in Fig. 41a, a positive Lyapunov exponent of 0.01 was calculated, indicating that the system is “mildly” chaotic.

### 5.3. Freeplay with preload

Lee and Desrochers [65] studied only nonlinearities in the pitch degree of freedom. The elastic axis of the airfoil was placed at the  $\frac{1}{4}$  chord location (that is,  $a_h = -0.5$ ),  $r_\alpha$  and  $x_\alpha$  were kept constant at 0.5 and 0.25, respectively. Furthermore, they considered a bilinear spring (shown in Fig. 2) with  $M_f = 0$ , that is, the spring stiffness vanishes inside the freeplay  $\delta$ . The two properties of the airfoil being varied were  $\mu$  and  $\bar{\omega}$ . The effects of preload and freeplay were investigated by varying the values of  $M_0$ ,  $\alpha_f$  and  $\delta$ . In their report sixteen cases were considered and they investigated the effect of varying the preload for constant freeplay, effect of freeplay on constant preload, and effect of  $\mu$  and  $\bar{\omega}$  for different freeplays and preloads.

The intention of Lee and Desrochers' [65] investigation was to re-exam the results obtained by Woolston et al. [120, 121] using a digital instead of an analog computer. Their emphasis was on the influence of the geometry of the freeplay on flutter boundaries and the amplitudes of the plunge and pitch motions in the limit cycle oscillation regions. At the time of their investigation, chaotic behavior of nonlinear aeroelastic systems was not well researched and they have not encountered chaos or might even have inadvertently missed detecting it by not choosing the airfoil and freeplay parameters where chaotic motion can exist. Unlike the results given by Woolston et al. [120,121], Lee and Desrochers [65] detected islands of LCO in the damped oscillation region of the flutter diagram.

To determine the flutter boundary, Eqs. (78) and (79) are solved for given initial conditions. In their report, Lee and Desrochers [65] varied only the initial pitch displacement  $\alpha(0)$  while keeping  $\alpha'(0)$ ,  $\xi(0)$  and  $\xi'(0)$  zero. In their procedure, they determined the linear flutter speed  $U_L^*$  first, and this is equivalent to solving the problem for  $M_0 = \delta = \alpha_f = 0$ . In the nonlinear case, once  $\alpha(0)$  is specified, a value of  $U^*$  is selected and  $\alpha$  and  $\xi$  are obtained by the time marching finite difference scheme. For the type of structural nonlinearity considered, the solution is divergent for  $U^* > U_L^*$ , and the nonlinear divergent flutter speed is the same as  $U_L^*$  for all the cases they considered. They observed that for  $\alpha(0) > M_0$  decreasing  $U^*$  below  $U_L^*$  results in limit-cycle flutter. The oscillation is self-excited and maintains a constant amplitude which is self-limited. The boundaries between divergent and limit-cycle flutter in their examples are vertical lines at  $U^*/U_L^* = 1$  for values of  $\alpha(0)$  ranging from  $-10^\circ$  to  $20^\circ$ . The choice of  $\alpha(0)$  should be such that the steady-state pitch and plunge amplitudes are small enough for linear aerodynamics to be used. This point was discussed in Section 5.2. Throughout their study, the value of the time step  $\Delta\tau$  was taken to be  $1/128$  of the shorter period of the two coupled modes of oscillation of the airfoil in the absence of aerodynamic forces. In numerical time-integration schemes, Bathe and Wilson [7] pointed out that the amplitude decays due to numerical errors and is dependent on  $\Delta\tau$ . The value of  $\Delta\tau$  used in Lee and Desrochers' study [65] is sufficiently small to give good accuracy in determining the flutter boundaries while ensuring the computation time is not excessive [52].

As  $U^*$  decreases away from  $U_L^*$ , a value will be reached where any further decrease will result in damped oscillations of the airfoil. Boundaries can be identified in the  $\alpha(0)$  versus  $U^*/U_L^*$  plots separating the regions of limit-cycle flutter with the stable regions where the airfoil motion decays to its equilibrium condition from the initial displacement after the transients die out.

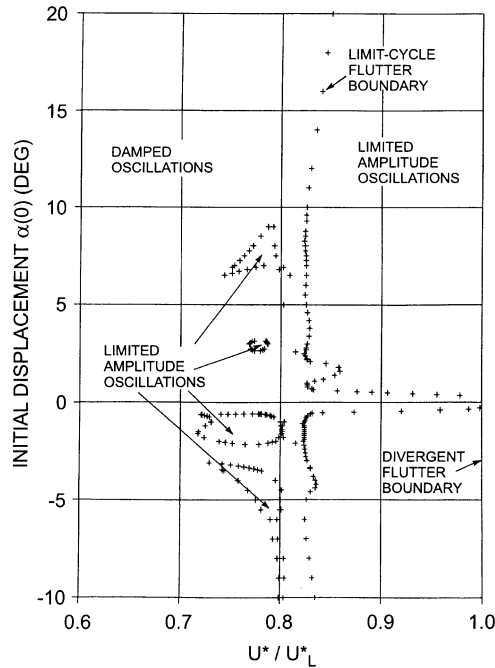


Fig. 42. Flutter boundary for  $\bar{\omega} = 0.2$ ,  $\mu = 100$ ,  $\alpha_f = 0.25^\circ$ ,  $\delta = 0.5^\circ$ , and  $M_0 = 0.25^\circ$  (from Ref. [65]).

Fig. 42 shows the flutter boundary obtained by Lee and Desrochers [65] for  $\mu = 100$ ,  $\bar{\omega} = 0.2$ ,  $M_0 = 0.25^\circ$ ,  $\alpha_f = 0.25^\circ$  and  $\delta = 0.5^\circ$ . There are pockets in the damped oscillation region where the airfoil oscillates with constant amplitude. These LCO regions are determined using a binary search complemented with linear grid scans. This by no means assures that all such regions, especially the small ones, have been identified, but those that are found can be considered to be quite accurately defined.

Time series showing the behavior of  $\alpha$  and  $\xi$  in the various regions inside the divergent flutter boundary were given by Lee and Desrochers [65]. In the main LCO region which lies between  $0.825 \leq U^*/U_L^* \leq 1$  in Fig. 42, the airfoil transients damp out fairly rapidly and the oscillations are mainly sinusoidal and no noticeable harmonics are detected. Inside a LCO pocket, a strong harmonic is always present.

Comparison of results for a freeplay  $\delta = 0.5^\circ$  and three values of  $M_0 = \alpha_f = 0.25, 0.5$  and  $1^\circ$  shows the region of limit-cycle flutter decreases with increasing values of the preload. Another observation is the non-symmetry of the boundaries between decaying oscillation and limit-cycle flutter with initial displacement  $\alpha(0)$ . For values of initial displacement less than the preload, the system moves on the linear part of the moment displacement curve shown in Fig. 2, and at velocities below the linear flutter speed, the system is stable. Increasing  $\alpha(0)$  will have a destabilizing effect, but this is only restricted to the LCO regions. The variations of the LCO amplitudes  $\alpha_A$  and  $\xi_A$  with speed ratio  $U^*/U_L^*$  show that they are independent of the initial displacement  $\alpha(0)$  for this freeplay and the three values of  $M_0$  investigated.

The pockets of LCO in the damped oscillation region are only observed for the smallest value of  $M_0 = 0.25^\circ$  and are not detected when  $M_0$  increases to  $0.5$  or  $1^\circ$  for the freeplay considered.

To investigate the effect of freeplay on the flutter boundary, Lee and Desrochers [65] considered three cases where  $\bar{\omega} = 0.2$ ,  $\mu = 100$ ,  $M_0 = \alpha_f = 0.5^\circ$  and  $\delta = 0.25, 0.5$  and  $1^\circ$ . Decreasing the freeplay decreases the LCO region and moves the limit-cycle flutter boundary closer to the divergent flutter boundary. In the limit, as the freeplay tends to zero, the two flutter boundaries coincide at  $U^*/U_L^* = 1$  which is to be expected since the system is acted on by linear spring forces. Because of the preload, the flutter boundaries are not symmetrical about  $\alpha(0) = 0$ .

The LCO amplitudes  $\alpha_A$  and  $\xi_A$  are independent of the initial displacement  $\alpha(0)$ , but for given speed ratio, higher amplitudes are obtained when  $\delta$  increases. It was found by Lee and Desrochers [65] that the flutter boundary for  $M_0 = \alpha_f = 0.25^\circ$  and  $\delta = 0.5^\circ$  when compared to that for  $M_0 = \alpha_f = 0.5^\circ$  and  $\delta = 1^\circ$  is identical if the vertical scale for  $\alpha(0)$  for the former is multiplied by a factor of 2, which is the ratio of the two values of preload. Similarly, the amplitudes  $\alpha_A$  and  $\xi_A$  in the two cases differ also by a factor of two. From the limited results of the two cases considered, they concluded that for a particular combination of preload and freeplay, similar results are obtained for other values of preload and freeplay if the ratio of preload to freeplay is kept the same. The flutter boundary curves can be made identical if the vertical scales are multiplied by factors equal to the ratio of the preloads. Also, the amplitudes of the plunge and pitch oscillations differ from those with other values of preload and freeplay by the same factors.

The effect of airfoil–air mass ratio was carried out for  $\bar{\omega} = 0.2$ ,  $M_0 = \alpha_f = 0.5^\circ$ ,  $\delta = 0.5^\circ$  with  $\mu = 50, 100$  and  $250$ . It was found that the boundaries for limit-cycle flutter move towards  $U^*/U_L^* = 1$  for increasing  $\mu$ . Comparison of the curves for  $\alpha_A$  shows that the amplitude of pitch motion in the region between the limit-cycle and divergent flutter boundaries practically does not change with  $\mu$ . On the other hand,  $\xi_A$  is found to increase with  $\mu$ . At  $\bar{\omega} = 0.8$ ,  $\alpha_A$  decreases slightly with increasing  $\mu$  while the decrease in  $\xi_A$  is much larger. This behavior where  $\mu$  has an effect on the plunge degree of freedom but with no noticeable effect on the pitch motion is also observed for a cubic nonlinearity in the restoring moment reported by Lee and LeBlanc [64].

Lee and Desrochers [65] also investigated the effects of uncoupled plunge to pitch natural frequency ratio  $\bar{\omega}$  on flutter boundaries. When  $\bar{\omega}$  is close to unity, the LCO pockets disappear for the freeplay geometry they investigated, but large irregularities at the limit-cycle flutter boundary are detected. The amplitudes  $\alpha_A$  and  $\xi_A$  also vary with  $\bar{\omega}$ . For the lowest value of  $\bar{\omega} = 0.2$  considered in their study, larger oscillatory motions in both degrees of freedom are observed than those at  $\bar{\omega} = 0.8$ .

Price et al. [88] extended the study of Lee and Desrochers [65] and investigated the dynamics of the airfoil motion in greater details. They gave results for the case  $\bar{\omega} = 0.2$ ,  $\mu = 100$ ,  $M_f = 0$ ,  $\alpha_f = 0.25^\circ$ ,  $\delta = 0.5^\circ$  and  $M_0 = 0.25^\circ$ . The results they obtained are similar to Fig. 42 and they reached similar conclusions that the existence of pockets of LCO was very dependent on the freeplay and preload conditions. They carried out power spectral densities (PSDs) of the time series and typical example are shown in Fig. 43. In Fig. 43a the pitching motion in one of the LCO islands, at  $U^*/U_L^* = 0.79$  is presented. The motion is dominated by two frequencies at  $0.335\omega_x$  and  $0.67\omega_x$ . Although there are a number of other very distinct frequency peaks in the spectrum, their amplitudes are small compared to the fundamental and first harmonic. The plunge motion (not shown) has one significant peak only, at a frequency of approximately  $0.34\omega_x$  which is close to the pitch frequency and probably they are the same if the frequency can be resolved more accurately. In the main region of the LCO motion both the pitch and plunge motion have only one dominant

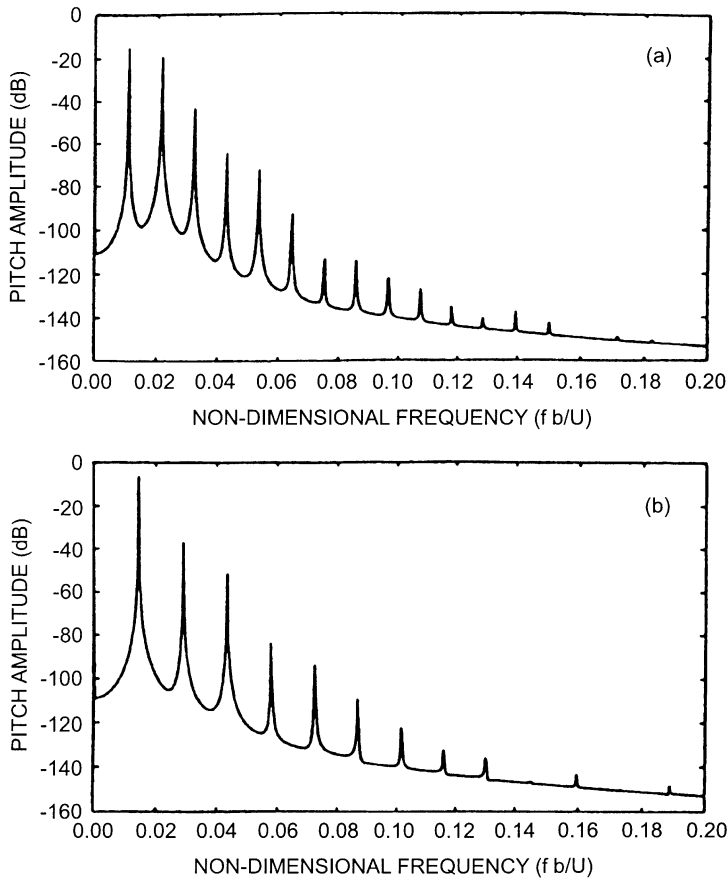


Fig. 43. Power spectral density of the pitch motion of the airfoil,  $\bar{\omega} = 0.2$ ,  $\mu = 100$ ,  $\alpha_f = 0.25^\circ$ ,  $\delta = 0.5^\circ$ ,  $M_0 = 0.25^\circ$ ,  $\alpha(0) = 7.5^\circ$ : (a)  $U^*/U_L^* = 0.79$  and (b)  $U^*/U_L^* = 0.85$  (from Ref. [88]).

frequency, e.g., at  $U^*/U^* = 0.85$  both the plunge and pitch motion frequencies are  $0.48 \omega_\alpha$ . Fig. 43b shows the PSD for the pitch motion.

Fig. 42 represents only a two-dimensional section through a five-dimensional boundary between stable oscillations and LCO; the five dimensions being  $U^*/U_L^*$ ,  $\alpha(0)$ ,  $\alpha'(0)$ ,  $\xi(0)$  and  $\xi'(0)$ . A two-dimensional section obtained by Price et al. [88] which is similar to that shown in Fig. 42 but with  $\alpha'(0) = 0.229b/U$  deg/s is shown in Fig. 44. Once again pockets of LCO are obtained below the main LCO boundary, but the shape of both these islands and the main boundary are very different to that shown in Fig. 42. An interesting feature in Fig. 44 is the multitude of small islands of LCO for  $0.79 \leq U^*/U_L^* \leq 0.84$ , approximately. If a different two-dimensional section through the five-dimensional boundary is taken, the stability boundary as a function of  $\alpha(0)$  and  $\alpha'(0)$  for constant  $\xi(0)$ ,  $\xi'(0)$  and  $U^*/U_L^*$  is presented in Fig. 45 for  $U^*/U_L^* = 0.83$ , showing a very complex boundary between LCO and stable motion. Indeed, based on the totality of results they obtained, Price et al. [88] concluded that the five-dimensional boundary is in fact a continuous geometric shape with a number of protuberances that spiral out from the main body; furthermore, the

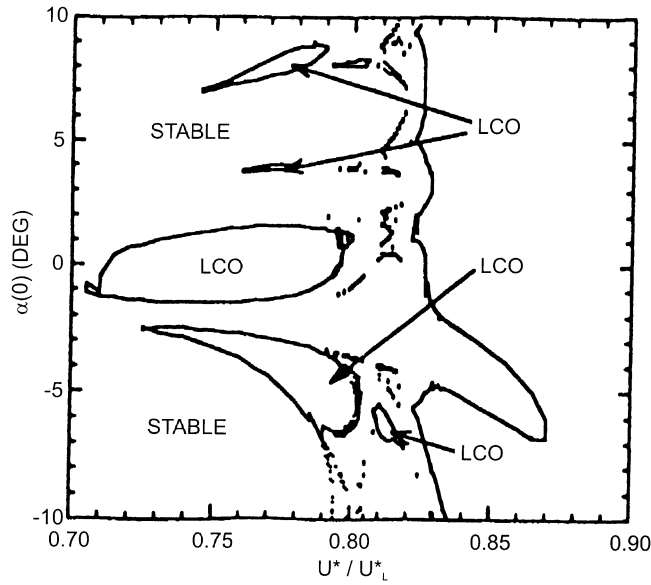


Fig. 44. Stability boundary for the airfoil as a function of initial pitch displacement,  $\bar{\omega} = 0.2$ ,  $\mu = 100$ ,  $\alpha_f = 0.25^\circ$ ,  $\delta = 0.5^\circ$ ,  $M_0 = 0.25^\circ$ ,  $\alpha'(0) = 0.229$  b/U deg/s,  $\xi(0) = \xi'(0) = 0$  (from Ref. [88]).

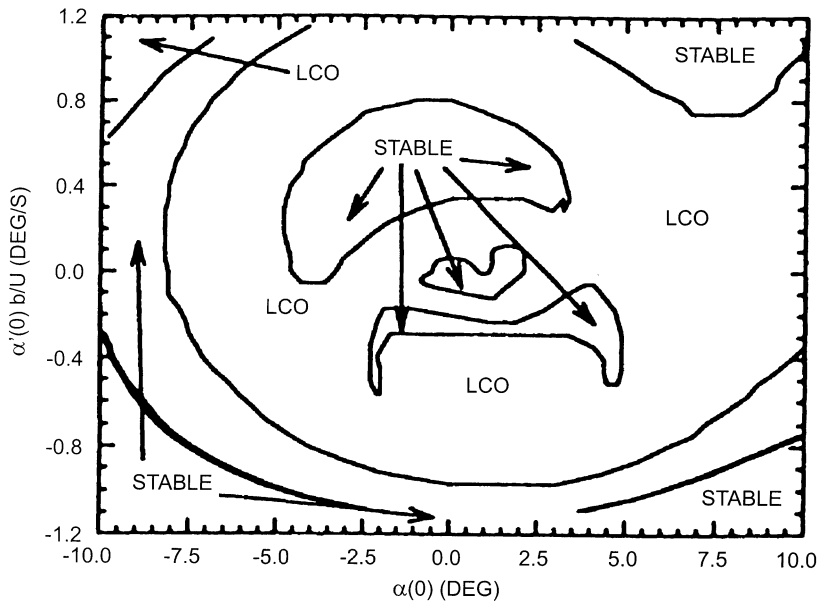


Fig. 45. Stability boundary for the airfoil as a function of  $\alpha(0)$  and  $\alpha'(0)$  for constant velocity,  $\bar{\omega} = 0.2$ ,  $\mu = 100$ ,  $\alpha_f = 0.25^\circ$ ,  $\delta = 0.5^\circ$ ,  $M_0 = 0.25^\circ$ ,  $\xi(0) = \xi'(0) = 0$ ,  $U^*/U_L^* = 0.83$  (from Ref. [88]).

apparent islands that appear in Figs. 42 and 44 are due to taking two-dimensional sections through this five-dimensional body.

Price et al. [88] carried out a second example for  $\bar{\omega} = 0.2$ ,  $\mu = 100$ ,  $M_f = 0$ ,  $\alpha_f = 0.25^\circ$ ,  $\delta = 0.5^\circ$  and  $M_0 = 0.0^\circ$ . Note this differs from the previous example only in the value of  $M_0$  and in this case there is no preload in the freeplay. For this set of parameters it was found that for some velocities below the linear flutter speed, no matter how long the simulation was allowed to run, the time histories never reached a steady-state condition (see, e.g., Fig. 46). It was suspected that this may indicate chaos, and this was investigated initially by forming PSDs of the time traces, a typical example of which is shown in Fig. 47. The spectrum is typical of chaotic motion where the spectrum is mainly broadband without sharp dominant frequency peaks [81]. To add further evidence to the existence of chaos, phase-plane plots and Poincaré sections were obtained; typical examples of which are shown in Fig. 48, for the data of Figs. 46 and 47. The phase-plane section shown in Fig. 48a is typical of a “two-well potential” and is indicative of chaos. This is very similar to the phase-plane plot obtained by Tang and Dowell [101] for their analysis with a freeplay nonlinearity. The Poincaré section shown in Fig. 48b has a very distinct structure that lends further evidence to the existence of chaotic motion; this is in contrast to the results of Tang and Dowell [101] where the Poincaré section was fairly random and showed no distinct structure. Although the results presented cannot be said to conclusively prove the motion to be chaotic, the time histories, PSDs, phase-plane section, and Poincaré sections are all strongly indicative of the existence of chaos, and thus, Price et al. [88] concluded that the motion is indeed chaotic.

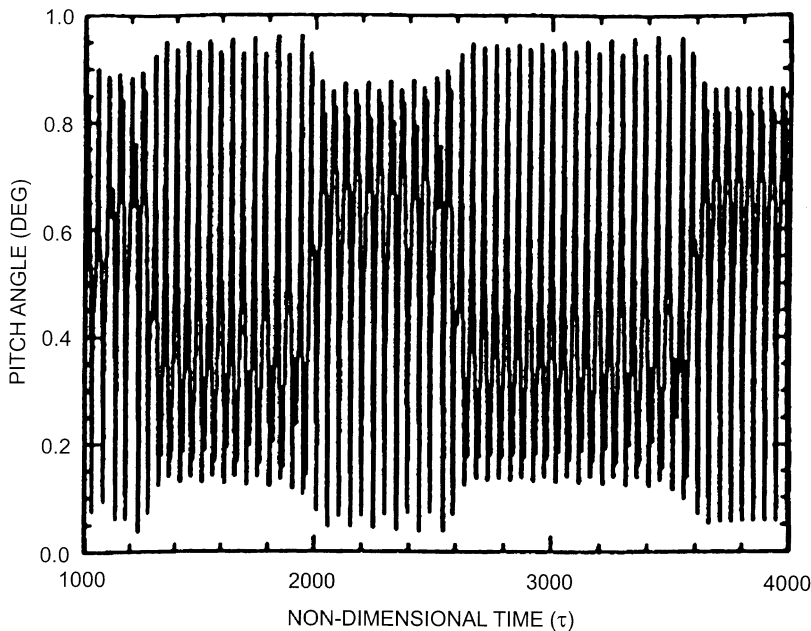


Fig. 46. Time history of airfoil pitch motion,  $U^*/U_L^* = 0.3$ ,  $\bar{\omega} = 0.2$ ,  $\mu = 100$ ,  $\alpha_f = 0.25^\circ$ ,  $\delta = 0.5^\circ$ ,  $M_0 = 0.0^\circ$ ,  $\alpha(0) = 7.0^\circ$ ,  $\alpha'(0) = \zeta(0) = \zeta'(0) = 0$  (from Ref. [88]).



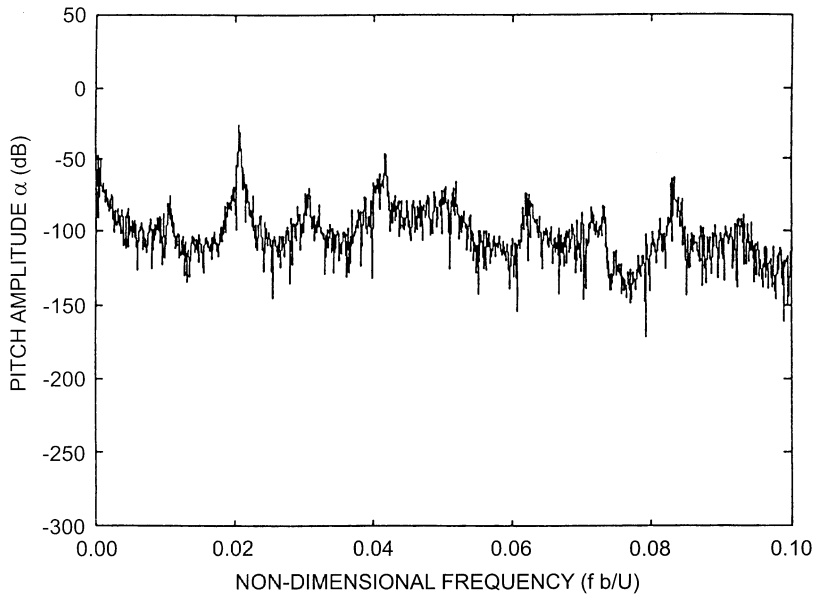


Fig. 47. Power spectral density of airfoil pitch motion,  $U^*/U_L^* = 0.3$ ,  $\bar{\omega} = 0.2$ ,  $\mu = 100$ ,  $\alpha_f = 0.25^\circ$ ,  $\delta = 0.5^\circ$ ,  $M_0 = 0.0^\circ$ ,  $\alpha(0) = 7.0^\circ$ ,  $\alpha'(0) = \xi(0) = \xi'(0) = 0$  (from Ref. [88]).

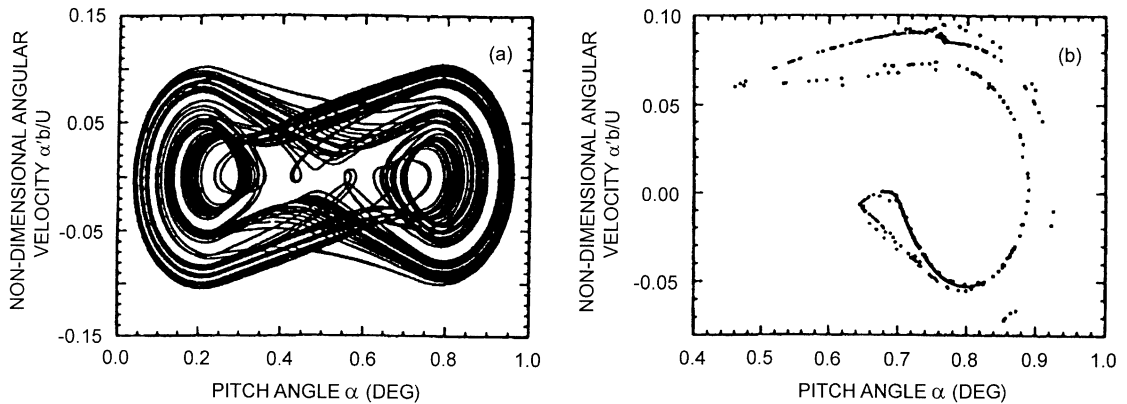


Fig. 48. (a) Phase-plane, and (b) Poincaré map (for  $\xi' = 0$  and  $\xi \geq -0.02$ );  $U^*/U_L^* = 0.3$ ,  $\bar{\omega} = 0.2$ ,  $\mu = 100$ ,  $\alpha_f = 0.25^\circ$ ,  $\delta = 0.5^\circ$ ,  $M_0 = 0.0^\circ$ ,  $\alpha(0) = 7.0^\circ$ ,  $\alpha'(0) = \xi(0) = \xi'(0) = 0$  (from Ref. [88]).

Numerous simulations of the type discussed above were completed, over a wide range of velocities, to determine the range of this chaotic motion; these are best illustrated via a bifurcation diagram as shown in Fig. 49. This diagram shows, as a function of  $U^*/U_L^*$ , the value of  $\alpha$  when  $\alpha' = 0$ . The significance of the bifurcation diagram is as follows. If at a particular  $U^*/U_L^*$  the system is stable, then a single point is obtained, e.g.,  $U^*/U_L^* \leq 0.13$ , approximately. If the motion is an LCO with one frequency, then two points are obtained ( $0.14 \leq U^*/U_L^* \leq 0.22$ , approximately),

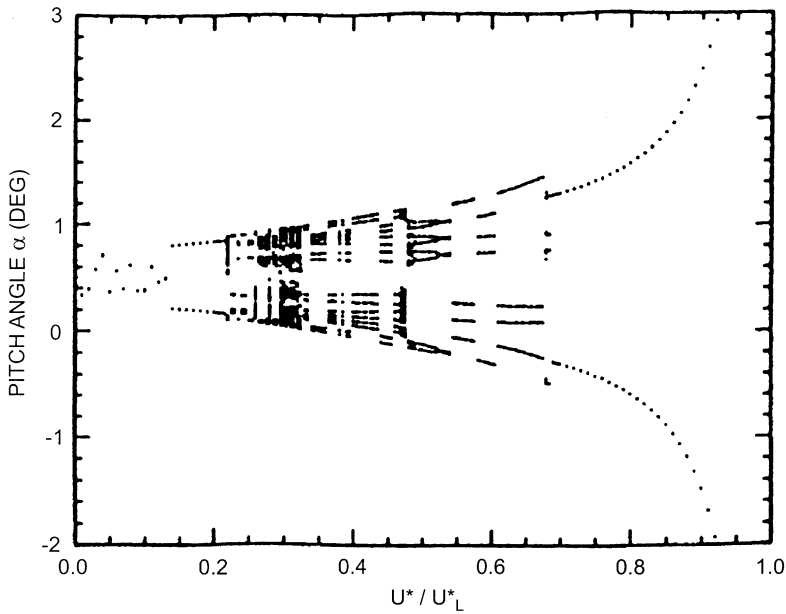


Fig. 49. Bifurcation diagram showing  $\alpha$  for  $\alpha' = 0$ ;  $\bar{\omega} = 0.2$ ,  $\mu = 100$ ,  $\alpha_f = 0.25^\circ$ ,  $\delta = 0.5^\circ$ ,  $M_0 = 0.0^\circ$ ,  $\alpha(0) = 7.0^\circ$ ,  $\alpha'(0) = \xi(0) = \xi'(0) = 0$  (from Ref. [88]).

and an LCO with two frequencies gives four points, etc. However, for some velocities a large number of points are obtained (giving what appears to be almost a vertical line on the bifurcation diagram) indicating chaos; examples of this can be seen in Fig. 49 for  $0.29 \leq U^*/U_L^* \leq 0.33$ , approximately. The bifurcation diagram shown in Fig. 49 suggests that the route to chaos is via period-doubling.

Using a large number of bifurcation diagrams for different initial values of  $\alpha(0)$ , a map showing the boundaries of the different types of motion was obtained and is presented in Fig. 50. It is apparent that the initial value of  $\alpha(0)$  has much less effect in this case than that obtained with preload, as suggested by Figs. 42 and 44. Price et al. [88] have not investigated in detail the effect of changing  $\alpha'(0)$ ,  $\xi(0)$ ,  $\xi'(0)$ , and did not elaborate on the manner in which the regions of chaotic motion are affected by these parameters.

In a later study, Price et al. [89] considered a more general freeplay by considering a bilinear spring. The properties of the nonlinearity is the same as that used to obtain the previous figures except that  $M_f$  was not set to zero and a describing function was also used to analyse the airfoil motion following the method outlined in Section 4.3.

Using the following airfoil and freeplay properties:  $\bar{\omega} = 0.2$ ,  $\mu = 100$ ,  $M_0 = 0.5^\circ$ ,  $\alpha_f = 0.25^\circ$ ,  $\delta = 0.25^\circ$ , and  $M_f = 0.05/\text{rad.}$ , Price et al. [89] compared the limit cycle amplitude obtained from the finite difference scheme and the describing function technique. Fig. 51 shows the pitch amplitude plotted against  $U^*/U_L^*$  for  $\alpha(0) = -1^\circ$ ,  $\alpha'(0) = \xi(0) = \xi'(0) = 0$ . This is a typical bifurcation diagram where the results from the finite difference scheme are given for the value of  $\alpha$  when  $\alpha' = 0$ . For period-one motion the value of  $\alpha$  shown in the figure represents the magnitude of the limit cycle oscillation. It should be realised that the finite difference solution may possibly be

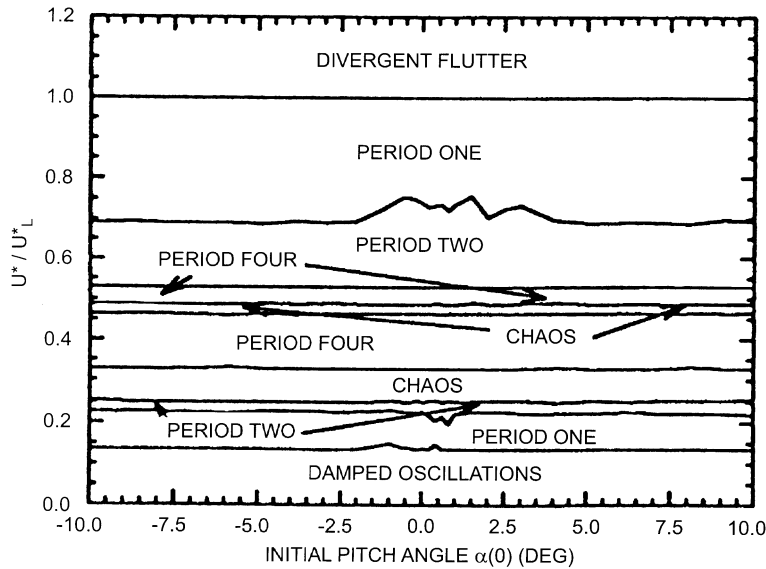


Fig. 50. Approximate stability boundaries for the airfoil as a function of initial pitch displacement,  $\bar{\omega} = 0.2$ ,  $\mu = 100$ ,  $\alpha_f = 0.25^\circ$ ,  $\delta = 0.5^\circ$ ,  $M_0 = 0.0^\circ$  (from Ref. [88]).

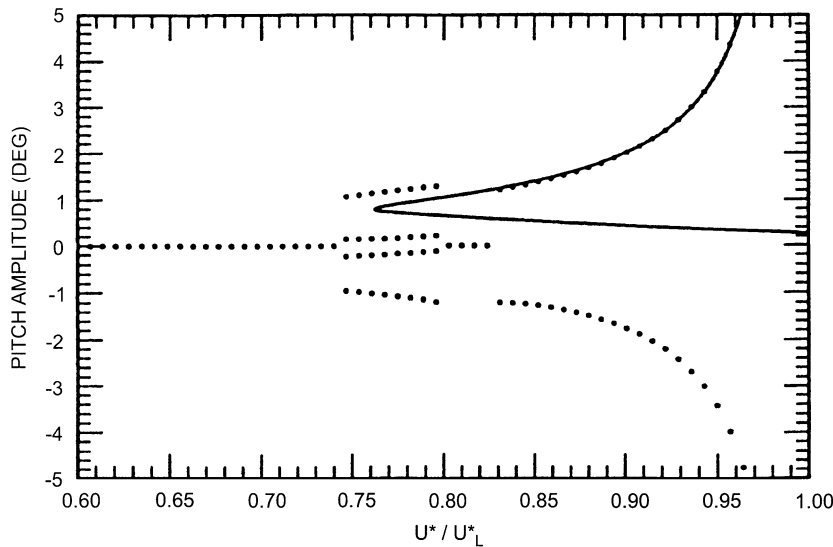


Fig. 51. Comparison of limit cycle amplitude obtained from finite difference and describing function methods for the bilinear nonlinearity;  $\bar{\omega} = 0.2$ ,  $\mu = 100$ ,  $\alpha_f = 0.25^\circ$ ,  $\delta = 0.5^\circ$ ,  $M_0 = 0.25^\circ$ ,  $M_f = 0.05/\text{rad.}$ ;  $\bullet$  finite difference method for  $\alpha(0) = -1.0^\circ$ ,  $\alpha'(0) = \xi(0) = \xi'(0) = 0$ ; — describing function method (from Ref. [89]).

dependent on the particular set of initial conditions for the airfoil. Thus, this bifurcation diagram is particular to the particular set of initial conditions Price et al. [89] chose for their study. The finite difference solution predicts that the initial loss of stability at  $U^*/U_L^* = 0.75$  is via a subcritical Hopf bifurcation and, furthermore, it results in a period-two motion. This is followed

by a re-stabilization at  $U^*/U_L^* = 0.8$  and finally by the onset of period-one motion at  $U^*/U_L^* = 0.83$ . Thus, it is clear that there is a region of period-two LCO for velocities less than those required for the main body of period-one LCO. Although not immediately apparent, closer examination of Fig. 51 shows that the finite difference solution is not symmetric about the  $\alpha = 0$  axis; this is due to the small preload on the airfoil in this case.

The describing function solution (see Section 4.3) gives two values of  $A$  ( $A_1$  and  $A_2$ ) each value of  $U^*/U_L^*$ ; furthermore, because there is a preload, in this case  $B$  is nonzero. Hence, what is presented in the figure is  $B + A_1$  and  $B + A_2$ . Although not proven because of the non-analytical nature of the bilinear nonlinearity, after comparison with the finite difference solution presented in Fig. 51 and other results presented in Fig. 52, it is apparent that the larger value of  $A$  shown in Fig. 51 represents a stable LCO, while the smaller value represents an unstable LCO. The unstable LCO gives a dividing line between stable and unstable motion: for  $\alpha(0)$  less than this line the subsequent motion tends back to the stable equilibrium condition, and for  $\alpha(0)$  greater than this line the subsequent motion tends towards the stable LCO.

The finite difference and describing function solutions presented in Fig. 51 do not agree on the value of  $U^*/U_L^*$  at which instability first occurs, but once the period-one motion commences the describing function method gives excellent agreement with the finite difference solution. As the amplitude of oscillation increases, the effective nonlinearity of the bilinear stiffness decreases and, hence, better agreement is obtained between the finite difference and describing function methods at higher values of  $U^*/U_L^*$ .

If the finite difference solution is repeated for the same airfoil with exactly the same nonlinearity as used for the results of Fig. 51, but with different initial conditions for the airfoil, then it is found that whether or not LCO occur is very dependent on the particular initial conditions. This is indicated in Fig. 52a where a two-dimensional section of the “basin of attraction” for LCO is shown. The complete basin of attraction is five-dimensional, the dimensions being  $\alpha(0)$ ,  $\alpha'(0)$ ,  $\xi(0)$ ,  $\xi'(0)$  and  $U^*/U_L^*$ , but the two-dimensional section shown is for constant  $\alpha'(0) = \xi(0) = \xi'(0) = 0$ . Similar to the discussion in Fig. 42, there are apparent “islands” of LCO below the main body of

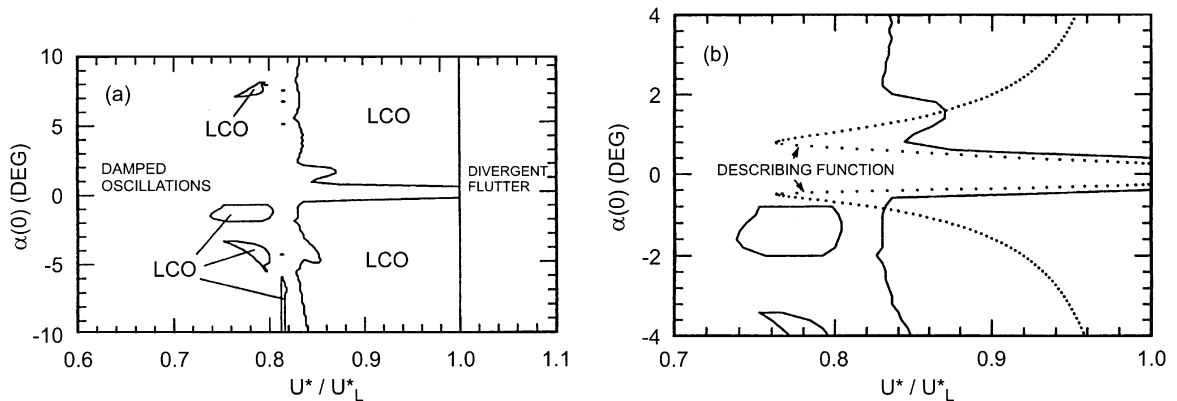


Fig. 52. Two-dimensional section of the basin of attraction for LCO for the bilinear nonlinearity obtained from the finite difference method;  $\bar{\omega} = 0.2$ ,  $\mu = 100$ ,  $\alpha_f = 0.25^\circ$ ,  $\delta = 0.5^\circ$ ,  $M_0 = 0.25^\circ$ ,  $M_f = 0.05/\text{rad}$ ,  $\alpha'(0) = \xi(0) = \xi'(0) = 0^\circ$ . (a) general view; (b) enlarged view for a smaller region of  $\alpha(0)$  and  $U^*/U_L^*$ ; • describing function solution (from Ref. [89]).

LCO for some values of  $\alpha(0)$ ; it is one of these islands of instability which gives the period-two motion for  $0.75 \leq U^*/U_L^* \leq 0.83$  shown in Fig. 51. This is in agreement with the observations from Fig. 42 with a free-play nonlinearity. For both the free-play and bilinear nonlinearities the LCO in the islands of instability is period-two; hence, it is not surprising that the agreement between the finite difference and describing function solutions in these islands is not as good as elsewhere.

As shown in Fig. 52a, for small initial values of  $\alpha(0)$ , typically in the range  $-0.5^\circ \leq \alpha(0) \leq 0.5^\circ$  instability is not obtained for  $U^*/U_L^* \leq 1$ . Qualitatively, this is in agreement with the unstable branch of the describing function solution presented in Fig. 51 where the describing function solution from Fig. 51 is superimposed on the results. An enlarged view of the results for small  $\alpha(0)$  is shown in Fig. 52b. The solutions  $B - A_1$  and  $B - A_2$  are presented in addition to  $B + A_1$  and  $B + A_2$  which are shown in Fig. 51. As shown, there is reasonable, but not exact, agreement between the unstable LCO branch of the describing function method and the finite difference solution. Quite possibly the agreement between these two solutions for the unstable LCO motion could be improved if the finite difference solution were given for other values of  $\alpha'(0)$ ,  $\xi(0)$  and  $\xi'(0)$ .

All of the results presented so far by Lee and Desrochers [65] and Price et al. [88] have been for zero structural damping, but it is of interest to see what the effect of structural damping is on the aeroelastic response of the airfoil. Fig. 53 shows three bifurcation diagrams for the airfoil with a bilinear nonlinearity with the following parameters:  $\bar{\omega} = 0.2$ ,  $\mu = 100$ ,  $M_0 = -0.0025^\circ$ ,  $\alpha_f = 0.25^\circ$ ,  $\delta = 0.5^\circ$ , and  $M_f = 0.01/\text{rad}$  with initial conditions  $\alpha(0) = 3^\circ$ ,  $\alpha'(0) = \xi(0) = \xi'(0) = 0$ .

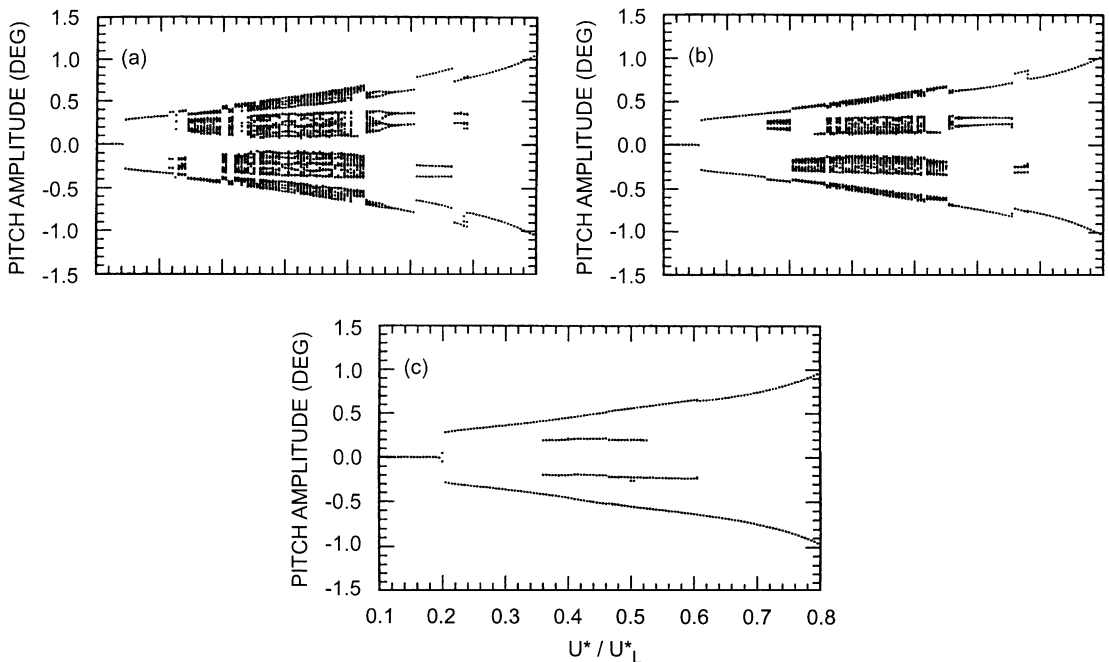


Fig. 53. Bifurcation diagrams showing  $\alpha$  for  $\alpha' = 0$  as a function of  $U^*/U_L^*$  for  $\bar{\omega} = 0.2$ ,  $\mu = 100$ ,  $\alpha_f = -0.25^\circ$ ,  $\delta = 0.5^\circ$ ,  $M_0 = -0.0025^\circ$ ,  $M_f = 0.01/\text{rad}$ ,  $\alpha(0) = 3^\circ$ ,  $\alpha'(0) = \xi(0) = \xi'(0) = 0$ . (a)  $\zeta_x = \zeta_\xi = 0.02$ ; (b)  $\zeta_x = \zeta_\xi = 0.05$ ; (c)  $\zeta_x = \zeta_\xi = 0.1$  (from Ref. [89]).

Three different values of structural damping  $\zeta_\alpha$  and  $\zeta_\xi$  were used. The bifurcation diagram shown in Fig. 53a with 2% critical structural damping for both  $\zeta_\alpha$  and  $\zeta_\xi$  is very similar to that with zero structural damping. It is seen in the range of velocity  $0.32 \leq U^*/U_L^* \leq 0.53$  there is a very large number of points in the bifurcation diagram at any particular velocity, suggesting non-periodic motion. Interestingly, as the velocity is increased beyond this nonperiodic region and approaches the divergent flutter condition, the airfoil motion goes from being non-periodic (probably chaotic) to period-four, then period-two and finally period-one. Increasing the structural damping  $\zeta_\alpha$  and  $\zeta_\xi$  to 5% of critical reduces the regions of apparently chaotic motion as shown in Fig. 53b, and for 10% of critical damping it is clear that the airfoil motion is now periodic as shown in Fig. 53c. Thus, it seems that a reasonably large amount of structural damping can eliminate the chaotic motion of the airfoil which is present for small amounts of structural damping.

Price et al. [89] concluded that where the LCO is period-one there is good agreement between the finite difference and describing function solutions. However, by its very nature, the describing function solution used here is not capable of predicting the higher order periodic motion unless modifications are made following the approach by Johnson [51] who took into consideration the next higher harmonic term.

Alighanbari and Price [1] carried out a bifurcation analysis of the airfoil using the same airfoil parameters and freeplay properties in the earlier studies by Price et al. [88,89]. They used Eqs. (27) and (28) and approximated the freeplay by a third-order rational curve fit given in Eq. (167). The freeplay they considered has the properties  $M_0 = \alpha_f = 0.25^\circ$ ,  $M_f = 0$  and  $\delta = 0.5^\circ$ . This gives values of  $c_1 = 0.00021$ ,  $c_2 = 0.9277$ ,  $c_3 = -134.7957$ ,  $c_4 = 5954.619$ ,  $c_5 = -121.2787$ ,  $c_6 = 6414.885$  and  $c_7 = 1064.4611$  for the constants in Eq. (167). The rest of the airfoil parameters are the same as those used to derive Fig. 42. The nonlinear equations of motion have been analyzed for different cases using both the Runge–Kutta method and AUTO [23].

The fixed points of the system can be evaluated by solving  $\mathbf{X}' = 0$  in Eq. (138). By using the curve-fit results for the freeplay, Alighanbari and Price [1] showed that the fixed point occurs at  $\alpha = -0.0012^\circ$  and  $\xi = 0.0001U^{*2}$ . The difference from the true fixed point at  $\alpha = \xi = 0$  is small and is due to the error in the approximated third-order rational curve fit.

Stability of the fixed point is analyzed by linearizing the dynamic equations of the system about this point. The eigenvalue analysis of the linearized equations shows that the system is stable for  $U^*/U_L^* < 0.98$  and unstable for higher velocities. Two purely imaginary eigenvalues at  $U^*/U_L^* = 0.98$  are an indication of a Hopf-bifurcation. For the exact freeplay the Hopf-bifurcation occurs at  $U^*/U_L^* = 1$ ; again the difference is small and is due to the approximate curve fit of the true freeplay.

A bifurcation diagram, evaluated using AUTO [23], showing both the stable and unstable solutions is presented in Fig. 54. In this diagram the horizontal axis is the bifurcation parameter  $U^*/U_L^*$  and the vertical axis is the maximum value of the pitch angle  $\alpha$ . For a stationary solution  $\alpha$  is plotted and for a periodic solution the maximum values of  $\alpha(\tau)$  during each period of oscillation are presented. The origin is a stable fixed point until  $U^*/U_L^* = 0.98$ , point 1, which is near the linear flutter speed. As predicted by the eigenvalue analysis, at point 1 a Hopf-bifurcation makes the origin unstable and an unstable period-one limit cycle solution begins showing that the Hopf-bifurcation is subcritical. The branch changes its direction at a limit point 2, and finally, this unstable period-one solution becomes stable at point 3, with amplitudes increasing to infinity when  $U^*$  approaches the linear flutter velocity. At point 3 a Floquet multiplier is equal to  $-1$ ; this

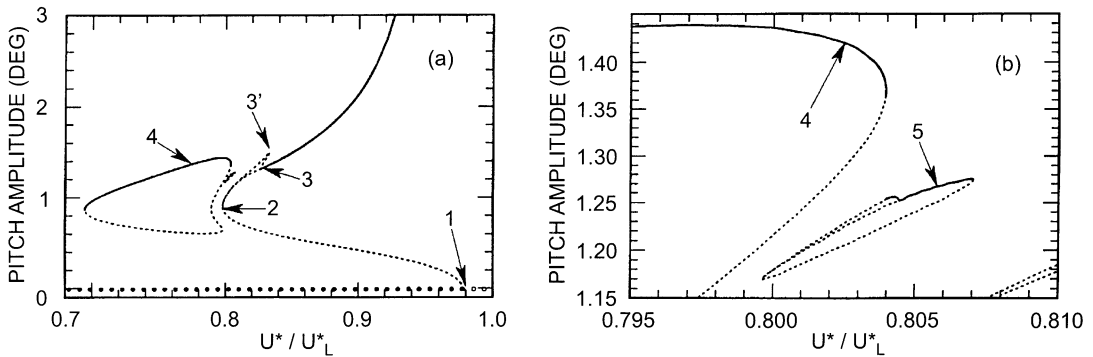


Fig. 54. (a) Bifurcation diagrams showing both stable and unstable solutions for pitch motion obtained using AUTO, (b) expanded view of partial region from (a).  $\bar{\omega} = 0.2$ ,  $\alpha_f = 0.25^\circ$ ,  $\delta = 0.5^\circ$ ,  $M_0 = 0.25^\circ$ . ● stable fixed point; ○ unstable fixed point; — stable limit cycle, --- unstable limit cycle (from Ref. [1]).

indicates a period doubling bifurcation. A period-two branch also starts at point 3 (branch 3-3') but does not lead to any stable solutions. However, another unstable branch, 3'-2, starts at point 3', is attracted to branch 2-3 and joins it at point 2.

Other periodic solutions are obtained by starting the process from known stable limit cycles, points 4 and 5, evaluated using the Runge–Kutta method for the same nonlinearity. Two separate islands of period-two and period-four stable and unstable solutions are found, as shown in Fig. 54a and b. Since some solutions separate from the main body of periodic oscillations have been found, there is the possibility that even more solutions, stable or unstable, may exist but have not been detected in this analysis. The corresponding bifurcation diagram for plunge motion is shown in Fig. 55. As can be seen, islands of periodic solutions also exist for plunge motion, but the limit cycles are confined to being either period-one or period-two, unlike the pitch response where period-four motion was also obtained.

Fig. 56 represents the bifurcation diagrams obtained using the Runge–Kutta method for the same parameters as Fig. 54, along with the results given by AUTO previously presented in Fig. 54. The results presented from the Runge–Kutta method show the value of  $\alpha$  when  $\alpha' = 0$  for the particular initial conditions given by  $\alpha(0) = 8^\circ$  and  $\alpha'(0) = \xi(0) = \xi'(0) = 0$ . Both methods predict essentially the same magnitude of stable limit cycle motion. However, in order to completely determine all possible branches of the stable solution the Runge–Kutta method should be repeated with a large number of different initial conditions and the total set of results considered. In the range of air-speed around  $U^*/U_L^* = 0.78$ , the Runge–Kutta results indicate two points at each  $U^*/U_L^*$ ; it should be noted that both points correspond to only one limit cycle, and this suggests period-two motion. AUTO also predicts a period-two limit cycle, but it shows only one point which is the maximum amplitude of the oscillation.

The bifurcation diagrams obtained for this nonlinearity are in good agreement with the finite different results previously presented by Price et al. [88] for the true freeplay nonlinearity. Using the approximate equation for the freeplay, complete branches of stable and unstable solutions could be determined using Alighanbari and Price's [1] analysis, and the type of bifurcations could also be determined via calculation of the Floquet multipliers. The results given by Price et al. [88]

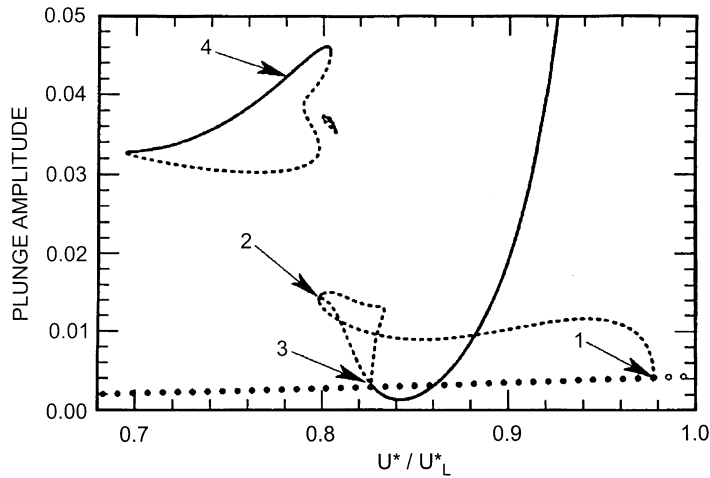


Fig. 55. Bifurcation diagrams showing both stable and unstable solutions for plunge motion obtained using AUTO.  $\bar{\omega} = 0.2$ ,  $\alpha_f = 0.25^\circ$ ,  $\delta = 0.5^\circ$ ,  $M_0 = 0.25^\circ$ . ● stable fixed point; ○ unstable fixed point; — stable limit cycle, --- unstable limit cycle (from Ref. [1]).

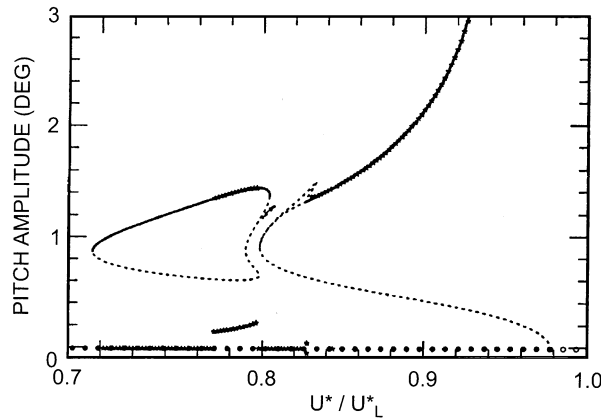


Fig. 56. Comparison of the bifurcation diagrams obtained using Runge–Kutta method and AUTO.  $\bar{\omega} = 0.2$ ,  $\alpha_f = 0.25^\circ$ ,  $\delta = 0.5^\circ$ ,  $M_0 = 0.25^\circ$ . \* Runge–Kutta results; ● AUTO (stable fixed point); ○ AUTO (unstable fixed point); — AUTO (stable limit cycle); --- AUTO (unstable limit cycle) (from Ref. [1]).

show only stable branches of the solution and the specific type of bifurcation could not be inferred.

Alighanbari and Price [1] also considered a freeplay nonlinearity without preload given by  $M_0 = M_f = 0$ ,  $\alpha_f = 0.25^\circ$ , and  $\delta = 0.5^\circ$ . This gives values of  $c_1 = -0.00422$ ,  $c_2 = 1.6164$ ,  $c_3 = -194.6997$ ,  $c_4 = 7436.942$ ,  $c_5 = -143.1963$ ,  $c_6 = 8207.7659$  and  $c_7 = -175.107$ . There are now three fixed points obtained by solving the equation  $\mathbf{X}' = 0$ . They are:  $\alpha = 0.691^\circ$ ,  $\xi = -0.00603U^{*2}$ ;  $\alpha = 0.309^\circ$ ,  $\xi = -0.00270U^{*2}$ ; and  $\alpha = 0.500^\circ$ ,  $\xi = -0.00436U^{*2}$ . The stability of these fixed points can be analyzed by linearizing the equations of motion about them. The



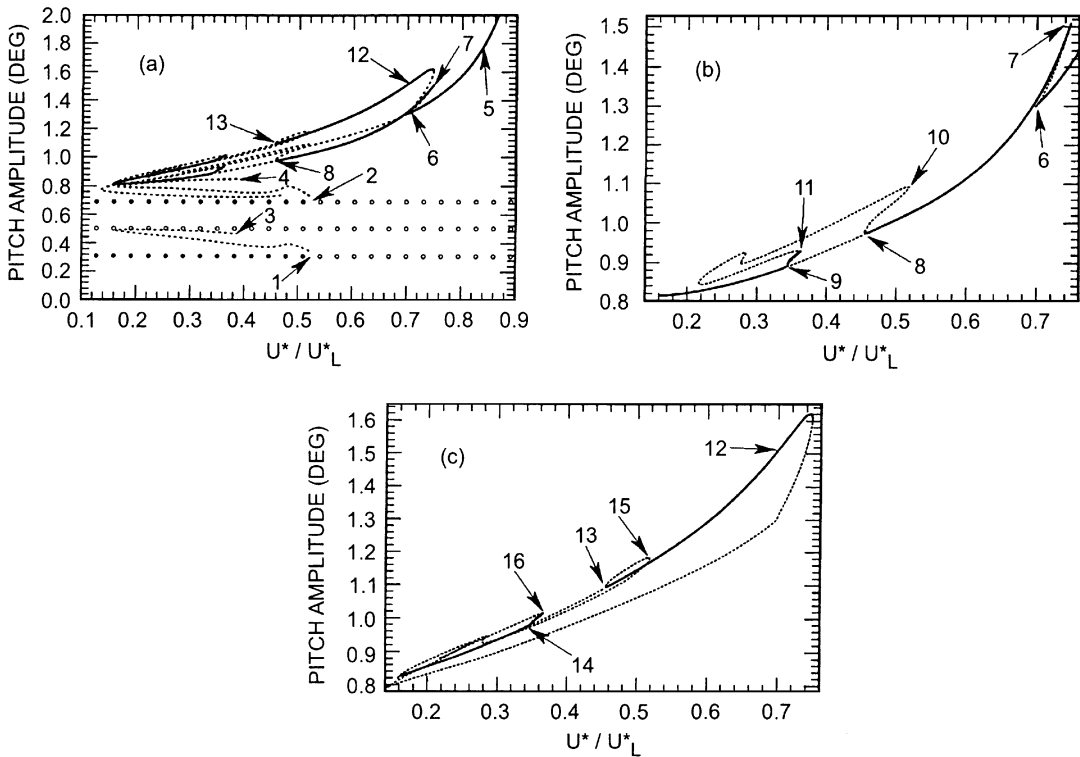


Fig. 57. (a) Bifurcation diagrams showing both stable and unstable solutions for pitch motion using AUTO, (b) expanded view of branch 6-7-8, (c) expanded view 12-13.  $\bar{\omega} = 0.2$ ,  $\alpha_f = 0.25^\circ$ ,  $\delta = 0.5^\circ$ ,  $M_0 = 0.25^\circ$  (from Ref. [1]).

eigenvalue analysis of the linearized equations shows that the first and second fixed points are stable for velocities below  $U^*/U_L^* = 0.529$  and that they are unstable for higher velocities. However, the third fixed point is unstable for  $U^*/U_L^* \geq 0$ .

Fig. 57 shows the bifurcation diagram constructed using AUTO for this nonlinearity. Three fixed points are shown in Fig. 57a, at low velocities two of these are stable and one unstable. As predicted by the eigenvalue analysis increasing  $U^*/U_L^*$  causes both of the stable fixed points to become unstable via Hopf-bifurcations at points 1 and 2, and the other fixed point remains unstable. Unstable periodic solutions are initiated at these bifurcation points which indicates a subcritical type of instability. However, these branches of periodic solutions do not lead to any further stable solutions, and after suggesting some bifurcations these branches cease to exist at points 3 and 4 of Fig. 57a.

Other branches are found by initiating the procedure from either of the two stable periodic solutions, given by points 5 and 12, which were obtained from the Runge–Kutta method. Starting from point 5 the amplitude of the stable periodic solution increases and approaches infinity as  $U^*/U_L^*$  approaches unity. However, by decreasing  $U^*/U_L^*$  the system undergoes more bifurcations. In an attempt to clarify the results this part of the solution, branch 6-7-8-9, is presented separately in Fig. 57b. The first bifurcation occurs at point 6; one of the Floquet multipliers crosses the unit circle at  $+1$  and the periodic solution does not merely become unstable, instead it

disappears entirely indicating a saddle node bifurcation [13]. The unstable solution originating from point 6 stabilizes after a limit point at 7. The results shown in Fig. 57b indicate two bifurcation points on the branch 7-8-9. Crossing the unit circle at  $-1$  the Floquet multipliers show a period doubling bifurcation at point 8. An unstable branch of period-four motion starts from this point, branch 8-10, indicating a subcritical (indirect) type of period doubling at point 8. The main branch, 7-8-9, which is unstable between 8 and 9, is restabilized after another period doubling bifurcation at point 9; contrary to the previous bifurcation at point 8, a new stable branch of period-four motion starts from point 9 showing a supercritical (direct) period doubling. This new stable branch of period-four motion, becomes unstable after a saddle-node bifurcation at point 11. The period-four branches of 8-10 and 9-11 are also connected through other unstable solutions, as shown in Fig. 57b.

The Runge–Kutta results also give another stable periodic solution at  $U^*/U_L^* = 0.7$ . Starting from this point, labelled 12 in Fig. 57a, more branches of stable and unstable periodic solutions are evaluated; these are presented in Fig. 57c. The branch 12-13-14 shows inverse and direct period doubling bifurcations, labeled 13 and 14, respectively, at the same air speeds as branch 7-8-9 shown in Fig. 57b. The period-four branches 13-15 and 14-16 are also connected via unstable solutions as shown in Fig. 57c.

The results presented in Fig. 57 show that a large number of stable periodic solutions, with no stable limit cycles, are given for  $0.36 < U^*/U_L^* < 0.44$ . On the other hand there is no possibility of divergent flutter in this velocity range since  $U^*/U_L^* < 1$ . These multiple unstable solutions indicate the possibility of chaotic oscillations.

Alighanbari and Price [1] have shown for those cases where the limit cycles are stable Runge–Kutta integration and AUTO give virtually identical results, both in terms of the velocities at which the bifurcations occur and the magnitude of the limit cycles. However, only AUTO is capable of predicting unstable solutions. By using periodic solutions obtained from the Runge–Kutta numerical integration as starting solutions for AUTO many stable and unstable periodic solutions are detected, resulting in extremely complex bifurcation diagrams.

#### 5.4. Hysteresis nonlinearity

The earliest attempt to study hysteresis effects in aeroelastic systems was carried out by Woolston et al. [120,121] using an analog computer to determine flutter of a two-dimensional airfoil oscillating in 2- and 3-DOF with incompressible indicial aerodynamics. Shen and Hsu [95] and Shen [96,97] studied the approximate behavior of nonlinear flutter problems by the describing function method and re-examined a few examples of a wing-control surface flutter with nonlinear structural stiffness previously analyzed by Woolston et al. [120,121]. They also considered the bending-torsion-control surface flutter of a two-dimensional airfoil-flap system in incompressible flow. The describing function method was also used by Breitbach [18,19] to analyse aircraft structures with hysteresis. Little numerical simulation work has been carried out except for the recent study by Chan [21].

Fig. 11 shows a symmetrical structural hysteresis nonlinearity that can be represented by the superposition of two free-plays. For increasing  $\alpha$ , the notations follow that used to describe a freeplay given in Fig. 2b. For decreasing  $\alpha$ , the freeplay starts at  $-\alpha_F$ . The loop has a flat-spot with width  $\delta$  between  $\alpha_F \leq \alpha \leq \alpha_F + \delta$  and  $-\alpha_F \leq \alpha \leq -\alpha_F - \delta$ . We can generalize the hysteresis

by assigning an arbitrary slope to the flat-spot. In Chan's [21] analysis, the slope was set to zero, and to preserve symmetry, the line joining the mid-points of the flat-spots on the upper and lower branches of the loop must pass through the origin of the moment versus displacement diagram.

The equations of motion of the airfoil are given in Eqs. (19) and (20). With the initial values  $\alpha(0)$ ,  $\alpha'(0)$ ,  $\xi(0)$ ,  $\xi'(0)$  specified, these two equations were integrated numerically by Chan [21] using a fourth-order Runge–Kutta scheme. Only a hysteresis nonlinearity in the pitch degree of freedom was considered and the investigation was limited to an airfoil with  $a_h = -1/2$ ,  $r_\alpha = 0.5$ ,  $x_\alpha = 0.25$ . The other airfoil parameters and hysteresis geometry were varied according to Table 2.

A typical displacement curve  $\alpha$  in the pitch degree-of-freedom versus nondimensional time  $\tau$  is shown in Fig. 58 for the hysteresis considered in Case 13 of Table 2. The value of  $U^*/U_L^*$  is 0.875 which gives an amplitude of pitch oscillation of  $3.2^\circ$  approximately. Only five cycles of the curve are shown from time between 2000 and 2400 where the motion has long reached steady state. The moment curve is also shown and it is in phase with the displacement. The constant values in the  $M(\alpha)$  curve corresponds to those instances when the displacement reaches the flat-spots on the hysteresis loop in the directions of increasing and decreasing  $\alpha$  respectively. Since  $\delta = 1^\circ$ , we see that the discontinuities in the moment curve occur between  $0^\circ < \alpha < 1.0^\circ$  and  $-1.0^\circ < \alpha < 0^\circ$  when projected on the displacement curve.

Fig. 59 shows the flutter boundary for Case 13 in Table 2. The initial conditions are  $\alpha'(0) = \xi(0) = \xi'(0)$  and  $\alpha(0)$  varies between the range  $\pm 20^\circ$ . This value of  $\alpha(0)$  is probably too large and at small values of time may invalidate the linear aerodynamic assumptions of Section 3.1. The remarks made in Section 5.2 concerning  $\alpha(0)$  also apply here.

Table 2  
Case studies from Chan [21]

Case	$\mu$	$\bar{\omega}$	$\alpha_f$ (deg)	$\delta$ (deg)	$M_0$ (deg)	$M_0/\delta$	$U_L^*$
1	50	0.2	0.0	2.5	1.25	0.5	4.525
2	50	0.2	0.5	1.5	1.25	0.833	4.525
3	50	0.2	1.0	0.5	1.25	2.5	4.525
4	50	0.8	1.0	0.5	1.25	2.5	3.074
5	100	0.2	0.0	2.5	1.25	0.5	6.285
6	100	0.2	0.25	0.5	0.25	0.5	6.285
7	100	0.2	0.5	1.5	1.25	0.833	6.285
8	100	0.2	1.0	0.5	1.25	2.5	6.285
9	100	0.8	0.0	2.5	1.25	0.5	4.114
10	100	0.8	0.5	1.5	1.25	0.833	4.114
11	100	0.8	1.0	0.5	1.25	2.5	4.114
12	100	0.2	0.0	0.5	0.25	0.5	6.285
13	100	0.2	0.0	1.0	0.5	0.5	6.285
14	100	0.2	-0.125	0.5	0.125	0.25	6.285
15	100	0.2	-0.25	1.0	0.25	0.25	6.285
16	250	0.2	0.0	2.5	1.25	0.5	9.710
17	250	0.2	0.5	1.5	1.25	0.833	9.710
18	250	0.2	1.0	0.5	1.25	2.5	9.710
19	250	0.8	1.0	0.5	1.25	2.5	5.962

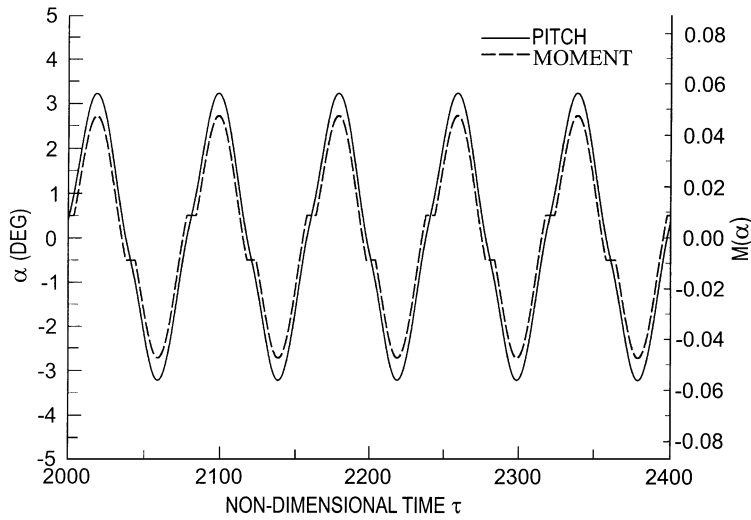


Fig. 58. Time variation of  $\alpha$  and  $M(\alpha)$  with  $\tau$  for Case 13 in Table 2 (from Ref. [21]).

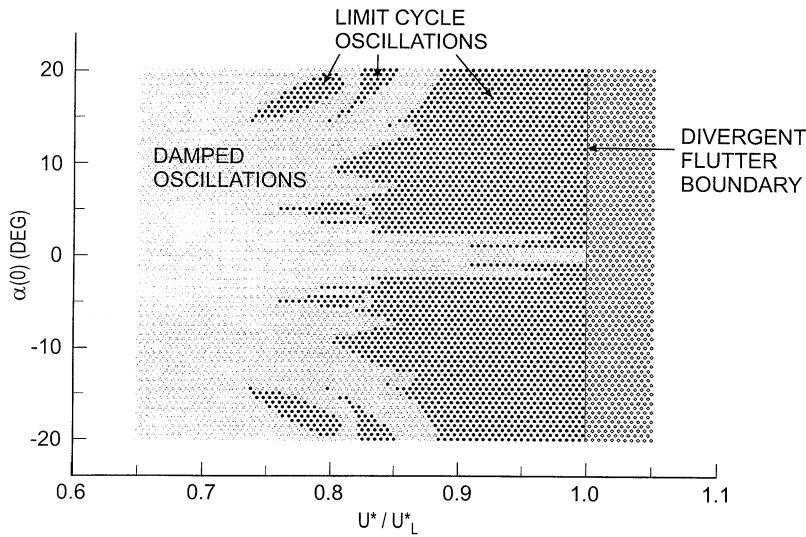


Fig. 59. Flutter boundary for a hysteresis structural nonlinearity for Case 13 in Table 2 (from Ref. [21]).

The grid size used in obtaining the flutter boundary is  $\Delta(U^*/U_L^*) = 0.01$  and  $\Delta\alpha(0) = 1^\circ$ . A time step  $\Delta\tau = 0.025$  is used in all the numerical simulations. Other values were tried but this time step was chosen based on efficiency and accuracy [52]. This type of flutter boundary diagram is similar to those shown for a freeplay nonlinearity. Note that the diagram is symmetrical about  $\alpha(0) = 0$ .

Comparisons with Woolston et al. [120] results show the flutter boundary to be similar, but the numerical simulations give more details on the boundary curves and the existence of

isolated pockets of LCO inside the main flutter boundary which was not observed by Woolston et al. [120].

The grid used to generate Fig. 59 is reasonably small and most of the LCO regions should have been identified with sufficient accuracy. To ensure that none has been missed, we re-examined the region  $0.75 \leq U^*/U_L^* \leq 0.9$  and  $-20^\circ < \alpha(0) \leq 0^\circ$  and used a finer grid to locate the LCO regions as shown in Fig. 60. The spacings are  $\Delta(U^*/U_L^*) = 0.00125$  and  $\Delta\alpha(0) = 0.2^\circ$ . Comparisons with Fig. 59 shows that the coarser grid gives sufficiently accurate results.

The flutter boundary shows that for  $U^*/U_L^* > 1$  the oscillations become divergent. The divergent rate usually increases with increasing values of  $U^*/U_L^*$ . Fig. 61 shows a typical time series for the pitch DOF at  $U^*/U_L^* = 1.001$  and  $\alpha(0) = 1.0^\circ$  for Case 13 in Table 2. Flutter is gradual and not explosive in character like those for higher values of  $U^*/U_L^*$ .

In the LCO region we show in Fig. 62 a typical time series at  $U^*/U_L^* = 0.95$  and  $\alpha(0) = 10^\circ$ . The transients die out in approximately 2 cycles and the pitch angle reaches an amplitude of  $7.5^\circ$ . The signal is seen to be close to a sinusoid with a dominating fundamental and possibly very weak higher harmonics for some values of  $U^*/U_L^*$  approaching the convergent region of the flutter boundary. This shows that the assumption of a dominating frequency in the harmonic balance or describing function technique is a good approximation in this LCO region.

Inside one of the pockets between  $0.73 \leq U^*/U_L^* \leq 0.85$  and  $\pm 20^\circ \leq \alpha(0) \leq \pm 15^\circ$ , the characteristics of the LCO are different from those in the main LCO region. The amplitudes are smaller and the oscillation is periodic but the presence of higher harmonics is clearly noticeable. This has been shown to be the case from power spectral density plots of the time series. Fig. 63 gives a time series for  $U^*/U_L^* = 0.775$  and  $\alpha(0) = -17.5^\circ$ . Steady state is reached after approximately 2 cycles and the amplitude is lower than those in the main LCO region with an amplitude of  $2.5^\circ$  in this case. In this region, the assumption in Shen's [96] harmonic balance analysis is not good and higher approximations such as sinusoidal method describe by Johnson [51] should be used.

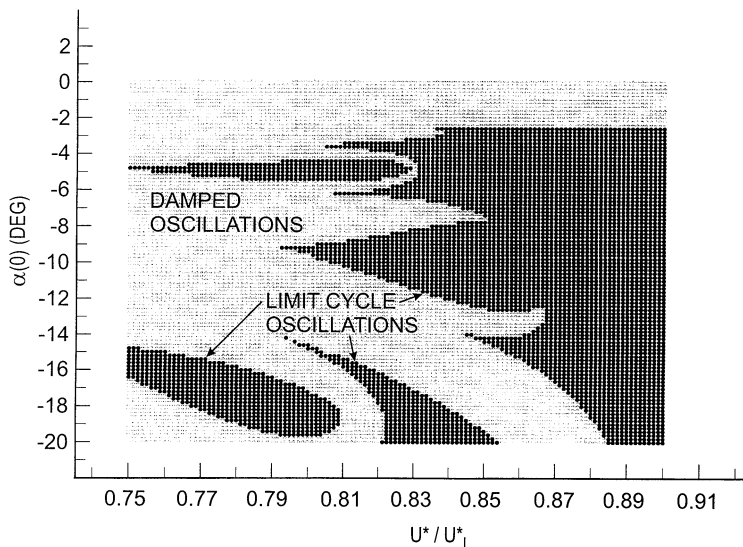


Fig. 60. Enlarged view of the flutter boundary of Fig. 59 (from Ref. [21]).

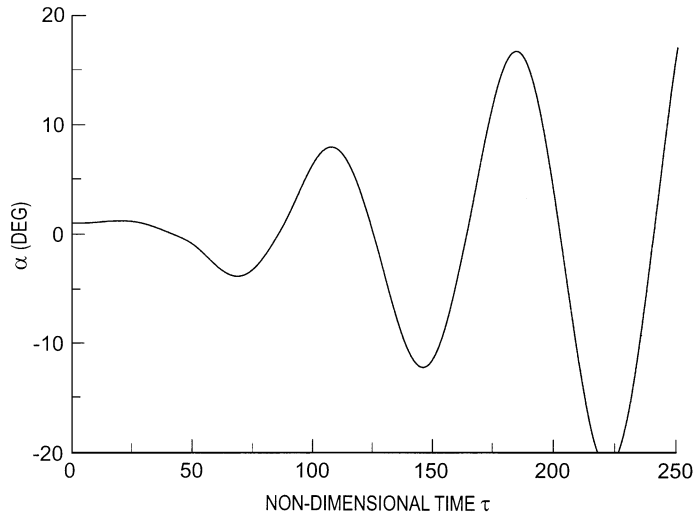


Fig. 61. Typical time series showing divergent oscillations (from Ref. [21]).

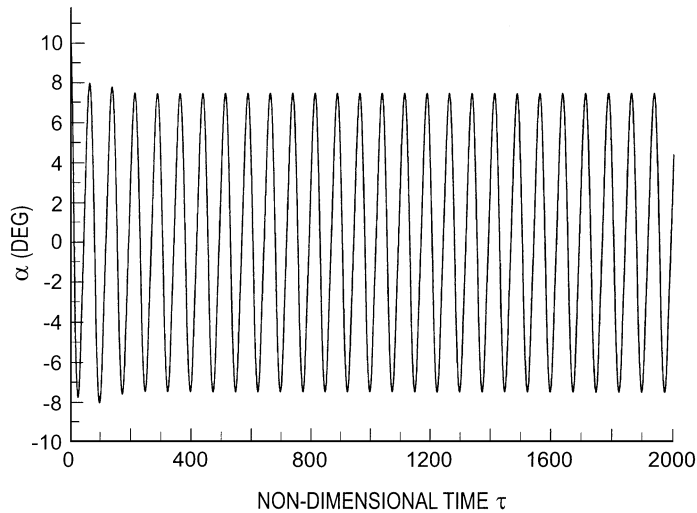


Fig. 62. Typical time series showing limit cycle oscillations in the main LCO region (from Ref. [21]).

The final time series we show in Fig. 64 corresponds to a condition inside the convergent region where  $U^*/U_L^* = 0.675$  and  $\alpha(0) = 12^\circ$ . It takes approximately 8–10 cycles for the motion to decay to stationary values. The rate of decay depends on the velocity ratio  $U^*/U_L^*$ .

A plot of the pitch amplitude versus velocity ratio is shown in Fig. 65. Notice that at  $U^*/U_L^* = 0.81$ , there is a small decrease in the amplitude curve. On examining the curve closely, we see that there are actually two curves for the range  $0.735 \leq U^*/U_L^* \leq 0.81$  and  $0.81 \leq U^*/U_L^* \leq 1.0$ . It is interesting to note that the amplitude is independent of initial condition  $\alpha(0)$ .

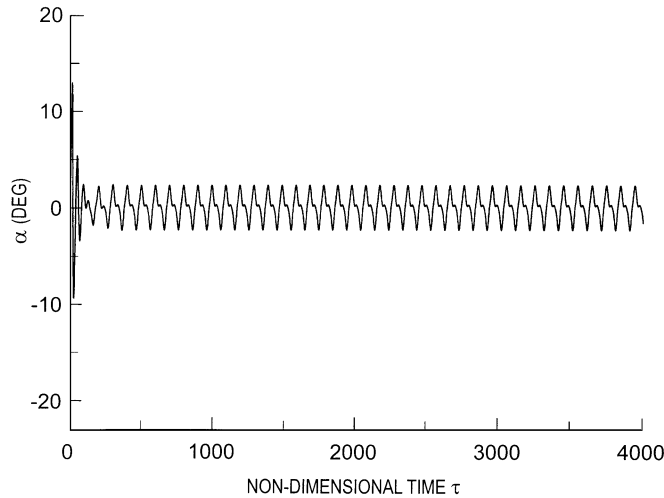


Fig. 63. Typical time series showing limit cycle oscillations in a LCO pocket (from Ref. [21]).

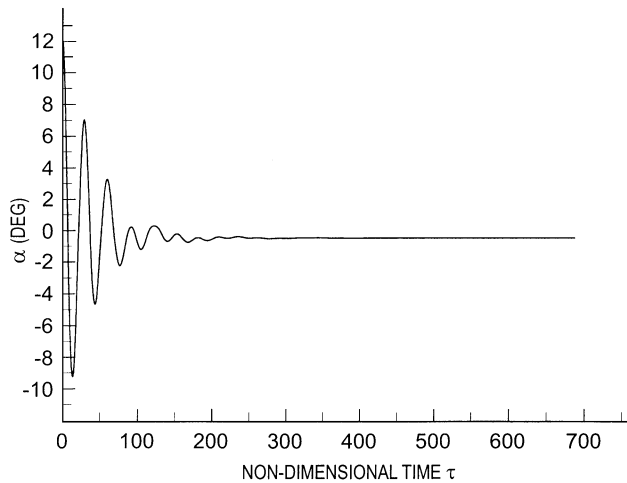


Fig. 64. Typical time series showing convergent oscillations (from Ref. [21]).

If we compare this figure with the results from a harmonic balance analysis such as that given by Shen [96], we found the shape of the curves to be similar. In Shen's [96] results,  $\alpha_A$  was used instead of  $\alpha(0)$  in plotting the flutter boundary curve. The reader should be cautioned that for  $U^*/U_L^* > 0.975$ , the amplitude  $\alpha_A$  is greater than  $10\text{--}15^\circ$  which is the limit where linear aerodynamics theory should be used.

The frequency  $\omega$  is plotted against velocity ratio in Fig. 66. The two regions  $0.735 \leq U^*/U_L^* \leq 0.81$  and  $0.81 \leq U^*/U_L^* \leq 1.0$  detected in the previous figure are quite distinct and the variations of  $\omega$  with velocity ratio are very small for  $0.735 \leq U^*/U_L^* \leq 0.81$ . Similar to the amplitude, the frequency is independent of initial conditions  $\alpha(0)$ . In the range  $0.81 \leq U^*/U_L^* \leq 1.0$ ,  $\omega$  increases with velocity ratio quite rapidly.

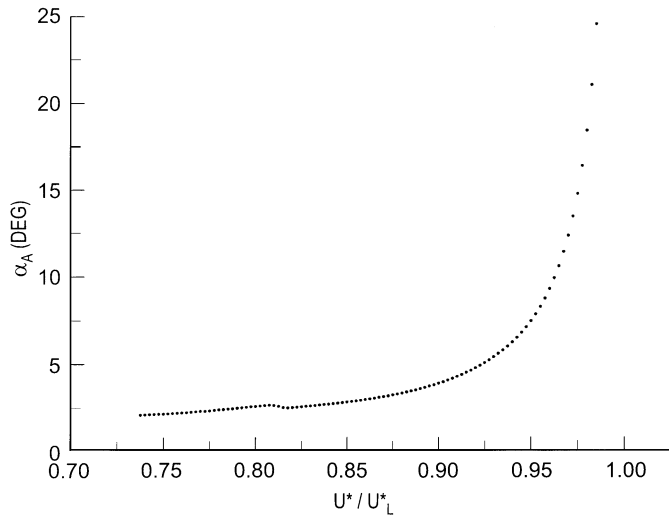


Fig. 65. Pitch amplitude versus velocity ratio for Case 13 in Table 2 (from Ref. [21]).

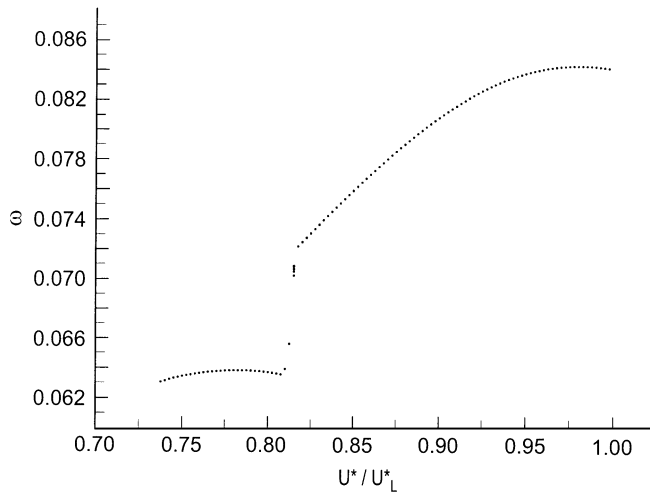


Fig. 66. Frequency versus velocity ratio for Case 13 in Table 2 (from Ref. [21]).

From the case studied by Price et al. [89] for a freeplay with preload having geometrical properties given by  $\alpha_f = 0.25^\circ$ ,  $\delta = 0.5^\circ$ , and  $M_0 = 0$ , we can construct a non-symmetrical hysteresis loop where  $\alpha_f$  is  $0.25^\circ$  when  $M_0 = 0$ . By nonsymmetrical we mean that the linear arm of the hysteresis loop for small  $M(\alpha)$  does not pass through the origin '0'. We see from Price et al. [89] results that there are regions of chaotic behavior at approximately  $0.25 < U^*/U_L^* < 0.33$  and  $0.46 < U^*/U_L^* < 0.49$  for  $-10^\circ \leq \alpha(0) \leq 10^\circ$  with  $\alpha'(0) = \xi(0) = \xi'(0)$ . If we construct hysteresis loops based on that freeplay by increasing  $M_0$ , we can study the effect of  $M_0$  on the types of nonlinear phenomena that are observed, namely, convergent motions, LCO and chaos. In Fig. 67



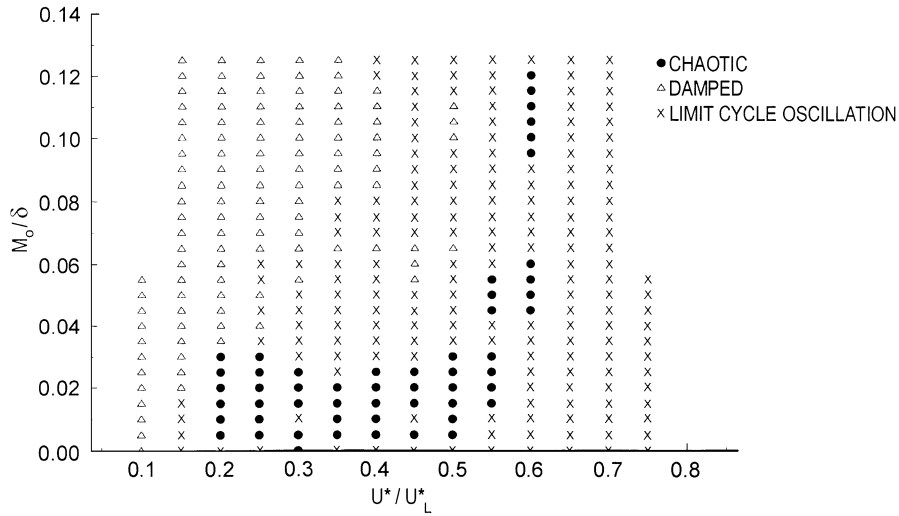


Fig. 67. Chaotic regions for a nonsymmetrical structural hysteresis nonlinearity (from Ref. [21]).

we plot  $M_0/\delta$  versus  $U^*/U_L^*$  and choose  $\alpha(0) = 7^\circ$  for all the numerical simulations. For fixed values of  $M_0/\delta$  and  $U^*/U_L^*$  a power spectral density plot from the time series was computed. From the shape of the power spectra, the oscillation was considered chaotic if no distinct or dominating peaks are detected in an otherwise broadband spectrum (see, for example, Price et al. [89]). The figure shows that a hysteresis nonlinearity with small values of  $M_0/\delta$  for this particular set of airfoil parameters enlarges the regions of chaotic motion beyond those for the freeplay studied by Price et al. [89]. This figure was obtained by choosing a region  $0 \leq M_0/\delta \leq 0.13$  and  $0.1 \leq U^*/U_L^* \leq 0.75$ . A grid was constructed using  $\Delta(U^*/U_L^*) = 0.05$  and  $\Delta(M_0/\delta) = 0.005$ , and at each grid point the motion was identified from the power spectral density plot to be either convergent, LCO or chaotic. We see that chaos is mainly confined to  $0 \leq M_0/\delta \leq 0.13$  and  $0.2 \leq U^*/U_L^* \leq 0.56$  using a rather coarse velocity increment in the present studies. This range is larger than that reported by Price et al. [89] for a freeplay and as  $M_0$  increases from 0 to higher values, the two chaotic regions in the freeplay merged. For larger values of  $M_0/\delta > 0.03$ , chaos is encountered only at  $U^*/U_L^* = 0.55$  and  $0.6$  for limited values of  $M_0/\delta$ . No numerical simulations were carried out beyond  $M_0/\delta > 0.13$  and it is suspected that chaos may not be found when the value of  $M_0/\delta$  for the hysteresis loop is sufficiently large. For  $U^*/U_L^* > 0.15$ , the figure shows that the decaying oscillation region decreases with  $M_0/\delta$ . When  $U^*/U_L^*$  reaches values greater than  $0.45$  the motion is mainly of the LCO type except for the chaotic cases. There are, however, a few conditions where the decaying solution was found and this cannot be explained.

No other values of initial conditions aside from  $\alpha(0) = 7^\circ$  were used in the computations. The dependence on initial conditions was not investigated and we may expect the chaotic regions to vary with  $\alpha(0)$ ,  $\xi(0)$  and their derivatives.

To investigate the effects of airfoil parameters, we vary  $\alpha_f$ ,  $\delta$ ,  $\bar{\omega}$ ,  $M_0$  and  $\mu$ . In order that the hysteresis loop is symmetrical about the line  $M(\alpha) = k\alpha$ ,  $\alpha_f$  and  $M_0$  cannot be varied independently.

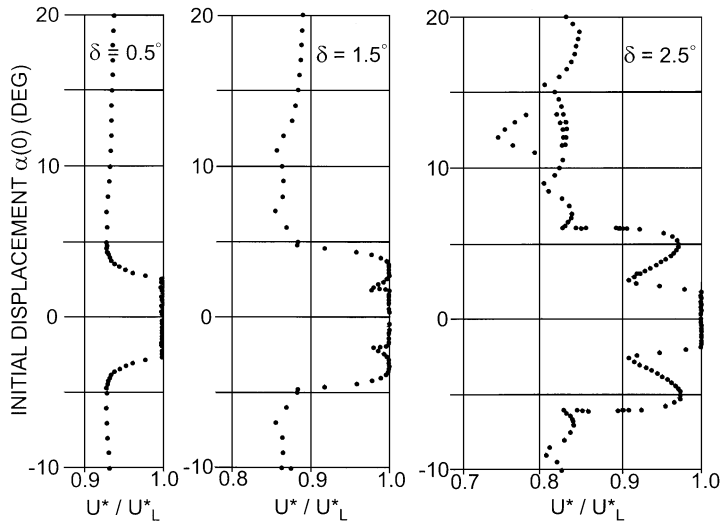


Fig. 68. Effect of flat-spot on flutter boundary (from Ref. [21]).

Fig. 68 shows the effect of  $\delta$  on the flutter boundaries for Cases 5, 7 and 8 in Table 2. The frequency ratio is kept at 0.2 and  $M_0 = 1.25$ ,  $\delta = 0.5, 1.5$  and  $2.5$  while  $\alpha_f$  varied in order that  $M_0$  can be kept constant. For  $\delta = 0.5$  ( $M_0/\delta = 2.5$ ) which has the smallest flat-spot (Case 8), the flutter boundary curve shows a typical behavior of the variations of the boundary with initial conditions  $\alpha(0)$  while keeping  $\alpha'(0) = \xi(0) = \xi'(0) = 0$ . At a velocity ratio equal to one, the boundary is vertical with increasing  $\alpha(0)$  until it reaches a value of  $2.5^\circ$ . It then moves in the direction of decreasing  $U^*/U_L^*$  with a small initial slope that increases rapidly until  $U^*/U_L^*$  reaches approximately 0.93 when the boundary line becomes almost vertical. The pitch amplitude increases from  $2.25^\circ$  at  $U^*/U_L^* = 0.93$  to  $10^\circ$  at  $U^*/U_L^* = 0.98$  while the corresponding plunge amplitude changes from 0.156 at  $U^*/U_L^* = 0.93$  and increases rapidly to a value of 0.375 at  $U^*/U_L^* = 0.98$ .

Increasing the value of  $\delta$  to 1.5 ( $M_0/\delta = 0.833$ ), we have for Case 7 a flutter boundary that resembles Case 8. There is a small indent at  $U^*/U_L^* = 1$  and  $\alpha(0)$  approximately  $2^\circ$ . The convergent/LCO boundary is almost vertical at  $U^*/U_L^*$  approximately 0.855 and  $\alpha(0) = 7^\circ$ .

For Case 5 where  $\delta = 2.5^\circ$  and  $M_0/\delta = 0.5$  the boundary has a more complex structure than those with smaller values of the flat-spot. The boundary between divergent and convergent oscillations remains at  $\alpha(0) = \pm 2^\circ$  as in the last case. The indent observed at  $\delta = 1.5^\circ$  grows to  $U^*/U_L^* = 0.9$ , and the point where the convergent/LCO boundary starts to become almost vertical has now moved to  $U^*/U_L^* = 0.825$  and  $\alpha(0) = 6^\circ$ .

If the loop is not symmetrical, Chan [21] compared Case 6 flutter boundary with that for Case 8 ( $\delta = 0.5^\circ$ ) and showed that off-setting the hysteresis by  $0.25^\circ$  and changing  $M_0$  to be 0.25 ( $M_0/\delta = 0.5$  vs. 2.5 for Case 8) the flutter boundary becomes non-symmetrical. The boundary between divergent and convergent oscillation near  $U^*/U_L^* = 1$  is very small, and the almost vertical boundary separating decaying oscillation and LCO moved to  $U^*/U_L^* = 0.825$  instead of 0.93. The plunge amplitude is small except near  $U^*/U_L^* = 1$  where comparisons are difficult since the slope of the amplitude–velocity curve is very large. The pitch amplitude is similar for the two cases in the range  $0.93 < U^*/U_L^* \leq 1$ .

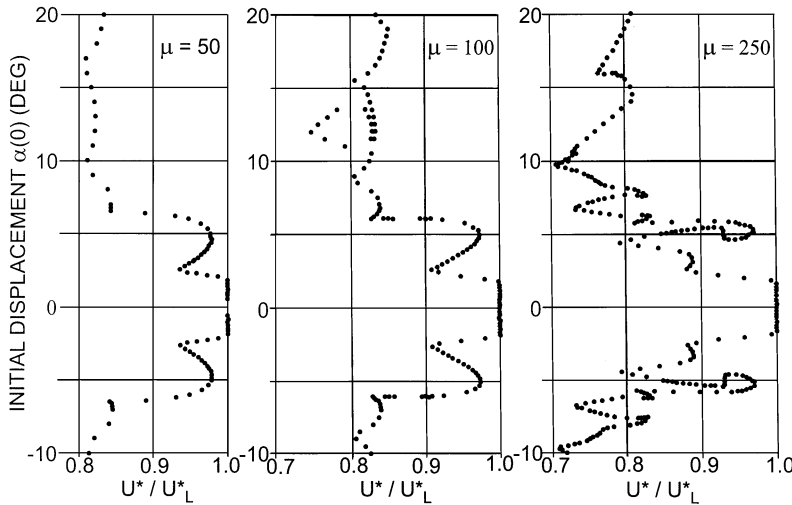


Fig. 69. Effect of  $\mu$  on flutter boundary (from Ref. [21]).

Fig. 69 shows the effect of  $\mu$  on the flutter boundary for Cases 1, 5, 16. At this value of  $\delta$  where the value of the flat spot is the largest used in the numerical simulations ( $\delta = 2.5^\circ$  and  $M_0/\delta = 0.5$ ) we found that at the lowest value of  $\mu = 50$  where the airfoil is the lightest, the flutter boundary is similar to that at  $\mu = 100$  (Case 5). The difference lies mainly in the vertical portion of the convergent/LCO boundary for  $\alpha(0) > 6^\circ$  where the lower  $\mu$  results show a smoother boundary. Chan [21] found that the pitch amplitude for  $\mu = 50$  is slightly below that at  $\mu = 100$  for  $U^*/U_L^* < 0.9$ . The plunge amplitude is noticeably lower and the difference can be as large as 25% at  $U^*/U_L^* = 0.825$ . Increasing  $\mu$  to 250, the flutter boundary is much more complex where decaying oscillations exist in narrow regions extending into the LCO regions. The boundary between decaying oscillations and LCO for  $\alpha(0) > 6^\circ$  decreases slightly for the heavier airfoil. The amplitudes of pitch motion show three distinct regions. For  $0.85 \leq U^*/U_L^* \leq 1$ , the curve is similar to those for the two lower values of  $\mu$  except that it has slightly higher values. Between  $0.76 \leq U^*/U_L^* \leq 0.85$ , the amplitude is slightly higher than those extrapolated from the curve between  $0.85 \leq U^*/U_L^* \leq 1$ . The curve between  $0.705 \leq U^*/U_L^* \leq 0.76$  shows a small increase with  $U^*/U_L^*$  initially, followed by a decrease as  $U^*/U_L^*$  approaches 0.76. The plunge amplitudes [21] also show the existence of these three regions and the amplitudes are very large, varying between 0.6 and 0.75 for the three regions, which are much greater than those for the other two values of  $\mu$ . It is found that for the heavier airfoil, the plunge is the more dominant DOF. The time series from these different regions especially those at the smaller values of  $U^*/U_L^*$  usually show the presence of higher harmonics with fairly large amplitudes.

Fig. 70 shows the effect of  $\bar{\omega}$  on the flutter boundary for Case 7 and 10 where  $\delta = 1.5^\circ$ . Increasing  $\bar{\omega}$  alters the bulge which starts at  $\alpha(0) = 2^\circ$  and moves it to a different location at  $U^*/U_L^* = 0.92$  and  $\alpha(0) = 9^\circ$ . Above  $\alpha(0) = 9^\circ$  the width of the LCO region is slightly larger at  $\bar{\omega} = 0.8$  where  $U^*/U_L^*$  has moved from 0.875 to 0.865. The pitch amplitude curve [21] is slightly higher at the lower frequency ratio while the plunge amplitude is again very large at  $\bar{\omega} = 0.2$  compared to those at  $\bar{\omega} = 0.8$  (e.g. 0.2875 compared with 0.0188 at  $U^*/U_L^* = 0.87$ ).

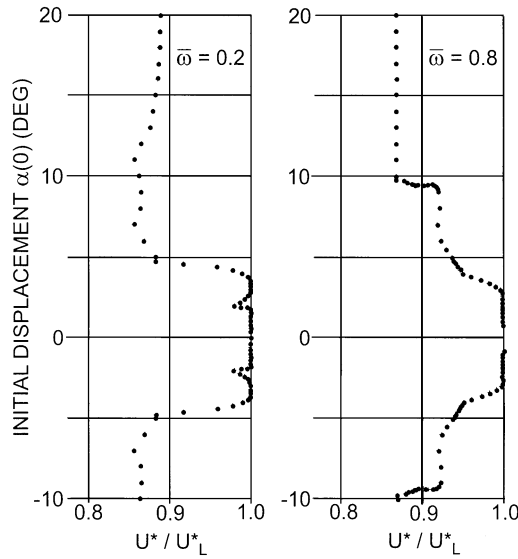


Fig. 70. Effect of  $\bar{\omega}$  on flutter boundary (from Ref. [21]).

For the largest value of the flat spot at  $\delta = 2.5^\circ$ , Cases 5 and 9 show that increasing the frequency ratio changed the flutter boundary substantially. At the lower frequency ratio, the boundary curve between convergent and LCO is not vertical but has a wavy profile. There exists also a pocket of LCO when  $2.5 < \alpha(0) < 6^\circ$  and there is a bulge with a maximum peak extending to  $U^*/U_L^* = 0.97$ . At  $\bar{\omega} = 0.8$ , these features are not present and the flutter boundary is quite smooth. The pitch amplitudes are larger for the smaller frequency ratio, the difference being greater at the lower values of  $U^*/U_L^*$ . The plunge amplitudes show large reductions by increasing  $\bar{\omega}$  to 0.8. For example, at  $U^*/U_L^* = 0.85$ ,  $\xi_A$  decreases from 0.406 to 0.025 when  $\bar{\omega}$  increases from 0.2 to 0.8. This difference increases with increasing  $U^*/U_L^*$ .

For the smallest flat-spot studied in Cases 8 and 11 for  $\delta = 0.5^\circ$ , the lower frequency ratio shows the flutter boundary to be fairly smooth. The boundary between divergent/convergent flutter is a vertical line at  $U^*/U_L^* = 1$  and terminates at  $\alpha(0) = 2.5^\circ$ . It decreases gradually with  $U^*/U_L^*$  until at a value of 0.93 it becomes almost a vertical line where  $U^*/U_L^*$  hardly changes with  $\alpha(0)$ . Increasing  $\bar{\omega}$  to  $\bar{\omega} = 0.8$ , Chan [21] showed that the LCO region is divided into 2 regions with one between  $0.985 \leq U^*/U_L^* \leq 1$  and the other starting at  $\alpha(0) = 9^\circ$  and  $U^*/U_L^* = 0.92$  which asymptotically reaches the left hand boundary of the first region at  $U^*/U_L^*$  approximate 0.985.

### 5.5. Forced oscillations

In the previous sections, the airfoil motion has been analysed for three common types of structural nonlinearities in the absence of external excitation forces. In other words, we considered only self-excited oscillatory motions. When  $P(\tau)$  and  $Q(\tau)$  in Eqs. (10) and (11) are not zero, the motion is dependent on the forcing frequency  $\omega$  of the applied force or moment. In aeroelasticity, forced motion has not been extensively studied, and even the simpler case of a coupled nonlinear

mechanical system has not been analysed thoroughly. Some recent studies by Lee et al. [69] and Gong et al. [36] show the complexity of such coupled mechanical systems.

A numerical simulation of the forced oscillation of a two-dimensional airfoil was carried out by Lee et al. [69] for incompressible aerodynamics with cubic nonlinear restoring forces of the form given by  $G(\xi) = \xi + \beta_\xi \xi^3$  and  $M(\alpha) = \alpha + \beta_\alpha \alpha^3$  in Eqs. (19) and (20). Lee et al. [69] used the following airfoil parameters:  $x_\alpha = 0.2$ ,  $r_\alpha = 1$ ,  $U^* = 1$ ,  $\bar{\omega} = 0.8944$ ,  $\zeta_\alpha = 0.05$ ,  $\zeta_\xi = 0$ ,  $\beta_\alpha = 0.1$ , and  $\beta_\xi = 0.125$ . These were chosen to coincide with a set of differential equations that the authors have previously studied [119].

It is useful to have some indication of the airfoil response in the absence of aerodynamic forces for comparison purposes. In this case, the governing equations become a coupled system of forced Duffing's equations. Fig. 71 shows the complex structure of the amplitude response curve  $R$  of  $\alpha(\tau)$  in degrees plotted against the excitation frequency  $\omega$  for  $F = 1.0$ , where  $F$  is defined in Eq. (111). Using the analysis given in Section 4.4, Lee et al. [69] found that at  $\omega = 1.5$  there are seven equilibrium points. Once these values are computed, the stability can be determined from the sign of the real part of all the eigenvalues, and only three equilibrium points are stable according to the linear stability analysis. Gong et al. [36] showed that for a certain range of system parameters, the forced couple oscillators admit both stable harmonic and stable quasi-periodic motions at the same frequency value.

A detailed numerical study was also carried out for this particular example to demonstrate some of the features of the coupled system. The existence of multi-valued harmonic solutions is confirmed by a numerical simulation using Eqs. (24) for different initial conditions.

To investigate the effects of aerodynamics in Eqs. (19) and (20), Lee et al. [69] choose  $a_h = -1/2$  and  $\mu = 25$ . Other values of  $a_h$  and  $\mu$  can be used since there are no restrictions on the parameters in the analysis. In order for the linear aerodynamics to be valid, the value of the forcing function  $F$  has to be kept small so that the pitch angle is less than  $10\text{--}15^\circ$  while at the same time the plunge motion  $\xi$  is within the range for Eqs. (15) and (16) to be applicable. Using these airfoil parameters, the

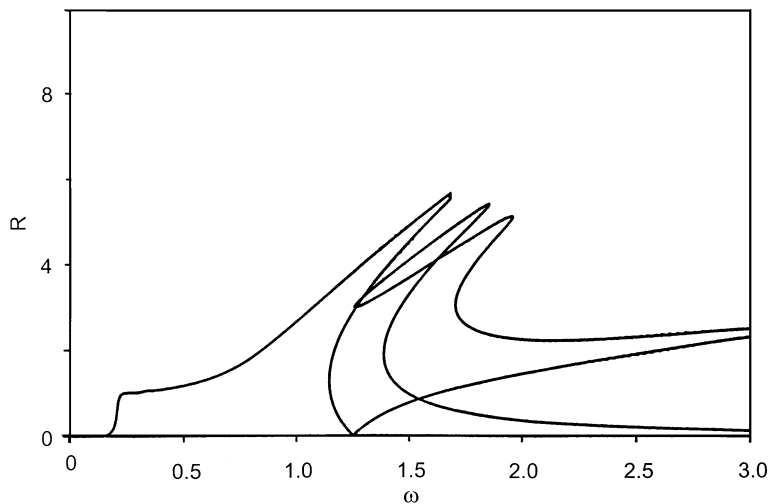


Fig. 71. Pitch amplitude response curve of a two-degree-of-freedom system with  $F = 1.0$  (from Ref. [69]).

linear flutter speed is obtained by setting the nonlinear stiffness terms to be zero, and its value  $U_L^*$  is found to be 2.423. Two values of  $U^*$  were used by Lee et al. [69], one at 41% and the other at 95% of  $U_L^*$ , that is,  $U^* = 1$  and 2.3019 approximately.

The  $\alpha$ -amplitude–frequency curve is shown in Fig. 72 for  $U^* = 1$  and  $F = 0.03$ . The case without consideration of aerodynamics is shown in Fig. 73. Both figures show the presence of two peaks at

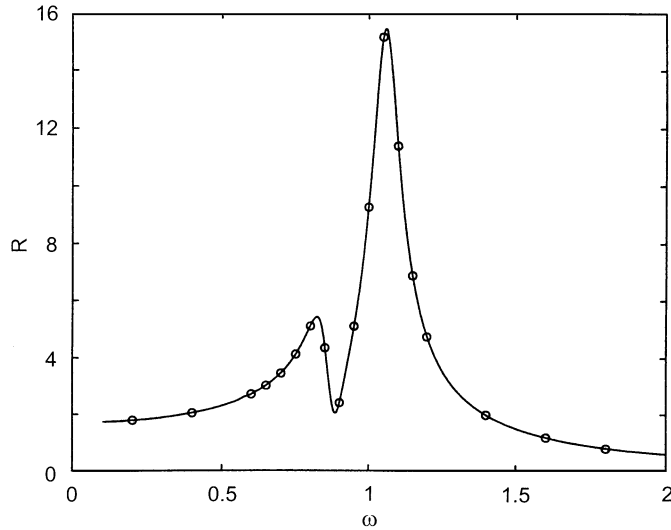


Fig. 72. Pitch amplitude response curve of a two-degree-of-freedom system for  $\mu = 25$ ,  $U^* = 1$  in a moving medium (from Ref. [69]).

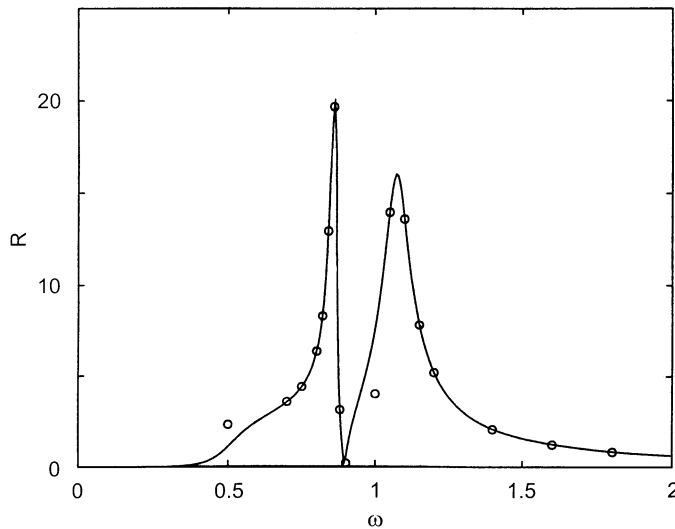


Fig. 73. Pitch amplitude response curve of a two-degree-of-freedom system for  $\mu = 25$ ,  $U^* = 1$  in a stationary medium (from Ref. [69]).

$\omega$  approximately 0.86 and 1.07. These frequencies can be estimated from Eqs. (19) and (20) since by decoupling the two equations, we can show that  $\omega_\alpha = 1/U^*$  and  $\omega_\xi = \omega_\alpha \bar{\omega}$  by definition. For  $U^* = 1$  and  $\bar{\omega} = 0.8944$  in this example, we obtain  $\omega_\xi = 0.89$  and  $\omega_\alpha = 1$  which are close to the observed values in the figures. The numerical simulation results are also included in the figure and they are denoted by the open circles. It is seen that good agreement is obtained. Comparison with Fig. 71 shows that the complex jump condition is not encountered. However, when the forcing amplitude  $F$  is increased to larger values, these jumps are detected, but the results are invalid since the amplitudes are very large and violated the linear aerodynamics assumptions.

Increasing  $U^*$  to  $0.95U_L^*$ , Fig. 74 shows the disappearance of one of the modes. It is seen from this figure that the peak occurs at  $\omega \approx 0.43$ . For the uncoupled modes, the natural frequencies  $\omega_\alpha$  and  $\omega_\xi$  are estimated to be 0.4344 and 0.3885, respectively for  $U^* = 2.3019$  and  $\bar{\omega} = 0.8944$ . The forcing amplitude in this case is  $F = 0.002$  which is very small. However, this is expected since only a weak external forcing to the airfoil is required in order to maintain a harmonic motion of fairly large amplitude as the linear flutter speed is approached. Also, near the flutter boundary, coalescence of the two modes accounts for the observation of only one peak in Fig. 74.

For the cubic nonlinearity studied by Lee et al. [69], only harmonic motions were observed. However, if the ratio  $\beta_3/\beta_1$  is large so that the cubic term dominates over the linear term in Eq. (31) while keeping  $\beta_0 = \beta_2 = 0$  to obtain the form of the nonlinearity studied by Lee et al. [69], the motion may be more complex. The discussion in Section 5.2 on cubic restoring force gives examples of chaotic motions from Price et al. [89] and Zhao and Yang [125] where they used large values of  $\beta_3/\beta_1$  in their studies. For other nonlinearities, such as the freeplay, it is possible that complex motions or chaos may be encountered for small values of the external forcing. Further studies are needed to confirm this even though results from Section 5.3 show that a freeplay generates many examples where bifurcation and chaos are detected. The method described by Gong et al. [36] on

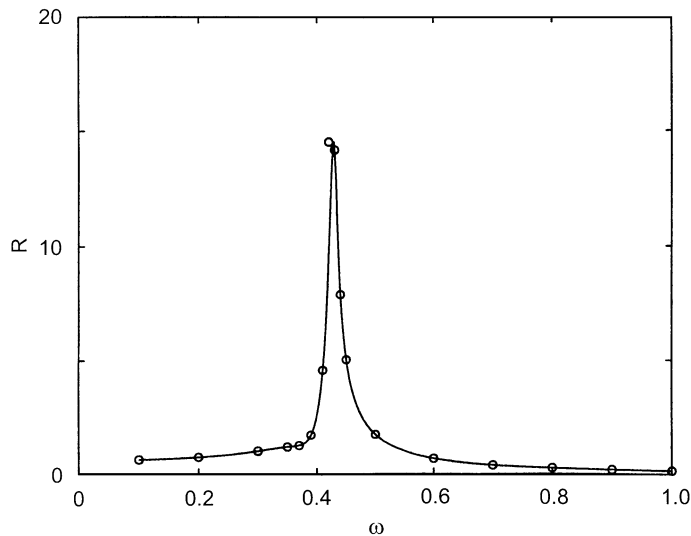


Fig. 74. Pitch amplitude response curve of a two-degree-of-freedom system for  $\mu = 25$ ,  $U^* = 0.95 U_L^*$  in a moving medium (from Ref. [69]).

the use of the Poincaré map for analysing bifurcation in system response to periodic forcing may be extended to more general nonlinearities other than the cubic spring, and possibly with the inclusion of aerodynamic terms in the governing equations.

## 6. Bifurcation and chaos of airfoils with aerodynamic nonlinearities

### 6.1. Transonic flows

In this section, we consider two examples of LCO caused by transonic aerodynamic nonlinearities. The first occurs in the presence of shock oscillation in an inviscid flow, and was studied by Kousen and Bendiksen [56,57]. They investigated a two-degree-of-freedom airfoil motion for a linear spring, and later extended the analysis to a structural freeplay nonlinearity. The other example is from Edwards [26] who considered a linear structure with attached and separated flow behind the shock wave.

Using a two DOF typical section model for bending-torsion motion, Kousen and Bendiksen [56] coupled the airfoil motion to an unsteady Euler solver to study transonic freestream Mach number effects. Unlike the transonic small disturbance formulation, Euler equations allow larger amplitude shock motion. However, neglecting viscous effects at large amplitude airfoil oscillation may not yield accurate results when significant flow separation takes place.

From Eq. (40), the NS equations can be reduced to the Euler equations by dropping the viscous terms. Bendiksen and Kousen [11] expressed the two-dimensional equations in integral form as follows:

$$\frac{\partial}{\partial t} \iint \mathbf{Q} \, dx \, dy + \int (\bar{\mathbf{F}} \, dy - \bar{\mathbf{G}} \, dx) = 0, \quad (168)$$

where  $\mathbf{Q}$  is given by Eq. (41) without the  $w$  term, that is,

$$\mathbf{Q} = \begin{pmatrix} \rho \\ \rho u \\ \rho v \\ \rho e \end{pmatrix}, \quad (169)$$

and  $\bar{\mathbf{F}}$  and  $\bar{\mathbf{G}}$  for the Euler equations in two dimensions can be written as

$$\bar{\mathbf{F}} = \begin{pmatrix} \rho(u - x_t) \\ \rho u(u - x_t) + p \\ \rho v(u - x_t) \\ \rho e(u - x_t) + pu \end{pmatrix}, \quad \bar{\mathbf{G}} = \begin{pmatrix} \rho(v - y_t) \\ \rho u(v - y_t) \\ \rho v(v - y_t) + p \\ \rho e(v - y_t) + pv \end{pmatrix}. \quad (170)$$

In these equations,  $\mathbf{Q}$  is the vector of independent variable,  $\bar{\mathbf{F}}$  and  $\bar{\mathbf{G}}$  are the  $x$ - and  $y$ -direction vectors of mass, momentum, and energy flux, respectively. For a perfect gas, the energy can be



written as

$$e = \frac{p}{(\gamma - 1)\rho} + \frac{1}{2}(u^2 + v^2), \quad (171)$$

where  $\gamma$  is the ratio of specific heats. Eqs. (168)–(170) represent a two-dimensional Euler formulation in which the velocity vector is defined as the instantaneous velocity at the moving boundary given by  $(x, y, t)$ . In this formulation, the velocity components  $u$  and  $v$  in the  $x$ - and  $y$ -directions are replaced by  $(u - x_t)$  and  $(v - y_t)$ , respectively. Note that for a fixed grid system,  $x_t = y_t = 0$ . These equations are solved by Bendikson and Kousen [11] on a nondeformable C-mesh of quadrilateral elements rigidly attached to the airfoil. Eq. (168) is applied to each cell  $(i, j)$  of the mesh and we have a system of ordinary differential equations written as

$$\frac{d}{dt}(S_{ij}Q_{ij}) + Q_{ij} - D_{ij} = 0, \quad (172)$$

where  $S_{ij}$  and  $Q_{ij}$  is the area and net flux out of the  $(i, j)$  cell, respectively.  $D_{ij}$  is a dissipative term added to prevent odd–even coupling in the mesh, and to suppress spurious oscillations. Eq. (172) is integrated forward in time using a five-stage Runge–Kutta scheme. Non-reflecting boundary conditions are used in the far field, and flow tangency boundary conditions are evaluated at the instantaneous position on the airfoil surface.

The airfoil motion is computed from Eq. (7) of Section 3.1 without the viscous damping term and the structure is assumed to be linear. Taking the Laplace transform and expressing it in finite difference form, we obtain

$$q_r(t_{n+1}) = q_r(t_n)\cos(\omega_r\Delta t) + \frac{1}{\omega_r}\dot{q}_r(t_n)\sin(\omega_r\Delta t) + \frac{1}{\omega_r}\int_0^{\Delta t} F_r(T)\sin[\omega_r(t - T)]dT, \quad (173)$$

where  $\Delta t$  is the time step and the generalized force  $F_r(t_{n+1})$  is written in difference form as

$$F_r(t_{n+1}) = F_r(t_n) + \left(\frac{\Delta F_r}{\Delta t}\right)_{n-1} \Delta t. \quad (174)$$

Kousen and Bendiksen [56] studied a NACA64A006 airfoil with  $a_h = -0.2$ ,  $x_a = 0.2$ ,  $r_a = 0.5385$ ,  $\bar{\omega} = 0.3433$  and  $\mu = 10$ . In the computations, a steady flowfield was first calculated around the airfoil. The airfoil was then forced in pitch at an amplitude of either 0.1 or 4° for three to five cycles. Forcing was then stopped and the airfoil allowed to come to a steady state condition. Generally, a time history containing 40–60 cycles were computed. The velocity range  $U^*$  was varied for  $M = 0.25, 0.6, 0.8, 0.85, 0.87$  and 0.9.

LCOs were observed only in the transonic range. Fig. 75 shows a bifurcation diagram of the pitch LCO for four  $M$  at 0.8, 0.85, 0.87 and 0.92. These are supercritical Hopf-bifurcations and the amplitudes grow monotonically from zero at the bifurcation point. Results for the two initial forced amplitudes show similar results for the limiting amplitude away from the linear flutter point, which coincides with the Hopf-bifurcation point. From the bifurcation diagram, we note that the linear flutter velocity increases with increasing Mach number. We can imagine an increase in  $U^*$  at

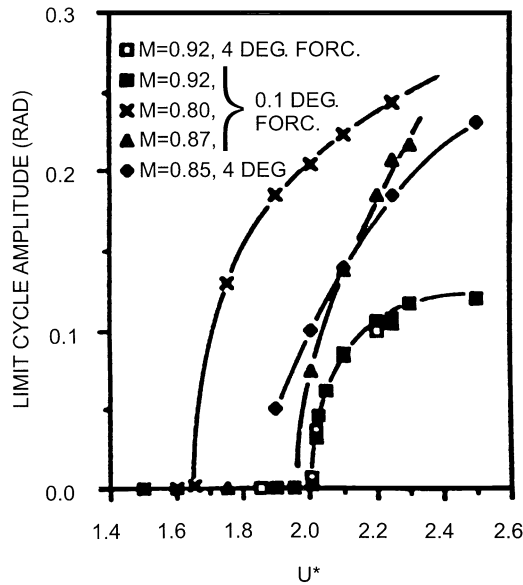


Fig. 75. Bifurcation diagram for transonic cases (from Ref. [56]).

constant  $M$  to be equivalent to a decrease in airfoil chord or the pitch natural frequency. Also limit cycle amplitudes generally decrease with increasing  $M$ .

An interesting phenomenon occurs when the torsional spring is given an initial pretwist. The pretwist was applied such that the torsional spring would have a zero moment about the elastic axis at a nonzero angle of attack  $\alpha_0$ . Using the system parameters given above, and choosing  $M = 0.85$  and  $U^* = 1.85$ , cases were computed with different values of  $\alpha_0$ . When  $\alpha_0 < 3.75^\circ$ , the airfoil approaches a limit cycle centered around a nonzero, positive angle of attack. Slightly below  $4^\circ$  in  $\alpha_0$ , significant harmonics are observed in the airfoil response. At  $\alpha_0 = 4^\circ$ , the response in pitch is shown in Fig. 76 and the oscillations are chaotic. At  $\alpha_0 = 4.75^\circ$ , Fig. 77 shows the motion to settle to some type of LCO behavior, but the amplitude is not constant and the mean angle of attack is  $-0.6^\circ$ . When  $\alpha_0 = 5^\circ$ , Fig. 78 shows the oscillations to decay to a stable offset of  $-0.6^\circ$ . Since the pretwist is  $5^\circ$ , this means that the computations predict the airfoil will twist  $5.6^\circ$  downward into a strong stable solution. The pressure distributions on the airfoil show the presence of multiple shocks on the lower surface and a large supersonic pocket on the upper surface extending almost to the trailing edge, thus producing the strong pitch-down moment.

In a later paper, Kousen and Bendiksen [57] used the same formulation but studied a freeplay nonlinearity in the torsional DOF. The airfoil parameters are the same as Kousen and Bendiksen [56] except that  $\mu = 60$ . They considered a symmetric freeplay without preload, having a value of  $\alpha_f = -1^\circ$ ,  $M_o = 0^\circ$  and  $\delta = 2^\circ$ . Only one Mach number at 0.87 was studied. For a linear spring, the phase-plane plot for  $\alpha$  at  $U^* = 2$  shows a slow approach towards LCO and the amplitude is small around 0.07 rad. Changing to a freeplay nonlinearity, Fig. 79 shows at  $U^* = 1.5$  a distorted character indicating the presence of higher frequency components. The initial forcing of the airfoil was  $0.1^\circ$ .

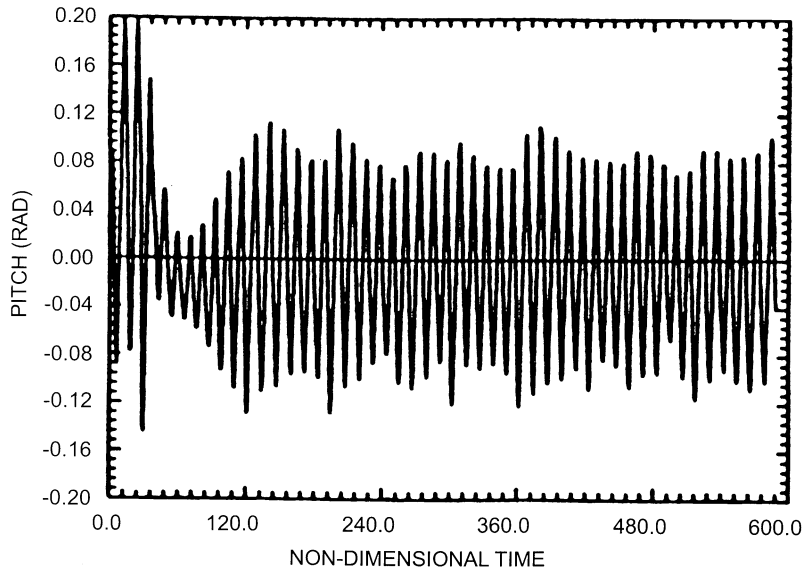


Fig. 76. Pitch amplitude for  $M = 0.85$ ,  $U^* = 1.85$ ,  $\alpha_0 = 4.0^\circ$  (from Ref. [56]).

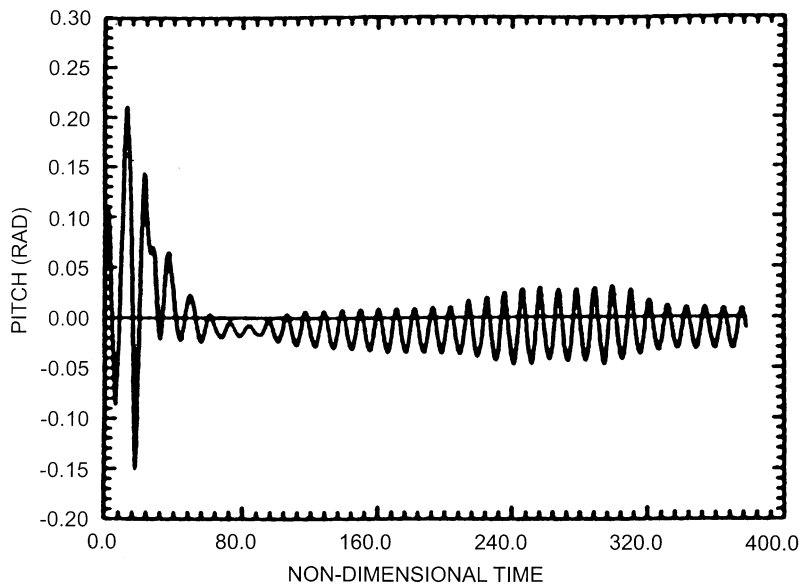


Fig. 77. Pitch amplitude for  $M = 0.85$ ,  $U^* = 1.85$ ,  $\alpha_0 = 4.75^\circ$  (from Ref. [56]).

Fig. 80 shows a bifurcation diagram for the freeplay nonlinearity. Initial forcings at the two values of  $0.1$  and  $4^\circ$  give similar results, and a case was tested at  $U^* = 1.7$  which showed the resulting limit cycle amplitudes differ by less than 2%. The bifurcation curve has a discontinuity at  $U^* = 0.5$ . The lack of torsional rigidity in the freeplay prevents the formation of pitch limit cycle

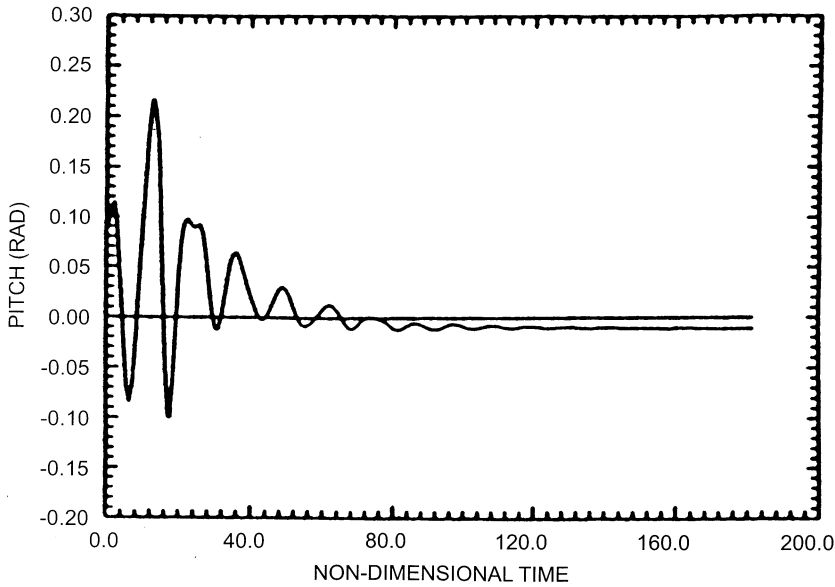


Fig. 78. Pitch amplitude for  $M = 0.85$ ,  $U^* = 1.85$ ,  $\alpha_0 = 5.0^\circ$  (from Ref. [56]).

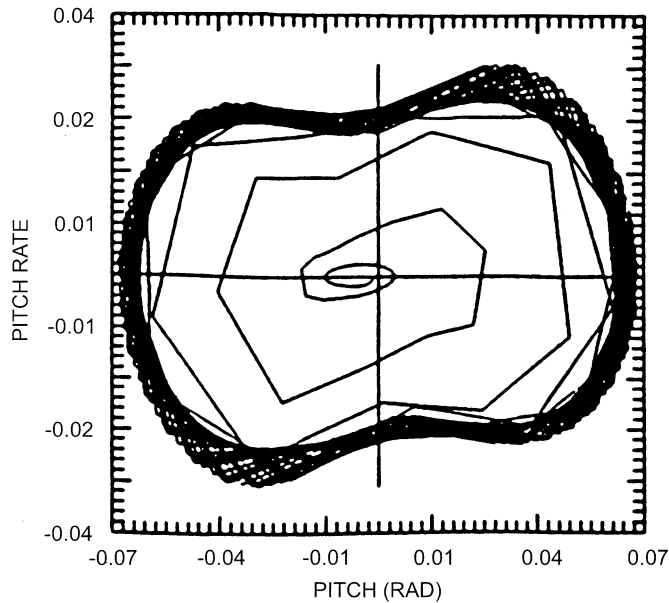


Fig. 79. Pitch phase plane for a freeplay  $U^* = 1.5$  (from Ref. [57]).

there. Therefore, at reduced velocities where the resulting pitch LCO amplitude might be less than  $1^\circ$ , the system is unable to respond in that manner. The linear flutter point has dropped significantly from about 1.9 without freeplay to around 0.5 with freeplay. In this respect, the freeplay is highly destabilizing.

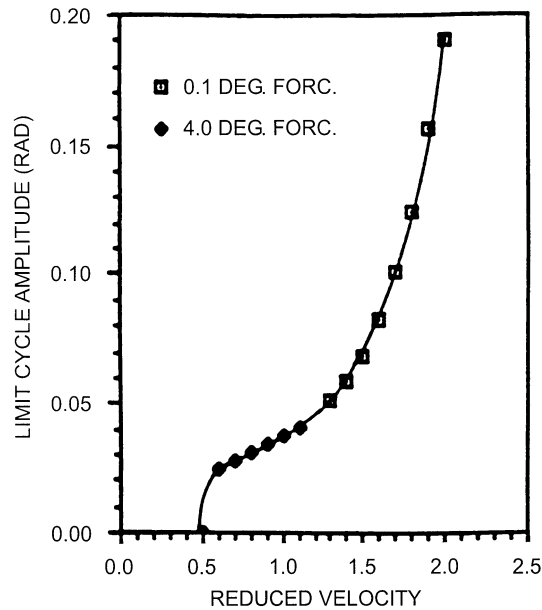


Fig. 80. Freeplay bifurcation diagram (from Ref. [57]).

When viscous effects are present, transonic shock-induced flow separation can cause self-excited shock oscillations. This phenomenon was discussed in Section 2.2 as a possible mechanism responsible for control surface buzz and wing buffeting. For moderate to strong shocks travelling a significant distance along the airfoil, flow separation is most likely to occur. Many attempts have been carried out using NS solvers for aeroelastic problems, but the computations are so demanding that very few configurations have been analyzed. Those that were investigated were mainly on the topic of dynamic stall [122]. The interactive boundary layer modeling IBLM proposed by Edwards [26] provides an alternative to the NS direct computation of flows involving viscous shear layers.

Edwards used the TSD equations [9] given in Section 3.2.1 to compute the inviscid flow. The reader should be reminded that the TSD equation is suitable only for weak shocks and hence Edwards' method should be restricted to weak-shock boundary-layer interaction where the resulting flow separation is not considered massive. The physical model is illustrated schematically in Fig. 81. Edwards [26] separated the flow into a region for the inner viscous boundary layer and an outer inviscid region. The superscripts "i" and "v" denote the inviscid and viscous regions respectively.

Starting from the leading edge of the airfoil, the boundary layer is approximated by the turbulent boundary layer on a flat plate. The description of the boundary layer solution is very involved and requires a lengthy discussion of the boundary layer equations and the various approximations used in solving those equations. We shall not go into the details of Edwards' method [26], but refer the reader to his earlier investigation.

The boundary layer equations are solved in a quasi-steady manner using a set of ordinary differential equations in the  $x$ -direction for the momentum thickness  $\theta$ , shape factor  $\bar{H}$ , and

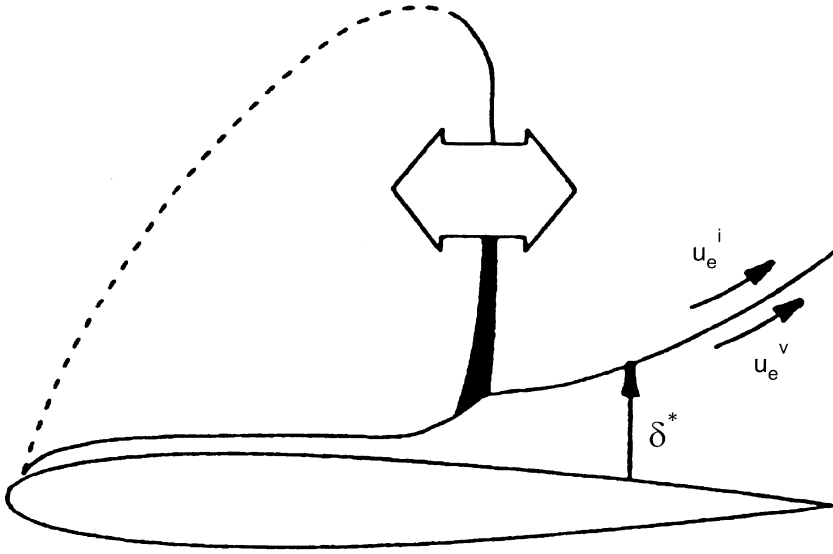


Fig. 81. Sketch of shock-boundary layer interaction (from Ref. [26]).

entrainment coefficient  $C_E$ . From these quantities, the displacement thickness  $\delta^*$  is calculated. The approach used by Edwards [26,27] utilizes the inverse boundary layer method. The inner and outer solutions are coupled through the boundary conditions on the wing and wake. The boundary conditions (Eq. (45)) become

$$\phi_z^\pm = S_x^\pm \pm S_t^\pm + \delta^* \quad \text{for } x_{LE} \leq x \leq x_{TE}, y \leq y_{TIP}, z = 0^\pm, \quad (175)$$

and on the wake we have

$$\Delta\phi_z = \Delta(\delta_x^*) \quad \text{for } x > x_{TE}, z = 0^\pm \quad (176)$$

and  $\Delta(\phi_x + \phi_t) = 0$  for  $x > x_{TE}, z = 0^\pm$ .

The coupling method is developed based on the observation that for transonic flow, the flowfield is unsteady, displaying oscillating shocks and separating and reattaching boundaries. The interacting boundary layer method is thus regarded as a simulation of two dynamic systems, the outer inviscid flow and the inner viscous flow, whose coupling requires special treatment to ensure that the coupling error between the two systems is minimised.

Edwards [26] demonstrated his method on a NACA 0012 airfoil and an 18% thick circular arc airfoil to show the onset of self-excited shock-induced oscillation for perfectly rigid airfoils. Of more interest is his study on wing flutter models.

The first wing flutter model is the AGARD Standard Aeroelastic Configuration [124] (AGARD 445.6) which was tested in the NASA LaRC Transonic Dynamics Tunnel. It is a semispan model having a quarter-chord sweep angle of  $45^\circ$ , taper ratio of 0.66 and is wall mounted to the wind tunnel. The wing had a NACA 65A004 airfoil section, and is modeled structurally using the first four natural vibration modes, with natural frequencies ranging from 9.6 Hz for the first bending mode to 91.54 Hz for the second torsion mode. Flutter calculations for this wing at Mach numbers

below and close to unity show that viscous modeling is required to achieve acceptable accuracy. In this region of  $M$  close to unity (subsonic  $M$ ), calculations show evidence of small amplitude LCO behavior. At  $M = 0.96$  and dynamic pressure  $Q = 0.75$  psi, Fig. 82 shows nonlinear response features from the time variation of the wing tip displacement  $z_{\text{tip}}$ . The early portion of the response shows positive damping of the flutter mode and a higher flutter frequency. The damping of the flutter mode decreases as the amplitude decays to approximately 0.12 in peak-to-peak, where stable LCOs persist. The initial portion of the time series can be considered as transients. This LCO behavior was further studied by sequentially increasing the dynamic pressure between computed runs from  $Q = 0.5$  to 0.81 psi. The resulting tip deflection time history is shown in Fig. 83 where eleven computer runs were carried out. The dynamic pressure was incremented as indicated in steps between restarted runs. For  $Q \leq 0.6$  psi the response is damped and for  $Q = 0.70$  psi small neutrally stable oscillations are seen. With  $Q$  increased to 0.78 psi slowly divergent oscillations develop and with further increase to 0.81 psi the divergent oscillations grow with increased negative damping until the amplitude reaches approximately 0.12 in peak-to-peak. The growth of the oscillations then quenches and it appears that a limit cycle condition will again develop. Further calculations are needed to fully establish this feature, but these have not been carried out

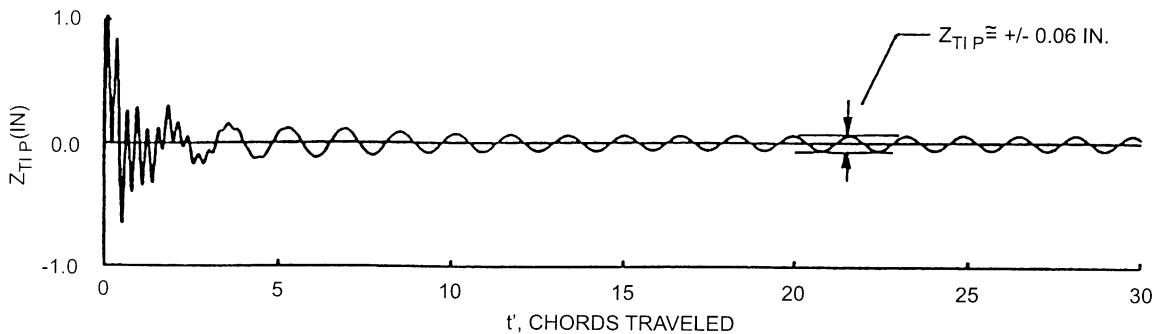


Fig. 82. Calculated AGARD 445.6 wing tip response in heavy gas for  $M = 0.96$  and  $Q = 0.75$  psi (from Ref. [26]).

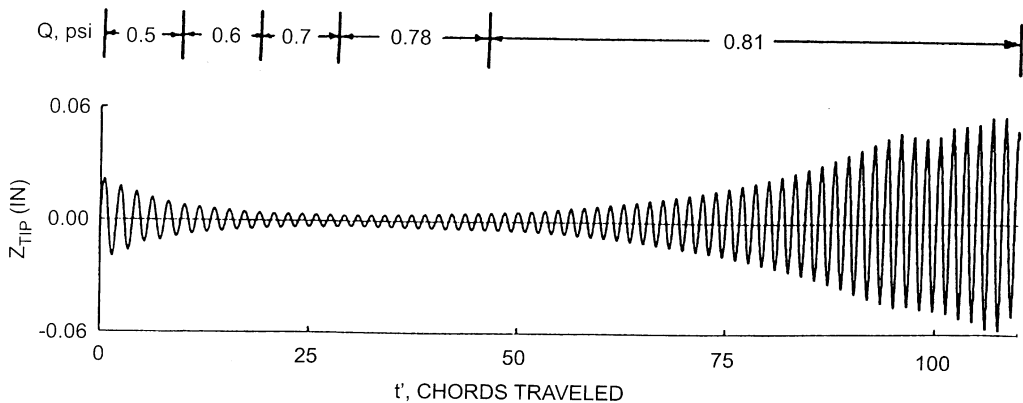


Fig. 83. Calculated AGARD 445.6 wing tip response in heavy gas for  $M = 0.96$  and increasing dynamic pressure (from Ref. [26]).

by Edwards [26]. This phenomenon of LCO is only observed at  $M = 0.96$  which was the highest  $M$  calculated. At this value of  $M$  and for the wing motions considered, the flow is fully attached since the wing is thin. Computations show significant regions of near sonic flow develop adjacent to the wing upper and lower surfaces as the wing oscillates. This is an example of nonlinear aerodynamics with attached flow interacting with the linear structure to produce LCO.

The second model is a typical business jet configuration also tested in the NASA LaRC Transonic Dynamic Tunnel. The wing has a taper ratio of 0.29 and a mid-chord sweep of  $23^\circ$ . The airfoil thickness varies from 13% at the symmetry plane to 8.5% at the wing tip. Six natural vibration modes were included in the calculations, with frequencies varying from 4.3 to 62.7 Hz. The wing is thicker than the AGARD 445.6 and the requirement for viscous modeling extends to lower Mach numbers.

At  $M = 0.888$  and at the flutter dynamic pressure of  $79 \text{ lb/ft}^2$ , Fig. 84 shows two transient responses indicating the existence of LCO. The first figure shows a wing tip initial displacement of about 7 in and the motion decays to LCO with amplitude of 5–6 in peak-to-peak. The second curve shows a growth from a small initial displacement to the LCO amplitude. This agrees with experimental observations on tests carried out at NASA LaRC. At the experimental flutter conditions for this  $M$ , the model undergoes constant amplitude wing oscillations with an amplitude of slightly less than one tip chord (6.3 in) peak-to-peak. Calculations show that the flow over the wing was intermittently separating and reattaching on the outboard upper and lower surfaces.

## 6.2. Dynamic stall

In addition to the airfoil parameters that we have discussed in previous sections, there are a number of other parameters which affect the aeroelastic response of an airfoil undergoing forced oscillations under dynamic stall conditions, such as, the nondimensional frequency of oscillation  $k$ , the magnitude of the applied torque, and the initial value of the airfoil pitch angle,  $\alpha_0$ . Bearing in mind that the airfoil response must be evaluated numerically it is clear that the effect of only a limited set of parameters can be considered.

Price and Keleris [90] considered only a one degree-of-freedom airfoil motion in pitch. Assuming a sinusoidal externally moment  $Q/mU^2 = Q_0 \sin k\tau$  is applied to the airfoil, they studied the effect of  $k$ ,  $U^*$  and  $Q_0$ , and presented results for  $\mu = 100$ ,  $r_\alpha = 0.5$ ,  $a_h = -0.5$ , and zero structural damping. The product of  $k$  and  $U^*$  gives the ratio of the forcing frequency,  $\omega$ , to the structural natural frequency in pitch,  $\omega_\alpha$ , hence, this product is also of interest. Appropriate values of  $Q_0$  should be of the same order of magnitude as the aerodynamic moment term,  $2C_M(\tau)/\pi\mu$ , and in the range of  $\mu$  and  $C_M$  they considered,  $2C_M(\tau)/\pi\mu$  lies between  $10^{-3}$  and  $10^{-5}$ , so values of  $Q_0$  were chosen to be of order  $10^{-4}$ . The results presented may conveniently be divided into two categories corresponding to what Price and Keleris [90] referred to as low and high frequencies of oscillation, and these are discussed separately in the following two sections. The examples given by Price and Keleris [90] are merely a limited subset of a more complete study carried out by Keleris [54].

### 6.2.1. High-frequency response

The results in this section are for  $U^* = 25.2$  and  $k = 0.088$ , corresponding to  $\omega/\omega_\alpha \approx 2.2$ ; hence, the forcing frequency is higher than the airfoil natural frequency. Some typical time histories of  $\alpha$  for four different  $Q_0$  are presented in Fig. 85, and the corresponding phase-plane plots are shown



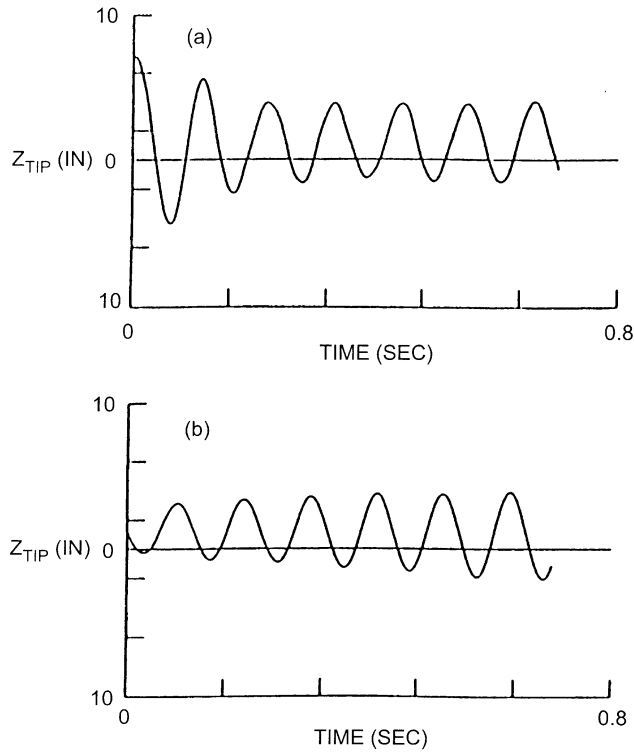


Fig. 84. Calculated limit cycle response for a business jet wing flutter model:  $M = 0.888$ ,  $Q = 79$  psf.,  $Re_c = 1.14 \times 10^6$  (from Ref. [26]).

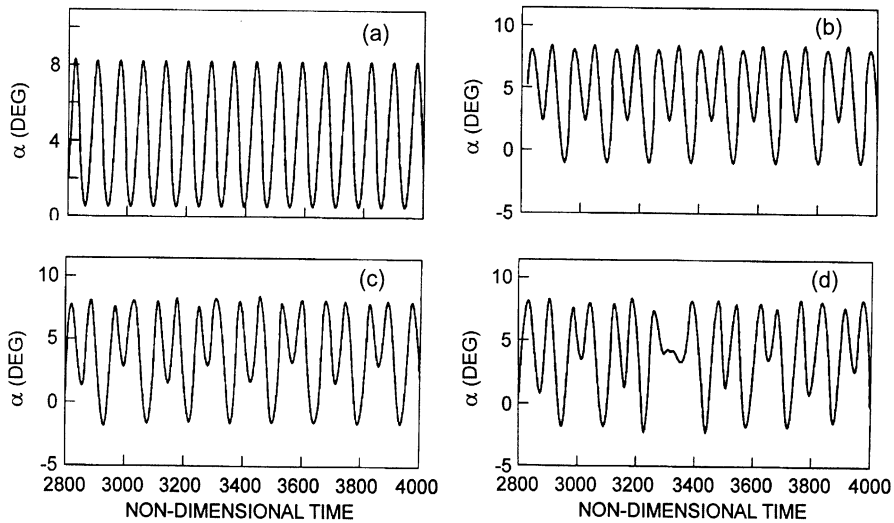


Fig. 85. Time histories of the airfoil response;  $\alpha_0 = 9.76^\circ$ ,  $U^* = 25.20$  and  $k = 0.088$ . (a)  $Q_0 = 0.550 \times 10^{-4}$ , (b)  $Q_0 = 0.640 \times 10^{-4}$ , (c)  $Q_0 = 0.675 \times 10^{-4}$ , (d)  $Q_0 = 0.73 \times 10^{-4}$  (from Ref. [90]).

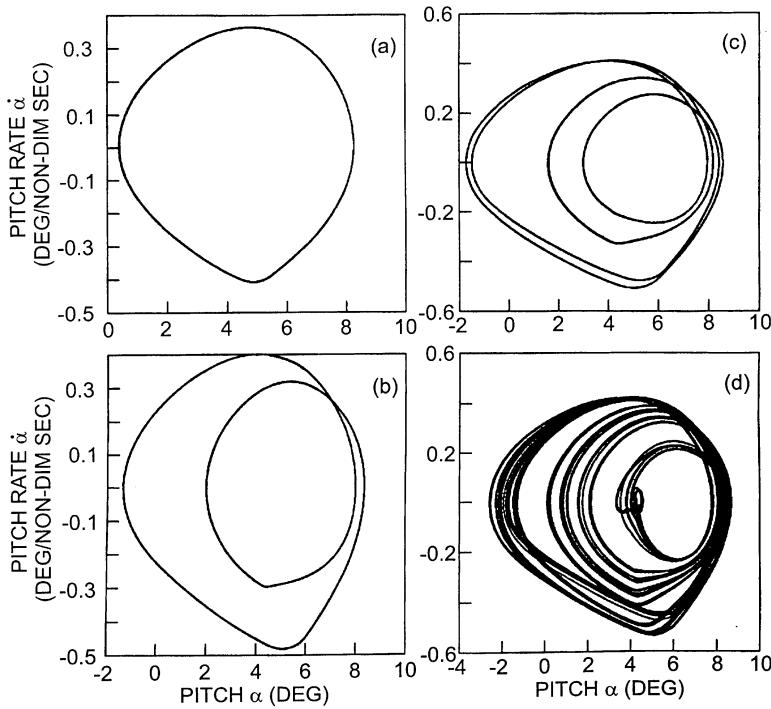


Fig. 86. Phase plane sections of the airfoil response;  $\alpha_0 = 9.76^\circ$ ,  $U^* = 25.20$  and  $k = 0.088$ . (a)  $Q_0 = 0.550 \times 10^{-4}$ , (b)  $Q_0 = 0.640 \times 10^{-4}$ , (c)  $Q_0 = 0.675 \times 10^{-4}$ , (d)  $Q_0 = 0.73 \times 10^{-4}$  (from Ref. [90]).

in Fig. 86. Fig. 85a shows a periodic limit cycle, with frequency corresponding to the forcing frequency of the applied torque  $Q_0$ ; this period-one motion is represented via a single curve in the phase plane plot of Fig. 86a. Upon increasing  $Q_0$  a period-two response is obtained, as shown in Figs 85b and 86b, and a further increase in  $Q_0$  yields the period-four response shown in Figs 85c and 86c. However, yet a further increase in  $Q_0$  yields what appears to be a non-periodic response for  $\alpha$  (see Figs. 85d and 86d).

This type of behavior is illustrated in Fig. 87 for a wide range of  $Q_0$  where a bifurcation diagram of  $\alpha$  versus  $Q_0$  is presented. The bifurcation diagram shows, for each value of  $Q_0$  the local value of  $\alpha$  when  $\alpha' = 0$ ; hence, for a period-one response, two points appear on the bifurcation diagram, corresponding to the minimum and maximum  $\alpha$ . For the period-two motion, the bifurcation diagram contains four points, while for  $Q_0 = 0.73 \times 10^{-4}$ , the bifurcation diagram contains an extremely large number of points, suggesting that the airfoil motion may possibly be chaotic.

The bifurcation diagram shows that the amplitude of  $\alpha$  generally increases as  $Q_0$  is increased, and at  $Q_0 \approx 5.75 \times 10^{-5}$  the response undergoes a period doubling bifurcation. The response undergoes another period doubling bifurcation at  $Q_0 \approx 6.5 \times 10^{-5}$ , and after this bifurcation the system quickly becomes unstable. It eventually restabilizes into a period-two oscillation at  $Q_0 \approx 9.2 \times 10^{-5}$ . The period-doubling was confirmed via a Fourier analysis of the time traces.

Although the results presented above are indicative of a chaotic response, because of the nonanalytic nature of the system it is not possible to prove that the response is chaotic using

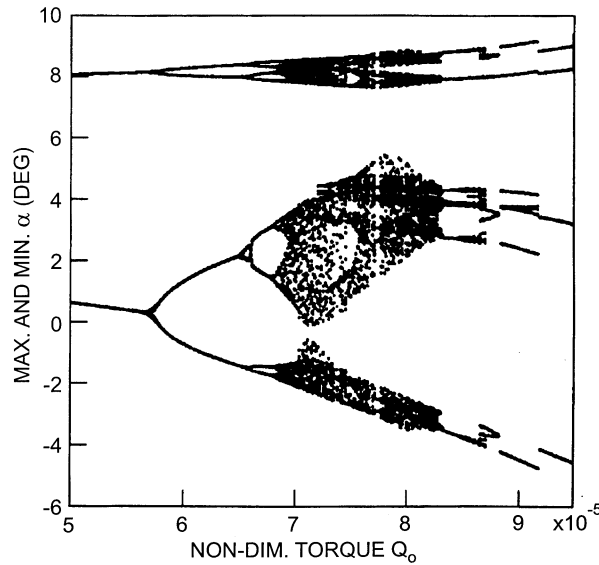


Fig. 87. Bifurcation diagram of the airfoil pitch motion;  $\alpha_0 = 9.76^\circ$ ,  $U^* = 25.20$ ,  $k = 0.088$  (from Ref. [90]).

standard tools, such as calculating the Lyapunov exponents. Furthermore, it is difficult to make any conclusions concerning the route to chaos. However, the bifurcation diagram shown in Fig. 87 suggests very strongly that the route to chaos is via a period doubling cascade. Further evidence for this can be gained from an examination of the Poincaré sections for values of  $Q_0$  close to the apparent boundary between chaotic and periodic motion. In Fig. 88a, the Poincaré section for  $Q_0 = 6.90 \times 10^{-5}$  (near the onset of chaos) is shown. The general shape of the attractor, consisting of four short lines, indicates that the response follows a marginally unstable period-four attractor. If the period-four attractor were stable, then the Poincaré section should consist of four distinct points, and indeed, this is what was obtained with  $Q_0 = 6.75 \times 10^{-5}$ , but the results are not shown here. However, in Poincaré section for a slightly higher value of  $Q_0$ , shown in Fig. 88b, the four part structure of the attractor, evident in Fig. 88a, has evolved into a two part attractor. The two pairs of curves of the previous attractor have grown to overlap each other so that only two independent curves can be distinguished. Although it may appear that these curves are one-dimensional, if a small part of the attractor is enlarged then it is evident that there is considerable internal structure to the attractor, as shown in Fig. 88c. The continued evolution, as  $Q_0$  is increased, of the original four part attractor into a chaotic attractor can be seen from Fig. 88d, where although four distinct regions of the attractor are apparent the attractor is typical of that obtained with a chaotic system.

#### 6.2.2. Low-frequency response

All the results in this section are for  $\alpha_0 = 8.9^\circ$ ,  $U^* = 21.0227$  and  $k = 0.044$ ; this corresponds to a frequency ratio  $\omega/\omega_\alpha = 0.925$ , hence, the forcing frequency is much closer to the natural frequency  $\omega_\alpha$  than for the results presented previously. A bifurcation diagram of  $\alpha$  as a function of  $Q_0$  shown in Fig. 89. Fig. 89a shows that the system undergoes two period doubling bifurcations, the first at

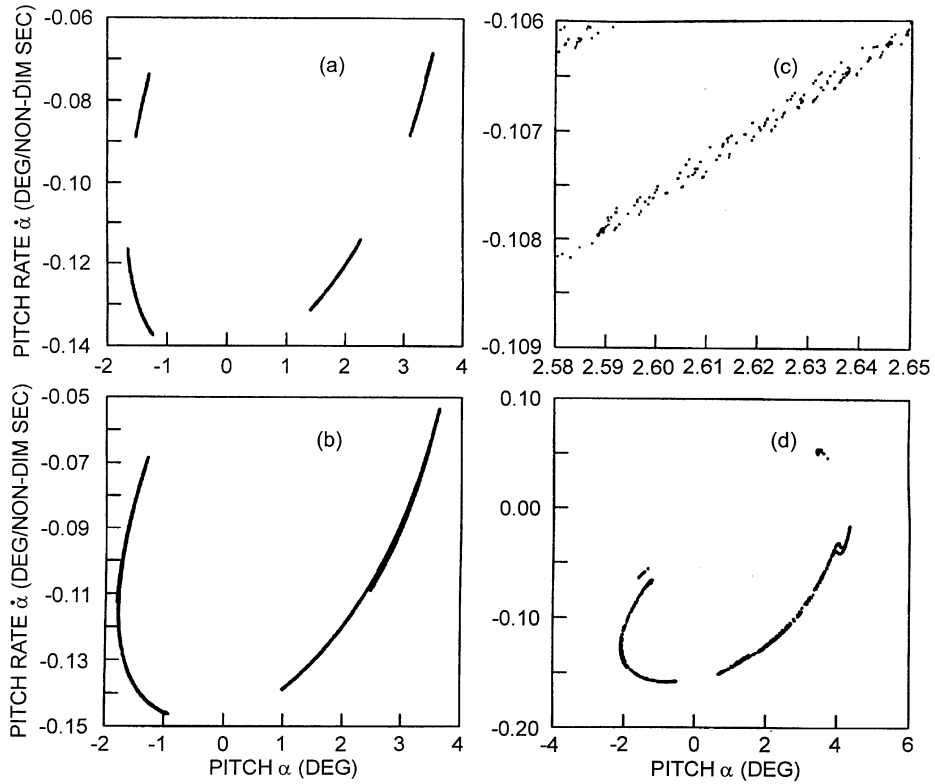


Fig. 88. Poincaré sections of the airfoil response;  $\alpha_0 = 9.76^\circ$ ,  $U^* = 25.20$ , and  $k = 0.088$ . (a)  $Q_0 = 0.690 \times 10^{-4}$ , (b)  $Q_0 = 0.700 \times 10^{-4}$ , (c) an enlarged view of the micro-structure for the attractor in (b), (d)  $Q_0 = 0.730 \times 10^{-4}$  (from Ref. [90]).

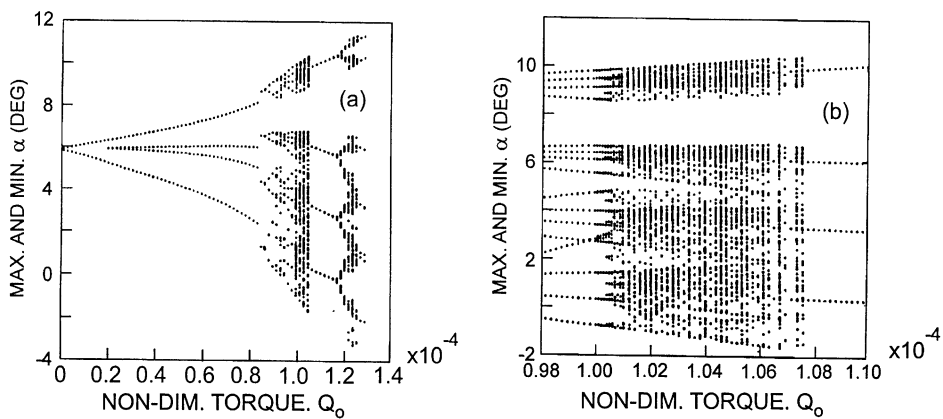


Fig. 89. (a) Bifurcation diagram for the airfoil response for  $0.1 \times 10^{-5} < Q_0 < 1.18 \times 10^{-4}$ , (b) expanded view of (a) for  $0.98 \times 10^{-4} < Q_0 < 1.10 \times 10^{-4}$ .  $\alpha_0 = 8.9^\circ$ ,  $U^* = 21.0227$ ,  $k = 0.044$  (from Ref. [90]).

$Q_o \approx 0.20 \times 10^{-4}$  and the second at  $Q_o \approx 0.88 \times 10^{-4}$ . Furthermore, a region of possibly chaotic motion can be seen to exist in the approximate range  $1.00 \times 10^{-4} < Q_o < 1.09 \times 10^{-4}$ .

The more detailed bifurcation diagram of Fig. 89b shows that as  $Q_o$  increases above  $0.98 \times 10^{-4}$  the well-defined lines, characteristic of periodic motion, begin to spread out or diffuse into one another. Furthermore, at  $Q_o \approx 1.003 \times 10^{-4}$  and  $1.0062 \times 10^{-4}$ , the system appears to undergo complicated bifurcations. This bifurcation diagram suggests that the system is possibly chaotic or quasi-periodic for approximately  $Q_o \geq 1.0062 \times 10^{-4}$ , and that the transition from periodic to chaotic or quasi-periodic behaviour is a gradual decrease in the stability of the periodic oscillations. After  $Q_o$  exceeds approximately  $1.079 \times 10^{-4}$ , the response returns to a stable period-two oscillation. Within the apparently chaotic region there are smaller regions where the response is periodic, for example near  $Q_o = 1.058 \times 10^{-4}$  and  $1.065 \times 10^{-4}$ .

To further assess the possibility of chaos, Fourier spectra, phase plane plots and Poincaré sections were constructed at a number of values of  $Q_o$ . Three typical Poincaré sections are shown in Fig. 90. The Poincaré section for  $Q_o = 1.00 \times 10^{-4}$ , Fig. 90a, has four groups of points indicating that the response is a period-four oscillation. However, since the groups are not exact points, this period-four oscillation is not perfectly stable. The Poincaré section for  $Q_o = 1.006 \times 10^{-4}$ , Fig. 90b shows that the four groups of points have diffused into fine lines, and an attractor is beginning to emerge. The structure of this attractor is clearly visible in the Poincaré section for  $Q_o = 1.02 \times 10^{-4}$  (Fig. 90c). This attractor is not as one-dimensional as Fig. 90c suggests, and an enlarged view of

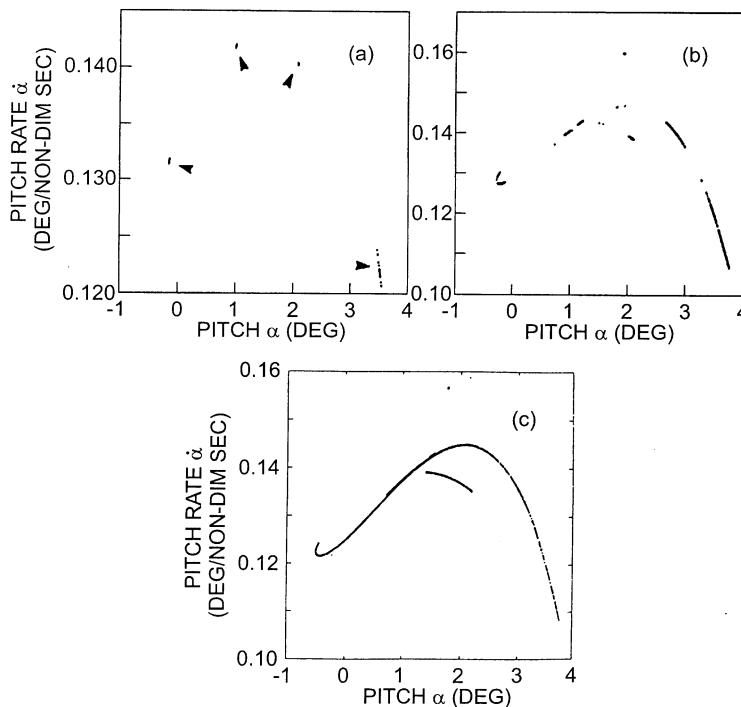


Fig. 90. Poincaré sections of the airfoil response,  $\alpha_0 = 8.9^\circ$ ,  $U^* = 21.0227$ , and  $k = 0.044$ : (a)  $Q_o = 1.000 \times 10^{-4}$ , (b)  $Q_o = 1.006 \times 10^{-4}$ , (c)  $Q_o = 1.020 \times 10^{-4}$  (from Ref. [90]).

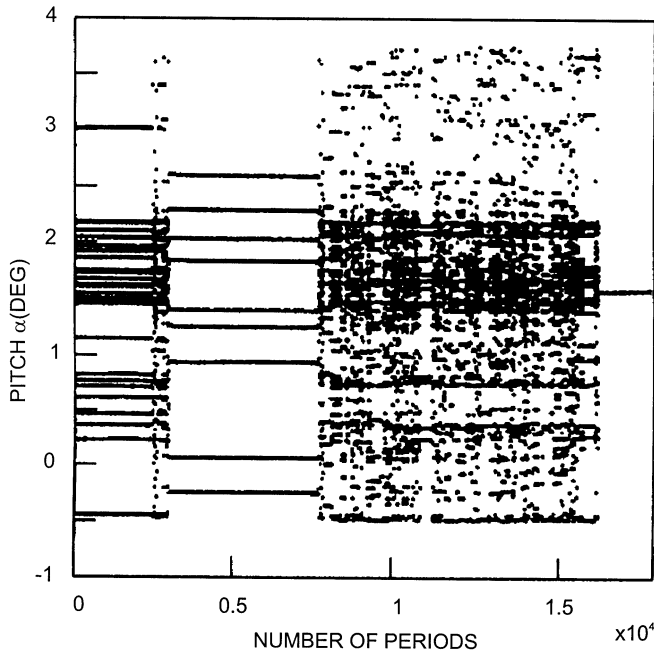


Fig. 91. Long-term behavior of the airfoil response,  $\alpha_0 = 8.9^\circ$ ,  $U^* = 21.0227$ ,  $k = 0.044$  and  $Q_0 = 1.020 \times 10^{-4}$  (from Ref. [90]).

certain regions indicates that the attractor varies in thickness with definite boundaries defining its shape.

To better appreciate the behavior illustrated in Fig. 90c the long-term response of the system for  $Q_0 = 1.02 \times 10^{-4}$  is presented in Fig. 91. Here, discrete values of  $\alpha$  at  $\alpha' = 0$  are plotted for each period of oscillation of  $Q_0$  during which they exist. Thus, a stable period-one type oscillation would appear as horizontal line, and a period-two motion as two horizontal lines, etc. However, the long-term behaviour of the system shown in Fig. 91 is much more complicated than this. Initially the response is a high-order periodic oscillation, and it remains in this state for approximately its first 2500 periods, then the response goes through approximately 500 periods where it is either quasi-periodic or chaotic, followed by a return to a periodic oscillation that remains stable for approximately the next 5000 periods. This periodic response then suddenly becomes unstable and the response undergoes frequent transitions from high-order periodic phases to quasi-periodic or chaotic phases. These high-order periodic phases appear in a seemingly random fashion and can remain stable for up to several hundred periods. On the other hand, the quasi-periodic or chaotic phases are usually very short, on average lasting only about ten periods before the response restabilizes into a new and different periodic phase. After approximately 8000 periods of this unstable response, the total number of elapsed periods being of order 17 000, the system stabilizes into a period-one oscillation lasting for approximately 400 periods. This then becomes unstable (not shown in this figure) and the more complicated behaviour returns.

The behavior illustrated in Fig. 91, particularly the time scale of the chaotic behaviour and the marginal stability of the response, suggests, at least superficially, that the response is intermittently

chaotic [13]. However, to give a more definitive assessment of this, and to see if the present system shares any characteristics with classical types I, II or III intermittency the Poincaré data is examined in more detail in the form of first and second return maps.

Type I intermittency involves the destabilization of a periodic trajectory. Its main characteristic is that a laminarization channel exists in the first return map, the response enters this channel and with successive iterations moves through it. While the response is in the channel it is reasonably stable, and therefore the behavior appears periodic. The length of time required for the response to move through the channel depends on the width of the channel, however, Bergé et al. [13] indicate that there will be some very short laminar phases and that there is a definite maximum laminar phase length which is system dependant. After the system leaves the channel it moves to another part of the phase plane where the attractor is chaotic, giving a chaotic outburst in the response. The system remains in the chaotic region of the phase plane until it is mapped back to the beginning of the channel.

To the authors' knowledge no examples of type II intermittency, either numerical or experimental, have been observed and so this type of intermittency will not be considered here.

Type III intermittency also has a laminarization channel, but in this case it is found in the second return map, and it is due to the first return map crossing the identity line at a slope slightly less than  $-1$ . While the system is in this channel the response is periodic, as in type I intermittency. An important characteristic of this type of intermittency is that the approach of the chaotic outburst is signalled by the growth of a subharmonic oscillation which increases in amplitude. The characteristic probability distribution of the average length of time for the laminar phase suggests that there is a definite minimum length for the laminar phases and that some laminar phases can last for a very long time.

The first and second return maps for the present system with  $Q_0 = 1.02 \times 10^{-4}$  are shown in Fig. 92. Unfortunately, these return maps do not appear to show any of the characteristics described previously for classical types I or III intermittency. Furthermore, the long-term behavior of the system, as shown in Fig. 91, is not typical of these types of intermittency. Firstly, the long-term response shows regions of both very long and very short periodic phases, suggesting a combination of types I and III intermittency, and secondly, after each chaotic burst the system does not return to the same periodic oscillation but instead tends to a new periodic state.

However, if the first return map of Fig. 92a is examined in more detail, as shown in Fig. 93, then some indication of the type of intermittency can be obtained. The internal structure of the attractor, shown in Fig. 93, consists of short lines or small groups of points; different combinations of these points corresponding to different periodic solutions. The quantized structure of the attractor implies a periodic response because it consists of a finite number of groups of points, but, since these groups of points have a two-dimensional structure the periodic responses are unstable. An example of the implications of the internal structure of the attractor can be seen from the following. According to Fig. 91, after approximately 16 500 periods the system begins a marginally stable period-one oscillation that persists for approximately 4000 periods. In order for a marginally stable period one oscillation to exist the attractor of the first return map must intersect the identity line at a slope slightly greater than  $-1$  or slightly less than  $+1$ , otherwise successive iterations of the map will quickly move away from the intersection point and the period-one oscillation will be unstable. The orientation of the attractor for the first return map, shown in Fig. 92a, suggests that the slope of the attractor at the intersection point is significantly less than  $-1$ , therefore, no stable

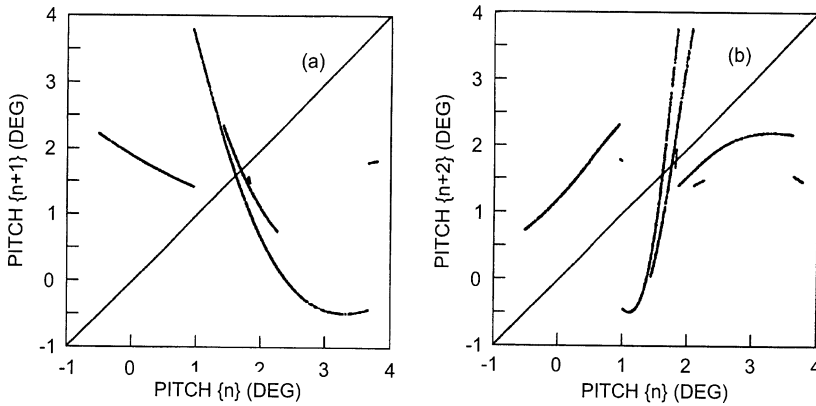


Fig. 92. (a) The first return map and (b) the second return map of the Poincaré data;  $Q_0 = 1.020 \times 10^{-4}$ ,  $\alpha_0 = 8.90^\circ$ ,  $U^* = 21.0227$  and  $k = 0.044$  (from Ref. [90]).

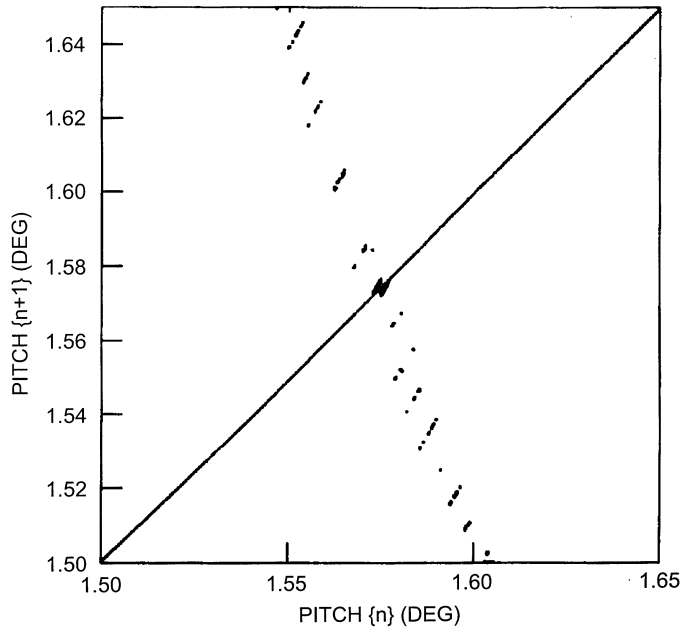


Fig. 93. The micro-structure of the first return map of the Poincaré data;  $Q_0 = 1.020 \times 10^{-4}$ ,  $\alpha_0 = 8.90^\circ$ ,  $U^* = 21.0227$  and  $k = 0.044$  (from Ref. [90]).

period-one oscillation should exist. However, as seen in Fig. 93, the microscopic structure of the attractor makes it possible for two of the internal structures of the attractor to intersect the identity line at slopes that result in a marginally stable period-two oscillation. The two internal structures are so close to the identity line that, on the normal scale of the Poincaré map, this marginally stable period-two oscillation appears as a period-one oscillation. Hence, by examining the Poincaré data



at the microscopic level, it is clear that the internal structure of the attractor plays an important role in the marginal stability of this type of chaotic response. However, how this particular internal structure develops is still unclear.

Lee and LeBlanc [63] also used the same approach to study forced oscillation of a 2-DOF airfoil with attached and separated flows. Only small plunge amplitudes were considered and a linear theory was used to predict the aerodynamic loads due to plunge motion.

The equations of motion are the same as those given by Eqs. (10) and (11). In addition to  $C_M$ , an empirical expression for the normal force coefficient  $C_N$  at dynamic stall was also obtained. Both the moment and normal force of the two degree-of-freedom system consist of two terms: one from the nonlinear pitch motion using Bielawa et al.'s [15] time synthesization technique and a linear term using indicial lift and moment functions given by Mazelsky and Drischler [78]. This is a very crude approximation since in a linear analysis where the airfoil motion is considered small, the superposition of  $C_M$  and  $C_N$  for pitch and plunge motions derived separately is permissible in determining the total moment and force coefficients. However, when the aerodynamic loads are nonlinear functions of the displacements, these coefficients have to be determined for combined motions in the two degrees of freedom. The approach used by Lee and LeBlanc [63] in modifying the Bielawa et al. [15] expressions for  $C_M$  and  $C_N$  should be treated as an approximation to an otherwise extremely complex flow phenomenon.

Lee and LeBlanc [63] used the same airfoil parameters as those investigated by Price and Keleris [90]. Different values of  $\bar{\omega}$ ,  $\omega_\alpha$ , and forcing frequency  $\omega$  were considered. The viscous damping for the plunge and pitch motion was set to zero. In the limit when  $\bar{\omega}$  is infinite, the motion degenerates to that for a 1-DOF system. For forced oscillation in the pitch DOF, the reduced frequency was kept constant and  $\omega/\omega_\alpha$  was varied. This implies that  $U^*$  has to be adjusted accordingly so that  $k$  is constant. In one example given by Lee and LeBlanc [63], response curves were computed for different forcing  $Q_0$  ranging from  $1 \times 10^{-4}$  to  $25 \times 10^{-4}$  for the NACA 0012 airfoil at  $\alpha_0 = 7.48^\circ$ ,  $k = 0.165$  and  $M = 0.6$ . In the regions where transition from attached to separated flow occurs, there are breaks in the response curves. The flow is highly unsteady and the time series do not reach constant amplitudes after a large number of cycles of oscillation. This is due to the modeling in the aerodynamics where the variations of the attached and separated flow aerodynamic coefficients with displacements have discontinuities in slopes. It was found in this particular example that for the larger values of  $\omega/\omega_\alpha$  ( $> 2$ ) and  $Q_0$  ( $> 8 \times 10^{-4}$ ) investigated, the time series do not reach a steady state and the motion is likely chaotic.

Lee and LeBlanc [63] also studied the response by holding  $Q_0$  constant and varied the driving frequency for different values of  $\omega_\alpha$ . The curves show the same characteristics as those for constant  $k$  and varying  $\omega/\omega_\alpha$ . For the NACA 0012 airfoil at  $\alpha_0 = 7.48^\circ$ , the response curves for a 2 DOF system with small plunge motions are similar to those for a 1DOF system. Typical response curves are shown in Fig. 94. For small values of  $\omega/\omega_\alpha$  the flow is attached and transition to separated flow occurs at  $\omega/\omega_\alpha \approx 1$ . As  $\omega/\omega_\alpha$  increases to values greater than 1.6, the flow becomes attached again. For the largest value of  $\bar{\omega} = 10$ , a steady condition is reached after approximately 20 cycles of oscillation. Decreasing  $\bar{\omega}$  results in failure to achieve a steady state condition for  $\omega/\omega_\alpha > 1.6$  even for a very large number of cycles. The flow remains attached but the amplitudes of pitch and plunge motions are scattered within the shaded regions shown by curves 2 and 3. The motion is probably chaotic, but Lee and LeBlanc [63] did not pursue this subject any further. They concluded for the

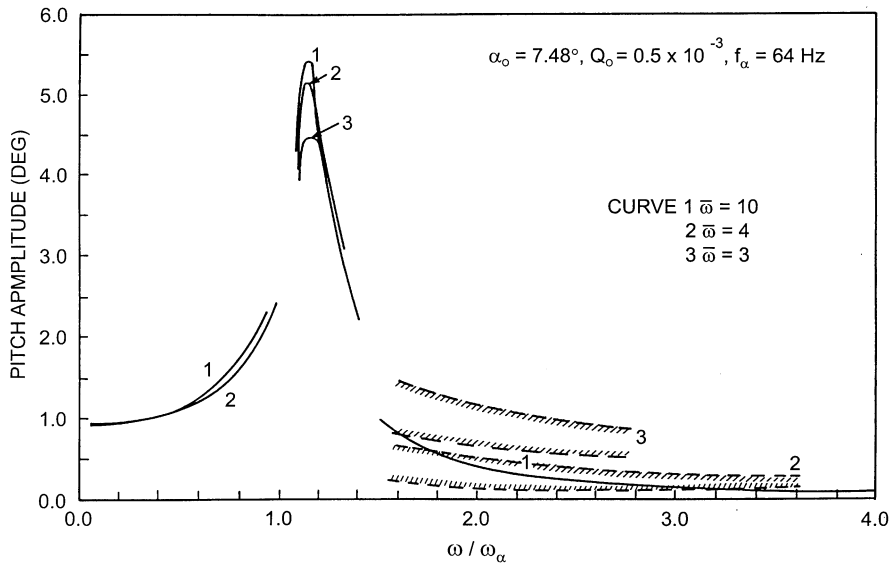


Fig. 94. Variation of the pitch amplitude with  $\omega/\omega_\alpha$  for an airfoil oscillating in pitch and plunge.  $\alpha_0 = 7.48^\circ$ ,  $f_\alpha = 64$  Hz and  $Q_0 = 0.5 \times 10^{-3}$  (from Ref. [63]).

airfoil parameters and type of motion they studied, a small plunge motion increases the pitch amplitude slightly for attached flow, while the opposite is true for separated flow.

In a recent paper, Li and Fleeter [74] investigated periodic and chaotic motions of an airfoil experiencing dynamic stall using a semi-empirical dynamic stall model by Gormont [37]. This relatively simple model captures the nonlinear behavior generated by the dynamic stall and is used to investigate bifurcations and routes to chaos.

A 2D airfoil was used and the dynamic equations are expressed in a set of nondimensional first-order differential equations (a four dimensional autonomous system in state space) and integrated numerically using a fourth-order Runge–Kutta scheme. The airfoil parameters are:  $\mu = 60$ ,  $r_\alpha = 0.69$ ,  $\bar{\omega} = 1.26$ ,  $a_h = -0.5$ ,  $x_\alpha = 0.5$ , and airfoil thickness-to-chord ratio = 12%. The static stall angle  $\alpha_s$  was  $9^\circ$ . The initial displacement  $\alpha(0)$  was  $12^\circ$  and they defined a nondimensional velocity  $\bar{U} = U^* \sqrt{\mu}/2$ .

Fig. 95 shows a bifurcation diagram of  $\alpha/\alpha_s$  versus  $\bar{U}$ . The torsion response amplitude is taken at which the phase plane trajectories cross the zero velocity axis as a function of the nondimensional air speed. Transients have decayed prior to the construction of this bifurcation diagram. A subcritical Hopf-bifurcation occurs at  $\bar{U} = 0.3038$ , and the airfoil motion is periodic between  $\bar{U} = 0.3038$  and  $0.3452$ . The motion becomes unstable when  $\bar{U}$  is further increased and bifurcates into a quasi-periodic oscillation. This does not lead to chaos, but instead a reverse secondary Hopf-bifurcation changes the motion back to periodic again. Beyond  $\bar{U} = 0.4607$ , another secondary Hopf-bifurcation occurs and further increase in velocity results in chaotic response. For the airfoil parameters investigated by Li and Fleeter [74], only the quasi-periodic route to chaos was observed. They also presented some other results for a different  $\mu = 80$  at the same  $\bar{\omega} = 1.26$  and for  $\mu = 60$  at  $\bar{\omega} = 1.6$ . The value of velocity where chaos occurs changes with  $\bar{\omega}$  for the same  $\mu$  and

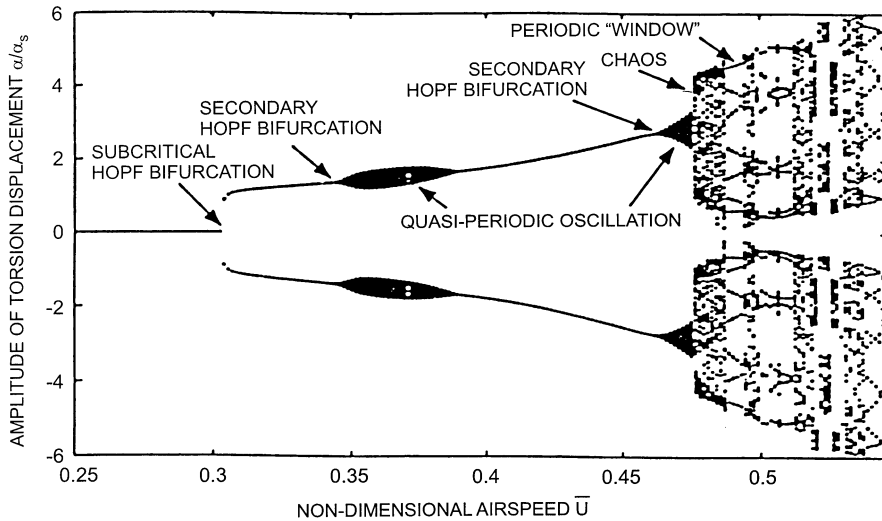


Fig. 95. Bifurcation diagram: amplitude of torsion displacement vs. airspeed  $\bar{U}$  ( $\mu = 60$ ,  $\bar{\omega} = 1.26$ ) (from Ref. [74]).

there is only one secondary Hopf-bifurcation to chaos. Increasing  $\mu$  but keeping  $\bar{\omega}$  fixed at 1.26, there is little change in  $\bar{U}$  at the onset of chaos, and the bifurcation diagram look very similar.

The route to chaos is different from that reported by Price and Keleris [90] since frequency doubling and intermittency were not observed by Li and Fleeter [74], but it should be remembered that Li and Fleeter [74] considered an unforced two degree-of-freedom system. Also, the empirical aerodynamics is different and it is not certain whether Bielawa et al. [15] formulation of  $C_N$  and  $C_M$  will make any difference to Li and Fleeter's [74] results.

## 7. Gust effects: airfoils in longitudinal atmospheric turbulence

One idealization made in the previous sections is that the airfoil is assumed to be free of any sources of perturbation, which in reality are always present. This raises, from both a practical and theoretical point of view, the question of the presence of random noise introduced via atmospheric turbulence. The problem of stochastic fluctuations has recently been reviewed in light of the understanding of chaotic behavior and related nonlinear dynamics. It has been shown that random noise can produce bifurcation phenomena and organized behavior which have no analog in their deterministic counterparts. These phenomena have been designated as “noise-induced transitions [45]”. They are a product of the interplay between stochastic fluctuations and nonlinear dynamics.

Atmospheric turbulence models can generally be categorized within two different approaches [6]. The methods associated with a discrete gust representation are usually of a deterministic nature. On the other hand, continuous turbulence methods allow a stochastic perspective. In this review, the interest lies in the effect of nonlinearities from a dynamics perspective; thus, a continuous stochastic approach is required. A deterministic gust model was used to study nonlinear

helicopter blade response, and the interested reader can refer to the work of Tang and Dowell [105].

In two-dimensional flow atmospheric turbulence is composed of vertical and longitudinal components. The vertical component acts as an external forcing function and does not alter fundamentally the low-dimensional dynamics of the otherwise deterministic airfoil response. On the contrary, the longitudinal turbulent field excitation, also known as head-on turbulence, is parametric as it acts on the airspeed. It is in this context that the stochastic system behavior departs from its deterministic counterpart and induces new bifurcation phenomena. Only the effect of longitudinal atmospheric turbulence is considered here.

In this review, the highlights of Poirel and Price [85] investigations are summarized. The spectral content of turbulence can be provided by either the von Karman or Dryden models, which are presently the two most widely accepted models. The Dryden model was used by Poirel and Price [85] since it is easier to handle mathematically. The one-sided PSD Dryden longitudinal gust representation is given as [44]

$$\Phi_g(\omega) = \sigma_g^2 2(L/\pi U_m)/(1 + (L\omega/U_m)^2), \quad (177)$$

and is presented in non-dimensional form in Fig. 96 for the particular scales of turbulence Poirel and Price [85] considered.  $\sigma_g^2$  in the above equation is the gust velocity variance. It can be shown that the scale of turbulence,  $L$ , divided by the mean free-stream velocity,  $U_m$ , is equal to the correlation time of the random excitation.

Only attached flow conditions with small amplitude oscillations are considered, hence, the aerodynamics is linear. The unsteady aerodynamics is modeled, assuming incompressible inviscid flow, via Duhamel's integral and the two-state representation of Wagner's function. This is usually referred to as arbitrary-motion theory. Classically, it considers motion in the structural degrees of freedom only, where the downwash at the three-quarter chord position represents the effective downwash on the airfoil [31].

Here, arbitrary-motion theory is extended to the case of a random time-varying airspeed based on the work of van der Wall and Leishman [114]. They show that arbitrary-motion theory compares very well with Isaacs' [48] theory for the case of periodic fore-aft movements of an airfoil, along with pitch and heave oscillations. In fact, the only difference appears to be attributable to the limited number of states used in the approximate representation of Wagner's function. Note that Isaacs [48] considered only periodic fore-aft and pitch oscillations. His theory was generalized by van der Wall [113] to include heave motion as well and can be considered exact for the preceding fluid assumptions.

It is important to note that fore-aft movement of an airfoil in a uniform stream is not physically the same as fluctuations of the free-stream velocity. In the first case the airflow is uniform along the chord, whereas a chordwise velocity gradient exists for a varying freestream velocity. This difference affects both the non-circulatory force and moment, as well as the bound vorticity of the circulatory terms. However, the free vortex sheet in the airfoil wake is the same in both cases. van der Wall and Leishman [114] showed that fore-aft movement aerodynamics is an approximation of the unsteady free-stream problem, which is valid only for small frequencies. The chordwise uniformity of the airflow assumption is considered here and is extended to the case of random fluctuations. This is supported by the atmospheric turbulence velocity spectrum being concentrated in the low frequency range. It is thus assumed that the aerodynamic forces induced by

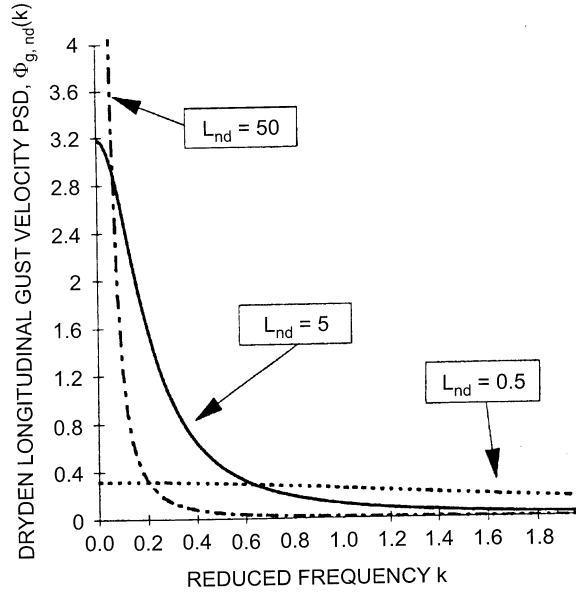


Fig. 96. Non-dimensional PSD of the Dryden longitudinal gust for different scales of turbulence; closed-form solution for  $\sigma_{g,nd}^2 = 1.0$  (from Ref. [85]).

random variations of the free-stream velocity, and accounting for arbitrary pitch and heave motions, can be accurately modelled by the following:

$$-L(t) = -\pi\rho b^2[\ddot{h} + \dot{U}\alpha + U\dot{\alpha} - ba_h\ddot{\alpha}] - 2\pi\rho bU\left[\Xi_{3/4}(t)\phi(0) - \int_0^t \Xi_{3/4}(s)\frac{d\phi(t-s)}{ds}ds\right], \quad (178)$$

and

$$M_{ea}(t) = \pi\rho b^2[ba_h\ddot{h} - b(1/2 - a_h)U\dot{\alpha} - b(1/2 - a_h)\dot{U}\alpha - b^2(a_h^2 + 1/8)\ddot{\alpha}] + 2\pi\rho b^2(a_h + 1/2)U\left[\Xi_{3/4}(t)\phi(0) - \int_0^t \Xi_{3/4}(s)\frac{d\phi(t-s)}{ds}ds\right], \quad (179)$$

where  $\Xi_{3/4}(t) = \dot{h} + U\alpha + b(1/2 - a_h)\dot{\alpha}$ . The dots denote differentiation with respect to  $t$ .

The first terms in the lift and moment expressions represent the noncirculatory forces, associated with fluid inertia. The circulatory forces, given by the second terms, model the effect of the bound vorticity and the shed wake, convecting downstream at velocity  $U(t) = U_m + u_g(t)$ .

In order to obtain a numerical solution via Runge–Kutta integration the equations of motion must be expressed in state space form, giving a seventh order system. Four states represent the structural degrees-of-freedom. Two of the other states are associated with the lag terms of the aerodynamics, which appear after reformulation of the integral in the circulatory force. This leads

to an additional second order ordinary differential equation, given by

$$\int_0^t \Xi_{3/4}(s) \frac{d\phi(t-s)}{ds} ds = -[\varepsilon_1 \varepsilon_2 / 2](U_m/b)^2 Z(t) - [\psi_1 \varepsilon_1 + \psi_2 \varepsilon_2](U_m/b) \dot{Z}(t), \quad (180)$$

where  $\ddot{Z}(t) + (\varepsilon_1 + \varepsilon_2)(U_m/b)\dot{Z}(t) + \varepsilon_1 \varepsilon_2 (U_m/b)^2 Z(t) = \Xi_{3/4}(t)$ .

The final state of the seventh-order system models the Dryden longitudinal gust, in the time domain, it is transformed as

$$\dot{u}_g(t) = -u_g(t)U_m/L + \sigma_g(2U_m/\pi L \Phi_{wn})^{1/2} G_{wn}(t), \quad (181)$$

where  $G_{wn}$  is Gaussian white noise, whose intensity is defined by a single-sided PSD of magnitude one, i.e.,  $\Phi_{wn} = 1$ . The Gaussian white noise is generated at each time step of the integration as discussed by Poirel and Price [85].

Poirel and Price [85] generated results using a fourth-order Runge–Kutta numerical scheme. Bearing in mind the stochastic nature of the process, they paid special attention to the size of the time step and number of iterations. The factors that determine the magnitude of the time step are numerical stability and noise correlation time,  $L/U_m$ . Accordingly, the time step is taken as the smallest of either 1/128 of the lowest uncoupled natural frequency of the airfoil or 1/5 of the noise correlation time. A very large number of iterations is necessary to ensure a smooth probability density distribution, PDD. This is particularly important when examining the dynamics of the system. For the work presented here  $4 \times 10^6$  to  $8 \times 10^6$  iterations were used.

Before presenting results showing the effect of longitudinal atmospheric turbulence on the flutter and post-flutter response, the dynamics of the deterministic (non-excited) airfoil will be discussed. The cases presented are for an airfoil with the following nondimensional parameters:  $\bar{\omega} = 0.6325$ ,  $x_\alpha = 0.25$ ,  $r_\alpha = 0.5$ ,  $\mu = 100$  and  $a_h = -0.5$ , the nonlinearity considered is a cubic restoring moment in pitch with  $\beta_1 = \beta_2 = 0.0$  and  $\beta_3 = 400$  (see Eq. (31)).

For comparison purposes, bifurcation diagrams of the airfoil response as the airspeed is increased, for both the nonexcited and excited cases, are presented in Fig. 97. At this point, however, only the nonexcited case will be discussed. The vertical axis shows both the traditional amplitude of oscillation and the variance of the airfoil pitch motion. At low air speeds the bifurcation diagram indicates a stable equilibrium point, which becomes unstable for air speeds  $U_m^* \geq 4.31$ . Here  $U_m^* = U_m/b\omega_\alpha$  is defined in Eq. (12). The point  $U_L^* = 4.31$  is the nondimensional flutter speed and corresponds to a supercritical Hopf-bifurcation (at higher airspeeds the equilibrium position is unstable, but a stable limit cycle oscillation, LCO, exists). The flutter speed and Hopf-bifurcation point are uniquely determined by either the amplitude of the pitch oscillation or its variance. In general terms, a bifurcation is defined as being where there is a qualitative change in the topological structure of the dynamic behavior [2]. In a deterministic system this definition corresponds exactly to the point where one of the Lyapunov exponents vanishes, and thus, it is associated with a critical slowdown of the dynamics. In this case, linearization of the system about the fixed point gives a complex conjugate pair of eigenvalues, whose real parts go to zero at the flutter speed. Although not presented here it was found that in the vicinity of the bifurcation point the reduced frequency of the LCO is approximately 0.18.

Since the main objective of this section is to examine the stochastic (randomly excited) case, it is relevant to describe the dynamics of the deterministic system in terms of a probability density

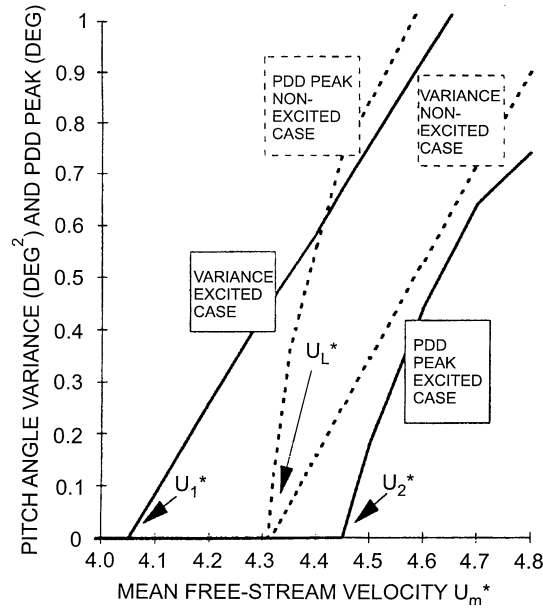


Fig. 97. Bifurcation diagram of the airfoil response for the excited and non-excited cases;  $\sigma_{g,nd}^2 = 1.0$ ,  $L_{nd} = 5.0$  (from Ref. [85]).

distribution (PDD) which is presented in Fig. 98. Note that the vertical axis shows the probability density multiplied by the variance of the response. This representation shows two qualitatively different regions of dynamical behavior; before and after the Hopf-bifurcation. Prior to the Hopf-bifurcation the response is characterized by a flat distribution, which indicates zero variance or no dynamics (for a pure PDD plot there would be a Dirac delta function centred at zero pitch angle). The LCO response after the Hopf-bifurcation is characterized by a “crater-like” shape, the peaks of which correspond to the most probable value that the pitch angle will take, and thus, to the amplitude of oscillation. Hence, as demonstrated in Fig. 98, the variance and location of the peaks of the PDD are two significant measures of the system dynamics.

The PDD multiplied by the variance of the stochastic pitch response as a function of mean free-stream velocity is presented in Fig. 99 (this is the equivalent of Fig. 98 but for the “excited case”); in these results the nondimensional gust variance is  $\sigma_{g,nd}^2 = \sigma_g^2 / (b\omega_\alpha)^2 = 1.0$  and the nondimensional scale of turbulence  $L_{nd} = L/b = 5.0$ . There are now three distinct regions of qualitatively different dynamic behaviour, separated by two critical airspeeds,  $U_1^* \approx 4.05$  and  $U_2^* \approx 4.45$ . This suggests that the response goes through two bifurcations instead of one. The first region, for velocities  $\leq U_1^*$ , is characterized by a flat distribution indicating no dynamics. It is only in the third region, for velocities  $\geq U_2^*$ , that the response demonstrates fully developed periodic oscillations and we recognize the double-peaked crater-like shape of the PDD representation which characterizes the LCO motion. The pitch angles at the peaks of the PDD are analogous to the amplitude of the LCO motion of the deterministic case. The second region, between  $U_1^*$  and  $U_2^*$ , is denoted by single peak with some diffusion about its mean, which occurs at zero pitch angle. Therefore, the most probable value that the pitch angle will take during this motion is zero.

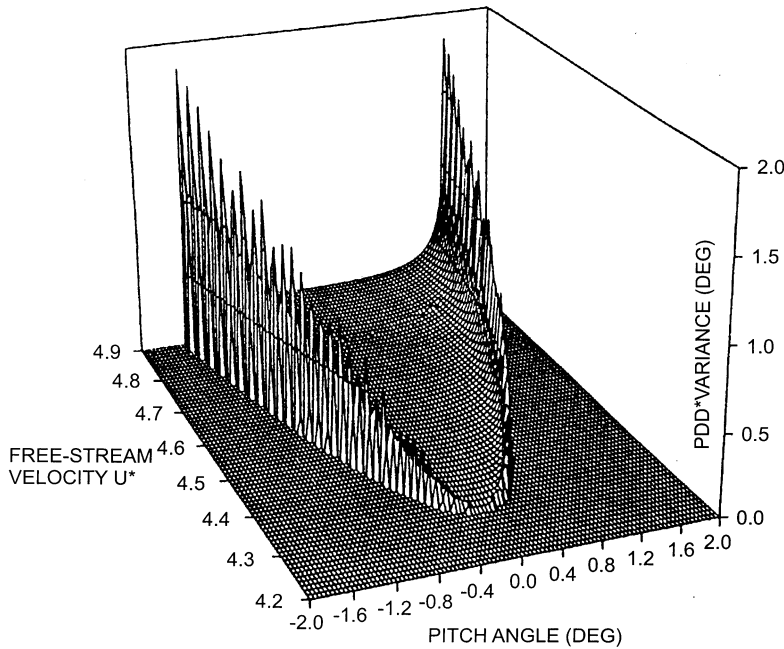


Fig. 98. Bifurcation diagram of the airfoil PDD response for the nonexcited case (from Ref. [85]).

A second observation is that the flutter speed and Hopf-bifurcation are apparently no longer coincident. It is suggested that  $U_1^*$  defines the stochastic flutter speed, as the equilibrium state becomes dynamically unstable at this velocity. Flutter bears its origin from a linear approach, and thus, can be observed with a linearized system. Because of the stochastic nature of the parametrically excited system it is difficult to pinpoint exactly the point of instability of the linear airfoil using a numerical time integration method. This is because the closer we are to the instability the lower the damping of the slow variable, thus, locally exceeding the maximum value permitted by the simulation – even though global statistical measures such as mean and variance are within an acceptable range. However, the flutter point can still be determined within an acceptable margin of error. To that extent, numerical solutions of the system with different magnitudes of the nonlinear stiffness coefficient,  $50 \leq \beta_3 \leq 800$  gave exactly the same flutter speed, confirming that this is a linear phenomenon.

The definition of the stochastic Hopf-bifurcation point is somewhat more ambiguous and leaves room for interpretation. Although the spectrum of Lyapunov exponents has not been calculated for the second bifurcation, intuitively it is suggested that this second topological change in the dynamics is not associated with a vanishing of the exponents or a critical slowdown of the dynamics. This is contrary to deterministic bifurcation phenomenon, and is purely a product of the interaction between the stochastic and nonlinear natures of the system. In stochastic nonlinear dynamical systems, this bifurcation is called a P-bifurcation [3] (P for Phenomenological). The first bifurcation is termed a D-bifurcation (D for Dynamical). Poirel and Price [85] argued that the P-bifurcation represents the stochastic Hopf-bifurcation and occurs at  $U_2^*$ , i.e., where the PDD



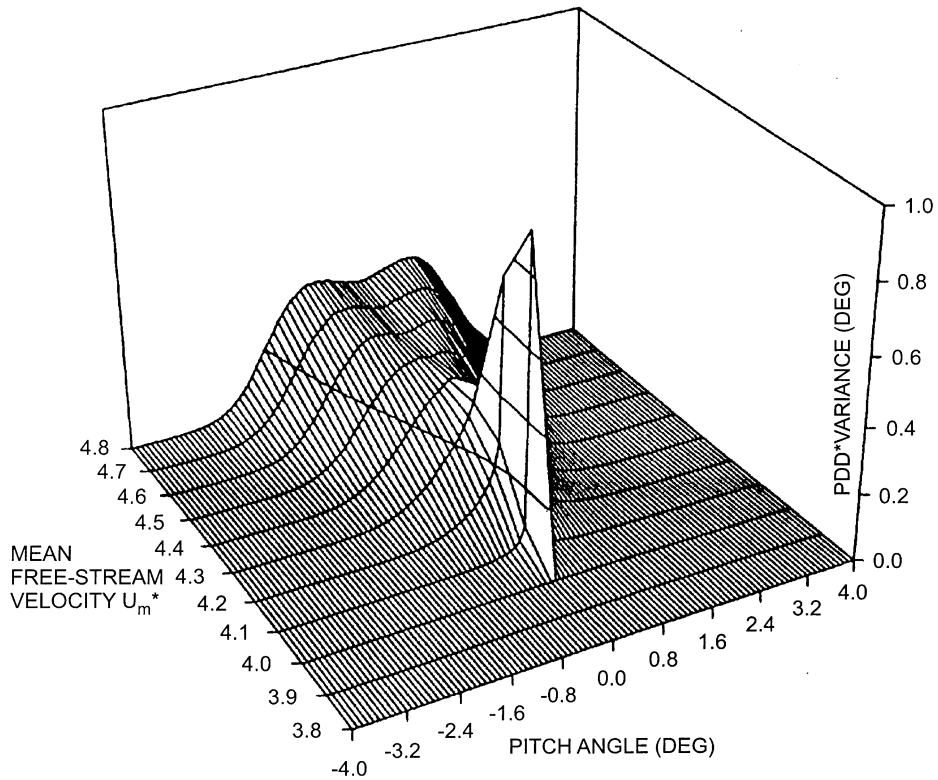


Fig. 99. Bifurcation diagram of the airfoil PDD response for the excited case;  $\sigma_{g,nd}^2 = 1.0$ ,  $L_{nd} = 5.0$  (from Ref. [85]).

changes from being single- to double-peaked, and also where fully developed periodic oscillations start to appear in the time history.

A final observation concerns the exact location of the two bifurcation airspeeds. This is best seen from the results of Fig. 97, where the vertical axis shows the variance and most probable value of the pitch state. For this particular set of parameters, interpolation of the variance results suggests the stochastic flutter point to be at  $U_1^* = 4.05$ , while the most probable value suggests that the stochastic Hopf-bifurcation occurs at  $U_2^* = 4.45$ . Also presented in Fig. 97 for comparison is the nonexcited deterministic case. Compared with the nonexcited case, the effect of the longitudinal random gust is to advance the flutter speed and to postpone the onset of the LCO. Advancement of the flutter point can be explained in part due to the quadratic airspeed term. The longitudinal gust increases the average magnitude of the dynamic pressure as defined by  $\rho \bar{U}^2/2$  or  $\rho(U_m^2 + u_g^2)/2$ , so that the dynamic pressure associated with the mean airspeed at which flutter occurs is lower than for the non-excited case. The presence of the random component in the linear airspeed also influences the location of the flutter point, but may advance or retard it, as discussed by Prussing and Lin [91]. In their work quasi-steady aerodynamics was employed, and the effect of the quadratic noise term was neglected, also white noise was assumed.

Some results showing the effects of gust intensity and frequency are presented in Fig. 100, where the two bifurcation airspeeds are plotted as a function of gust variance for three different scales of

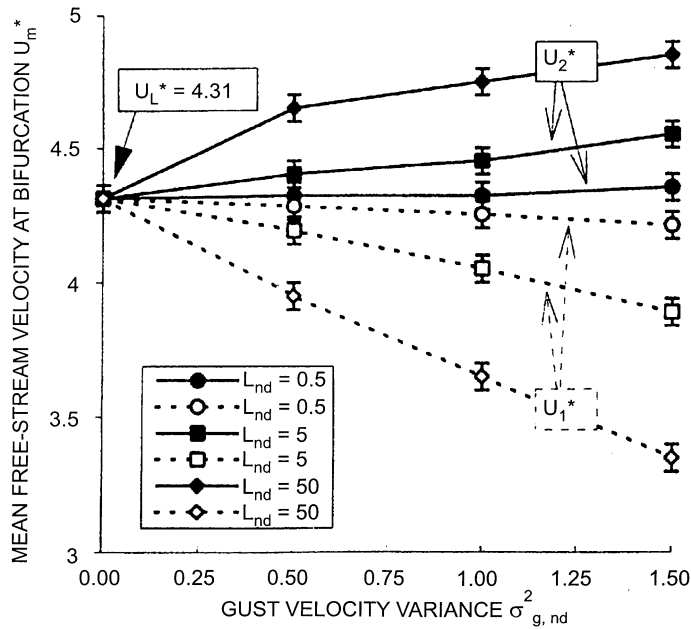


Fig. 100. Bifurcation diagram of the mean-free stream velocities as a function of the gust variance for three scales of turbulence (from Ref. [85]).

turbulence. Zero gust variance corresponds to the deterministic case, giving unique flutter and Hopf-bifurcation airspeeds,  $U_L^* = 4.31$ . As the variance is increased, the region of single peak PDD becomes larger for all three cases. However, the second bifurcation point,  $U_2^*$ , seems to depart from the nonexcited case at a lower rate than the first bifurcation. The effect of scale of turbulence, which is a measure of the frequency content, is perhaps more interesting. For equivalent gust variances, the two bifurcation airspeeds approach each other as the bandwidth of the gust is increased. This explained by noting that the effective portion of the excitation on the system, defined by the range of natural frequencies or time scales of the deterministic airfoil relative to the gust bandwidth, decreases for a larger total bandwidth. Fig. 96 shows that the area under the PSD curves for reduced frequencies lower than 0.18, which is the LCO frequency, decreases for smaller scales of turbulence.

Considering a more practical perspective to the behavior and significance of the single-peak region it is noted that this region has no analog in the deterministic case, as opposed to the two extreme regions. It cannot be approximated by either an equilibrium point, nor a limit cycle oscillation. As mentioned earlier although dynamical behavior is observed between  $U_1^*$  and  $U_2^*$ , the most probable value that the pitch (or plunge) variable takes during the motion is zero. This is of significance when considering structural fatigue limitations.

## 8. Conclusions

Classical theory in aeroelasticity assumes linear structures and aerodynamics in studying the interaction between the inertia, structural and aerodynamic forces. Many experiments, whether

performed in wind tunnels or on flight test of aircraft, show phenomena that are not predictable from linear theory, examples of which are limit cycle oscillations and random-like responses of aero-surfaces that are self-excited or occur in the presence of air turbulence and gusts.

This review introduces examples of nonlinearities, both in the structural and aerodynamic forces, and suggests methods to deal with them. The handling of the structure is simplified by considering only concentrated nonlinearities represented by the three classical types, namely, the cubic, bilinear and hysteresis restoring force of a nonlinear spring. The study is further simplified by considering only two-degree-of-freedom oscillations of an airfoil immersed in a subsonic flow field. Multi-degree-of-freedom oscillations introduce more complexities in the mathematical formulation, but the fundamental ideas of LCO, bifurcations and chaos can adequately be investigated from a binary system oscillating in pitch and plunge. The sensitivity to initial conditions in nonlinear aeroelasticity can only be studied from numerical integration of the equations of motion. The describing function technique assumes the airfoil motion to be harmonic, and is useful to predict the airfoil amplitudes when LCO have already set in. This method has the advantage that it can handle a complex aircraft configuration with a large number of vibration modes by essentially considering an equivalent linear system where tools routinely used by aircraft designers can compute flutter boundaries and response amplitudes. Analytical methods presented in this review for analyzing bifurcations can be used to determine the amplitudes and frequencies of supercritical post-Hopf-bifurcations, but they are limited to those cases where the structural nonlinearities can be represented by simple analytical functions, such as a cubic spring. However, much can be learned from the analytical analysis since it gives good physical insight into the bifurcation process.

Most of the analysis in this review deals with a single nonlinearity in the pitch degree of freedom. Only one example is given for a coupled cubic nonlinearity in the plunge and pitch motions. Even in the absence of aerodynamics, the equations of motion describing the coupled Duffing's oscillators show an extremely complex jump condition. There are infinite possibilities, and perhaps unknown complexities, of the airfoil motion that may occur when various types of nonlinearities are coupled. Also, the three basic nonlinearities can possess a large number of geometrical configurations. This, together with the fact that a number of parameters are needed to define the airfoil, makes a complete parametric study of the simple two-degree-of-freedom system practically impossible. In addition, four initial conditions specifying the plunge and pitch displacements and their time derivatives are required to uniquely define the problem. The examples in this review on concentrated structural nonlinearities are therefore incomplete, but leave opportunities for the interested reader to explore more complex airfoil motions that will be encountered with various coupled nonlinearities, airfoil parameters and initial conditions.

Aerodynamic nonlinearities are only briefly discussed in this review. This is due to the fact that analysis can only be carried out using complex aerodynamic codes that require large amount of computing time, and hence there are few examples in the literature that the authors can draw on to give a detailed and in-depth review of this subject. However, the basic solution techniques are given in this review. Because of the long computing time required to execute a coupled aerodynamics and structural dynamics code, only limited cases of interest can be studied.

Numerical simulations can isolate interesting phenomena so that they can be studied individually. This is unlike experiments in practical situations where a number of system phenomena may occur simultaneously, thus making the problem much more complex and difficult to handle. However, we must be prepared to deal with complex physical aeroelastic problems, and the

methodologies commonly used to handle linear problems fail in parametric identification of nonlinear systems. Extending the methods developed for nonlinear mechanical systems to aeroelastic systems is a challenging topic for aeroelasticians. The demand for reliable tools to predict aeroelastic characteristics of modern aircraft that fly in the high subsonic and transonic speed regimes has not been successfully met since transonic flights began nearly a quarter of a century ago. Aging and military aircraft carrying heavy external stores potentially face problems arising from nonlinearities in the structure. Learning the source of LCO, bifurcations and chaos can possibly lead to the discovery of methods to control these undesirable phenomena. This will result in more comfortable rides for passengers, better aircraft handling characteristics, and longer aircraft life span by reducing structural fatigue and other damaging effects associated with LCO.

## Acknowledgements

The authors would like to acknowledge the support they received from the Natural Sciences and Engineering Research Council of Canada.

## References

- [1] Alighanbari H, Price SJ. The post-Hopf-bifurcation response of an airfoil in incompressible two-dimensional flow. *Nonlinear Dyn* 1996;10:381–400.
- [2] Argyris J, Faust G, Haase M. An exploration of chaos – an introduction for natural scientists and engineers, Texts on computational mechanics, vol. VII. Amsterdam: North-Holland, 1994.
- [3] Arnold L, Jones C, Mischaikow K, Raugel G. Dynamical systems, Lectures given at the 2nd session of the Centro Internazionale Matematico Estivo. Berlin: Springer, 1995.
- [4] Ashley H. On the role of shock waves in the “sub-transonic” flutter phenomenon. AIAA 79-0765, AIAA/ASME/ASCE/AHS 20th Structures, Structural Dynamics, and Materials Conf, 4–6 April MO: St. Louis, 1979.
- [5] Ballhaus WF, Goorjian PM. Implicit finite-difference computations of unsteady transonic flows about an airfoil. *AIAA J*. 1977;15:1728–35.
- [6] Barnes TJ. Overview of the activities of the ad hoc committee of international gust specialists. AGARD-R-798, 1994.
- [7] Bathe KJ, Wilson EL. Numerical methods in finite element analysis. Englewood Cliffs, NJ. Prentice-Hall, 1976.
- [8] Batina JT. Unsteady transonic small-disturbance theory including entropy and vorticity effects. *J Aircraft* 1989;26:531–8.
- [9] Batina JT. Unsteady transonic algorithm improvements for realistic aircraft configurations. *J Aircraft* 1989;26:131–9.
- [10] Beddoes TS. A synthesis of unsteady aerodynamic effects including stall hysteresis. *Vertica* 1976;1:113–23.
- [11] Bendiksen OO, Kousen KA. Transonic flutter analysis using the Euler equations. AIAA 87-0911-CP, AIAA Dynamics Specialists Conf, Monterey, CA, April 1987.
- [12] Bennett RM, Eckstrom CV, Rivera JA Jr, Dansberry BE, Farmer MG, Durham MH. The benchmark aeroelastic models program – description and highlights of initial results. AGARD-CP-507, 1992:25.1–11.
- [13] Bergé P, Pomeau Y, Vidal C. Order within chaos, New York: Wiley, 1986.
- [14] Beyn WJ. Numerical methods for dynamical systems. In: Light W, editor. *Advances in numerical analysis*. Oxford: Oxford Science Publication, 1991.
- [15] Bielawa RL, Johnson SA, Chi RM, Gangwani ST. Aeroelastic analysis for propellers. NASA CR 3729, 1983.
- [16] Borland CJ, Rizzeta DP. Nonlinear transonic flutter analysis. *AIAA J* 1982;20:1606–15.

- [17] Borland CJ, Rizzetta DP, Yoshihara H. Numerical solution of three-dimensional unsteady transonic flow over swept wings. *AIAA J* 1982;20:340–7.
- [18] Breitbach EJ. Effect of structural nonlinearities on aircraft vibration and flutter. Presented at the 45th Structures and Materials AGARD Panel Meeting. AGARD Report 665. Voss, Norway, 1977.
- [19] Breitbach EJ. Flutter analysis of an airplane with multiple structural nonlinearities in the control system. NASA TP 1620, 1980.
- [20] Carr J. Applications of centre manifold theory. New York: Springer, 1981.
- [21] Chan Y. Numerical simulation of a two-dimensional airfoil with a hysteresis nonlinearity. National Research Council Canada, NRC summer student project Report IAR-97-1. September 1997.
- [22] De Ferrari G, Chesta, L, Sensburg O, Lotze A. Effects of nonlinearities on wing-store flutter. Mathematical modeling of linear and non-linear aircraft structures. AGARD-R-687, 1980.
- [23] Doedel EJ, Kernevez JP. AUTO: software for continuation and bifurcation problems in ordinary differential equations. Applied Mathematics Report. California Institute of Technology, 1986.
- [24] Dunn P, Dugundji J. Nonlinear stall flutter and divergence analysis of cantilevered graphite/epoxy wings. *AIAA J* 1992;30:153–62.
- [25] Edwards JW, Malone JB. Current status of computational methods for transonic unsteady aerodynamics and aeroelastic applications. AGARD-CP-507. March 1992;1.1–24.
- [26] Edwards JW. Transonic shock oscillations and wing flutter calculated with an interactive boundary layer coupling method. NASA Technical Memorandum 110284, NASA Langley Research Center, Hampton, Virginia, 1996.
- [27] Edwards JW. Transonic shock oscillations calculations with a new interactive boundary layer coupling method. *AIAA Paper* 93-0777, 1997.
- [28] Ericsson LE, Reding JP. Dynamic stall at high frequency and large amplitude. *J Aircraft* 1980;17:136–42.
- [29] Ericsson LE, Reding JP. Fluid mechanics of dynamic stall. Part I: unsteady flow concepts. *J Fluids Struct* 1988;2:1–33.
- [30] Ericsson LE, Reding JP. Fluid mechanics of dynamic stall. Part II: prediction of full scale characteristics. *J Fluids Struct* 1988;2:113–43.
- [31] Fung YC. An introduction to the theory of aeroelasticity. New York: Dover, 1993.
- [32] Gangwani ST. Prediction of dynamic stall and unsteady airloads for rotor blades. *J Am Helicopter Soc* 1982;27:57–64.
- [33] Gangwani ST. Synthesized airfoil data method for prediction of dynamic stall and unsteady airloads. Proc Annual Forum of the AHS. Washington, DC: American Helicopter Society, 1983.
- [34] Gangwani ST. Synthesized airfoil data method for prediction of dynamic stall and unsteady airloads. *Vertica* 1984;8:93–118.
- [35] Gelb A, Vander Velde WA. Multiple-input describing functions and nonlinear system design. New York: McGraw-Hill, 1968.
- [36] Gong L, Wong YS, Lee BHK. Dynamics of a coupled system of Duffing's equations. In Dynamics of continuous, discrete and impulsive systems, vol. 4. Waterloo: Watam Press, 1998:99–119.
- [37] Gormont RE. A numerical model of unsteady aerodynamics and radial flow for application to helicopter rotors. USAAMRDL-TR-72-67, 1973.
- [38] Gray L, Liiva J. Two dimensional tests of airfoils oscillating near stall. vol II, Data Report, USAAVLABS Technical Report 68-13B, USAAMRDL, Ft. Eustio, VA, 1968.
- [39] Guckenheimer J, Holmes P. Nonlinear oscillations, dynamical systems, and bifurcation of vector fields. Berlin: Springer, 1993.
- [40] Guruswamy GP, Goorjian PM, Merrit FJ. ATRAN3S: an unsteady transonic code for clean wings. NASA TM-86783, 1985.
- [41] Guruswamy GP. ENSAERO – A multidisciplinary program for fluid/structural interaction studies of aerospace vehicles. *Comput Systems Engng* 1990;1:237–56.
- [42] Hartman P. Ordinary differential equations, 2nd ed. Boston: Birkäuser, 1982.
- [43] Hayashi C. Nonlinear oscillations in physical systems. New York: McGraw Hill, 1964.
- [44] Hoblit FM. Gust loads on aircraft: concepts and applications. AIAA Education Series. Washington: AIAA, 1988.

- [45] Horsthemke W, Lefever R. Noise-induced transitions; Theory and applications in physics, chemistry and biology. Berlin: Springer, 1984.
- [46] Houbolt JC. A recurrence matrix solution for the dynamic response of elastic aircraft. *J Aeronaut Sci* 1950;17:540–50.
- [47] Hounjet MHL. A field panel/finite difference method for potential unsteady transonic flow. *AIAA J* 1985;23:537–45.
- [48] Isaacs R. Airfoil theory for flows of variable velocity. *J Aeronaut Sci* 1945;13:113–7.
- [49] Isogai K, Suetsugu K. Numerical simulation of transonic flutter of a supercritical wing. NAL Report TR-726T, National Aerospace Laboratory, Japan, 1982.
- [50] Isogai K. Numerical simulation of shock-stall flutter of an airfoil using Navier-Stokes equations. *J Fluids Struct* 1993;7:595–609.
- [51] Johnson EC. Sinusoidal analysis of feedback-control systems containing nonlinear elements. *Trans AIEE* 1952;71:169–81.
- [52] Jones DJ, Lee BHK. Time marching numerical solution of the dynamic response of nonlinear systems. Aeronautical Note NAE-AN-25, NRC No. 24131, National Research Council Canada, 1985.
- [53] Jones RT. The unsteady lift of a wing of finite aspect ratio. NACA Rept 681, 1940.
- [54] Keleris JP. Nonlinear dynamics of an airfoil forced to oscillate in dynamic stall. M Engng Thesis. McGill University, Montreal, Canada, 1994.
- [55] Kim SH, Lee I. Aeroelastic analysis of a flexible airfoil with a freeplay non-linearity. *J Sound Vib* 1996;193:823–46.
- [56] Kousen KA, Bendiksen OO. Nonlinear aspects of the transonic aeroelastic problem. Proc AIAA/ASME/ASCE/AHS 29th Structures, Structural Dynamics and Materials Conf, Williamsburg, Virginia, 18–20 April 1988:760–9.
- [57] Kousen KA, Bendiksen, OO. Limit cycle phenomena in computational transonic aeroelasticity. AIAA-89-1185-CP, 1989.
- [58] Kryloff N, Bogoliuboff N. Introduction to nonlinear mechanics (Solomon Lifschitz, Trans.). Princeton: Princeton University Press, 1947.
- [59] Kuznetsov YA. Elements of applied bifurcation THEORY. Berlin: Springer, 1995.
- [60] Laurenson RM, Trn RM. Flutter analysis of missile control surfaces containing structural nonlinearities. *AIAA J* 1980;18:1245–51.
- [61] Laurenson RM, Hauenstein AJ, Gubser JL. Effects of structural nonlinearities on limit-cycle response of aerodynamic surfaces. AIAA 86-0899, 1986.
- [62] Lee BHK. A study of transonic flutter of a two-dimensional airfoil using the U-g and p-k methods. Aeronautical Rept. LR-615, NRC No. 23959, National Research Council Canada, 1984.
- [63] Lee BHK, LeBlanc P. Forced oscillation of a two-dimensional airfoil with nonlinear aerodynamic loads. Aeronautical Report LR-617, National Research Council of Canada, 1986.
- [64] Lee BHK, LeBlanc P. Flutter analysis of a two-dimensional airfoil with cubic nonlinear restoring force. Aeronautical Note NAE-AN-36, NRC No. 25438, National Research Council of Canada, 1986.
- [65] Lee BHK, Desrochers J. Flutter analysis of a two-dimensional airfoil containing structural nonlinearities. Aeronautical Report LR-618, NRC No. 27833, National Research Council of Canada, 1987.
- [66] Lee BHK, Tron A. Effects of structural nonlinearities on flutter characteristics of the CF-18 aircraft. *J Aircraft* 1989;26:781–6.
- [67] Lee BHK. Oscillatory shock motion caused by transonic shock-boundary-layer interaction. *AIAA J* 1990; 28:942–4.
- [68] Lee BHK, Murty H, Jiang H. Role of Kutta waves on oscillatory shock motion on an airfoil. *AIAA J* 1994;32:789–96.
- [69] Lee BHK, Gong L, Wong YS. Analysis and computation of nonlinear dynamic response of a two-degree-of-freedom system and its application in aeroelasticity. *J Fluids Struct* 1997;11:225–46.
- [70] Lee BHK, Jiang LY, Wong YS. Flutter of an airfoil with a cubic nonlinear restoring force, AIAA Paper 98-1725, 39th AIAA/ASME/ASCE/AHS/ASC Structures, Structural Dynamics, and Materials Conf, 20–23 April, Long Beach, CA, 1998.
- [71] Lee BHK, Wong YS. Neural network parameter extraction with application to flutter signals. *J Aircraft* 1998;35:165–8.
- [72] Lee CL. An iterative procedure for nonlinear flutter analysis. *AIAA J* 1986;24:833–40.

- [73] Leishman JG, Beddoes TS. A semi-empirical model for dynamic stall. *J Am Helicopter Soc* 1989;34:3–17.
- [74] Li X, Fleeter S. Dynamic stall generated airfoil oscillations including chaotic responses. AIAA 97-1022, 38th AIAA/ASME/ASCE/AHS Structures, Structural Dynamics and Materials Conf, Kissimmee, FL, April, 1997.
- [75] Liu JK, Zhao LC. Bifurcation analysis of airfoils in incompressible flow. *J Sound Vib* 1992;154:117–24.
- [76] Liu L, Wong YS, Lee BHK. Application of the center manifold theory in nonlinear aeroelasticity. CEAS/AIAA/ICASE/NASA Langley International Forum on Aeroelasticity and Structural Dynamics. Williamsburg, VA, June 1999.
- [77] Loring SJ. General approach to the flutter problem. *SAE Trans* 1941;49:345–56.
- [78] Mazelsky B, Drischler JA. Numerical determination of indicial lift and moment functions for a two-dimensional sinking and pitching airfoil at mach numbers 0.5 and 0.6. NACA TN 2739, 1952.
- [79] Mehta UB. Dynamic stall of oscillating airfoil, AGARD-CP-227. *Unsteady Aerodynamics*. 1977;23:1–32.
- [80] Miller RK. The steady state response of systems with hardening hysteresis. Paper ASME 77-DET-71, 1977.
- [81] Moon FC. *Chaotic and fractal dynamics*, New York: Wiley, 1992.
- [82] Neil DJ, Johnson EH, Canfield R. ASTROS-A multidisciplinary automated structural design tool. *J Aircraft* 1990;27:1021–7.
- [83] Osher S, Hafez M, Whitlow W Jr. Entropy condition satisfying approximations for the full potential equation of transonic flow. *Math Comput* 1985;44:1–29.
- [84] Poincaré H. *Les méthodes nouvelles de la mécanique céleste*. Paris, 1893.
- [85] Poirel DC, Price SJ. Post-instability behavior of a structurally nonlinear airfoil in longitudinal turbulence. *J Aircraft* 1997;34:619–26.
- [86] Prenter PM. *Splines and variational methods*. New York: Wiley, 1975.
- [87] Press WH, Flannery BP, Teukolsky SA, Vetterling WT. *Numerical recipes, The art of scientific computing*. Cambridge, New York, 1986.
- [88] Price SJ, Lee BHK, Alighanbari H. Post instability behaviour of a two-dimensional airfoil with a structural nonlinearity. *J Aircraft* 1994;31:1395–401.
- [89] Price SJ, Alighanbari H, Lee BHK. The aeroelastic response of a two-dimensional airfoil with bilinear and cubic structural nonlinearities. *J Fluids Struct* 1995;9:175–93.
- [90] Price SJ, Keleris JP. Non-linear dynamics of an airfoil forced to oscillate in dynamic stall. *J Sound Vib* 1996;194:265–83.
- [91] Prussing JE, Lin YK. A closed-form analysis of rotor blade flap-lag stability in hover and low-speed forward flight in turbulent flow. *J Am Helicopter Soc* 1983;28:42–6.
- [92] Reddy TSR, Kaza KRV. A comparative study of some dynamic stall methods. NASA TM-88917, 1987.
- [93] Schuster DM, Vadyak J, Atta EJ. Flight loads prediction methods for fighter aircraft. WRDC-TR-89-3104, 1989.
- [94] Seydel R. *From equilibrium to chaos*. New York: Elsevier, 1988.
- [95] Shen SF, Hsu CC. Analytical results of certain nonlinear flutter problems. *J Aeronaut Sci* 1958;25:136–7.
- [96] Shen SF. An approximate analysis of nonlinear flutter problems. *J Aerosp Sci* 1959;26:25–32, 45.
- [97] Shen SF. Author's reply to: Remarks on Analytical results of certain nonlinear flutter problems. *J Aerosp Sci* 1959;26:52–3.
- [98] Steinhoff J, Jameson A. Multiple solutions of the transonic potential equation. *AIAA J* 1982;20:1521–5.
- [99] Stoker JJ. *Nonlinear vibrations in mechanical and electrical systems*. New York: Interscience Publishers, 1950.
- [100] Straganac TW, Mook DT, Mitchum MV. The numerical simulation of subsonic flutter. AIAA 87-1428, AIAA 19th Fluid Dynamics, Plasma Dynamics and Lasers Conf, Honolulu, Hawaii, 8–10 June 1987.
- [101] Tang DM, Dowell EH. Flutter and stall response of a helicopter blade with structural nonlinearity. *J Aircraft* 1992;29:953–60.
- [102] Tang DM, Dowell EH. Comparison of theory and experiment for non-linear flutter and stall response of a helicopter blade. *J Sound Vib* 1993;165:251–76.
- [103] Tang DM, Dowell EH. Experimental and theoretical study for nonlinear aeroelastic behaviour of a flexible rotor blade. *AIAA J* 1993;31:1133–42.
- [104] Tang DM, Dowell EH. Experimental investigation of three-dimensional dynamic stall model oscillating in pitch. *J Aircraft* 1995;32:1062–71.

- [105] Tang DM, Dowell EH. Nonlinear response of a non-rotating rotor blade due to a periodic gust. *J Fluids Struct* 1996;10:721–42.
- [106] Tang DM, Dowell EH. Nonlinear rotor aeroelastic analysis with stall and advanced wake dynamics. *J Aircraft* 1997;34:679–87.
- [107] Theodorsen T. General theory of aerodynamic instability and the mechanism of flutter. NACA Report 496, 1935.
- [108] Thompson JMT, Stewart HB. Nonlinear dynamics and chaos. Chichester: Wiley, 1986.
- [109] Tran CT, Petot D. Semi-empirical model for the dynamic stall of airfoils in view of the application to the calculation of responses of a helicopter blade in forward flight. *Vertica* 1981;5:35–53.
- [110] Tran CT, Falchero D. Application of the ONERA dynamic stall model to a helicopter blade in forward flight. *Vertica* 1982;6:219–39.
- [111] Ueda T, Dowell EH. Flutter analysis using nonlinear aerodynamic forces. *J Aircraft* 1984;21:101–9.
- [112] Ueda Y. Steady motions exhibited by Duffing's equation: a picture cook of regular and chaotic motions. In: Holmes PJ, editor. New approaches to nonlinear problems in dynamics. Philadelphia: SIAM, 1980:311–22.
- [113] Van der Wall BG. The influence of variable flow velocity on unsteady airfoil behavior. DLR-FB 92-22, 1992.
- [114] Van der Wall BG, Leishman JG. On the influence of time-varying flow velocity on unsteady aerodynamics. *J Am Helicopter Soc* 1994;39:25–36.
- [115] Verhulst F. Nonlinear differential equations and dynamical systems. Berlin: Springer, 1990.
- [116] Whitlow W Jr, Hafez MH, Osher SJ. An entropy correction method for unsteady full potential flows with strong shocks. AIAA Paper 86-1768-CP, 1986.
- [117] Wiggins S. Introduction to applied nonlinear dynamical systems and chaos. New York: Springer, 1990.
- [118] Wong YS, Lee BHK. Development of a three-dimensional unsteady transonic aerodynamics computer code for flutter analysis. Proc 17th Congress of the Int Council of the Aeronautical Sciences Stockholm, Sweden, 1990;1:19–29.
- [119] Wong YS, Lee BHK, Gong L. Dynamic response of a two-degree-of-freedom system with a cubic nonlinearity. 3rd Int Conf on Computational Physics. Chung Li, Taiwan, 1995.
- [120] Woolston DS, Runyan HL, Byrdsong TA. Some effects of system nonlinearities in the problem of aircraft flutter. NACA TN 3539, 1955.
- [121] Woolston DS, Runyan HL, Andrews RE. An investigation of effects of certain types of structural nonlinearities on wing and control surface flutter. *J Aeronaut Sci* 1957;24:57–63.
- [122] Wu JC, Kaza KRV, Sankar LN. Technique for the prediction of airfoil flutter characteristics in separated flows. *J Aircraft* 1989;26:168–77.
- [123] Yang ZC, Zhao LC. Analysis of limit cycle flutter of an airfoil in incompressible flow. *J Sound Vib* 1988;123:1–13.
- [124] Yates EC Jr. AGARD standard aeroelastic configurations for dynamic response. Candidate Configuration I. – Wing 445.6. NASA TM 100492, 1987.
- [125] Zhao LC, Yang ZC. Chaotic motions of an airfoil with nonlinear stiffness in incompressible flow. *J Sound Vib* 1990;138:245–54.

## Appendix

The coefficients of Eqs. (19) and (20) are given as follows:

$$c_0 = 1 + \frac{1}{\mu}, \quad c_1 = x_a - \frac{a_h}{\mu}, \quad c_2 = 2\zeta_\xi \frac{\bar{\omega}}{U^*} + \frac{2}{\mu}(1 - \psi_1 - \psi_2),$$

$$c_3 = \frac{1 + 2(1/2 - a_h)(1 - \psi_1 - \psi_2)}{\mu}, \quad c_4 = \frac{2}{\mu}(\psi_1 \varepsilon_1 + \psi_2 \varepsilon_2),$$

$$c_5 = \frac{2}{\mu}[(1 - \psi_1 - \psi_2) + (1/2 - a_h)(\psi_1 \varepsilon_1 + \psi_2 \varepsilon_2)],$$



$$c_6 = \frac{2}{\mu} \psi_1 \varepsilon_1 [1 - (1/2 - a_h) \varepsilon_1], \quad c_7 = \frac{2}{\mu} \psi_2 \varepsilon_2 [1 - (1/2 - a_h) \varepsilon_2], \quad c_8 = -\frac{2}{\mu} \psi_1 \varepsilon_1^2,$$

$$c_9 = -\frac{2}{\mu} \psi_2 \varepsilon_2^2, \quad d_0 = \frac{x_a}{r_a^2} - \frac{a_h}{\mu r_a^2}, \quad d_1 = 1 + \frac{1 + 8a_h^2}{8\mu r_a^2},$$

$$d_2 = 2 \frac{\zeta_a}{U^*} + \frac{1 - 2a_h}{2\mu r_a^2} - \frac{(1 + 2a_h)(1 - 2a_h)(1 - \psi_1 - \psi_2)}{2\mu r_a^2},$$

$$d_3 = -\frac{(1 + 2a_h)(1 - \psi_1 - \psi_2)}{\mu r_a^2} - \frac{(1 + 2a_h)(1 - 2a_h)(\psi_1 \varepsilon_1 + \psi_2 \varepsilon_2)}{2\mu r_a^2},$$

$$d_4 = -\frac{(1 + 2a_h)(1 - \psi_1 - \psi_2)}{\mu r_a^2}, \quad d_5 = -\frac{(1 + 2a_h)(\psi_1 \varepsilon_1 + \psi_2 \varepsilon_2)}{\mu r_a^2},$$

$$d_6 = -\frac{(1 + 2a_h)\psi_1 \varepsilon_1 [1 - (1/2 - a_h) \varepsilon_1]}{\mu r_a^2}, \quad d_7 = -\frac{(1 + 2a_h)\psi_2 \varepsilon_2 [1 - (1/2 - a_h) \varepsilon_2]}{\mu r_a^2},$$

$$d_8 = \frac{(1 + 2a_h)\psi_1 \varepsilon_1^2}{\mu r_a^2}, \quad d_9 = \frac{(1 + 2a_h)\psi_2 \varepsilon_2^2}{\mu r_a^2}$$

The coefficients of Eqs. (27) and (28) are given below:

$$m_1 = 1 + \frac{1}{\mu}, \quad m_2 = x_a - \frac{a_h}{\mu}, \quad m_3 = (\varepsilon_1 + \varepsilon_2) \left( 1 + \frac{1}{\mu} \right) + \frac{2(1 - \psi_1 - \psi_2)}{\mu} + 2\zeta_\xi \left( \frac{\bar{\omega}}{U^*} \right),$$

$$m_4 = \frac{1}{\mu} + 2(1 - \psi_1 - \psi_2) \frac{(1/2 - a_h)}{\mu} + (\varepsilon_1 + \varepsilon_2) \left( x_a - \frac{a_h}{\mu} \right),$$

$$m_5 = \varepsilon_1 \varepsilon_2 \left( 1 + \frac{1}{\mu} \right) + \frac{2(\varepsilon_1 + \varepsilon_2 - \psi_1 \varepsilon_2 - \psi_2 \varepsilon_1)}{\mu} + 2\zeta_\xi (\varepsilon_1 + \varepsilon_2) \left( \frac{\bar{\omega}}{U^*} \right),$$

$$m_6 = \varepsilon_1 \varepsilon_2 \left( x_a - \frac{a_h}{\mu} \right) + \frac{(\varepsilon_1 + \varepsilon_2) + 2(1 - \psi_1 - \psi_2)}{\mu} + \frac{2(1/2 - a_h)(\varepsilon_1 + \varepsilon_2 - \psi_1 \varepsilon_2 - \psi_2 \varepsilon_1)}{\mu},$$

$$m_7 = \frac{2\varepsilon_1 \varepsilon_2}{\mu} + 2\varepsilon_1 \varepsilon_2 \zeta_\xi \left( \frac{\bar{\omega}}{U^*} \right), \quad m_8 = \frac{\varepsilon_1 \varepsilon_2}{\mu} + \frac{2\varepsilon_1 \varepsilon_2 (1/2 - a_h)}{\mu} + \frac{2(\varepsilon_1 + \varepsilon_2 - \psi_1 \varepsilon_2 - \psi_2 \varepsilon_1)}{\mu},$$

$$m_9 = 0, \quad m_{10} = \frac{2\varepsilon_1 \varepsilon_2}{\mu}, \quad n_1 = \left( x_a - \frac{a_h}{\mu} \right) \frac{1}{r_a^2}, \quad n_2 = \left( 1 + \frac{a_h^2 + 1/8}{\mu r_a^2} \right),$$

$$n_3 = (\varepsilon_1 + \varepsilon_2) \left( x_a - \frac{a_h}{\mu} \right) \frac{1}{r_a^2} - \frac{2(1/2 + a_h)(1 - \psi_1 - \psi_2)}{\mu r_a^2},$$

$$n_4 = (\varepsilon_1 + \varepsilon_2) \left( 1 + \frac{a_h^2 + 1/8}{\mu r_\alpha^2} \right) + 2\zeta_\alpha \frac{1}{U^*} + \frac{(1/2 - a_h) - 2(1/2 + a_h)(1/2 - a_h)(1 - \psi_1 - \psi_2)}{\mu r_\alpha^2},$$

$$n_5 = \frac{\varepsilon_1 \varepsilon_2}{r_\alpha^2} \left( x_\alpha - \frac{a_h}{\mu} \right) - \frac{2(\varepsilon_1 + \varepsilon_2)(1/2 + a_h)}{\mu r_\alpha^2} + \frac{2(1/2 + a_h)(\psi_2 \varepsilon_1 + \psi_1 \varepsilon_2)}{\mu r_\alpha^2},$$

$$n_6 = \varepsilon_1 \varepsilon_2 \left( 1 + \frac{a_h^2 + 1/8}{\mu r_\alpha^2} \right) + (\varepsilon_1 + \varepsilon_2) \left[ \frac{2\zeta_\alpha}{U^*} + \frac{(1/2 - a_h)(1 - 2(1/2 + a_h))}{\mu r_\alpha^2} \right] \\ + \frac{2(1/2 + a_h)[-1 + \psi_1 + \psi_2 + (1/2 - a_h)(\psi_2 \varepsilon_1 + \psi_1 \varepsilon_2)]}{\mu r_\alpha^2},$$

$$n_7 = \frac{-2\varepsilon_1 \varepsilon_2 (1/2 + a_h)}{\mu r_\alpha^2},$$

$$n_8 = \varepsilon_1 \varepsilon_2 \left[ \frac{2\zeta_\alpha}{U^*} + \frac{(1/2 - a_h)[1 - 2(1/2 + a_h)]}{\mu r_\alpha^2} \right] + \frac{2(1/2 + a_h)[\psi_2 \varepsilon_1 + \psi_1 \varepsilon_2 - (\varepsilon_1 + \varepsilon_2)]}{\mu r_\alpha^2},$$

$$n_9 = 0, \quad n_{10} = \frac{-2(1/2 + a_h)\varepsilon_1 \varepsilon_2}{\mu r_\alpha^2}.$$